University of Texas at El Paso
ScholarWorks@UTEP

Open Access Theses & Dissertations

2023-05-01

Novel Pathways To Tailor Charge And Spin In Materials And Investigating The Impact On Sensing And Electrochemical Energy Applications

Aruna Narayanan Nair
University of Texas at El Paso

Follow this and additional works at: https://scholarworks.utep.edu/open_etd

 Part of the Chemistry Commons

Recommended Citation

Narayanan Nair, Aruna, "Novel Pathways To Tailor Charge And Spin In Materials And Investigating The Impact On Sensing And Electrochemical Energy Applications" (2023). *Open Access Theses & Dissertations*. 3882.
https://scholarworks.utep.edu/open_etd/3882

This is brought to you for free and open access by ScholarWorks@UTEP. It has been accepted for inclusion in Open Access Theses & Dissertations by an authorized administrator of ScholarWorks@UTEP. For more information, please contact lweber@utep.edu.

NOVEL PATHWAYS TO TAILOR CHARGE AND SPIN IN MATERIALS AND INVESTIGATING THE IMPACT ON SENSING AND ELECTROCHEMICAL ENERGY APPLICATIONS

ARUNA NARAYANAN NAIR

Doctoral Program in Chemistry

APPROVED:

Sreeprasad Sreenivasan, Ph.D., Chair

Geoffrey Saupe, Ph.D.

Lela Vukovic, Ph.D.

Dino Villagran, Ph.D.

Ramana Chintalapalle, Ph.D.

Stephen L. Crites, Jr., Ph.D.

Dean of the Graduate School

Copyright © by

Aruna Narayanan Nair

2023

NOVEL PATHWAYS TO TAILOR CHARGE AND SPIN IN MATERIALS AND INVESTIGATING THE IMPACT ON SENSING AND ELECTROCHEMICAL ENERGY APPLICATIONS

By

Aruna Narayanan Nair, M.S

DISSERTATION

Presented to the Faculty of the Graduate School of

The University of Texas at El Paso

in Partial Fulfillment

of the Requirements

for the Degree of

DOCTOR OF PHILOSOPHY

THE DEPARTMENT OF CHEMISTRY AND BIOCHEMISTRY

THE UNIVERSITY OF TEXAS AT EL PASO

May 2023

Acknowledgements

I am deeply grateful to my advisor, Dr. Sreenivasan, for his unwavering support, invaluable guidance, and constant motivation throughout my graduate studies. His profound knowledge, patience and unwavering dedication have been instrumental in shaping my research and guiding me towards academic excellence. Being his first graduate student has been a tremendous honor, and I am incredibly grateful for the opportunity to be part of his research group.

I would like to extend my sincere thanks to my committee members Dr. Saupe, Dr. Lela, Dr. Ramana, and Dr Villagran for their continuous guidance, feedback, and support throughout these years. I would like to extend my sincere gratitude to all individuals, past and present, who have contributed to my research endeavors and helped me complete this thesis. To my past lab members, Dr. Saptasree Bose, Dr. Surya Chava, Dr. Deepesh Gopalakrishnan, Ashley Gomez, and Dr. Mohamed Sanad, I express my sincere thanks for their continuous support, insightful discussions, and valuable contributions to my research. Their knowledge, expertise, and willingness to collaborate have been invaluable, and I am grateful for their contributions to my work. I am also deeply appreciative of my current lab members, Lissette Garcia, Kavish Saini, Sara Fernandez, Ana Martinez, Alexis Maurel and Daniel Gomez for their contributions and the collaborative environment we have built together in the lab. I am also grateful to the Department of Chemistry and Biochemistry and all the faculty members who have supported me throughout my journey.

Finally, I would like to extend thanks to my loved ones, who have provided me with unwavering support, encouragement, and inspiration throughout my academic journey.

Abstract

Catalysis is integral to our daily lives, as it streamlines and accelerates numerous chemical reactions essential for producing various materials, fuels, and chemicals. With the rising demand for clean, sustainable energy sources, optimizing catalytic materials and processes becomes increasingly vital. In the realm of renewable energy production, catalysis is crucial for efficiently converting energy from sustainable resources, such as solar, wind, and biomass, into chemical energy stored in fuels or directly into electrical energy.

The electronic charge distribution in materials significantly influences their physical and chemical properties, facilitating the development of advanced electronic, optoelectronic, sensing, and energy conversion devices. Since catalysis inherently involves electron transfer, electronic modulation can substantially enhance the performance of catalysts. Thus, to meet future energy demands, it is imperative to harness the power of catalysis in renewable energy devices, propelling us towards a sustainable future while mitigating climate change impacts and reducing dependence on polluting fossil fuels.

Critical to addressing future energy needs are electrochemical energy generation systems, such as fuel cells, metal-air batteries, and comprehensive water-splitting devices. At the core of these technologies are the oxygen reduction reaction (ORR), oxygen evolution reaction (OER), and hydrogen evolution reaction (HER), which are fundamental to their effectiveness. The efficiency of all these reactions depends on catalysts, and developing efficient, inexpensive, and durable catalysts is essential for their widespread adoption and the sustainability of the future energy sector.

In recent decades, the development of electrocatalysts for electrocatalytic water splitting applications has evolved from trial-and-error methodologies to rational and directed approaches at the

atomic level, primarily through modulating the electronic properties of active sites. This thesis investigates the effect of charge modulation—specifically, employing techniques such as chemical doping, strain, and heterostructure formation—and its implications for electrochemical energy generation. The primary focus is on noble metal-free nanostructured materials and low-dimensional material-based electrocatalysts, which exhibit more significant impacts on their physical, chemical, and electronic properties compared to their bulk counterparts when utilizing these strategies.

Apart from electrochemical energy applications, electronic charge modulation also plays an important role in determining the efficiency of materials for analytical sensing. The thesis also focuses on the potential of charge modulation to enhance the sensing performance of materials for pollutants, such as heavy metal ions, using two different analytical sensing techniques, Photoluminescence (PL) based, and Surface Enhanced Raman Spectroscopy (SERS). Specifically, in photoluminescence-based sensing using quantum dots the band structure modulation via foreign atom doping can be utilized to improve the quantum efficiency and limit detection.

The thesis also explores innovative strategies for spin modulation in materials. In chemistry, many chemical processes, in addition to their dependence on free and activation energies, are electron spin dependent. Recognizing the potential role of hydrogen in future energy systems, we select the OER as the model spin-dependent chemical process and investigate how spin modulation can influence its overall efficacy. Specifically, we investigate the role of spin modulation in nanostructured materials using external aids, such as magnetic fields and chiral molecule incorporation. Our findings reveal that external magnetic fields and chiral spin potentials can induce spin polarization in materials, lifting the degeneracy of spin-up and spin-down electrons. Our studies indicate that

such spin polarization can lead to enhanced OER activity by facilitating a lower tunneling barrier pathway and thereby aiding in selective electron transfer with the desired spin.

In summary, this thesis underscores the profound importance of employing innovative techniques to accurately manipulate materials' charge and spin properties, which hold great promise for a wide range of applications. By carefully selecting materials and employing external aids in a rational manner, it is possible to achieve exceptional sensing and electrocatalytic performance. The discoveries presented here not only contribute to a deeper understanding of charge and spin-dependent effects in nanostructured materials, but also offer valuable insights for designing materials with advanced functionalities tailored to specific applications. The findings have the potential to inform and inspire the development of next-generation materials that harness charge and spin modulation, ultimately enabling breakthroughs in fields such as energy conversion, sensing, and optoelectronics, paving the way towards a more sustainable and technologically advanced future.

Table of Contents

List of Figures

List of Tables

Chapter 1

Introduction

1.1 Charge modulation in materials

The electronic charge distribution in materials are fundamental aspects that dictate their physical and chemical properties, including conductivity, optical properties, and reactivity. Modulating the electronic charge distribution emerged as an efficient and highly explored approach for the rational design of materials for development of advanced electronic, optoelectronic, sensing and energy conversion devices. For instance, tuning of graphene's Fermi level by modulation of charge decides its conductivity, mobility, electronic band gap and carrier concentration.[1] Such variation of the Fermi level in graphene offers potential for field-effect transistors with tunable properties, photodetectors/gas or bio sensors with high sensitivity and response, improved solar cell performance by optical transmittance and conductivity variation etc.[2-4] Among the various applications, electrochemical energy storage and sensing are two technologically relevant areas where charge modulation can have profound implications as discussed below.

The ever-growing rapid depletion and heavy reliance of fossil fuels have triggered the world energy security concern and global environmental pollution issue. As a result, electrochemical technologies like fuel cells, metal-air batteries, and water electrolysis are gaining attention in research for both fundamental and practical purposes.[5] However, the energy efficiencies and practical applications of these technologies are largely restricted by several critical electrocatalytic reactions, such as, HER, OER and ORR.[6] The state-of-the-art catalysts for these reactions are still noble-metal-based materials, e.g., Pt-based materials for ORR and HER, RuO_2/IrO_2 for OER. Hence, developing efficient low cost electrocatalysts to enhance the sluggish reaction kinetics and lower

the energy barriers of the above electrocatalytic processes is imperative. The rate of an electrocatalytic reaction is often related to the electronic charge distribution on the catalyst. For instance, an electrocatalyst's intrinsic electronic structure dictates the thermodynamic and kinetic factors, including the intermediate adsorption energetics and reaction energy barriers of the reactions. The efficiency of an electrocatalyst is mainly influenced by the ability of each active center to transfer charges to the intermediates. The Sabatier principle suggests that a material's ability to catalyze a reaction can be qualitatively assessed by its binding energy with the reaction intermediates.[7] An ideal electrocatalyst often experiences a favorable interaction with reactants and reactive intermediates, which is neither too strong nor too weak. Thus, optimizing the charge density in materials can improve interactions with the adsorbates.

With the advancements in technology, numerous sensing strategies utilizing diverse materials have been devised to detect toxic environmental pollutants. Achieving high sensitivity and accuracy is a crucial goal in the development of sensors, including those for environmental pollutants, as they are required to meet stringent low/trace requirements and provide early warning of environmental safety hazards. One approach to enhance the sensitivity and lower the limit of detection (LOD) is to manipulate the electronic charge distribution of the sensor materials. For instance, improved LOD in electrochemical sensing of toxic heavy metal ions by quantum dots is reported after enhancement in fluorescence, conductivity, and optimum band structure by tailoring the electron cloud. Several literature points towards the fact that enhancement in conductivity, PL, absorbance etc. via charge modulation can be leveraged to build a superior sensor.[8, 9] SERS-based ultrasensitive sensing platform has also gained attention as a promising methodology to detect targeted molecules as it offers high specificity, high sensitivity and a quick readout.[10] Charge modulation of

the SERS substrate and increased electronic distribution form hotspots where the Raman effect from analyte can be amplified.

The following section is divided into two parts. The first section will discuss various methods reported to control the charge distribution in electrocatalyst, including (i) strain engineering-aided electronic modulation, (ii) introduction of defects and local electronic changes and (iii) creation of heterostructure and heterojunctions. The second part investigates the effect of charge modulation via doping and heterostructure formation for analytical sensing.

1.1.1 Charge modulation for electrocatalysis

1.1.1.1 Strain engineering-aided electronic modulation

Strain can control the distribution of electrons in materials, and changing lattice strain is used to modify the electronic properties of materials such as semiconductors, metals, and insulators. Lattice strain is a change in the distance (either an increase or a decrease compared to standard distance) between atoms on a particle surface or in a specific area. The intensity of the strain ε on a three-dimensional (3D) system can be defined as:

$$\varepsilon = \frac{d_p - d_s}{d_s} \qquad (1)$$

where d_p is the atom-atom distance on the particle surface or a local area, d_s refer to a standard atom-atom distance in the bulk material. Accordingly, the strain on materials can be compressive or tensile and can be introduced by defects, [11, 12] size/shape change,[13] clusters,[14, 15] lattice mismatch,[16, 17] bending of flexible substrates[18, 19] and dopants in solid alloys.[20-22] Norskov et al. explained the effect of strain on catalysts and the resulting activity improvement through the d-band model for transition metal-containing 3D catalysts. [23, 24] During a reaction, the interaction between

the adsorbate and metal d states splits the d states into bonding and anti-bonding orbitals and the valence state of the adsorbate couples with metal s states. The d-band model states that the strength of adsorbate binding is influenced by the occupation of bonding and anti-bonding states, and the anti-bonding state occupancy is based on its position relative to the Fermi level. For a transition metal like Fe with more than half-filled d-band, the d-band center will shift up relative to the Fermi level to maintain the fixed d occupancy. This shift moves the anti-bonding d states up and reduces their occupation, leading to a more robust interaction with reaction intermediates and improved efficiency. Similarly, A downshift in the d-band center weakens the interaction with reaction intermediates. Not just d-orbital occupancy of the metal (half-filled vs. more-than half-filled), but the type of strain (compressive vs. tensile) affects different d-orbitals differently. For example, a tensile strain helps fill in-plane orbitals ($d_{x^2y^2}$) and a compressive strain helps fill out-of-plane orbitals (d_{z^2}) in 3D catalysts. In low-dimensional Platinum-based bimetallic nanostructures, tensile lattice strain upshifts the d-band center, causing a stronger interaction with adsorbates in HER and ORR. In contrast, compressive strain downshifts the d-band center, thus weakening the interaction.[25] Interestingly, a 1% change in strain can cause a ~0.1 eV shift in the d-band center of Platinum, affecting the adsorption strength of reactants on the surface. A similar d band model has also been utilized to explain the lattice strain effect of Pt towards enhancing the ORR activity. The nanoporous gold (NPG)-Pt sample with the maximum lattice compression exhibits the best ORR activity, ~5 times higher specific activity and ~16 times higher mass activity relative to Pt/C.[26] Nevertheless, the trend mentioned only applies to late transition metals with more than half-filled d orbitals, but early transition metals with less than half-filled d orbitals show lower adsorption energy when the lattice expands.[27] This apparent discrepancy can also be explained based on the classical d-band model. The increased surface strain reduces the overlap of wavefunctions in

metals, narrowing the d-band. In late transition metals, this band narrowing increases the d-band population and shifts the d-band center upward to preserve the degree of d-band filling.[28] However, for early transition metals, it shifts the d-band center downward.

Introducing lattice strain in materials can change the lattice spacing and symmetry, affect the electronic band structure, and lower the barrier for electrocatalytic reactions by altering the electron density and energy levels of bonding electrons.[29, 30] Further, strain in two dimensional (2D) materials can also affect bond lengths and angles, leading to distinct properties (Figure 1.1). Tensile stress weakens the bonds in catalysts and decreases lattice vibrations (phonon softening), leading to a reduction in the bandgap due to modifications in out-of-plane orbitals and stronger metal-adsorbate bonds during electrocatalysis. For example, strain affects the bandgap in TMDs by deforming the X-X bond length and X-M-X bond angle, which affects the interaction between d orbitals of the transition metal (M) and p orbitals of the chalcogen (X).[31] Johari et al. showed through first-principles calculations that the bandgap in TMDs decreases rapidly under biaxial tensile strain and leads to a transition from semiconductor to metal at 10% strain, caused by the overlap of the d_{z^2} orbital at the Fermi level.[32] The strain-induced transition between indirect and direct bandgap is also observed in other 2D materials, including MoS_2,[33] WS_2,[34] antimonene,[35] black phosphorous (BP)[36], etc. Density functional theory (DFT) calculations showed that a 2% biaxial tensile strain on a MoS_2 monolayer caused a bandgap transition, change in charge carrier density, and shift of the Fermi level into the

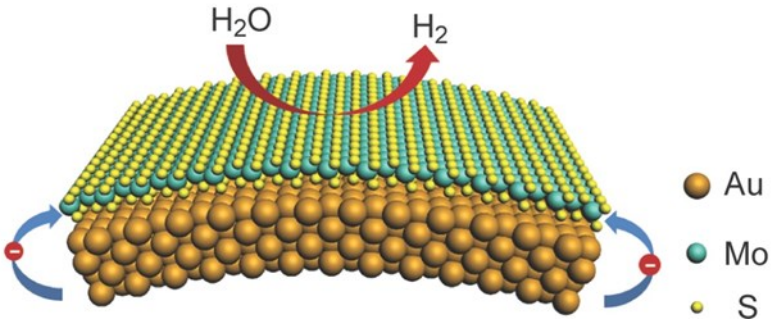

Figure 1.1: Schematic showing strain in materials. Reprinted with permissions from ref 22. Copyright © 2014, John Wiley & Sons - Books

conduction band, resulting in a metallic nature.[37] These band structure and carrier density changes can significantly impact the electrocatalytic activity of the structures, improving their efficacy towards water splitting. For instance, ultrahigh conductivity and subsequent high electrocatalytic activity in pH-universal HER have been demonstrated in chemical vapor deposition (CVD) derived 1T-$NiTe_2$.[38] The increased conductivity leads to faster interfacial charge transfer promoting the rate of catalysis. Ma et al recently reported that strain effects on 2D Pt-doped Ti_2CF_2 (Pt-VF-Ti_2CF_2) can improve the catalytic performance for ORR and OER. Pt-VF-Ti_2CF_2 under a compressive strain of 14% and tensile strain of 4% shows the highest ORR and OER catalytic performance with an overpotential of 0.45 V and 0.43 V, respectively. The enhanced catalytic performance by strain engineering can be attributed to the shift of the d-band center and work function modulation.[39]

It has been reported that combining strain and proton/electron affinity can optimize the Gibbs free energy change (ΔG) for the HER in nanostructured systems such as monolayer disulfides. The biaxial tensile strain is more effective in improving HER activity compared to the uniaxial tensile strain. On the other hand, compressive strain is thought to reduce HER activity. Thermodynamics analysis of the system revealed a proportional relationship between the change in free energy (ΔG) and the electron affinities (E_{ea}), given as:

$$\Delta G = -\left(E'_{ea} + E'_{pa}\right) + \Delta E_{ZPE} - T\Delta S_H + \Delta E_{cp} \quad (2)$$

where ΔG is the Gibbs free energy change, E'_{ea} and E'_{pa} are the electron affinity and proton affinity, ΔE_{ZPE} the difference of Hydrogen zero point energy between the adsorbed state and the molecular state, ΔE_{cp} and $T\Delta S_H$ are calculated to be 3.38 and 0.21 eV, respectively (using density functional theory). Further mechanistic analysis on different materials showed that tensile strain

increases the adiabatic electron affinity and decreases the adiabatic proton affinity. Hence, Tensile strain causes a downward shift in the conduction-band minimum, leading to a significant increase in the effective electron affinity E'_{ea}, reducing the energy barriers for HER.[40] Furthermore, Wang et al reported the successful synthesis of strain-stabilized $Ni(OH)_2$ nanoribbons (NR-$Ni(OH)_2$ via an electro-oxidation route.[41] Introduction of tensile strain along the length direction in NR-$Ni(OH)_2$ stabilizes the four coordinated Ni, resulting in higher positive charge states and lower OH- adsorption energy, improving the OER efficacy.

Even in one dimensional (1D) material, strain can lead to orbital rehybridization, increasing their electrocatalytic activity. Our recent study found that bending 1D graphene nanoribbons (GNRs) introduces a strain and causes changes in their lattice structure, leading to a rehybridization of π and σ orbitals. This strain-induced orbital rehybridization affects the distribution of electrons and results in variations in the density of states. The study found that the changes in electron density caused by the bending of GNRs create hotspots towards the center of the GNRs and facilitate a better charge transfer with adsorbed protons, improving the HER efficiency.[42] Applying tensile strain to 1D cobalt (II) oxide nanorods causes an expansion in their lattice structure, resulting in an increased number of oxygen vacancies. This increase in oxygen vacancies speeds up the process of water dissociation, leading to improved performance in catalytic reactions. Additionally, the changes in the electronic structure caused by the tensile strain in cobalt (II) oxide nanorods help to weaken hydrogen adsorption, leading to a further enhancement in their electrocatalytic activity.[43] Chang et al fabricated highly catalytic platinum–palladium nanowires (Pt_nPd_{100-n} NWs) with a subtle lattice strain and Boerdijk–Coxeter helix type morphology through a surfactant-free, thermal single phase solvent method. The maximum activity was shown when the ratio of Pt:Pd was ~78:22, close to 3:1, in which its composition showed lattice shrinking.[44] Hence, the strain applied

to materials (depending on the nature of the constituent atoms) can change the charge density, conductivity, and band structure, leading to improved electrocatalytic performance.

1.1.1.2 Introduction of defects and local electronic changes

Defects in materials can locally change their electronic and surface properties and are commonly recognized as active sites in electrocatalytic processes.[45, 46] Defects in solids can be classified into four categories based on their dimensions: zero dimensional (0D) point defects, 1D line defects, 2D planar defects, and 3D volume defects. These categories describe the spatial extent of the defects within the material and provide a useful framework for understanding and analyzing their impact on their properties. Point defects, small disruptions in a material's crystal structure, are the most commonly studied type of defect. Point defects can be divided into vacancy, doping, and interstitial defects. Here doping-induced point defects is discussed in detail, as they are the basis for the multidimensional activity of electrocatalysts (Figure 1.2). Doping refers to the substitution of host atoms with foreign atoms. The perturbation due to defect atom replacing a host atom is given by,

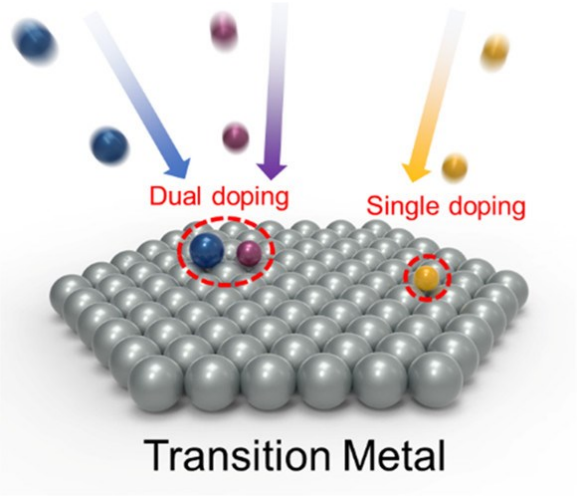

Figure 1.2: Schematic of Doping. Reprinted with permissions from ref 45. Copyright © 2019, American Chemical Society

$$\Delta V = V(D) - V(H) \quad (3)$$

where V(D) and V(H) are the potentials of the substitutional defect atom (D) and the host site (H), respectively. The magnitude of the perturbation and the extent of the change in electronic state in materials caused by doping will be determined by factors such as the difference in electronegativity

and size between the dopant and host atoms. The Fermi level in materials is determined by all charged defects in the system and is not a free parameter. The equilibrium Fermi level is estimated using the charge neutrality conditions, which consider the contributions of all defects, dopants, and their chemical potentials and concentrations. Doping can cause significant changes in the electron distribution at the nanoscale and have a greater effect on low dimensional materials (LDMs). In addition, dopants can be located near the surface and can actively participate in reactions. This makes introducing dopants into catalysts an effective method for tailoring their catalytic properties. For instance, replacing host atoms with impurity atoms in TMDs introduces excess electrons or holes that redistribute the surface charge density. This creates electron-deficient and electron-rich, which modulates the energy required to adsorb intermediates, resulting in improved electrocatalytic performance.[47]

Several successful examples of heteroatom doped catalysts, where metallic atoms (such as Fe, Co, Ni, and Mn) and non-metallic atoms (such as B, S, N, and O) are introduced into the catalyst lattice, demonstrating enhanced electrocatalytic activities is reported. For example, MXenes are new 2D materials with many favorable properties, including abundant active sites, hydrophilic surface, efficient charge transfer, high electrical conductivity, and good stability. A recent theoretical investigation proposed that doping $M_3X_2O_2$ type MXenes with late transition metal atoms may create two types of single-atom catalysts (SACs). In one class (SAC1), the single atom is adsorbed on a stable hollow site above the outer oxygen layer, and in the other type (SAC2), they replace a subsurface metal layer. By controlling the adsorption energy, stable intermediates are produced with dual catalytic activity for both HER and OER. Further, single Ni or Co atoms in MXenes provide enough electrons for either an adsorbate evolving mechanism (SAC1) or a lattice oxygen mechanism (SAC2).[48] Additionally, Fu et al investigated the influence of non-metal atom doping (B, N,

Si, P, S) on the ORR catalytic activity of SAC Co−gN_4 using DFT calculations. It is revealed that the ORR process on Co site can be promoted when the carbon next to N is replaced by Si/P/S by promoting the rate-limiting step (OOH formation).[49]

While post-synthetic doping of materials is possible, it is challenging to maintain uniformity and regularity, limiting the ability to modify their properties. The 2D covalent organic frameworks (COFs) have a regular, porous structure, high stability, and chemical versatility, making them suitable starting materials for creating heteroatom-doped porous carbon-based layered materials. Yang et al. created nitrogen and phosphorus-doped porous carbons through the carbonization and phosphorization of COFs. The synergistic effect of N and P doping modified the electronic structure, increased edge effects, and stabilized C-N species, leading to high HER activity.[50] Metal-organic frameworks (MOFs) consist of transition metals and coordinating organic ligands and can provide a porous platform, are also excellent electrocatalysts. For example, Pan et al. created Fe-doped Ni-MOF nanosheets grown in situ on conductive nickel foam as an efficient oxygen evolution reaction catalyst using only one type of metal salt precursor. The ultrathin sheet structure has a high surface area and conductive metal sites, improving the OER performance due to efficient charge transfer abilities.[51] Not only in 2D structure, heteroatom doping (metal and nonmetal atoms) in 0D quantum dots, particularly graphene quantum dots, is also known to alter their physical and chemical properties, such as charge transport, Fermi level, and local electronic states significantly.[52, 53] Nonmetal dopants can produce uniform doping because of their size similarity to carbon, resulting in variations in the electronic structure. For example, doping graphene quantum dots (GQDs) with boron creates holes, and doping with nitrogen increases the number of electrons, thus enhancing the conductivity. While boron doping in graphene reduces the bandgap and lowers the Fermi energy,

resulting in p-type semiconductor properties, nitrogen doping produces n-type behavior, making them valuable material for catalysis.[54, 55]

In addition to point defects, 1D and 2D defects can also improve their electrocatalytic activity, although to a lesser extent. 1D defects or line defects, such as screw dislocations, edge dislocations, and mixed dislocations, are introduced into the crystals during their solidification. For instance, in spiral $MoTe_2$ nanosheets, the screw dislocation lines that connect the layers allow for electron hopping between the layers, providing vertical conductivity. The enhanced conductivity and Te vacancies at edge steps lead to significantly increased HER activity of 3000 $mAcm^{-2}$ at an overpotential of 0.4 V.[56] Lastly, surface defects, which are 2D defects, are represented by boundaries that divide the material into regions with the same crystal structure but different orientations. Li et al. showed that the abundant edge dislocation defects in the (001) facets of Co_3O_4 improved OER catalysis.[57] Strain from edge dislocation defects in Co_3O_4 nanomaterials promotes vacancy formation, affecting reactant diffusion and adsorption. This, along with the influence on the electronic structure and chemical properties, improves the material's intrinsic catalytic activity. The unique edge structure of 2D defective holey materials, such as graphene, MoS_2, and layered double hydroxides (LDHs), has been studied as they possess highly active atoms with lower coordination number on the edge.[58] The 2D defective holey materials, including graphene, MoS_2, and layered double hydroxides (LDHs), are being studied for their unique edge structure properties and their effect on reducing coordination numbers. The electronic depletion regions on the edge sites promote the adsorption of intermediates, leading to improved activity.

1.1.1.3 Creation of heterostructure and heterojunctions

A heterostructured catalyst is made of multiple materials (e.g., metals, semiconductors, insulators), held together through physical or chemical interactions, which work better together than each material alone.[59] The unique properties of heterostructures are due to electronic interaction and bonding at the interface, resulting in improved catalytic performance due to: variations in work function, band bending and associated shift in valence/conduction band positions, changes in the density of states, formation of new active sites at the interface, and presence of faster electron paths transfer at the interface. The charge transfer between components in a heterostructure creates a dipole moment that tunes the overall reactivity[60], and strong electron interaction and coupling can lead to a shift in electronic states and optimize the physicochemical properties (adsorption, conductivity, etc.)[61] of the active center atoms at the interface, leading to improved catalytic activity.

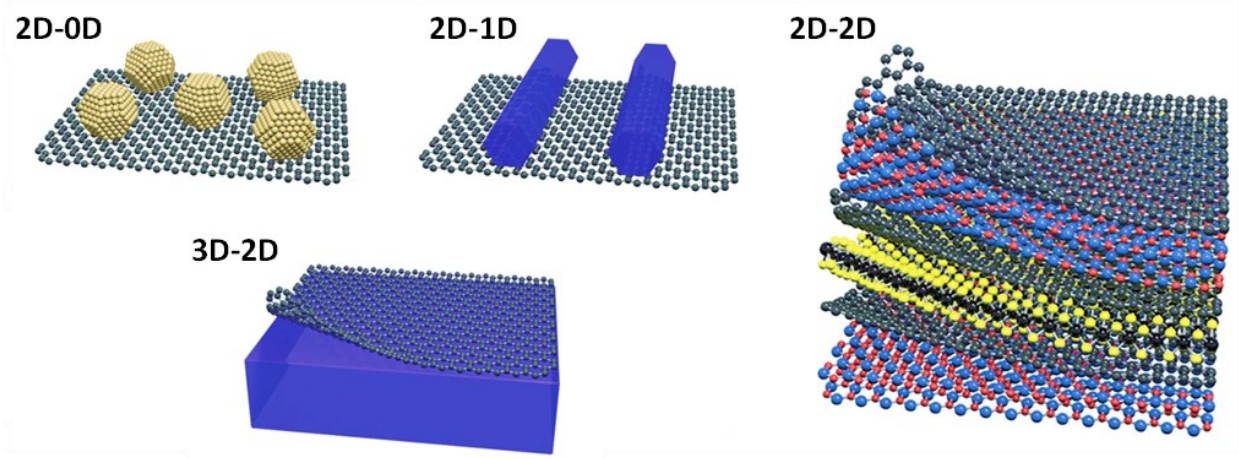

Figure 1.3: Schematic showing heterostructures between various LDMs. Reprinted with permissions from ref 65. Copyright © 2016, Macmillan Publishers Limited

A heterojunction, either semiconductor-semiconductor (S-S) or metal-semiconductor (M-S), can form a band alignment or rectifying contact at the interface if the Fermi levels (or work functions) at the interface match. The band alignment at heterojunction is determined by Anderson's rule for S-S junctions and Schottky-Mott's rule for M-S junctions. Anderson's rule states that the vacuum levels of the two semiconductors should align in the final energy band diagram. According to

Anderson's rule, the conduction band offset (ΔE_C) in S-S heterostructures is determined by the difference in electron affinity (χ) of the two semiconductors (where the conduction band of semiconductor A is closer to the vacuum level than that of semiconductor B) and can be depicted as follows.

$$\Delta E_C = \chi_B - \chi_A \qquad (4)$$

Thus, Anderson's rule determines the direction of electron flow in S-S heterojunction by aligning vacuum levels, creating electron accumulation/depletion regions affecting its intrinsic catalytic activity. Similarly, the Schottky-Mott model predicts band bending at the semiconductor side in M-S junctions[62, 63], and the height of the Schottky barrier can be predicted by the Schottky-Mott rule based on energy level alignment.

$$\phi_{SB,n} = \phi_M - \mathrm{X}_S \qquad (5)$$

$$\phi_{SB,p} = I_S - \phi_M \qquad (6)$$

Where ϕ_M is the work function of the metal, X_S and I_S are the electron affinity and ionization potential of the semiconductor, correspondingly, and $\phi_{SB,n}$ and $\phi_{SB,p}$ are the Schottky barrier heights for electrons and holes, respectively. The Schottky-Mott model may not accurately predict the Schottky barrier height due to chemical disorder and Fermi-level pinning at M-S interfaces.[64] Hence, an accurate prediction of the Schottky barrier height is vital for the heterostructures' catalytic performance as it affects the relocalization of charge carriers at the interface.

Heterostructures can be formed through covalent or non-covalent (including van der Waals (vdW) and electrostatic) interactions. Covalent heterostructures are difficult to fabricate due to the challenge of precise atomic lattice alignment at the interface. Non-covalent heterostructures can have

improved surface contact for more intimate junctions. The weaker inter-layer interactions in vdW heterostructures allow for a broader range of structures to be created by isolating, mixing, and matching dissimilar atomic layers without the limitations of lattice matching and processing compatibility (Figure 1.3).[65] Charge transfer in such vdW heterostructures is influenced by the diffusion rate in each layer and the band offset between layers caused by surface charge accumulation.[66] The 2D/2D heterostructures, with their large surface area, good contact, and ultrathin 2D components, offer unique advantages for catalysis compared to other heterostructures, including 2D/0D and 0D/1D. Further, 2D/2D heterostructures can be designed with contact interfaces in both vertical and lateral directions,[63, 67] making it possible to create both non-covalent vertical heterostructures held together by vdW interactions and covalent lateral heterostructures through bonding interactions. Hu et al. reported a 2D Fe-containing cobalt phosphide/cobalt oxide (Fe-CoP/CoO) lateral heterostructure with an optimized electronic structure for improved OER activity. The charge transfer between Co-P and Co-O generated strong coupling at the CoP/CoO interface, enhancing the adsorption of OH- ions. The improved OER activity of the Fe-CoP/CoO lateral heterostructure is due to synergistic effects of Fe and the CoP/CoO interface, resulting in a modulated electronic structure and increased charge carrier density.

The discovery of new 2D materials like hexagonal boron nitride (h-BN),[68, 69] black phosphorus,[70, 71] MOFs[72] and COFs [73, 74]has made it possible to create new 2D/2D heterostructures with unique properties and strong charge transfer interactions. A recent report showed that a 2D/2D black phosphorous (BP)/N-doped graphene heterostructure (NGP) has unique charge transfer at the interface and efficient bifunctional catalytic activity for overall water splitting in alkaline media.[75] In the BP/NGP heterostructure, the electronic structures were adjusted to enhance the intrinsic abilities of BP and graphene. The Fermi level of exfoliated BP is lower than N-doped graphene, enabling

directional charge transfer at the interface through dual-phase electronic interaction. The interfacial charge transfer increases electron density on BP, optimizing hydrogen adsorption/desorption for HER. Simultaneously, abundant positive carbon sites are generated in the N-doped graphene framework, providing a favorable environment for OER intermediates to anchor. Similarly, Ge et al. created BP/2D MOF (BP@MOF) heterojunctions by growing 2D MOF-Fe/Co nanoplatelets on exfoliated BP nanosheets. The strong interaction between BP and MOF-Fe/Co and the resulting electron transfer from BP to Fe/Co ions in the BP@MOF heterostructure enhance both HER and OER activity.[76] Furthermore, Jiang et al fabricated a 2D/2D Fe–N–C/MXene superlattice-like heterostructure with the help of metal clusters. Fe cluster-directed surface charge manipulation of Fe–N–C nanosheets leads to superior ORR activity with a positive onset potential of 0.92 V, four-electron transfer pathway, and strong durability of 20 h in alkaline electrolyte.[77]

In inter-dimensional vdW heterostructures, the interface between the layers is less restricted as lattice matching is not required. The abrupt change in the density of states at the interface causes changes in the band structure and potential energy barriers, leading to charge transfer through tunneling or hopping. Such charge transfer can significantly affect the observed catalytic activity. The class of 0D-1D and 0D-2D vdW heterostructures are widely explored, where 0D materials could be fullerenes, carbon nano-onions, small organic molecules, and quantum dots. The most studied 1D component in the vdW heterostructures includes single/multi-walled carbon nanotubes (SWCNTs, MWCNTs), polymer chains, nanoribbons, and nanowires. Prasannachandran et al. created a Phosphorene quantum dot-MoS_2 0D-2D heterostructure with bifunctional HER and OER activity. They interspersed phosphorene quantum dots evenly on few-layered MoS_2 nanosheets to allow for better electron transfer, resulting in improved reaction kinetics.[78] The C_{60} molecule has excellent electron-accepting properties and is suitable for making interdimensional

heterostructures. Our recent study showed the presence of two catalytic waves for HER in a 0D-2D MoS_2/C_{60} heterostructure due to different C_{60} arrangements on MoS_2. Electron tunneling from the C atoms at the interface to in-plane MoS_2 polarizes the Mo-S bonds decreasing the enthalpy for hydrogen adsorption. By selecting the proper component ratios, we modulated the interaction between MoS_2 and C_{60} and between C_{60} and C_{60} and achieved the best ΔGH (-0.03 eV).[79] Wang et al. investigated the use of a nitrogen-doped fullerene dimer $(C_{59}N)_2$ combined with MWCNTs to create a metal-free 0D-1D heterostructure for electrocatalytic water oxidation. The electronic rearrangement in $(C_{59}N)_2$ and intermolecular charge transfer reduces the free energies required to produce OER intermediates at the $(C_{59}N)_2$/MWCNTs interface.[80]

1.1.2 Charge modulation for sensing

Over the years, significant progress has been made in the development of materials and technologies for the detection of various pollutants. From the first chemosensor for Al^{3+} by Goppelsroeder in 1867, there has been a growing demand for sensitive, low-cost, and reliable sensors to analyze and determine pollutants in various media, protecting both the environment and people at risk of exposure. However, conventional analytical methods such as gas chromatography (GC), atomic absorption spectrometry (AAS), high-performance liquid chromatography (HPLC), GC/mass spectrometry (GC/MS), capillary electrophoresis, and inductively coupled plasma mass spectrometry (ICP-MS) are often limited by time-consuming pretreatment preparation, complex instrumentation, and high analytical costs. Therefore, it is imperative to develop cost-effective, reliable, and rapid techniques for the determination of different pollutants in the environment. These techniques include electrochemical sensors, gas sensors, field-effect transistor (FET)-based sensors, lab-on-a-chip microfluidic devices, and PL-based sensors. These methods offer highly sensitive and specific detection of pollutants and are valuable tools for environmental monitoring and control.

Electrochemical sensors can be divided into two general categories, potentiometric sensors and voltammetric and amperometric sensors. In potentiometric sensors, the change in potential of sensor occurs with respect to concentration of analyte. Nevertheless, in voltammetric and amperometric sensors, oxidation-reduction reaction creates a current that is relative to concentration of electroactive analyte. Among various materials, carbon-based systems have been intensively exploited for construction of electrochemical sensors owing to their prominent electrochemical properties like high effective surface area, excellent electrical conductivity, electrocatalytic activity as well as high porosity and adsorption capability. Lu et al reported a novel 3D bismuth nanoparticle decorated N-doped carbon nanosheet (Bi-NCNF) nanocomposite with porous and honeycomb-like network structures, for effective simultaneous assay of Cd^{2+} and Pb^{2+}.[81] The Nitrogen doping tuned the charge modulation rendering enhanced conductivity and surface area with good sensitivity and high repeatability, reproducibility and stability for detection. Pang et al fabricated $NiCo_2O_4$ nanoparticles decorated N, S co-doped reduced graphene oxide (NCO/N, S-rGO) composites via the hydrothermal synthesis technique.[82] The existence of pyridine N can effectively promote charge transportation while $NiCo_2O_4$ nanoparticles helps in reducing the charge transfer resistance resulting in LOD of 59, 77 and 164 nM for Cd^{2+}, Cu^{2+} and Hg^{2+}, respectively.

Compared to 3D materials, LDMs are ideal scaffolds for the development of highly sensitive and selective sensors which are unexpensive and easy to fabricate, enabling fast and reliable detection of specific chemical species in liquid and gas media. Due to their nanometric size and highest surface to-volume ratio, and easiness to modulate their electronic charge properties via doping, they are suitable candidates for environmental pollution sensing and remediation. For instance, a dopant with electron-donating or electron-withdrawing character can increase electron or hole carrier density in graphene resulting in decrease of sheet resistance and increase in mobility. Recently,

Kwon et al investigated gas sensing performance of the graphene FET by molecular n-doping with ethylene amines having two, three, and four amine units (EDA, DETA, and TETA).[83] Theoretical calculations revealed that the selective adsorption of NO_2 on n-doped graphene is caused by the attractive electrostatic interaction between electron-rich n-doped graphene and electron-deficient NO_2. The flexible graphene sensor before molecular doping (bare) exhibited no response to 1 ppm of NO_2, while the DETA-doped flexible graphene sensor exhibited an extremely high response of −80% as well as excellent recovery under the same condition. Additionally, Urbanos et al developed MoS_2-based FETs as platforms for polycyclic aromatic hydrocarbons (PAHs) sensing, relying on the affinity of the planar polyaromatic molecules for the basal plane of MoS_2.[84] It was observed that the analyte PAH exposure to MoS_2 FET give rise to p-type doping affecting the electrical readout.

Among the various physiochemical characteristics of LDMs, their optical properties, i.e., their fluorescence emission with high quantum yield and size-dependent photoluminescence (especially in quantum dots or QDs), make them favorable for PL based pollutant sensing. The fundamental sensing mechanism for the use of QDs as sensory probes is based upon analyte-induced quenching or enhanced fluorescence of an already quenched QD-quencher complex (through an electron/energy transfer mechanism with an electron withdrawing or accepting analyte). One of the widely explored platforms in this area is using carbon or graphene QDs where doping enhances the PL leading to improved sensing performances. For example, Gu et al fabricated a Sulfur and Nitrogen Co-doped Graphene Quantum Dot (SN-GQD) via infrared (IR)-assisted pyrolysis technique. GQD samples showed their PL quenching abilities in the presence of Hg^{2+} ions within the tested concentration ranges of 10 ppb^{-10} ppm.[85] The improved sensitivity of SN-GQDs compared to individual S or N doping is ascribed to the fact that S doping coordinates with phenolic groups on the

edges of SN-GQDs and facilitate improved electron transfer from the excited state of SNGQDs to the 4f orbits of Hg^{2+}. This would facilitate added nonradiative electron/hole recombination annihilation, thereby additionally imparting significant PL quenching. Apart from detection of heavy metal ions, Nitrogen doped GQDs (N-GQDs) were used as a fluorescent probe for the sensing of explosive 2,4,6-trinitrophenol (TNP) in aqueous medium. Nitrogen doping was found to tune the luminescence and electronic properties of GQDs and act as energy donor in the fluorescence resonance energy transfer (FRET) mechanism. Fluorescence quenching was observed owing to energy transfer from the excited electron rich N-GQDs to the electron deficient TNP.[86]

Apart from the above sensing methods, SERS based detection is capable of detecting molecules even at the single-molecule scale on or near the surface of plasma nanostructures, which greatly expands the application scope of standard Raman spectroscopy.[87] The effectiveness of SERS is highly dependent on the physicochemical properties of the substrate materials. The substrate material provides active surfaces for light-matter interaction and molecular adherence, resulting in SERS enhancement. Plasmonic metals such as gold (Au) and silver (Ag) with corrugated surfaces are the most commonly used substrate materials.[88, 89] They have prominent electromagnetic enhancements that generate electromagnetic hot-spots, leading to significant SERS enhancement. Recently, various non-metal materials, including graphene, MXenes, transition-metal chalcogens/oxides, and conjugated organic molecules, have been reported to have boosted SERS activities.[90, 91] These materials offer alternative options for SERS substrates that exhibit comparable or even superior performance to traditional plasmonic metal substrates. Optimization of charge in materials is key to maximizing SERS sensitivity by increasing the electromagnetic field intensity or enhancing chemical interactions with the target analyte along with improved stability, reproducibility, and sensitivity of SERS. The formation of heterostructure between metallic SERS

active nanoparticles and a conducting material can enhance the SERS signals via charge transfer between the nanoparticles and the substrate. The electronic hotspots at the interface between the materials when in contact with the analyte can show improved activity compared to metallic nanoparticles alone.

1.2 Modulation of spins on materials

The intrinsic angular momentum carried by an electron, known as its electronic spin, gives the electron a magnetic moment with a definite magnitude and orientation. The spin selection rule, also known as Wigner's spin conservation rule, states that the spin angular momentum must remain constant during electronic transitions, irrespective of whether the transition occurs intra or interatomically. Spin interactions and selection rules strongly affect the structure, chemical reactivity, dynamics, and magnetic properties of materials. As the reactant and product have the same spins, HER is spin insensitive. However, electrocatalytic reactions, including OER, oxygen reduction reaction (ORR), Nitrogen reduction reaction (NRR), CO_2 reduction reaction (CO_2RR), etc., are all spin-sensitive reactions. The OER and ORR involve triplet O_2 and singlet OH- as reactant or product, and there is a direct spin inversion during OER/ORR. Hence, they should be spin-dependent. The role of spin selectivity in NRR and CO_2RR is more indirect and is related to intermediate steps. Spin selectivity is also known to boost the first protonation step to form *NNH (* refers to adsorbed) in NRR and the M–COOH intermediate in CO_2 RR. The concept of spin polarization is gaining increased attention to aid spin-dependent reactions. Spin polarization is a transient local property for materials with non-zero net spin density sites. Such a polarized region can enhance spin-dependent reactions by facilitating electronic transitions with lower energy pathways. The following section discusses different methods to induce spin polarization in catalysts to improve electrocatalytic activity, with an emphasis on OER. The fundamentals explained here are easily

adaptable for other spin-sensitive reactions. One pathway to induce spin polarization and enhance OER efficiency is to modify the magnetic properties of catalysts through intrinsic magnetic ordering or an external magnetic field. Applying an external magnetic field or the formation of intrinsic magnetic spin channels leads to the splitting and polarization of spin-up and spin-down bands, allowing selective screening of specific electron spins through a lower energy transfer channel, thereby increasing OER efficiency. The efficacy of chiral molecules in selectively transferring spins (chiral-induced spin selectivity, CISS) and its impact on OER is also investigated.

1.2.1 Modulation of magnetic properties through intrinsic order or external magnetic field

Solid-state magnetism is the result of interactions between atomic moments (spins). A combination of electrostatic repulsion between electrons, quantum mechanics, and the Pauli exclusion principle leads to atomic-scale exchange interactions in magnetic materials. Positive interactions result in ferromagnetic order, with parallel spin alignment (↑↑) and a non-zero net magnetization, while negative interactions result in antiparallel spin alignment (↑↓) and antiferromagnetic conformation. Without such interactions, the spins would point in random directions, leading to a smaller but non-zero net magnetization. The direct exchange mechanism, where orbitals of two sites are close enough to allow for a significant overlap of their lobes, allows for direct electron hopping between magnetic centers. However, magnetostatic, or direct exchange interaction cannot explain ferromagnetism at or above room temperature. Further, magnetostatic interactions alone cannot explain the presence of spontaneous magnetism in some materials or the behavior of strongly correlated materials.

Magnetic materials also have complex exchange interactions known as indirect exchange interactions with a quantum mechanical origin. These indirect interactions include Ruderman-Kittel-

Kasuya-Yosida (RKKY), anisotropic exchange interaction, super-exchange, and double exchange. Indirect interactions are caused by the correlated movement of electrons with the same spin, resulting in an effective reduction of electronic Coulomb repulsions. Exchange in solids is often indirect, mediated by conduction electrons or intermediate atoms like oxygen. Super-exchange and double-exchange occur when electron hopping occurs between non-neighboring magnetic centers with the help of non-magnetic atoms like oxygen p-orbitals. For example, transition-metal oxides frequently exhibit exchange bonds of type M^{m+}-$O^{2-}M^{m+}$, where M^{m+} is the transition-metal cation. Double exchange occurs in mixed valence oxides, such as Fe_3O_4. This oxide contains Fe^{3+} and Fe^{2+} ions on B-sites. The latter can be considered as Fe^{3+} ions plus an extra electron that can hop more or less freely between the d^5 ion cores. The exchange interaction of localized magnetic moments in metals is mediated by conduction electrons, known as the RKKY mechanism. Anisotropic exchange interaction, or Dzyaloshinsky–Moriya interaction, stabilizes chiral spin textures.

The concept of Quantum Spin Exchange Interactions (QSEIs) explains how the indirect exchange interactions create magnetic ordering and spin polarization, which enhances OER catalysis. QSEI stabilizes open-shell orbital configurations with unpaired electrons in magnetic compositions, which are critical for catalysts with unpaired electrons. QSEI reduces the mutual Coulomb repulsion of two indistinguishable electrons with the same spin by allowing them to interchange their orbitals, position, and momentum in the quantum regime. In addition to QSEI spin potential and other indirect exchange interactions, spin potentials, such as spin-orbit potential (arising from spin-orbit coupling (SOC), also a part of Rashba effect and the Dzyaloshinskii-Moriya interaction), direct spin-spin interaction, and Zeeman potential (under external magnetic field), also exist in materials and affect the Hamiltonian and result in spin polarization of electrons with different spins. This spin polarization can create a spin-selective channel to filter specific electron spins

during catalytic reactions, increasing catalytic activity during the triplet O_2 generation/conversion step. Hence, magnetic spin polarization in catalytic systems can be achieved through various methods, and the synergistic effect of different spin potentials can be enhanced, as discussed below.

1.2.1.1 Spin polarization through intrinsic magnetic Ordering: Materials with ordered structures, such as ferromagnetic materials, can produce spin channels by arranging their constituent particles to enable the preferential flow of spin-polarized electrons. Such arrangement makes these materials ideal for use as spin-selective catalysts. For example, $LiCoVO_4$, a layered antiferromagnetic inverse spinel oxide, has parallel spins for Co^{2+} ions within Co-O layer layers and reverse spins between layers, creating spin-up and down channels. Here the high spin Co^{2+} (S = 3/2) in bulk octahedrons promotes OER activity due to the enhanced electron transfer through a spin-polarized channel.

It is worth noting that magnetic ordering can also enhance HER, even if not through spin-selection. Intrinsic ferromagnetic ordering is reported to improve HER activity by tailoring the spin density. For instance, in single-atom-thick MoS_2 sheets, long-range ferromagnetic order induced by cobalt doping leads to delocalization of the spin states of Mo 4d-electrons and an increase in sp electronic density around the Fermi level. The rise in sp electronic density results in a modification of the electronic structure of the basal plane S atoms, which enhances their ability to adsorb hydrogen, leading to improved HER activity.[92]

1.2.1.2 External Magnetic Field: An external magnetic field can regulate the electron transfer between the orbitals in the catalyst and the chemisorbed reactants by inducing the spin orientation of electrons in magnetic catalysts. A general expression of the Hamiltonian of an N electron system can be defined in the absence external magnetic field as

$$\widehat{H} = T_{e^-}^{Kinetic} + V_{N+e^-}^{Coulomb} + V_{e^-+e^-}^{Coulomb} + V_L + V_{SOC} \quad (7)$$

where $T_{e^-}^{Kinetic}$ is the kinetic energy of the electrons, $V_{N+e^-}^{Coulomb}$ is the Coulomb attraction between the nucleus and electrons, $V_{e^-+e^-}^{Coulomb}$ is the energy factor of the electron-electron Coulomb repulsions, V_L is the potential due to the crystal field and V_{SOC} is the energy factor due to the spin–orbit coupling. In the presence of an external magnetic field, an extra spin-dependent potential is added to the Hamiltonian.

$$\widehat{H} = T_{e^-}^{Kinetic} + V_{N+e^-}^{Coulomb} + V_{e^-+e^-}^{Coulomb} + V_L + V_{SOC} + \mu H \quad (8)$$

where μH indicates the energy contribution of the interaction between the electrons of the system and the external magnetic field. Under the magnetic field, the spins of the active center align in a parallel fashion due to exchange interactions, leading to the polarization of spin-up and spin-down electrons. The spin polarization enables the selective transport of favorable spin and facilitates the formation of intermediate ↓O…O↓ and the product ↓O=O↓ in the triplet state. A static magnetic field and an alternating magnetic field (AMF) can positively impact the parallel arrangement of oxygen atoms. Still, the latter is also reported to induce internal spin flip of magnetic catalysts through local magnetic heating. In addition, both static and alternating magnetic fields can improve mass transport to the electrode surface by affecting the electrolyte convection by Lorenz force

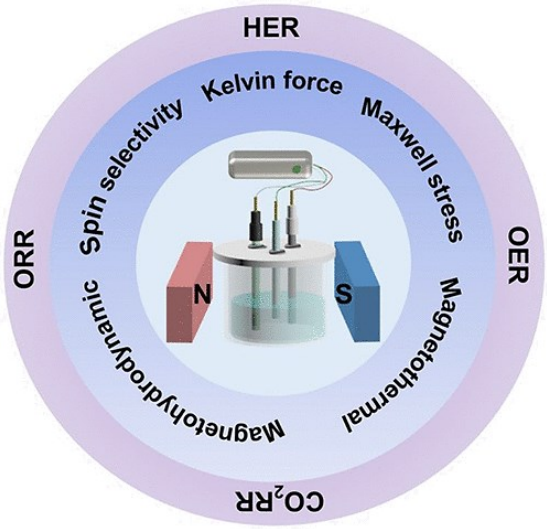

Figure 1.4: Schematic showing magnetic field enhancement mechanisms. Reprinted with permissions from ref 93. Copyright © 2020, American Chemical Society

(magnetohydrodynamic (MHD) and micro-MHD effects), diffusion of paramagnetic intermediates, and removing gas bubbles by Kelvin force (magnetic field gradient forces) (Figure 1.4).[93] However, these effects do not directly impact the spin selection and will not be discussed further.

1.2.1.2.1 Effect of Static Magnetic Field: The activity of all catalysts based on ferromagnetic coupling may be modified by the presence of a static external magnetic field. Several studies demonstrated an enhancement in OER activity when a moderate magnetic field is applied to catalysts with different magnetic properties, with the greatest enhancement seen in highly magnetic systems.[94, 95] Ren et al. found that under a static magnetic field, a ferromagnetic ordered catalyst ($CoFe_2O_4$) will work as a spin polarizer for spin selection and improve the kinetics of the first electron transfer step in OER. Their study revealed that the observed enhancement is due to indirect QSEI, not weak direct spin-spin interactions from the magnetic field.[96] Garces-Pineda et al. studied the impact of a direct magnetic field on OER electrocatalysts with varying magnetic properties (non-magnetic IrO_2, antiferromagnetic NiO, spinel $ZnFe_2Ox$ and ferromagnetic $NiZnFe_4Ox$ and NiZnFeOx). They found that improvement in OER activity with a moderate magnetic field of 450 mT. The study established a trend between the magnetic nature of the catalysts and their activity, with non-magnetic catalysts showing little effect and highly magnetic systems experiencing maximum enhancement. [97]

1.2.1.2.2 Alternating Magnetic Field: Magnetic nanoparticles subjected to an alternating magnetic field (AMF) generate heat from Néel relaxation caused by the internal flip of spins relative to the crystal lattice. This intense localized heating in the immediate vicinity of magnetic nanoparticles under an external high-frequency AMF is generally termed the magnetothermal effect or magnetic hyperthermia (Figure 1.5).[98] The local thermal disturbances induced by AFM can change the magnetic structure and spin configuration of the material by causing electron hopping and spin flipping.

The ability to convert electromagnetic energy into thermal energy using magnetic nanoparticles can be measured using specific loss power (SLP). The SLP is calculated by,

$$SLP = \frac{\mu\pi\chi''(f)H^2 f}{\rho\phi} \qquad (9)$$

Where f, ρ, Φ, and χ'' are the frequency of the magnetic field, the density and volume fraction of nanoparticles, and the imaginary part of the susceptibility, respectively. Utilizing this, recently, Liu et al. demonstrated that the localized magnetic heating induced by AMF could lead to a spin flip and reconfiguration in $Co_{0.8}Mn_{0.2}$ MOF through designing thermal-differentiated superlattices. Recently, Liu et al. showed that magnetic heating from an AMF could lead to a spin flip and a reconfiguration in $Co_{0.8}Mn_{0.2}$ MOFs by creating thermal-differentiated superlattices and enhance the OER process. The AFM-induced spin rearrangement of unfilled t_{2g} orbitals allowed the catalytic sites to more readily accept valence electrons of the reactant, making it more favorable for the adsorption of *OH and starting an OER cycle. [99] In addition to spin-flip and electronic reconstruction, AMF also helped to induce spin polarization and triplet O_2 formation, leading to an OER enhancement. Gong et al. demonstrated that AMF could improve the OER activity of low dimensional Co@MoS_2 SACs prepared by anchoring Co single atoms on MoS_2. Compared to parent MoS_2, the anchoring of Co single atoms led to room-temperature ferromagnetic properties that favored the parallel spin arrangement of oxygen atoms under an external

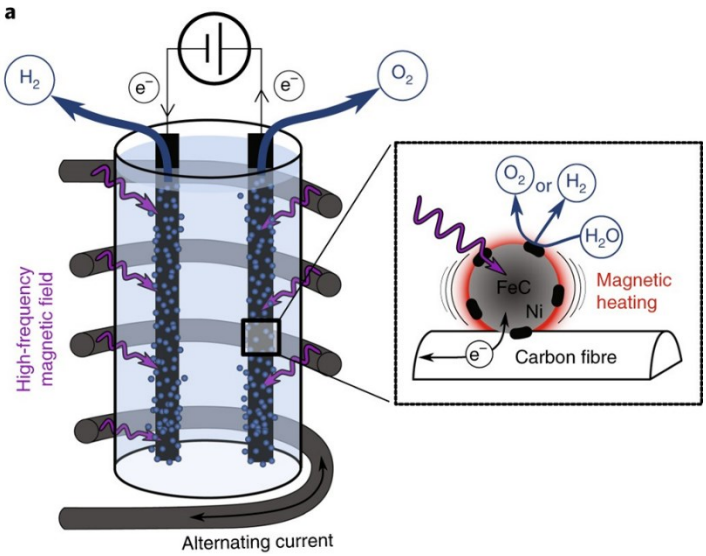

Figure 1.5: Schematic showing effect of alternating magnetic field. Reprinted with permissions from ref 98. Copyright © 2018, Springer Nature

magnetic field. Further, the magnetic heating generated from AMF reduced the activation barrier and improved the OER kinetics. [100]

Most research on magnetic field-enhanced electrocatalysis (both static and AMF) focuses on 3D or bulk materials, as the effects of magnetic fields and exchange interactions in LDMs can be complex. For example, compared to bulk MoS_2, 2H phase monolayer MoS_2 with a direct band gap has a strong SOC which can strongly affect spin polarization. Further, multiple competing fundamental interactions, such as indirect RKKY and Kondo effect, can occur simultaneously in low-dimensional multi-spin systems. Thus, more research is needed to understand the potential of magnetic field enhancement for OER catalysis in these systems.

1.2.2 Anchoring chiral centers to induce chirality-induced spin selectivity (CISS)

Chiral molecules can transport preferential spin for long distances with little or no loss of spin coherence. In 1999, Ron Naaman and colleagues showed that electrons passing through chiral molecular films are transmitted in a spin-specific manner, with only one type of electron spin being allowed to pass through the molecule, a phenomenon referred to as "chiral-induced spin selectivity." This ability of chiral molecules to filter spins makes them good candidates for use as spin valves in OER, where the spin-polarization obtained using a chiral catalyst can help screen specific orientations of spins for triplet oxygen production. Research in CISS has found a strong link between molecule spin orientation and symmetry, offering opportunities to control material properties by manipulating electron spin. Consequently, the CISS effect, first observed in organic films, has significant implications for controlling chemical reactions, separating enantiomers, and recognizing biological molecules.[101] Through the CISS effect, electrons with a specific spin orientation preferentially traverse a chiral molecule in one direction, while electrons with the opposite spin

orientation traverse the same molecule more quickly in the opposite direction (Figure 1.6). The spiral motion of electrons through a chiral molecule or material is influenced by the centripetal force (F_B) that acts perpendicular to electrons velocity and is caused by the potential energy associated with the curvature of the chiral system. The direction of force experienced by the electron depends on the 'handedness' (left versus right) of the material and its potential energy. Further, F_B experienced by the electrons forces it to take a helical path similar to an electron's motion in a homogeneous external magnetic field (B). The electron stays within the curved potential, and the effective magnetic field acts on the magnetic moment of the electron, stabilizing one spin direction and destabilizing the other. The additional stabilization of one spin direction results in a preferential transfer of electrons with one spin orientation over the other. This means that the tunneling probability for an electron to pass through a chiral material depends on its spin orientation, and the difference in transmission between different spins can be as high as 100 times. While it is unknown if the spin transfer occurs by tunneling, resonances, or hopping, spin polarization and selective transfer, have been observed in long-range electron transport through a 50 nm chiral perovskite film.[102] The impact of such selective transfer electrons with ideal spins can be significant in multi-electron catalytic processes such as the OER.

The initial observations of CISS effects were followed by attempts to explain the data theoretically. Most works describe how a chiral potential (energy associated with the chirality of a system) acts as a spin filter but do not explain the magnitude of the effect. The SOC of the chiral molecule being the source for spin selectivity is a likely explanation.[103] The effective SOC of systems is given by

$$SOC = \vec{\mu} . B \qquad (10)$$

where μ is the magnetic moment of the spin. The SOC on each atom in the chiral molecule can be represented as λ*L*σ, where λ is the SOC observed for individual atoms, L is the angular momentum, and σ the Pauli spin matrix. The total SOC of the chiral molecules is the vector sum of the atomic terms:

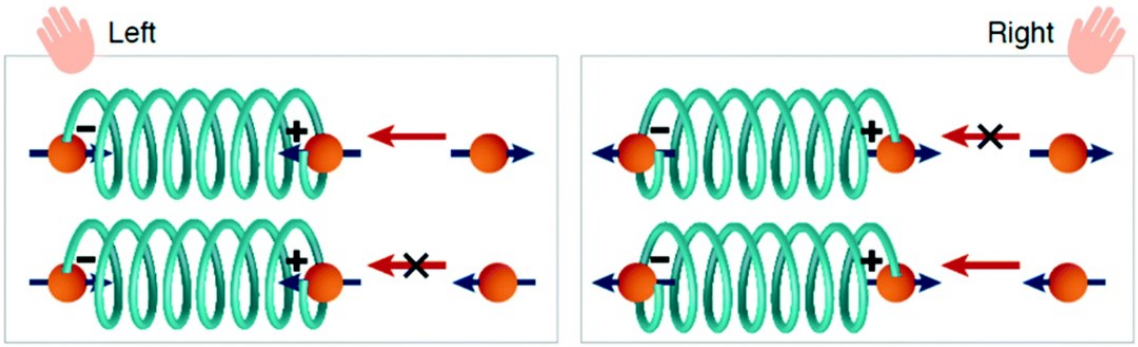

Figure 1.6: Schematic showing illustrates the spin polarization induced enantioselective reaction mechanism. Reprinted with permissions from ref 106. Copyright © 2020, Royal Society of Chemistry

$$H_{SOC} = \sum_{i=0}^{n} \lambda_i \vec{L}_i . \vec{\sigma}_i \qquad (11)$$

so that the SOC for the chiral chain can be up to an order of magnitude larger than the atomic value. This SOC, along with accidental degeneracies in the spectrum of chiral molecules, is expected to cause a significant spin polarization.[104-106] Theoretical analysis by Gersten et al. introduced the concept of "induced spin filtering," where the selectivity in the transmission of the electron's orbital angular momentum can induce spin selectivity if there is strong SOC in the substrate.[103] Moreover, the scattering probability can be spin-dependent and contribute to CISS, even when incoherent processes play a role in electron transport.[107, 108] Many-electron interactions, such as the polarization induced in a molecule during electron transfer, may also contribute to the size of the effect.

The CISS can affect the spin of electrons at the surface of catalysts without help from an external magnetic field. This effect on spins can alter the reaction pathway and enhance the OER beyond

the standard limits set by the Sabatier principle, which governs the relationship between the overpotential and the current density in electrochemical reactions. The spin states of radical intermediates on the electrode surface significantly impact the generation of O_2 and the production of H_2O_2. Recent experiments have shown that coating the anode of an electrochemical cell with a monolayer of chiral molecules,[109, 110] a film of chiral polymer, [111] or a chiral inorganic oxide[112] trigger spin-selective electron transfer from the OH^- to the anode, which in turn decreases the overpotential and reduces H_2O_2 production. When the spins of radical intermediates, such as hydroxyl radicals ($OH\cdot$), are parallel, the production of H_2O_2 is suppressed, and the generation of oxygen becomes favored. Bian et al. reported that hybrid chiral MoS_2 layers intercalated with methylbenzylamine molecules exhibit high spin polarization and conductivity for the OER.[113] The spin polarization value was calculated using Spin-Polarized Conductive-Atomic Force Microscopy (AFM) measurements, using the following relation.

$$Spin\ polarization\ = \frac{I_{Up}-I_{Down}}{I_{Up}+I_{Down}}\ x\ 100\% \quad (12)$$

where I_{Up} and I_{Down} are the currents measured when the tip was magnetized along the upward and downward orientations, respectively. The hybrid 2D chiral system in the study by Bian et al. activates multiple tunneling channels in the chiral layers, leading to a spin polarization of 75%. The spin selectivity also suppresses the production of the H_2O_2 by-product and promotes the formation of ground-state O_2 molecules during OER. Furthermore, Liang et al. observed an enhancement of up to 130% for OER using a monolayer chiral molecule and 2D electrocatalyst in a sandwich configuration.[114] The chirality of hetero-helicenes such as thiadiazole-[7] helicene and bis(thiadiazole)-[8] helicene boosted the OER activity of 2D NiOx and NiFeOx oxo-hydroxides on gold due to the spin polarization of the interface resulting from chiral molecule adsorption. The chiral

molecules were anchored between the catalytic material and the substrate (gold) to avoid blocking the active centers and promote electron transfer through the spin polarizers for optimal activity enhancement. A comparison of activity enhancement (current densities at 1.65 V vs. RHE) between CISS and external magnetic field reported by Garcés-Pineda et al. revealed that using chiral molecular functionalization to cause spin polarization resulted in more prominent enhancement (61%) of activity compared to using an external magnetic field (10%).[97] Better OER enhancement seen in the case of chiral molecular functionalization compared to the use of an external field could be due to the stronger spin polarization caused by chiral potentials compared to the weaker interactions seen in magnetic systems (QSEI interactions). The study of chiral molecules and their potential for influencing chemical reactions and material properties is a new and emerging field. More theoretical and experimental work should be done to explore ways to utilize chirality and harness its full potential.

Chapter 2 of the thesis focuses on charge modulation using foreign metal atom inclusion (doping) and is comprised of two sections. The first section investigates the impact of metal and non-metal doping on graphene quantum dots for heavy metal ion sensing. The second section examines the effect of foreign atom doping on gallium oxide materials for use as bifunctional OER/ORR catalysts, as well as in Zn-air batteries. Both sections describe the manipulation of the band structure, conductivity, and electronic charge distribution through the process of doping, and examine how these modifications can enhance the properties of materials for use in OER/ORR catalysis and PL based sensing applications. Chapter 3 concentrates on the formation of heterostructures between various dimensional materials and subsequent charge modulation. The first section investigates the superiority of the Ni-Ag/MXene heterostructure as a substrate for SERS detection. The second part investigates the use of graphene nanoribbons/MoS_2 quantum dot LDM heterostructure for

enhanced HER activity. Both sections highlight the significance of heterostructure formation and interfacial sites, as well as the resulting synergistic effects, in the modulation of charge and its impact on HER catalysis and SERS based sensing applications. Chapter 3 of this thesis focuses on the methodologies for incorporating spin polarization in materials and optimizing them to achieve higher activity towards OER. The first section investigates the effect of external magnetic fields and chirality on OER enhancement in superparamagnetic and ferrimagnetic iron oxide materials. Additionally, the prospect of spin polarized OER current enhancement to be utilized as sensing platform is also discussed. The second section explores the chirality-induced spin selection in Ni/MXene heterostructures for improved OER activity. Chapter 3 provides insights into the novel and emerging techniques for spin modulation and the fundamental mechanisms behind the observed enhancement. Overall, the aim of this work is to provide insights into the role of potential pathways to tailor charge and spin in materials for the development of electrochemical energy and sensing platforms.

Chapter 2

Introduction of defects and local electronic changes

Introducing foreign atoms (e.g., N, B, P, etc.) into materials has been a widely used approach to modulate their physicochemical, electronic properties, and chemical activities, which can enhance their applicability across various fields. Such insertion can be achieved either through in-situ doping during the synthesis stage or by post-chemical or physical treatments using atom-containing precursors. This chapter investigates the impact of doping on the PL-based sensing and electrochemical OER and ORR activities of materials. In particular, the chapter will delve into the use of GQDs doped with foreign atoms for detecting mercury ions in water, as well as the incorporation of tin atoms into gallium oxide for bifunctional oxygen evolution and reduction reactions, and its application in zinc-air batteries.

Fluorescent GQDs derived from low-cost, sustainable precursors are highly sought after for various applications such as luminescence-based sensing, optoelectronics, and bioimaging. Lignin, with its unique structural and compositional variety and abundant aromatic carbon, serves as a renewable precursor for the eco-friendly synthesis of advanced carbon-based materials, including GQDs. However, the low photoluminescence quantum yield of GQDs from natural precursors like lignin limits their practical use. We demonstrate that leveraging the innate presence of heteroatoms in lignosulfonate can yield in situ heteroatom doped GQDs with exceptional photophysical properties. The resulting lignosulfonate derived GQDs exhibit strong blue fluorescence and a high quantum yield of 23%, attributed to in situ S and N doping, confirmed by X-ray photoelectron spectroscopy and Fourier transform infrared spectroscopy analyses. By further engineering the in-situ doping with a metal atom dopant, we achieved an enhanced quantum yield of 31%—the

highest for any lignin-derived GQDs. Fundamental photoluminescence studies reveal multiple emissive centers, with edge states as the dominant emission centers. Moreover, we showcase the application of luminescent, metal- and nonmetal-co-doped lignin-derived GQDs as highly selective sensors for sub-nanomolar level detection of mercuric ions in water.

The ability to tailor fundamental material properties such as acidity/basicity, work function, and density of states near the Fermi level can impact the charge distribution on catalysts' active sites. Rechargeable metal-air batteries offer enhanced safety, superior energy, and power density, making them ideal energy storage systems for applications in energy grids and electric vehicles. However, the lack of a cost-effective, stable bifunctional catalyst to replace expensive platinum (Pt)-based catalysts for promoting OER and ORR at the air cathode hinders their wider adoption. We demonstrate that Tin (Sn) doped β-gallium oxide (β-Ga_2O_3) in bulk form can efficiently catalyze ORR and OER, making it suitable for use as a cathode in Zn-air batteries. The Sn-doped β-Ga_2O_3 sample with 15% Sn (Snx=0.15-Ga_2O_3) exhibited exceptional catalytic activity for a bulk, non-noble metal-based catalyst. As a cathode, the excellent electrocatalytic bifunctional activity of Snx=0.15-Ga_2O_3 resulted in a prototype Zn-air battery with a high-power density of 138 mW cm^{-2} and improved cycling stability compared to devices using benchmark Pt-based cathodes. A combination of experimental and theoretical exploration revealed that the Lewis acid sites in β-Ga_2O_3 help regulate electron density distribution on Sn-doped sites, optimize adsorption energies of reaction intermediates, and facilitate the formation of the critical reaction intermediate (O*), leading to enhanced electrocatalytic activity.

2.1 In Situ Doping Enabled Metal and Nonmetal Co-doping in Graphene Quantum Dots: Synthesis and Application for Contaminant Sensing

2.1.1 Introduction

GQDs with tailored structure can be synthesized from corresponding precursors through chemical disproportionation, carbonization, or pyrolysis.[115-118] However, common synthetic precursors employed for GQDs synthesis are non-renewable, expensive, and not eco-friendly. Hence, synthesis of GQDs from sustainable and inexpensive precursors, including biomass/food waste and biomass by-products, has attracted significant research interest recently.[119-125] Recently, GQDs were also synthesized from alkali lignin through a simple reorganization and refusion of aromatics.[123] However, similar to other renewably resourced GQDs, lignin-derived GQDs showed inferior properties compared to their counterparts synthesized from synthetic precursors. For example, the photoluminescence quantum yield (PLQY) of alkali lignin-derived GQDs was 21%, lower than the PLQYs of GQDs synthesized from non-renewable precursors, thus limiting their potential use.[123] Heteroatom doping in the GQD lattice (i.e., the introduction of non-carbon foreign atoms) is routinely performed to embellish the quantum-enabled properties of GQDs. Conventionally, doping is achieved through the addition of the co-reactants consisting of dopant atoms in the synthesis process. In addition to influencing quantum confinement, surface functional groups, and edge effects, heteroatom doping is also known to introduce more active vacancies and significantly alter GQDs intrinsic characteristics. For example, photoluminescence, one of the most exciting properties of GQDs, is known to get amplified by doping GQDs with nonmetal or metal heteroatoms.[126, 127] Especially the PLQY was significantly increased upon doping due to the creation of new defect/edge states in GQDs.[128, 129] Previous studies on alkali lignin-derived GQDs by Ding et al.[123] through N-doping and Wang et al.[130] through S, N co-doping lead to a constant PLQY of 21%. The

inadequacy of simple doping strategies to increase the PLQY in lignin derived GQDs indicates that enhancing PLQY in these systems is not trivial. Typically, doping GQDs with different elements (co-doping) can significantly enhance their properties through synergistic effects.[85, 131] Though co-doping using different nonmetals is frequently performed, studies on metal-nonmetal co-doping in the GQD matrix are minimal, probably due to the increased complexity of the reaction.[126, 132-134] Nonetheless, co-doping of metals and nonmetals in GQDs leads to superior properties due to the more defect sites created, the increased availability of vacant energy levels, and the synergistic electron-donating/withdrawing ability of dopants.

Here, we demonstrate that by co-reacting lignosulfonate that contain heteroatoms (S and N) in its structure[135] and a metal precursor, metal and nonmetal co-doped GQDs with significantly enhanced optical properties can be synthesized. The S and N atoms present in the lignosulfonate lead to in-situ doping with S and N, while the external metal precursor helps to integrate the metal atoms. Due to the reported ability of manganese (Mn) to enhance the photophysics of GQDs,[126] Mn was selected as the model metal dopant. By synthesizing lignosulfonate-derived, in-situ S, N co-doped GQDS (LGQDs) and LGQDs containing Mn (Mn-LGQDs), we also investigated the emissive centers in the LGQDs with and without Mn doping and, from a fundamental band structure point of view, explain the observed changes in the luminescence properties. Capitalizing on the excellent PL of the Mn-LGQDs, we further illustrate its potential for the selective sub-nanomolar detection of mercuric ion, a water contaminant with acute toxicity, [136] in drinking water.

2.1.2 Materials and Methods

2.1.2.1 Materials and Chemicals

All chemicals and reagents used in this work were commercially available, of analytical grade and used as received without any further purification unless otherwise specified. Lignosulfonic acid sodium salt (MW ~52000) was purchased from Beantown chemicals and precursor salts $MnCl_2$, $CuCl_2$, $ZnCl_2$, $AgNO_3$, $CoCl_2$, $NiCl_2$, $FeCl_2$, $Cd(NO_3)_2$, $MgCl_2$, $CaCl_2$, $Pb(NO_3)_2$, $Hg(NO_3)_2$ were purchased from Alfa Aesar. Nitric acid (70%) used for LGQD synthesis, quinine sulfate (the standard sample used for PLQY measurements) and $HgCl_2$ were purchased from Millipore Sigma. Stock solutions of Hg^{2+}, Ag^{+}, Ca^{2+}, Cd^{2+}, Co^{2+}, Cu^{2+}, Fe^{3+}, Mg^{2+}, Mn^{2+}, Zn^{2+}, Ni^{2+} and Pb^{2+} ions were prepared by dissolving corresponding metal salts in DI water. Ethylenediaminetetraacetic acid (EDTA) was purchased from Millipore Sigma.

2.1.2.2 Synthesis of doped GQDs from Lignin

The synthesis of both LGQDs and Mn-LGQDs was performed by following a modified hydrothermal method[123] as described below. Note that there was a minor difference in the case of Mn-LGQDs synthesis in which additional Mn precursor salt was added in the reaction mixture. For the LGQD synthesis, first, 3 g of lignosulfonic acid sodium salt was dissolved in 15 mL of deionized (DI) water. Then, 5 mL of nitric acid was gradually added to this solution with continuous stirring. The resulting dispersion was ultrasonicated for 12 h (at 40 kHz frequency and 110 W) and diluted with DI water. The dispersion was vacuum filtered using a 0.22 μm microporous membrane and the residue was re-dispersed in 40 mL of DI water to create the carbonized precursor. Subsequently, the precursor solution was transferred to a teflon-lined autoclave for the hydrothermal reaction at 200°C. To introduce Mn into the LGQDs, $MnCl_2$ was added (0.6 to 4% by weight) as a co-reactant into the hydrothermal reaction mixture. The hydrothermal reaction parameters including

temperature, duration, dopant concentration, etc. were varied to optimize the reaction conditions. The hydrothermal reaction product was filtered through a 0.22 μm microporous membrane to remove insoluble carbon. The brown filtrate was then centrifuged at 20k rpm for 30 minutes, and the supernatant containing LGQDs was collected. Finally, this supernatant with LGQDs was lyophilized and stored as a powder

2.1.2.3 Photoluminescence based detection of Hg^{2+} ion in water

For mercuric (Hg^{2+}) ion sensing studies, the LGQDs sample solutions (0.1 mg /mL) were mixed with calculated amounts of Hg^{2+} ions (in the range of 2 nM to 1 μM) and the resultant changes in fluorescence spectra were investigated. Similarly, for Mn-LGQDs (2% doping), a pH of 5.5 and a solution concentration of 0.1 mg/mL was used, where the maximum PL emission intensity was observed. The PL spectrum was recorded by fixing the excitation wavelength (λ_{ex}) at 340 nm. In a typical experiment, the PL spectra of the LGQD/Mn-LGQDs was first measured under ideal excitation condition, followed by PL spectra measurement after adding Hg^{2+} solution. Throughout this study, the volume of the Hg^{2+} (different concentration) introduced into the LGQD/Mn-LGQD mixture was kept constant to mitigate dilution-based effects. The dilution effect on the luminescence was evaluated by the addition of an equal volume of DI water to the LGQD/Mn-LGQDs. The selectivity of Mn-LGQDs towards Hg^{2+} detection was investigated by studying the luminescence spectra of Mn-LGQD solution containing different metal ions prepared as explained above. The PL spectrum of the Mn-LGQDs was first measured under an optimal excitation wavelength of 340 nm. Subsequently, a specific concentration of Hg^{2+} solution (250 nM and 1000 nM) was added to the LGQD solution and PL spectrum was analyzed after the addition of the ions, to note the PL quenching. In order to regain the PL, we added stoichiometric amounts of EDTA solution into the mixture and was sonicated for 10 minutes. Finally, the PL spectrum was re-measured to observe

the increased intensity. Post PL regain experiments, we further tested the reusability of the GQD-based sensors using 250 nM Hg^{2+} concentration. The sensing of low and high concentrations of Hg^{2+} was also performed in tap water.

2.1.2.4 Calculation of HOMO and LUMO levels

The E_{HOMO} and E_{LUMO} were determined from Linear sweep voltammetry measurements. The HOMO and LUMO levels for LGQDs and Mn-LGQDs are calculated as follows;

$$E_{HOMO}\,(\text{in eV}) = -(Ø_{OX} + 4.74) \quad (1)$$

$$E_{LUMO}\,(\text{in eV}) = -(Ø_{RED} + 4.74) \quad (2)$$

Where $Ø_{OX}$ and $Ø_{RED}$ are potentials corresponding to oxidation and reduction in anodic and cathodic scan, respectively.

2.1.2.5 Quantum yield measurements

The quantum yield (QY) measurements of the LGQDs, Mn-LGQDs were determined according to an established procedure using Quinine sulfate (with QY of 54%, 0.1 M H_2SO_4 as a solvent) as a reference. The QY of the QDs was calculated according to the below equation.

$$Ø_x = Ø_{re}\left(\frac{I_x}{I_{re}}\right)\left(\frac{A_{re}}{A_x}\right)\left(\frac{n_x}{n_{re}}\right)^2 \quad (3)$$

Where φ is the QY, I is the measured integrated emission intensity, A is the absorbance and n is the refractive index of the solvent. The subscript "x" refers to the sample and "re" refers to the reference with known QY. For these solutions, $\eta_x = \eta_{re}$.

2.1.2.6 Sustainability metrics calculation

Raw materials: The raw material used is lignosulfonate biomass. The advantages of low cost and being bio-renewable makes them attractive as precursors for the synthesis of carbon-based materials. Nitric acid was used in very less quantity. The mass intensity was calculated to be 21.1, and the water intensity (WP) was calculated to be 50.[1-3]

$$Mass\ intensity = \frac{mass\ of\ all\ reactants\ excluding\ water}{mass\ of\ product} \text{kg/kg} \quad (4)$$

$$= 21.1$$

$$Water\ Intensity\ (W_P) = \frac{mass\ of\ all\ water\ used}{mass\ of\ product} \text{ Kg/Kg product} \quad (5)$$

$$= 50$$

The reaction mass efficiency for LGQD synthesis was calculated to be 4.73% as shown below.

$$Reaction\ mass\ efficiency\ (RME) = \frac{mass\ of\ products}{mass\ of\ all\ reactants} \text{ X } 100\% \quad (6)$$

$$= 4.73\%$$

$$E\ factor = \frac{[kg(raw\ materials) - kg(desired\ product)]}{kg(total\ product\ excluding\ water)} \quad = 20.1$$

2.1.3 Results and Discussion

Our synthetic process, which converts lignosulfonate into LGQDs with designed architecture, follows a two-step hydrothermal process that includes oxidative scission and aromatic reintegration (Figure 2.1a).[137] Here, the oxidative scission was performed with nitric acid, and the resultant lig-

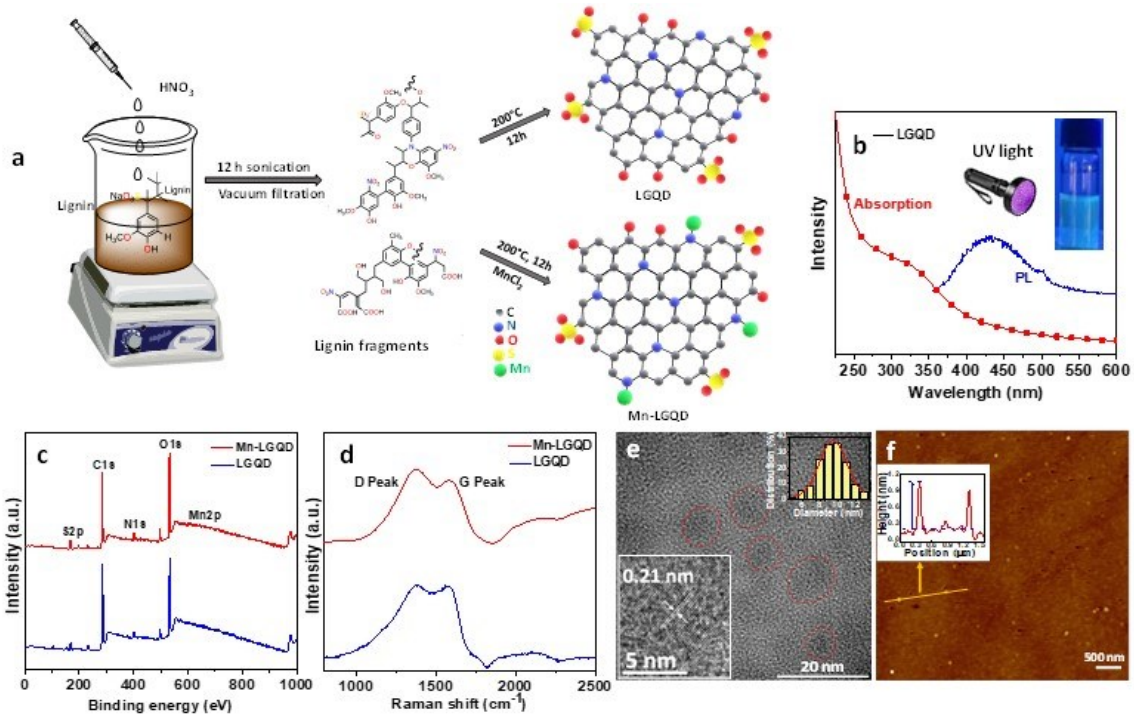

Figure 2.1: (a) Schematic of the hydrothermal synthesis of LGQDs and Mn-LGQDs. (b) UV-Vis absorption and PL emission spectrum of LGQDs. Inset shows a photograph of LGQDs emitting blue light when excited with a UV lamp. (c) XPS survey spectrum of LGQDs and Mn-LGQDs and (d) Raman spectrum of LGQDs and Mn-LGQDs.(e) TEM image of Mn-LGQDs, scale bar is 20nm. (Inset at the top right shows the histogram for the Mn-LGQDs size distribution and bottom inset shows the HRTEM, scale bar is 5nm). (f) AFM topography image of Mn-LGQDs, scale bar is 500nm.(Inset shows height scan of the Mn-LGQDs indicated by the arrow).

nosulfonate segments were further aromatically re-fused into crystalline LGQDs via hydrothermal treatment. A co-reactant ($MnCl_2$) was added to the cleaved and carbonized lignosulfonate fragments to incorporate Mn atoms in LGQDs lattice for Mn-LGQD's synthesis. When irradiated with a UV lamp, the LGQD sample solutions emitted an intense blue light, due to the quantum confinement induced bandgap effect, indicating the successful formation of GQDs. Figure 2.1b shows a representative absorbance and PL spectra of LGQDs and a photograph of blue-light emitting

LGQD solution (inset of Figure 2.1b). Previous studies suggested that the hydrothermal process parameters can control the size, surface chemistry, and resultant properties of GQDs.[138] Hence, we systematically varied the process parameters that include hydrothermal reaction temperature and time, to tune the size and surface chemistry of LGQDs and to optimize their PLQY, which is a critical aspect of the study. First, we prepared different LGQD samples at reaction temperatures of 160°C, 180°C, 200°C, and 210°C respectively, by keeping the reaction duration (12h) constant. The PL measurements showed a maximum intensity for the sample synthesized at 200°C (Figure 2.2a). In a similar study carried out at a constant reaction temperature of 200°C for different reaction duration, the maximum PL was observed (Figure 2.2b) for a reaction time of 12h. Thus, we confirmed that a reaction temperature of 200°C and a duration of 12h is optimal for procuring LGQDs with superior photoluminescence. The PL properties did not show a significant change when the initial concentration of lignosulfonate is varied. For Mn-LGQDs, we also

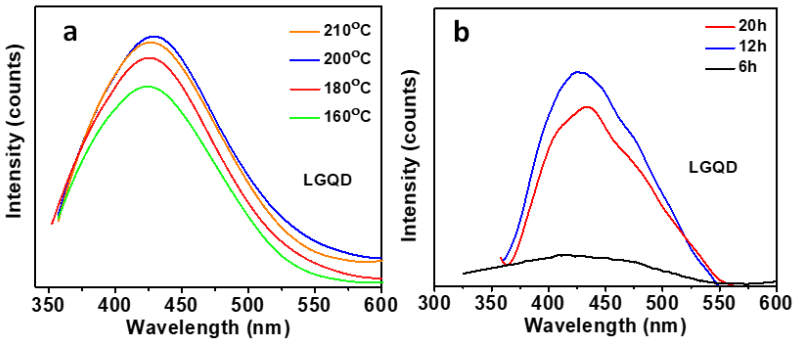

Figure 2.2: (a) Temperature and (b) Time dependence on PL of LGQDs

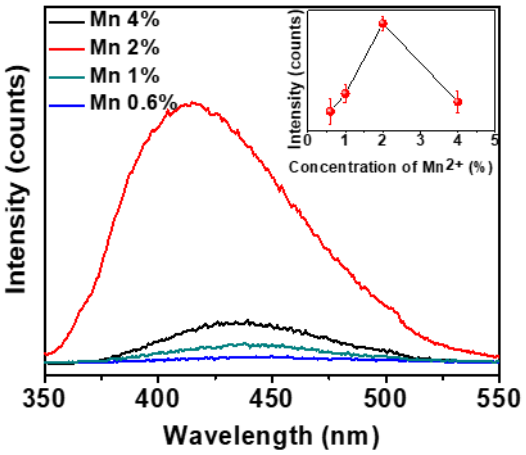

Figure 2.3: Dependence of PL on concentration of Mn in Mn-LGQDs

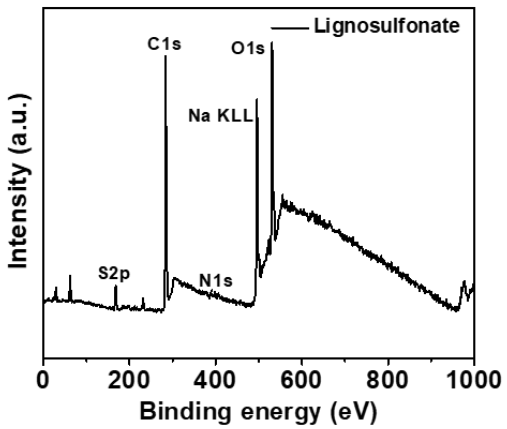

Figure 2.4: Survey spectrum of Lignosulfonate

investigated the effect of heteroatom concentration on the PL intensity. Figure 2.3 shows the PL spectra of Mn-LGQDs with Mn doping percentage varied from 0.6% to 4%. The dopant percentages referred here are the initial weight percentage of dopant precursors introduced into the hydrothermal reaction. As shown in Figure 2.3, PL spectra demonstrated a strong dopant concentration dependence. From this figure, it is evident that the 2% doping of Mn yielded the highest QY as compared to the other dopant concentrations. The PLQY was found be lower for concentrations below or above 2%. The strong dopant concentration-dependent PL demonstrated by Mn-LGQDs suggests that even a minimal change in dopant concentration can substantially alter their optical activity. A decrease in PL intensity was seen as we increased the doping percentage above the optimal doping. A similar PL response with doping was reported by Kadian et. al.[139] One of the mechanisms for enhanced PLQY for functionalized GQDs is the surface passivation of defects by functional groups.[140-142] However, upon increasing the number of dopants (Mn in the present case), the integration of dopant into the GQD lattice can not only create more defects, but also disrupt the passivation effects by metal coordination with the functional groups. Hence, beyond optimal concentration of the

Table 2.1: Atomic percentages of different elements in Lignosulfonate, LGQD and Mn-LGQD.

Element / Sample	C1s	O1s	N1s		S2p	Mn2p	QY %
			Graphitic	Pyridinic			
Lignosulfonate	65.6	30.09	1.03	0.32	2.96	0	-
LGQD	67.87	24.93	4.33	0.56	2.31	0	23
Mn-LGQD	63.67	26.97	5.15	1.36	2.61	0.24	31.6

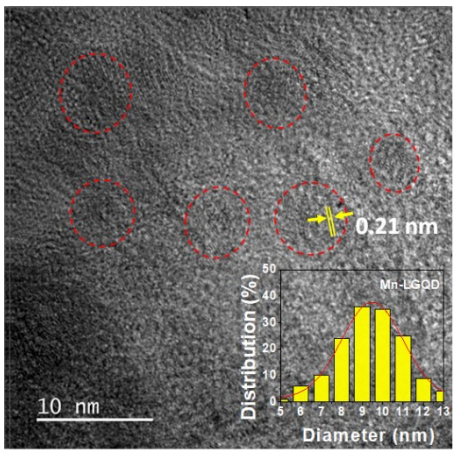

Figure 2.5: TEM image of the Mn-LGQDs showing corresponding lattice spacing

dopant, the newly created defects (which could function as the quenching centers) in combination with reduced surface passivation leads to a decrease in quantum yield.[139, 143-145]

The GQD samples were analyzed using XPS to ascertain the success of doping. The XPS survey scan of LGQDs demonstrated features at 167.72 eV, 284.5 eV, 398.58 eV, 532.14 eV, corresponding to the binding energies of S2p, C1s, N1s, and O1s, confirming the presence of C, O, N, and S in the LGQD (Figure 2.4). Since the XPS analysis confirmed the existence of S and N in the lignosulfonate precursor, it is prudent to hypothesize that the use of lignosulfonate with S and N in

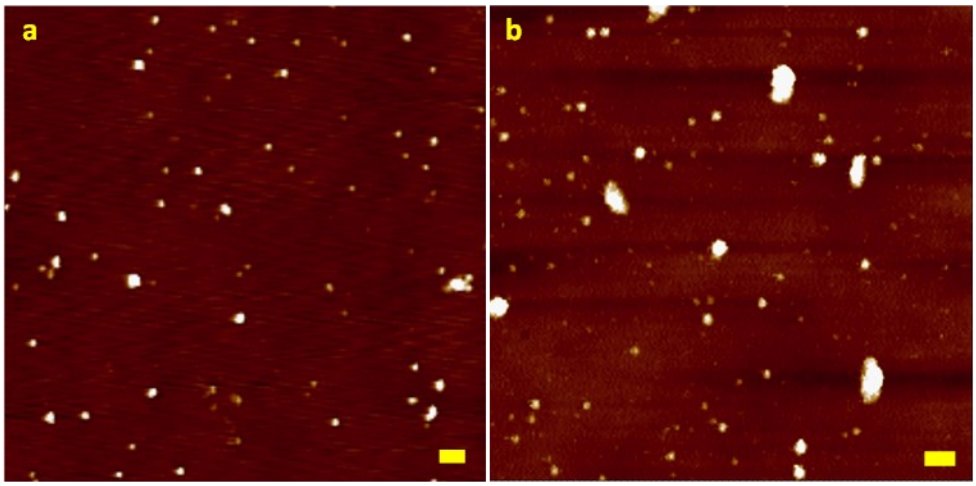

Figure 2.6: AFM images of (a) Mn-LGQDs, (b) LGQDs, scale bar is 200 nm

its native structure leads to the formation of in-situ S, N-doped LGQDs. It is worth noting that

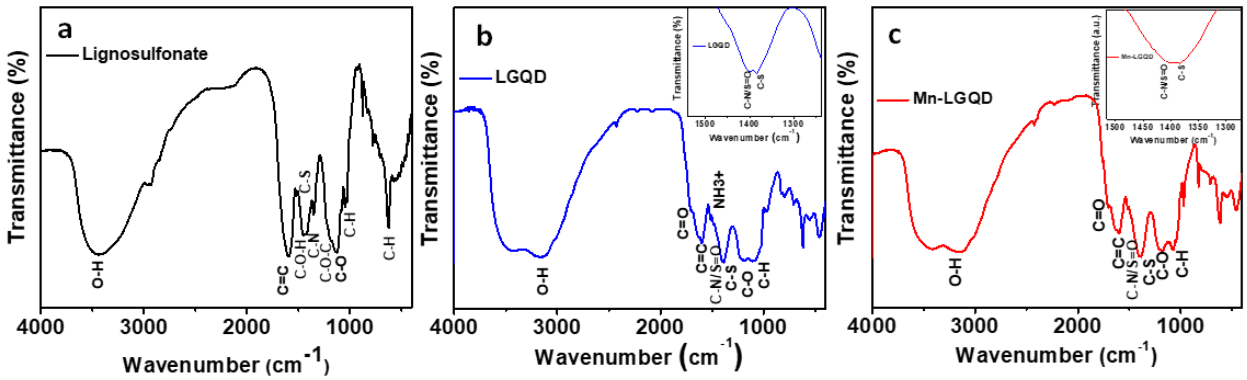

Figure 2.7: FT-IR spectrum of (a) Lignosulfonate (b)LGQD and (c) Mn-LGQD

besides the S, N atoms present in lignosulfonate precursor, the N atoms from the nitric acid treatment during synthesis, also likely contribute towards N doping in LGQDs.[123] The XPS survey scan

for Mn-LGQDs (Figure 2.1c), in addition to S2p, C1s, N1s, and O1s, illustrated a feature at 642.29 eV corresponding to Mn2p, confirming the successful metal (Mn)-nonmetals (S and N) co-doping in the Mn-LGQDs. Table 2.1 shows the atomic percentages of elements present in the lignosulfonate, LGQDs, and Mn-LGQDs calculated from the XPS data. The elemental quantification indicated a relatively lower carbon content in the case of Mn-LGQDs compared to LGQDs (Table 2.1). The observed lower carbon content could be attributed to the replacement of C atoms in the lattice by dopant atoms via substitutional doping (mostly O and N). Hence, the XPS characterization results confirmed that aided by the in-situ doping afforded by the lignosulfonate precursor, Mn, S, and N atoms get incorporated into the Mn-LGQDs resulting in metal-nonmetal co-doped GQD system. After confirming the successful formation of the doped GQDs, the samples were analyzed using different microscopic and spectroscopic techniques to derive in-depth understanding regarding their morphology, structure, surface chemistry, and photo-physics. The graphenic structure and the defect density of LGQDs and Mn-LGQDs were evaluated using Raman

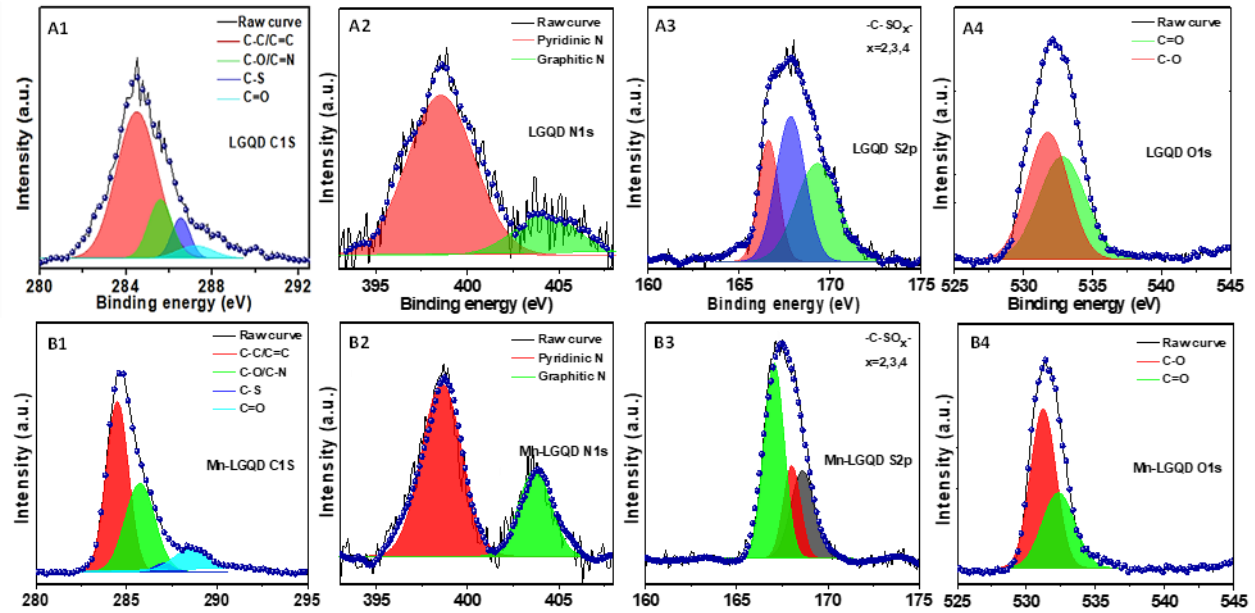

Figure 2.8: High-resolution XPS spectra corresponding to C1s, N1s, S2p and O1s of LGQDs (A1-A4) and Mn-LGQDs (B1-B4).

spectroscopy. The Raman spectra of LGQDs and Mn-LGQDs (Figure 2.1d) showed a prominent G-band at ~1570 cm^{-1} corresponding to the first-order scattering or the E_{2g} vibrational mode of the sp^2 carbons emphasizing the presence of graphenic regions.[146] Another prominent feature appeared in the Raman spectra at ~1375 cm^{-1} called the D-band and points to the disorder in both LGQDs and Mn-LGQDs. Hence, Raman studies also confirmed the conversion of the polymeric lignosulfonate into LGQDs, complementing the XPS and XRD data. In general, the intensity ratio (I_D/I_G) of the D-band and G-band is considered a quantitative measure of the defect density in graphenic matrices. Our analysis indicated that the I_D/I_G is higher for Mn-LGQDs (1.17) compared to LGQDs (1.01). The higher I_D/I_G is plausibly due to the introduction of a relatively higher number of defects in Mn-LGQDs compared to LGQDs. Figure 1e and f show the morphological and topographical images of the Mn-LGQDs obtained using TEM and AFM. The TEM image and corresponding size distribution histograms (inset Figure 2.1e and Figure 2.5) clearly show that Mn-LGQDs and LGQDs have an average size of ~10 nm. The lattice-resolved HRTEM image (inset of Figure 2.1e) depicted characteristic (010) plane of the graphitic lattice with an interplanar distance of 0.21nm, indicating the crystalline, graphenic nature of LGQDS and Mn-LGQDs. The AFM topography and a representative height scan profile for Mn-LGQDs (inset) is shown in Figure 2.1f. The ~1 nm height calculated here indicates that Mn-LGQDs consist of a maximum of three graphene layers. However, it was previously reported that even single layer solution dispersed GQDs can show

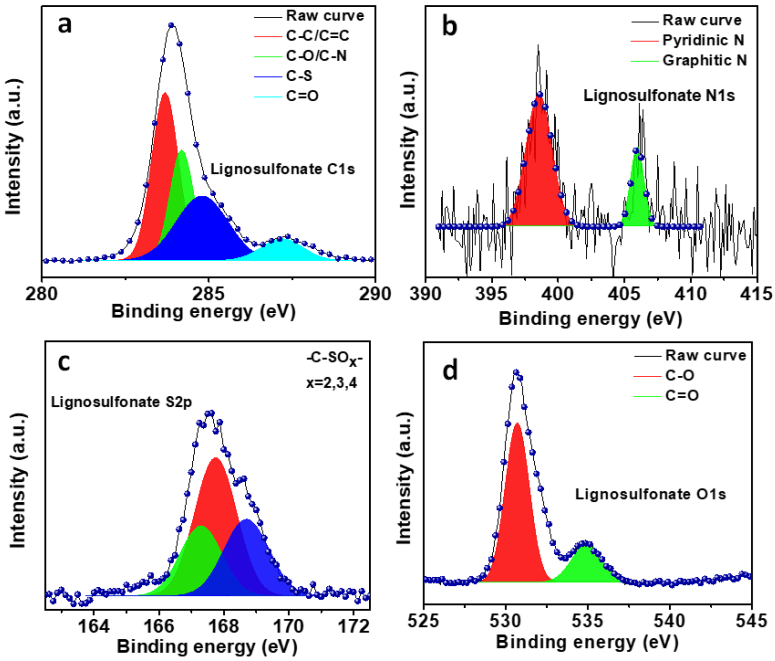

Figure 2.9: High resolution XPS spectrum of Lignosulfonate

height profiles up to 1 nm in AFM.[147] AFM images corresponding to LGQDs are shown in Figure 2.6. After evaluating the structural and morphological properties of LGQDs, we probed the surface chemistry of LGQDs and Mn-LGQDs using FTIR and high-resolution XPS. Figure 2.7 shows the FTIR spectra of lignosulfonate, LGQDs, and Mn-LGQD samples. The presence of vibrational bands at 1600 cm^{-1} (aromatic C=C stretching vibration), 1091 cm^{-1}, 830 cm^{-1}, and 798 cm^{-1} (the in-plane and out-of-plane deformations of aromatic C–H) confirmed the preservation of aromatic moieties during the conversion of lignosulfonate to LGQDs. Further, the C-O-C linkages (ether) found in lignosulfonate did not exist in the IR spectrum of LGQDs (and Mn-LGQDs), indicating the cleavage of ether during the LGQDs formation. The IR spectra of LGQDs also showed a broad vibrational band at 3350 cm^{-1} (OH vibration), 1637 cm^{-1}, and 1191 cm^{-1} (C=O and C–O), representing the edge

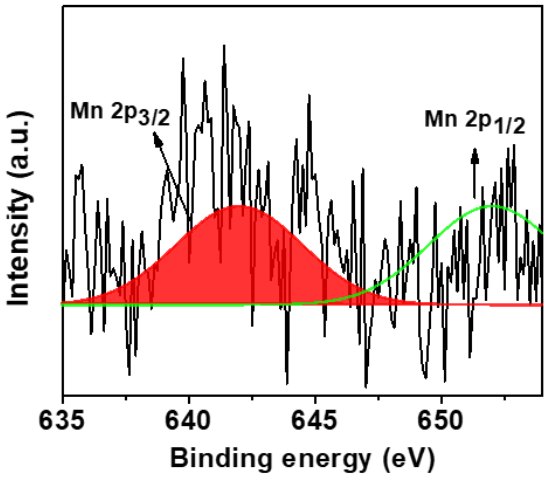

Figure 2.10: High resolution XPS spectrum of Mn

functional groups, including ketones, carboxylic acids, and alcohols. Besides, LGQDs and Mn-LGQDs also exhibited a vibrational feature at 1404 cm^{-1}, which could result from C-N or S=O vibration, signifying the lattice incorporation of nitrogen and/or sulfur.[148] The peak observed around 1350 cm^{-1} in LGQDs and Mn-LGQDs is attributed to the stretching vibration of C-SO_x confirming the presence of sulfur. It is worth noting that sulfur, in general, is known to be incorporated in the GQD lattice in oxide form.[131, 149] Based on previous studies, we expect that introduction of Mn dopant atoms into the graphitic lattice can occur either through substitutional doping or binding of Mn atoms to N atoms.[126, 150] In the first case, the Mn-dopants are located ~1.20Å above the vacancy of the graphene lattice.[150] Alternately, the Mn doping in nitrogen-containing GQDs can occur through the binding of Mn onto the doped lattice N atoms.[126] Here, a comparison of the FTIR spectrum between LGQDs and Mn-LGQDs demonstrated the disappearance of N-H

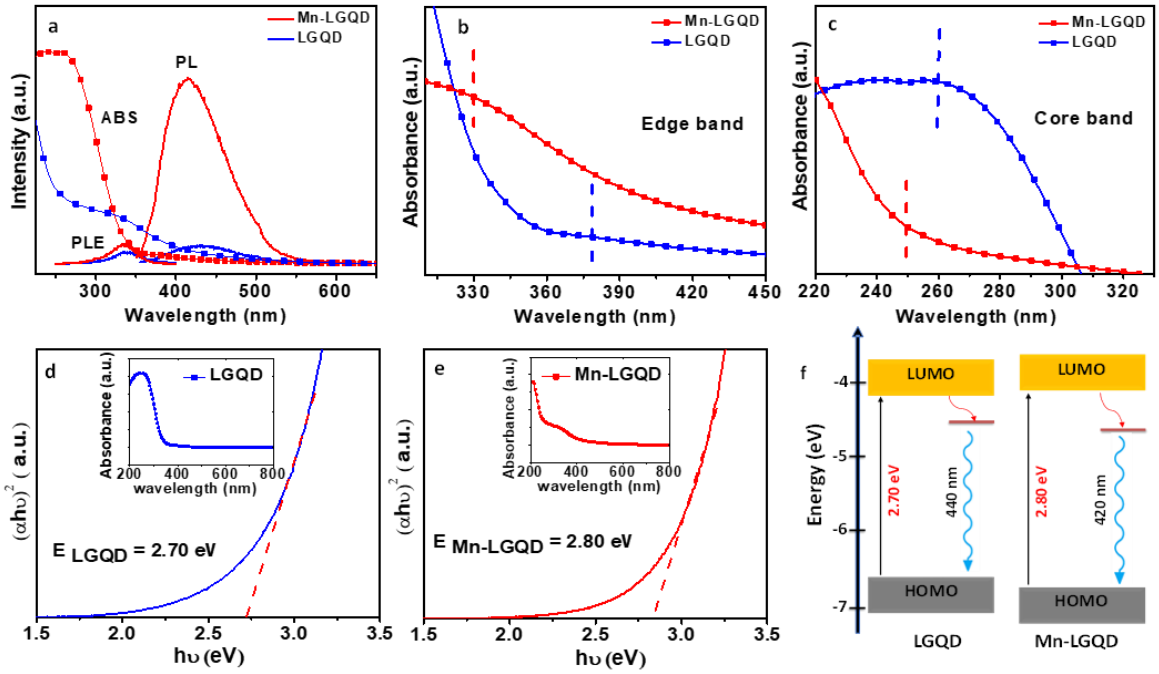

Figure 2.11: (a) UV-Vis absorbance spectrum, PL excitation (PLE) and PL emission (PL) of LGQDs and Mn-LGQDs. (b, c) Core band and Edge band observed in the absorbance spectra of LGQDs and Mn-LGQDs. (d, e) Band gap measurement using Tauc plots for LGQDS and Mn-LGQDs (inset shows corresponding UV-Vis absorbance spectrum). (f) Schematic showing the band structure and corresponding PL. As shown here, the optical bandgap of Mn-LGQD is higher compared to LGQDs due to Mn-doping.

bending peak at 1484 cm^{-1}, pointing to the N-aided anchoring of Mn in Mn-LGQDs. Further, the retention of higher N in Mn-LGQDs than LGQDs, based on the XPS analysis, also supports the N-assisted anchoring of Mn in Mn-LGQDs.

To assimilate a detailed understanding of individual elements in LGQDs, including their oxidation states, the high-resolution XPS scans of the elements (C, N, O, S, and Mn) were recorded, deconvoluted, and analyzed. The high-resolution scans of C1s (Figure 2.8 A1 and B1 and Figure 2.9) for lignosulfonate, LGQDs, and Mn-LGQDs were taken and deconvoluted which signifies the existence of four types of carbons including graphitic carbon at 284.5 eV, C–O and C-N at 285.6 eV, C=O at 287.3 eV, and carbon bound to sulfur (C-SO_x) at 286.53 eV. Notably, the C=C component is the most intense peak among all deconvoluted peaks in all GQD samples, implying the graphitic structure. Moreover, the increased carbon content in LGQDs compared to lignosulfonates is due to the cleavage of ether bonds and refusion into the aromatic skeletons. The deconvoluted high resolution spectrum of N1s indicated the existence of nitrogen in two different configurations, namely, graphitic (basal plane) and pyridinic (edge) N, represented by the components at binding energies 405 eV and 398 eV, respectively (Figure 2.8 A2 and B2). The pyridinic N peak at 398.5 eV may have masked the N-H peak observed at ~401 eV.[151] It is worth noting that the pyridinic nitrogen content is more in Mn-LGQDs. The additional electron pairs provided by the pyridinic N atoms to the π cloud can result in the delocalization of electrons, thus potentially contribute to enhanced photophysical properties in Mn-LGQD (discussed later).[152] We also analyzed the high resolution sulfur spectrum and the S2p feature at ~ 168.65 eV confirms sulfur doping in the oxide-S form in LGQDs well as Mn-LGQDs (Figure 2.8 A3 and B3). The absence of $2p_{3/2}$ (~ 164 eV) and $2p_{1/2}$ peaks (~165 eV) in the S2p spectra exclude the possibility of sulfur existing in the thiophene form.[131] For Mn-LGQDs, we analyzed the Mn 2p region, which indicated that Mn exists in

the Mn^{2+} state, bound to the N atoms in Mn-LGQDs (Figure 2.10). After understanding the structure and surface chemistry, we investigated the optical properties of LGQDs and Mn-LGQDs. The optical properties of GQDs are controlled by their size and electronic structure (e.g., bandgap, surface functional groups, and defect density).[153] Since our morphological and topographical analysis (via TEM and AFM) indicated similar sizes for LGQDs and Mn-LGQDs; the doping-induced changes in the electronic structure should dictate their optical properties. We analyzed their absorption and emission spectra to unravel the doping effect on the photophysical properties of LGQDs. The UV-Vis absorption spectrum of lignosulfonate demonstrated a peak below 300 nm, characteristic of the aromatic units. Interestingly, the absorption spectrum of LGQDs (Figure 2.11a) showed two distinct absorption peaks around 270 nm and >300nm. The first peak (~ 270 nm) is due to π–π* transition of C=C bond (generally referred to as the core band).[129] The second absorption peak at >300 nm is a result of both the n–π* transitions of C–N, C-S, C=O/C-O groups, and the π–π* charge-transfer transition of the GQD edge (edge band).[129, 154] Similarly, the UV-Vis absorption spectra of Mn-LGQDs also displayed two bands corresponding to the core (<300nm) and edge

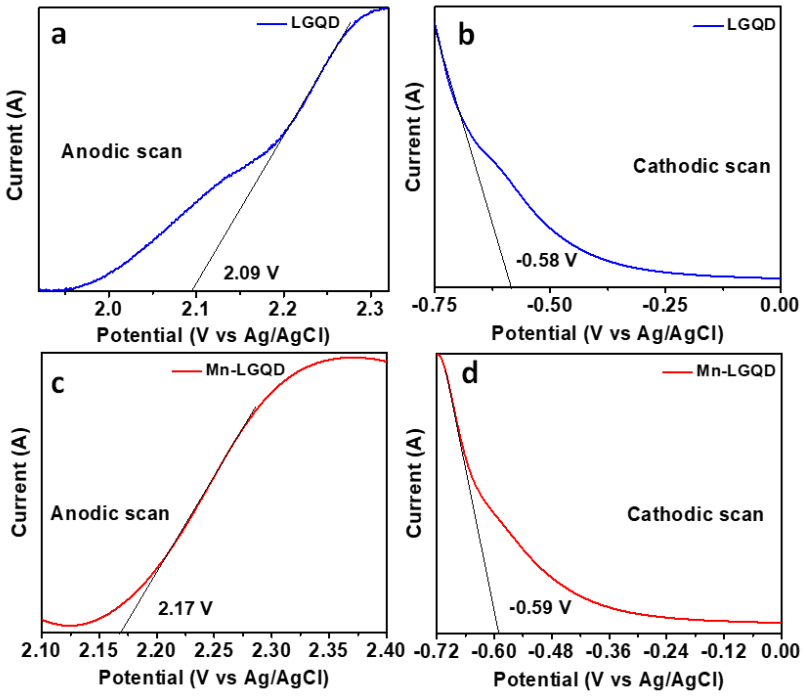

Figure 2.12: Linear sweep voltammetry measurements for HOMO and LUMO level determination. Anodic scan for determining the valence band maximum at 20 mVs^{-1}(a,c), Cathodic scan for determining the conduction band minimum at 20 mVs^{-1} (b,d)

band (>300nm) transitions (Figure 2.11 b and c). However, the wavelengths corresponding to the maximum absorption ($\lambda_{abs,\ max}$) of the core and edge bands for Mn-LGQDs showed a slight shift compared to the corresponding peak maximum observed in the case of LGQDs. Note that π–π* (representing HOMO-LUMO) transition typically corresponds to the bandgap and therefore, the shift in π–π* transition maximum should be a consequence of bandgap change that may occur due to changes in GQD size and/or doping.[129] Since the sizes of LGQDs and Mn-GQDs found to be almost identical, we attribute the shift observed in the π–π* band of Mn-LGQD compared to LGQD to the band structure modifications due to the introduction of Mn-dopant atoms. To confirm the doping induced bandgap changes, we compared the optical bandgap values of both LGQDs and Mn-LGQDs which were calculated by employing Tauc relation on UV-Vis absorption data (Figure 11 d and e). The Tauc relation[155] used for the optical band gap calculation is given by:

$$(\alpha h\upsilon)^{1/n} = \alpha_0\left(h\upsilon - E_g\right) \qquad \textbf{(8)}$$

where α, hυ, α_0, E_g and n are the absorption coefficient, photon energy, a constant, optical band gap, and an empirical constant, respectively. Here α is obtained from the UV-Vis absorption spectrum measurements. Typically, n values of 1/2 and 2 are assumed for calculating the bandgaps of direct and indirect bandgap semiconductors. Assuming LGQDs/Mn-LQGDs are direct bandgap materials,[155] we used n=1/2 in this study. Figure 2.11 d and e show the $(\alpha h\upsilon)^2$ vs. hυ graphs for LGQDs and Mn-LGQDs. As shown in these graphs, the optical bandgap (E_g) is given by the intercept of the linear fit of the $(\alpha h\upsilon)^2$ vs. hυ curves with energy (hυ) axis. The optical bandgaps estimated from these fits are 2.7eV for LGQD and 2.8 eV for Mn-LGQDs. From our results, it is clear that the introduction of Mn atoms resulted in a higher bandgap for Mn-LGQD compared to

LGQDs, and therefore, we can confirm that observed blue shift in the core band peak is due to higher bandgap of Mn-LGQDs. The absorption peaks corresponding to edge transitions (Figure 2.11c) also showed a similar trend, with a ~47 nm blue shift in Mn-LGQD compared to LGQDs. A schematic band diagram depicting the HOMO-LUMO level positions and bandgaps for both

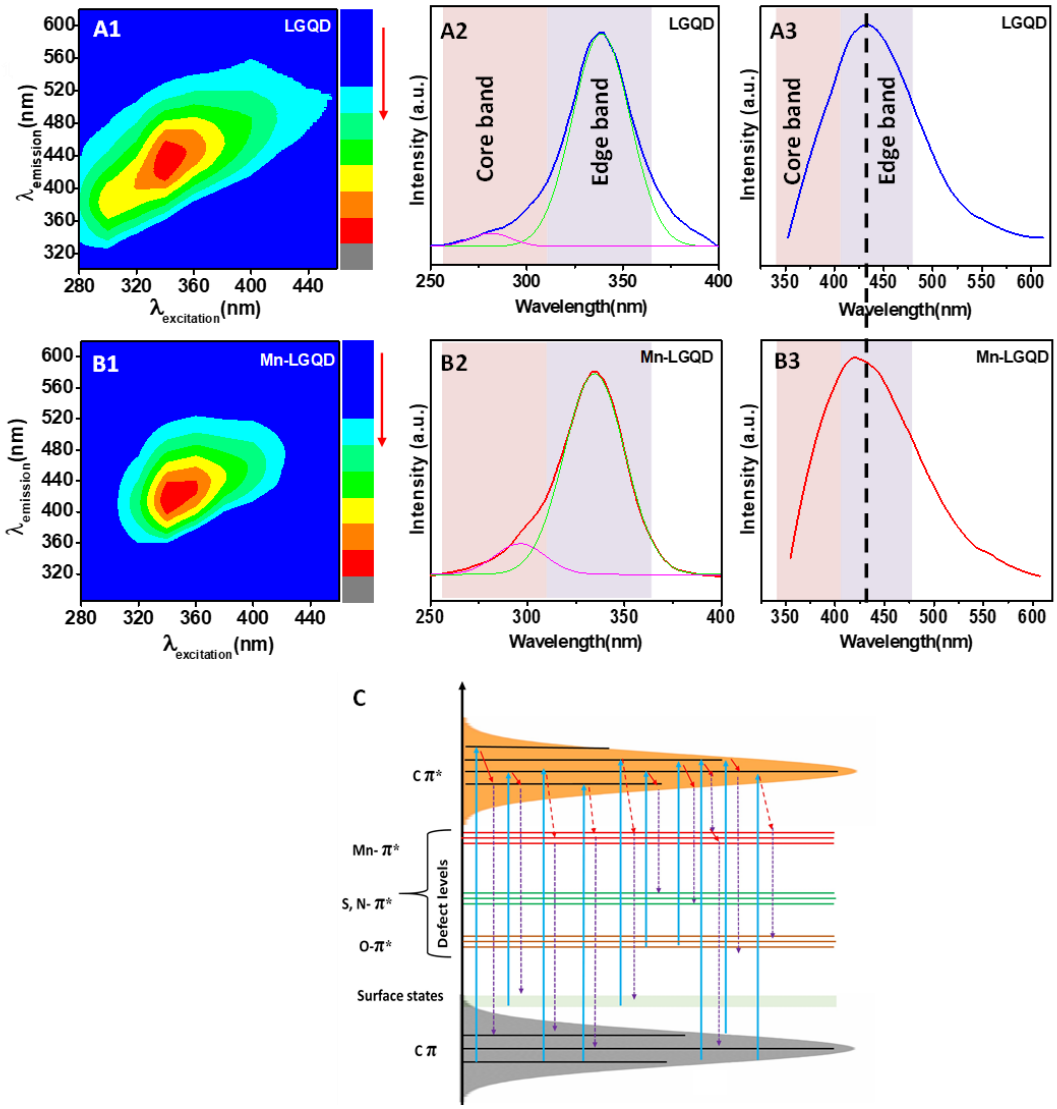

Figure 2.13: Photoluminescence studies of LGQDs and Mn-LGQDs with optimized doping. Excitation wavelength dependent 2D PL excitation-emission contour maps of LGQDs (A1) and Mn-LGQDs (B1). The Z scale bars in the figures indicate the PL intensity. The PL excitation (PLE) spectra of LGQDs (A2) and Mn-LGQDs (B2). The PL emission spectrum of LGQDs (A3) and Mn-LGQDs (B3) under an excitation of 340 nm. (C) A schematic of Mn-LGQD band structure depicting different possible excitation and emission transitions.

LGQDs and Mn-LGQDs is presented in Figure 11f. The exact energy values of the HOMO and LUMO for the LGQDs and Mn-LGQDs were calculated from LSV scans, as shown in Figure 2.12. To comprehend the doping-dependent luminescence, we investigated the photoluminescence excitation (PLE) and emission spectra (PL) of the LGQDs and Mn-LGQDs as a function of excitation wavelengths (λ_{ex}) in the range of 280 nm to 460 nm. Figure 2.13 A1 and B1 shows the corresponding PL spectra contour maps with the Z scale bar indicating the PL emission intensity of LGQDs and Mn-LGQDs at each point in the maps. From Figure 2.13 A1 and B1, it is clear that both spectral range and the peak wavelength of the PL spectra ($\lambda_{em,\ max}$) shifts as a function of λ_{ex}. The excitation-dependent emissive properties of the LGQDs and Mn-LGQDs could be plausibly due to the distribution of multiple emissive centers on the quantum dots. Like the UV-Vis absorption spectrum, the PLE spectrum of LGQDs and Mn-LGQDs also consists of two characteristic bands in the UV regime, with their peaks centered around ~290nm and ~340nm, ascribed to the core and edge bands. Note that the small differences (stokes shift) between the UV-Vis absorption spectrum and PLE are commonly observed in chemically prepared GQDs.[129] The co-existence of two PLE bands in LGQDs and Mn-LGQDs further confirms the presence of multiple-emissive centers in LGQDs (Figure 2.13 A2 and B2). Another similarity observed in the PLE spectra of LGQDs and Mn-LGQDs is that the PLE peak at ~340 nm has a higher intensity than the PLE peak at ~290nm. The relatively higher intensity of the edge bands implies that they are the dominant emissive centers in both LGQDs and Mn-LGQDs. Subsequently, we investigated the PL spectra of the LGQDs and Mn-LGQDs to validate the emissive centers and the changes induced through doping. The PL intensity maximum ($\lambda_{em,\ max}$) for LGQD and Mn-LGQDs was observed at 440 nm and at 420 nm (blue shifted), respectively, when excited at 340 nm. Similar to the absorption spectrum, the PL spectra (Figure 2.13 A3 and B3) also showed two co-existing components (ascribed to the core

and edge bands) again confirming the presence of two emissive centers in LGQDs and Mn-

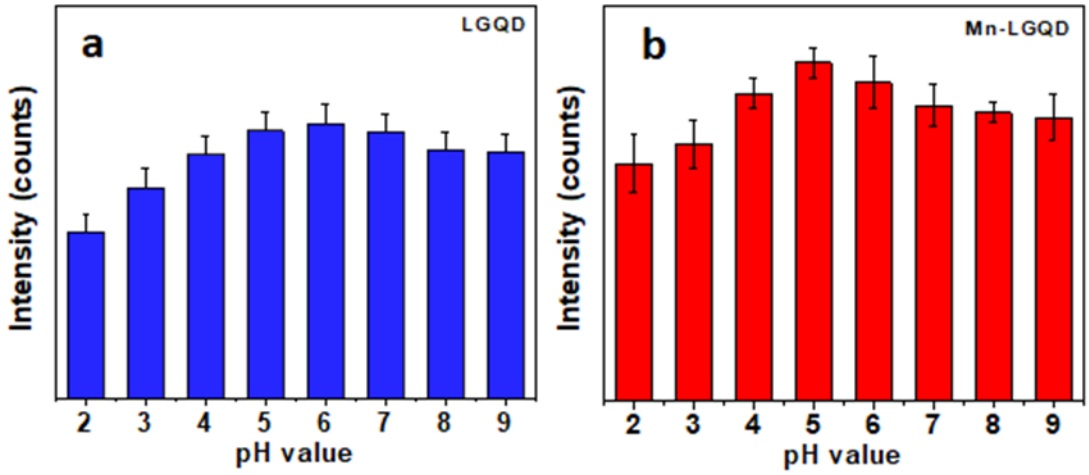

Figure 2.14: pH measurements of (a) LGQD (b) Mn-LGQD

LGQDs. It is important to note that, in both PLE and PL spectra, the doping resulted in significant changes in band-II (edge band transition) compared to band-I (core band transition). This is understandable since doping is known to create edge states which will play a significant role in PL.

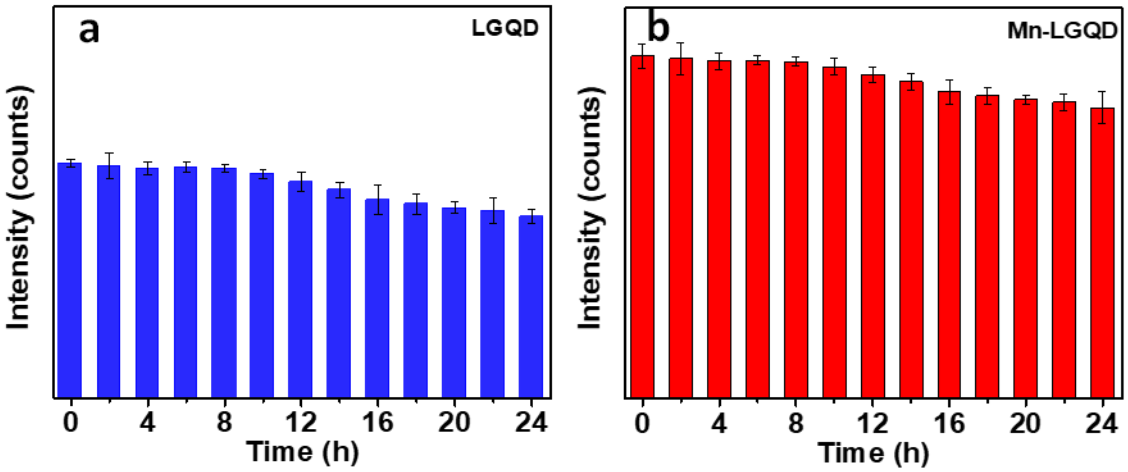

Figure 2.15: Photostability measurements of (a) LGQD (b) Mn-LGQD

Consistent with the absorption spectra, a blueshift was observed for the edge band in Mn-LGQDs (Figure 2.13 B3). Besides the edge bands, the PL core bands also showed a shift with doping. The core band peaks (Figure 2.13 A3 and B3) in the case of Mn-LGQDs show a blue shift in comparison to the core band peak of LGQDs. This shift can be attributed to the modification of electronic

band structure (e.g., shifts in HOMO-LUMO levels) in Mn-LGQD compared to LGQD via the introduction of dopant atoms in the graphenic lattice, as observed in the band structure.[129, 156] It is worth noting that the PLE, in contrast to PL, did not show a considerable increase in intensity with doping (Figure 2.11a) because the PLE transitions correspond to transitions from the ground state (Cπ) and surface states. The doping-induced band structure changes can show a profound effect on the PLQY, an important metric used to represent the fluorescence efficiency of LGQDs and Mn-LGQDs quantitatively. The PLQY values for both these samples were estimated using the QY of quinine sulfate as a standard. The calculated QY for LGQDs is 23%, which is higher than most of the previously reported works on lignin derived GQDs as well as some GQDs prepared from other precursors/methods. The high PLQY in LGQDs can be ascribed to in-situ S, N doping effect resulting from the sulfur and nitrogen present in the lignosulfonate precursor. Similarly, the incorporation of Mn in Mn-LGQDs resulted in a substantially higher PLQY (estimated as 31%, which is ~35% enhancement in PLQY compared to LGQDs), indicating the effectiveness of metal-non-metal co-doping. The enhanced PLQY observed for Mn-LGQD in comparison to LGQDs could be plausibly due to a synergistic effect of multi-atom doping and a relatively higher number of "defect sites".[157] The defects can potentially create new energy levels between C π and π*, thus providing new electron transition pathways in the band structure of Mn-LGQDs. The proposed energy band diagram for the Mn-LGQD system depicts the electronic absorption, inter-band crossing, and radiative emission through the energy levels, including HOMO-LUMO levels of carbon, surface states, anti-bonding orbitals, etc. All the possible radiative emission transition pathways that could contribute to the observed high PLQY in Mn-LGQDs are depicted in Figure 2.13C. Since the PL emission corresponding to the core band is weak, the radiative PL emission should predominately happen from the defect levels created due to Mn doping. Further, we postulate that

the peak PL emission in Mn-LGQDs is blue-shifted as new defect levels related to Mn-doping are located closer to the C π* level. Therefore, the electrons in the excited C π* state can now transition to Mn π* via inter-band crossing and then relax to the ground state via radiative emission. In addition, it has been reported that metal doping can result in charge transfer, accelerate the electron mobility on the graphene quantum dots surface and the presence of valence electrons in the dopant metal could be utilized to enhance QY.[158, 159] In addition to the changes in the material properties, including electronic band structure and surface chemistry of LGQDs/Mn-LGQDs, the solution's pH can also influence the PL properties. Therefore, we investigated the effect of pH on the PL (Figure 2.14) for LGQDs and Mn-LGQDs. The results indicated that the emission intensity remains relatively stable at moderate pH, with a maximum PL observed at a pH of 5. However, a reduced PL intensity was seen under strongly acidic or alkaline conditions. The comparatively low PL at extreme pH conditions, could be due to the protonation and deprotonation of functional groups at the edge of the Mn-LGQDs (and LGQDs) and the resultant aggregation.[137, 160-162] In addition to PLQY, a stable photoluminescence emission under continuous irradiation is another important requirement for practical applications.[163, 164] The PL spectra measured under continuous irradiation showed a stable PL emission intensity indicating our LGQDs/Mn-LGQDs are resistant to photobleaching (Figure 2.15).

The high PLQY coupled with stable luminescence at moderate pH ranges suggests that Mn-LGQDs are suitable for luminescence-based applications such as bio-imaging and sensing. Here, we investigated the utility of Mn-LGQDs and LGQDs with maximum PLQY for sensing contaminants present in water bodies. Considering the acute toxicity of mercuric ions even at ultra-low concentrations,[136] inorganic mercury was selected as the model contaminant. We studied the changes in the PL spectra of Mn-LGQDs and LGQDs after adding mercuric (Hg^{2+}) ions to the Mn-

LGQD and LGQD solutions. The PL intensities of both LGQD and Mn-LGQD systems decreased with an increase in the Hg^{2+} concentration. Figure 2.16a shows the corresponding Hg^{2+} concentration-dependent PL emission spectra of Mn-LGQDs. As shown, with an increase in the Hg^{2+} ion concentration, the intensity of maximum emission peak (at 420 nm) in the PL spectra of Mn-LGQDs decreased without any change in the peak position. The intimate concentration-dependent intensity changes confirm that the Mn-LGQDs with high PLQY can be leveraged as a sensitive reporter for detecting Hg^{2+} ions in the solution. The decrease in PL emission intensity followed a linear trend as we increase the Hg^{2+} concentration in the Mn-LGQD solution in the range of 2–100

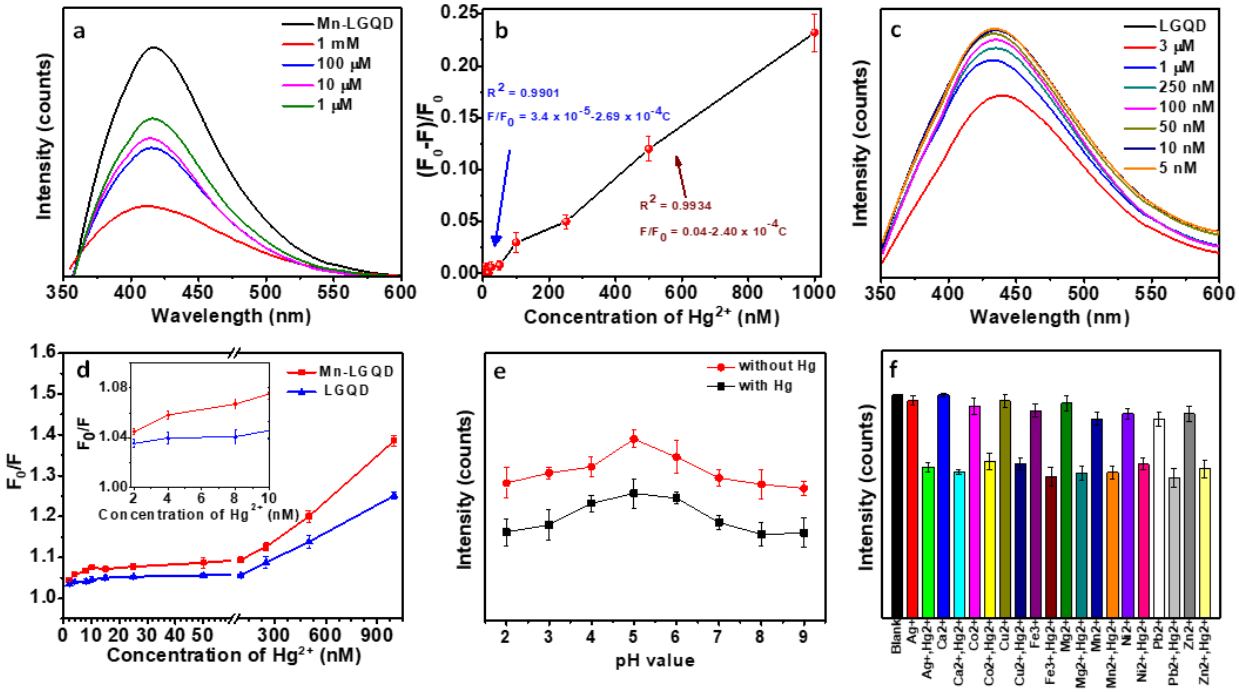

Figure 2.16: Fluorescence-based mercury detection studies using LGQDs and Mn-LGQDs. (a) PL spectra (λ_{ex} = 340 nm) of Mn-LGQDs measured in the presence of different concentrations of Hg^{2+}. (b) Plots of intensity ratio (F/F_0) versus the concentrations of Hg^{2+} in the case of Mn-LGQDs. (c) PL emission spectra (λ_{ex} = 340 nm) of LGQDs measured in the presence of different concentrations of Hg^{2+}. (d) Stern-Volmer plot for LGQD and Mn-LGQD. (e) Variation in PL maximum of Mn-LGQDs before and after the addition of 10µM Hg^{2+}ions as a function of pH value. (f) PL responses of Mn-LGQDs to the different metal ions with and without Hg^{2+}.

nM (inset of Figure 2.16b). By plotting the changes in the fluorescence intensity with concentration, the limit of detection (LOD) is estimated to be 0.56 nM. The existence of two linear regions

with different slopes can be seen for higher (200nM-1μM) and lower (1nM-100nM) concentrations in Figure 16b.[165, 166] The LOD is calculated here is for the lower concentration regime using the formula LOD=3σ/s, where σ is the standard deviation of the lowest signal and s is the slope of the linear-fit.

Additionally, the mercury detection capability of LGQDs was also studied (Figure 2.16c) and compared with the performance of Mn-LGQD. The LOD for Hg^{2+} detection using LGQDs is estimated to be 7 nM. The better (i.e. lower) LOD of Mn-LGQDs compared to LGQDs could be due to superior binding affinity of Hg^{2+} ions to the functional groups on the surface of the Mn-LGQDs.[126] It is worth noting that the augmented LOD of Mn-LGQDs (0.56 nM) for Hg^{2+} detection achieved through metal doping in this work is well below the allowed upper limit of Hg^{2+} ion levels in drinking water around the world.[167]

The observed PL quenching is potentially due to increased non-radiative decay of excited state electrons via adjacent energy levels of the Hg^{2+} ions. The fluorescence quenching, due to non-radiative decay, in the presence of quenching molecule (or analyte) was modeled using the Stern-Volmer equation given by:

$$F_0/F = 1 + K_{SV}C \qquad (9)$$

where F and F_0 are the fluorescence intensities in the presence and absence of quencher, K_{SV} is the Stern-Volmer quenching constant and C is the concentration of the quencher or analyte.[85] The fluorescence kinetics can be analyzed using K_{SV} which is a product of reaction rate constant (k_q) and the lifetime of emissive excited states (τ_0) without the presence of quenching molecules. The K_{SV} values given by the slope of the Stern-Volmer equation are 3.49 x 10^5 M^{-1}, and 2.19 x 10^5 M^{-1} for Mn-LGQD and LGQD respectively (Figure 2.16d). The high K_{SV} value (which is also a measure of the sensitivity of the luminescence-based sensors) of Mn-LGQDs compared to LGQDs

can be attributed to increase in its reaction rate constant, again pointing to the increased affinity of Hg^{2+} towards Mn-LGQDs. However, detailed investigations including time-dependent PL studies are required to confirm the quenching mechanism.

Furthermore, we investigated the effect of the solution pH on the Hg^{2+} detection capabilities of Mn-LGQDs. For this, the PL spectra of Mn-LGQDs were recorded by introducing Hg^{2+} under different pH conditions. These PL results suggest that the quenching efficiency is constant both in high acidic and alkaline conditions (Figure 2.16e) implying Mn-LGQDs can detect Hg^{2+} across all pH ranges. For practical applications, it is critical to ensure the fluorescent Mn-LGQD probes are also selective towards Hg^{2+} ion (i.e., analyte of interest). To test the selectivity of Mn-LGQDs, we studied the PL spectra of Mn-LGQD solutions by mixing it with different metal ion solutions (5μM) including Cu^{2+}, Mn^{2+}, Ag^{+}, Pb^{2+}, K^{+}, Zn^{2+}, Ca^{2+}, Co^{2+}, Hg^{2+}, Fe^{3+}, Ni^{2+} and Mg^{2+}. From these results, it can be inferred that the PL emission intensity of Mn-LGQDs is quenched by Hg^{2+} ions only while all other metal ions showed no significant interference (Figure 16f), thus confirming the high selectivity of Mn-LGQDs towards Hg^{2+} over other metal ions. Additionally, to test the influence of mercury salt (anion effect), we conducted PL quenching studies using two different mercury salts. To confirm the reusability of our samples, the ability of Mn-GQDs to restore the PL (after being quenched by mercuric ion) were investigated. For this, EDTA, a chelating agent with high affinity to Hg^{+2} ions, was introduced into the Mn-GQD-Hg (II) system. When EDTA is added to the solution that contains mercury salt and GQDs, owing to the higher complexation constant between EDTA and Hg,[168-170] Hg^{2+} ions detach from the GQDs and chelates the Hg^{2+} ions to form EDTA-Hg complex. The removal of Hg^{2+} from the GQDs leads to the disaggregation of Mn-LGQDs, and finally restore the PL (Figure 2.17 a, b). We have also evaluated some of the relevant sustainability parameters to understand the “greenness” of the material as well as the synthesis

method.[171, 172] Therefore, the lignosulfonate precursor derived Mn-LGQDs offer a highly sustain-

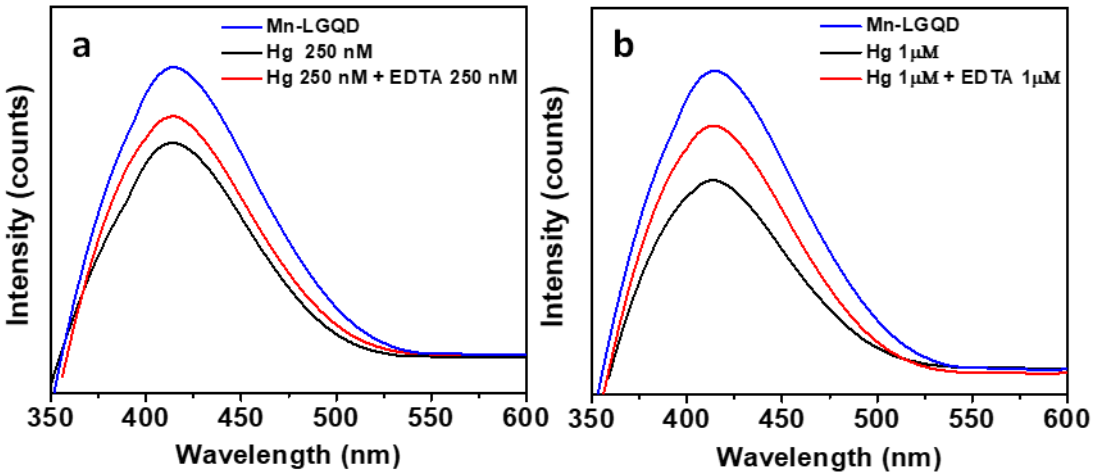

Figure 2.17: Partial PL regain data of Mn-LGQDs at (a) 250 nM and (b) 1μM using EDTA

able, sensitive, and selective fluorescent platform for detecting Hg^{2+} in water samples.

2.1.4 Conclusions

In summary, we synthesized metal and nonmetal co-doped GQDs from lignosulfonate (Mn-LGQDs) via an efficient and sustainable synthetic strategy. An in-depth microscopic and spectroscopic characterization study confirmed the in-situ S, N doping in lignosulfonate derived LGQDs because of S and N atoms present in the precursor. The in-situ doping also helps to easily integrate metal and nonmetal in the GQD matrix. The LGQDs and Mn-LGQDs exhibited excellent photoluminescence and photo-stabilities. The metal and non-metal co-doping in Mn-LGQDs results in significantly enhanced PLQY making them a viable candidate for a variety of fluorescence-based sensing applications. The wavelength-dependent PL measurements of LGQDs and Mn-LGQDs indicates the existence of multiple emissive centers, with core band, resulting from carbon π–π* transitions in the sp^2 domain, and the edge band, originating from both the n–π* and π–π* transitions. Further, we successfully demonstrated Mn-LGQDs prepared using lignosulfonate have a very low LOD in addition to excellent selectivity and high sensitivity for detecting Hg^{2+} in polluted water. This study demonstrates the potential of lignosulfonate derived GQDs as an alternative,

environmentally friendly, and cost-effective fluorescent probes for detecting toxic metal ions in water.

2.2 Lewis Acid Site Assisted Bifunctional Activity of Tin doped Gallium Oxide and Its Application in Rechargeable Zn-air Batteries

2.2.1 Introduction

Zinc-air batteries are predicted to have a high theoretical specific energy density of 1086 W h kg^{-1}, which is 2.5 times higher than state-of-the-art lithium-ion batteries.[173-175] The key to the functioning of Zn-air batteries are two electrochemical reactions occurring at air cathode, namely ORR during discharging and OER during charging. Consequently, the inferior performance of the air cathode leads to the Zinc-air batteries displaying lower energy output than the theoretical value. Hence, catalysts with excellent catalytic efficacy towards ORR (e.g., Pt) and OER (e.g., RuO_2) are employed in the air cathode to enhance the performance of Zn-air batteries. However, the poor stability, high cost, and scarcity of state-of-the-art catalysts such as Pt or RuO_2 make the technology commercially untenable. Thus, the widespread adoption of Zinc-air batteries depends on discovering low-cost, highly active, stable, and potentially bifunctional electrocatalysts. Recently, transition metal oxide (TMO) systems emerged as viable ORR and OER electrocatalysts due to their competent activity and better stability.[176-181] A variety of non-precious metal oxide catalysts (Co_3O_4, FeO_x, and MnO_x, etc.), especially in the nanoform, demonstrated high catalytic activity.[182-186] Nonetheless, most nano-TMO catalysts suffer from poor conductivity and agglomeration-induced loss of active sites, leading to inferior or gradually degrading catalytic activity.

Recent research revealed that Lewis acid sites adjacent to the catalytic sites could influence their activity for oxygen redox reactions.[187] Theoretical studies indicated that in Lewis acid catalysts, the metal atoms could coordinate with an adjacent electronegative atom with a lone pair, resulting in a charge transfer between them.[188] Gallium oxide (Ga_2O_3) in its most stable form, β-Ga_2O_3 with

tetrahedral and octahedral Ga ions (Ga^{3+}), is a strong Lewis acid where tetrahedral Ga^{3+} is the Lewis acid center.[189] Recently, β-Ga_2O_3 based photocatalysts gained increased attention due to their significant potential for activating CO_2. They have also been recognized as alkane dehydrogenation catalysts because of their unique ability to activate hydrocarbons.[190, 191] However, despite their wide use in catalysis, the exploration of β-Ga_2O_3 as an electrocatalyst remains underexplored. Alternately, engineering the electron distribution and Lewis acidity of β-Ga_2O_3 could be the key to realizing inexpensive, high-performance, multifunctional, and stable catalysts without morphological and dimensional modifications. Recent research proved that lattice incorporation of appropriate dopants could modulate the electronic distribution, band structure, and catalytic activity of materials.[192-198] For example, Tin (Sn) doping improves the sluggish kinetics of OER/ORR because the oxygen-bound intermediates can interact favorably on the Sn surface.[189, 199-203]

Anticipating synergistic effects due to the Lewis acid sites in β-Ga_2O_3 and the favorable oxygen adsorption properties of Sn, we atomically doped β-Ga_2O_3 with Sn to derive excellent bulk bifunctional electrocatalyst towards ORR and OER. Here, the β-Ga_2O_3 was synthesized via the high-temperature, solid-state route and doped with different Sn percentages (x=0.05-0.20).[204] Interestingly, a superior bifunctional ORR and OER activity, the best activity reported for a bulk sample, was demonstrated at 15% doping of Sn (x=0.15, denoted as $Sn_{x=0.15}$-Ga_2O_3) with a lower overpotential and higher current density. Our experimental investigations revealed that the lattice incorporation of Sn leads to modification of the bandgap, increases the conductivity, and introduces new highly catalytic centers in the β-Ga_2O_3 lattice. Our theoretical exploration indicated that the addition of Sn near the Lewis acid coordination sites triggers an electron transfer from the Ga^{3+} to the adjacent Sn–O bond leading to a redistribution of the electron density and a significant decrease in activation energy on the surface of Sn doped β-Ga_2O_3, accounting for the enhanced catalytic

performance. Finally, we leveraged $Sn_{x=0.15}$-Ga_2O_3 as the air cathode of a Zn-air battery, which demonstrated significantly improved stability and reduced polarizability compared to devices with benchmark Pt and RuO_2 electrocatalysts, pointing to the potential of $Sn_{x=0.15}$-Ga_2O_3 for electrochemical energy storage applications.

2.2.2 Materials and Methods

2.2.2.1 Synthesis

The Sn mixed Ga_2O_3 compounds were produced via the high-temperature, solid-state chemical reaction method. To obtain the homogenous mixtures, high pure β-Ga_2O_3 and SnO_2 powders are mixed thoroughly. In the solid-state synthesis route adopted, we first initiated the process by grinding the powders using a mortar and pestle under a volatile liquid environment. This ensures the homogeneous mixing and formation of smaller size particles. The mixture was then heat treated, calcined, at a temperature closer to the melting point of the material. In this case, the mixed compound was heat treated at 1100 °C for 12 h in a muffle furnace. The ramp rate used for heating and cooling was 5°C/min. After calcination of the sample, the mixture was grinded again by introducing polyvinyl acetate (PVA). Under the presence of PVA, the mixture has been grinded into a fine powder, which is then used to make pellets. The pellets were made by pressing the final Sn_x-Ga_2O_3 powder at 1.5 tons for 1 minute. The pellets made were with an 8 mm diameter and 2 mm thickness. The second stage of compound synthesis involves the sintering process. The pellets were subjected to the second heat treatment i.e., sintering. The sintering temperature, which is typically higher than the calcination temperature, was set to 1350 °C for 12 h while maintaining the same ramp rate as in the calcination. The materials thus obtained were subjected to further characterization to understand the structure, composition, and electrochemical properties.

2.2.2.2 Material characterization

The XRD analysis was performed on a Rigaku Smartlab diffractometer in 0D mode with HyPix 3000 high energy resolution 2D HPAD detector. A trace amount of Sn_x-Ga_2O_3 powder was placed on a zero-diffraction plate to counter any diffraction peak arising from the sample holder. The X-ray source was set at the operating parameters of 44 kV and 40 mA. The step size was kept at 0.02 degrees. The diffraction data analysis or phase matching was carried out using proprietary PDXL software. The morphology of the Sn_x-Ga_2O_3 samples were studied using the FEI Magellan 400 scanning electron microscope. TEM samples were prepared by simple drop cast method for powder sample. To remove agglomerates, the powder was sonicated for 10 seconds to achieve a homogeneous dispersion. Then a drop from the dilute solution of each aliquot was drop cast over amorphous C-coated Cu grid. TEM studies were performed on a JEOL-Arm 200CF microscope operating at 200 kV equipped with a high dynamic range Gatan DIF camera for diffraction patterns. Total Gallium and Tin content in the GaSnO compounds were determined using inductively coupled plasma optical emission spectrometer (ICP-OES, Perkin-Elmer Optima 4300 DV, Shelton, CT). A calibrated Kratos Axis Ultra DLD spectrometer (Kratos Analytical, Manchester, U.K.) which has a high-performance Al Kα (1486.7 eV) spherical mirror analyzer is used for XPS analysis. Gas detection and quantitative analysis were performed by a SHIMADZU GC-8A gas chromatograph (GC).

2.2.2.3 Electrochemical measurements

The electrocatalytic performance of all catalysts was analyzed by CV, LSV, and chronoamperometric test by using an CHI6372E CH instrument workstation. The electrochemical workstation is coupled with a rotating disk electrode (Pine Research) system. All the experiments were

performed in a three-electrode configuration using platinum wire as a counter electrode, saturated calomel electrode (SCE) as a reference electrode, and a glassy carbon electrode having a 3 mm diameter as a working electrode. The electrolyte used was a 0.1 M aqueous KOH solution. All potentials reported in this work were calibrated versus the reversible hydrogen electrode (RHE) using the equation

$$E\,(RHE) = E\,(SCE) + (0.197 + 0.059 * pH) \quad (1)$$

The OER activity was obtained via CV at a low scan rate of 5 mV s^{-1}. The overpotential values corresponding to different current densities were determined from the cathodic going half cycle of the CV curves. The voltammograms were recorded with iR drop compensation automatically on the workstation. The capacitance of the catalytic surface was measured from the non-Faradaic capacitive current associated with double layer charging from the scan rate dependence of cyclic voltammograms. Cyclic voltammograms were recorded in a non-Faradaic region at various scan rates.

For the Zn–air battery test, the air electrode was prepared by uniformly coating the as-prepared catalyst ink onto a glassy carbon working electrode then drying it at room temperature. The mass loading was 4 mg cm^{-2} unless otherwise noted. A Zn foil was used as the anode. Both electrodes were assembled into a Zn–air battery setup and a 6 M KOH (pH 13.78) aqueous solution with 0.2 M zinc acetate solution was used as the electrolyte.

2.2.2.4 Faradaic Efficiency Calculation

Chronoamperometry measurement was performed in a gastight electrochemical two compartment H-cell using Pt wire and Hg/HgO as the counter electrode and the reference electrode, respectively. The working electrode and reference electrode were placed in the anode cell and the counter

electrode was put in the cathode cell. 50 mL 0.1 M KOH aqueous solution was used as electrolyte. Before the measurements, the solution was purged with Argon gas for 30 min to completely remove the oxygen gas in the system. The generated O_2 volume during electrolysis was measured using gas chromatography. Faradaic efficiency (F.E) was calculated using the equation,

$$F.E = \frac{Experimental\ moles\ of\ Oxygen\ gas}{Theoretical\ moles\ of\ Oxygen\ gas} \times 100 \quad (2)$$

The theoretical amount of O_2 gas was calculated from Faraday's law,

$$n = \frac{i\ X\ t}{z\ X\ F} \quad (3)$$

where n is the number of mol, i is the current in ampere, t is the time in seconds, z is the transfer of electrons (for O_2 z = 4), and F is the Faraday constant (96,485 C mol^{-1}).

2.2.2.5 Calculation of TOF

The turnover frequency was defined as moles of O_2 per moles of active site (Sn) evolved per second (s^{-1}). The geometric current densities (j) were extracted at 520 mV overpotential (1.75 V RHE, all reported potentials are iR corrected) from CV measurements. The total moles of Sn on the electrode were determined by ICP-OES prior to the measurement. A is the area of the GC electrode surface (3mm diameter). Assuming a z = 4 electron transfer for the overall reaction, TOF was calculated according to equation below,

$$TOF = \frac{j\ X\ A}{4\ X\ F\ X\ n} \quad (4)$$

2.2.2.6 Computational methods

The Vienna Ab initio Simulation Package was used for all spin polarized DFT computations (VASP).[205] To examine electron-electron exchange correlations, we used the projector augmented wave (PAW) approach to characterize the electron-ion interaction and the Perdew-Bruke-Ernzerhof (PBE) functional with generalized gradient approximations. The van der Waal (vdW) interactions for the substrates were described using Grimme's DFT-D3 technique. For the plane-wave (PW) basis computations, we employed a kinetic cutoff energy of 520 eV. With the addition of 20 Aº vacuum space along the z axis, the interaction between two nearby images was avoided. To examine the position of atoms and cell parameters, we used the conjugated gradient approach. For self-consistent electronic energy calculations, the convergence requirements were established at 10^{-4} eV in energy and 10^{-2} eV/ in force. The Brillouin zone was sampled using a 5 x 5 x 1 and 11 x 11 x 1 k-point mesh generated using the Monkhorst-Pack scheme for both geometric and electronic relaxations. The charge transfer during the ORR (OER) intermediate adsorption was determined using Bader charge analysis, and charge differences were calculated using the formula

$$\rho_b = \rho_{adsorbed\,state} - (\rho_{adsorbent} + \rho_{AM}) \quad (5)$$

Where $\rho_{adsorbed\ state}$, $\rho_{adsorbent}$, and ρ_{AM} represents the charge density of the pristine and Sn-Ga_2O_3 (AM) with adsorbed ORR (OER) intermediate species, pristine ORR(OER) species, and the AM, respectively. We used VESTA code to analyze the charge density difference.[206]

The binding energies of the ORR(OER) intermediate species with the substrates was calculated using the expression

$$\Delta E = E_{ads/sub} - E_{ads} - E_{sub} \quad (6)$$

Where $E_{ads/sub}$, E_{ads} and E_{sub} denotes the total energies for adsorbed species on substrate, adsorbed species and isloted substrate(AM) respectively.

The Gibbs free energy (ΔG) for each ORR (OER) intermediate step in the overall ORR (OER) process is calculated as

$$\Delta G = \Delta E + \Delta ZPE - T\Delta S + \Delta G_U + \Delta G_{pH} \quad (7)$$

Where ΔE is for adsorption energy, ΔZPE and TSΔ stand for the zero-point energy difference and entropy difference between the gas and adsorbed phases obtained from frequency calculations at 298.15 K, and ΔG_U stands for the applied electrode potential contribution (U). $\Delta GpH = k_B T \ln 10$ pH, where T = 300 K and k_B is the Boltzmann constant. For the acidic medium, we assume pH = 0 and for the alkaline medium, pH = 14.

2.2.3 Results and Discussion

Among the different crystal forms of Ga_2O_3, β-Ga_2O_3 is the most stable (melting point 1740 °C), with the oxide ions in distorted ccp arrangement and Ga^{3+} occupying distorted tetrahedral and

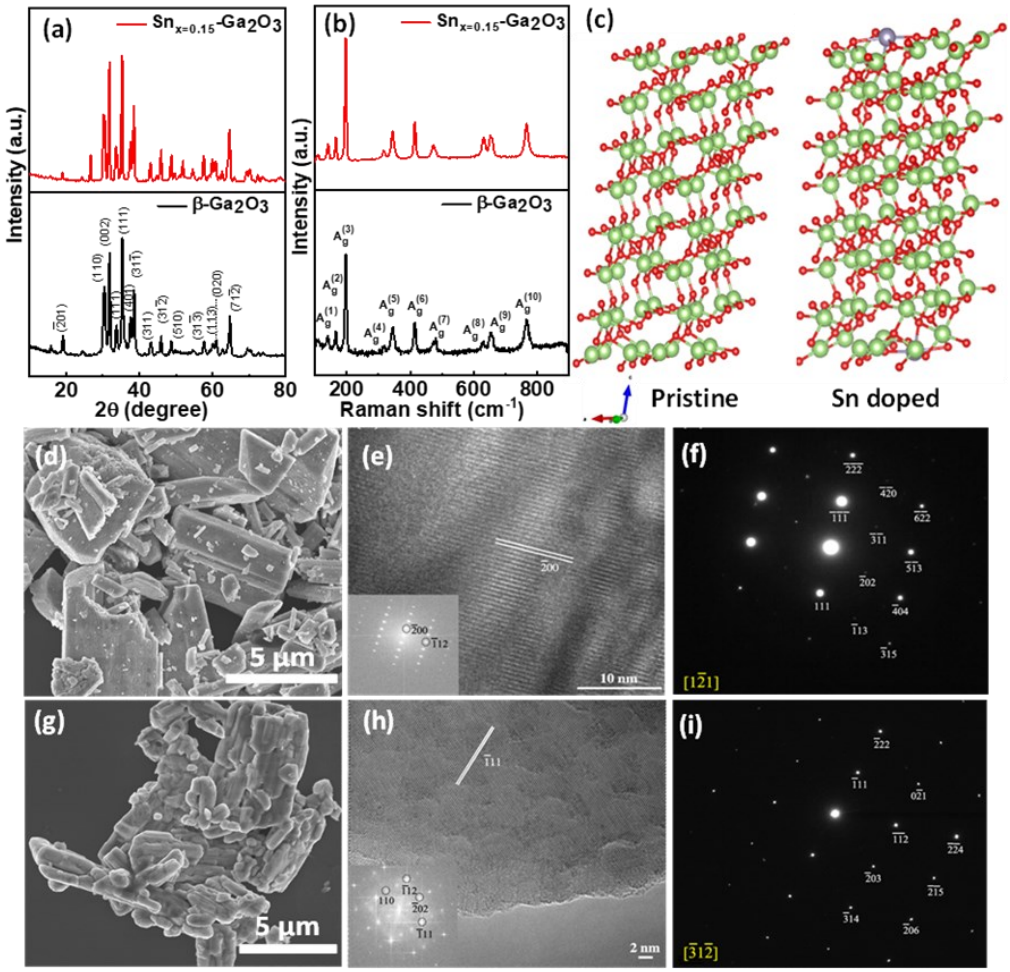

Figure 2.18: (a) XRD spectrum (b) Raman spectrum (c) Optimized structures of β-Ga_2O_3 (left) and Sn doped β-Ga_2O_3 (right) (d) SEM image of β-Ga_2O_3 (e) high-resolution TEM image for β-Ga_2O_3 (with -200 plane resolved) corresponding Fourier transform shown in the inset. (f) SAED pattern for β-Ga_2O_3 (g) SEM image of $Sn_{x=0.15}$-Ga_2O_3 (h) high-resolution TEM images for $Sn_{x=0.15}$-Ga_2O_3 showing a -111 plane; corresponding Fourier transform shown in the inset (i) SAED pattern

octahedral sites. Further, β-Ga_2O_3 is stabilized in monoclinic crystal symmetry with the C2/m space group at ambient conditions.[204, 207, 208] The prepared β-Ga_2O_3 and Sn_x-Ga_2O_3 samples were

analyzed using different microscopic and spectroscopic techniques to confirm the Sn doping and derive an in-depth understanding of their morphology, structure, and surface chemistry. We recently reported a detailed account of crystallography, Rietveld refinement, structure, and surface morphology of the Sn doped Ga_2O_3.[204] Figure 2.18a shows the XRD patterns of pristine β-Ga_2O_3 and $Sn_{x=0.15}$-Ga_2O_3.[209] While lower levels of doping lead to lattice incorporation, increasing concentration of Sn (e.g., $Sn_{x=0.2}$-Ga_2O_3) resulted in the formation of a secondary SnO_2 phase, as evidenced from the XRD.[204] Figure 2.18b shows the Raman spectra of β-Ga_2O_3 and $Sn_{x=0.15}$-Ga_2O_3 samples using a 532 nm laser excitation. The corresponding Raman spectrum of other Sn dopant ratios is given in Figure 2.19. The features in the Raman spectrum can be divided into three groups, namely low-frequency mode (below 200 cm^{-1}), mid-frequency mode (500–300 cm^{-1}), and high-frequency mode (770–500 cm^{-1}), all of which are related to different vibrational modes of Ga_2O_3.[210] All relevant Raman vibration modes of Ga_2O_3 are visible in parent β-Ga_2O_3 and Sn doped Ga_2O_3 samples (Figure 2.18b). The Raman bands at 140, 166, and 195 cm^{-1} are due to vibration of Ga-O chains; 345, 414, and 475 cm^{-1} belong to deformation of Ga*I*(O*I*)$_2$ octahedra; 652 and 767 cm^{-1} are because of the symmetric stretching of GaO_4 tetrahedra.[211] Figure 2.20 shows the Raman bands

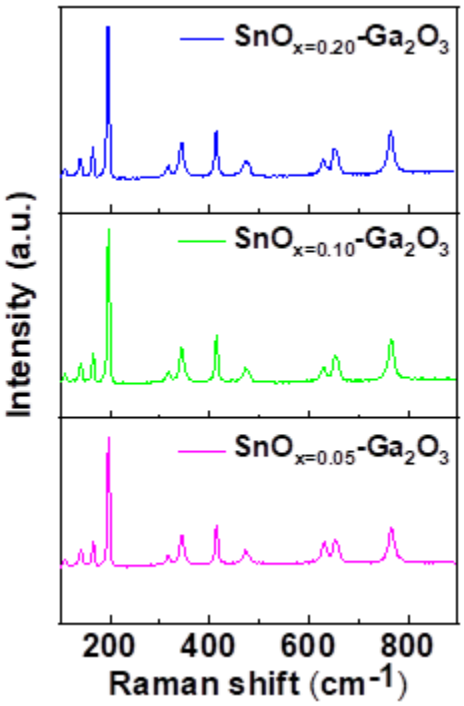

Figure 2.19: Raman spectrum of $Sn_{x=0.05}$-Ga_2O_3, $Sn_{x=0.10}$-Ga_2O_3 and $Sn_{x=0.20}$-Ga_2O_3 sample

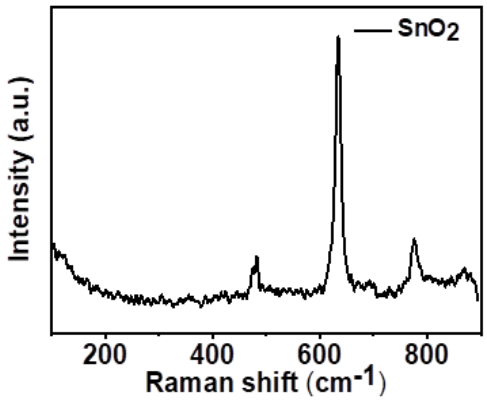

Figure 2.20: Raman spectrum of SnO_2

of the SnO_2 at 482, 633, and 775 cm^{-1}, which corresponds to the E_g, $A_{1g,}$ and B_{2g} vibrational modes, respectively.[212] The close overlap of features from β-Ga_2O_3 and SnO_2 made it challenging to confirm the Sn doping using Raman spectroscopy. However, the presence of relevant features of β-Ga_2O_3 in the undoped and doped samples confirmed the XRD observation that the structural integrity of the samples is preserved under moderate doping concentrations. Figure 2.18c depicts the optimized structures of β-Ga_2O_3 and Sn_x-Ga_2O_3 derived from DFT calculations. The Sn_x-Ga_2O_3 structure was modeled by replacing a single Ga atom from the [100] surface with an Sn atom. A 1 x 2 x 4 supercell of β-Ga_2O_3 was used for the calculations, and the calculated lattice parameter was 12.452 Å, which is consistent with other works.[213-215] Additionally, we found that the average bond length of Sn-O (2.14 Å) is greater than Ga-O (1.81 Å), which corresponds to the larger atomic radius of Sn $^{4+}$ (0.70 Å) compared to Ga $^{4+}$ (0.62 Å). Moreover, the calculated reduction in the bandgap upon Sn doping using DFT is well consistent with the literature.[216, 217] The morphology of β-Ga_2O_3 and $Sn_{x=0.15}$-Ga_2O_3 and the lattice structure were studied using scanning electron microscopy (SEM) and transmission electron microscopy (TEM). The SEM micrograph (Figure 2.18d and g) validates the bulk powder nature of β-Ga_2O_3 as well as $Sn_{x=0.15}$-Ga_2O_3. It is evident

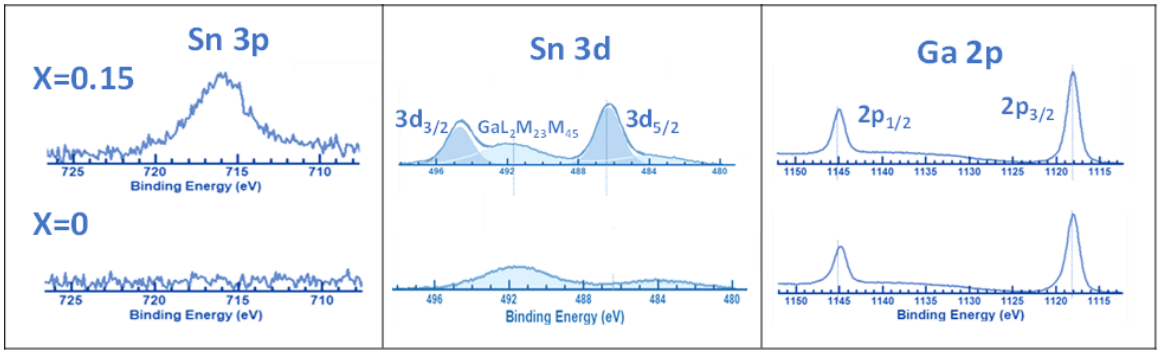

Figure 2.21: High resolution XPS spectrum of Sn 3p, Sn 3d and Ga 2p orbitals

that the rod-shaped nature of monoclinic β-Ga_2O_3 is mostly preserved with the introduction of Sn dopant into the lattice. We performed X-ray Photoelectron Spectroscopy (XPS) measurements to confirm the Sn doping. Figure 2.21 shows the Ga 2p, Sn 3p and Sn 3d high resolution XPS

spectrum for x=0 and x=0.15 dopant percentages. The peak position of Ga 2p confirm the existence of Ga in its highest oxidation state in the samples. No change in binding energy is observed with introduction of Sn content into β-Ga_2O_3 confirming that the Sn-incorporation didn't affect the chemical valence states of Ga ions.

To probe the atomic-level crystal structure (and validate our DFT calculations) and understand any lattice distortions or formation of interfacial compounds during Sn doping, we analyzed our sample using high-resolution TEM (HRTEM). Figure 2.18e-f and h-i show lattice resolved TEM image and selected area electron diffraction (SAED) of pure β-Ga_2O_3 and $Sn_{0.15}$-Ga_2O_3 samples. The HRTEM image in Figure 2.18e shows the 002 planes confirming the monoclinic structure of pure β-Ga_2O_3. The corresponding SAED pattern (Figure 2.18f) and the FFT pattern (inset of Figure 2.18e) confirmed the highly crystalline monoclinic phase of the sample. Interestingly, the $Sn_{x=0.15}$-Ga_2O_3 also exhibited a 111 plane (Figure 2.18h), and the crystalline nature in the SAED (Figure 2.18i) and the FFT (inset of Figure 2.18h), again emphasizing that the crystal structure is mostly preserved in samples up to Sn_x= 0.15. Thus, as established in our bulk XRD measurements,[204] the HRTEM and SAED analysis confirmed that no apparent change in the crystal structure or

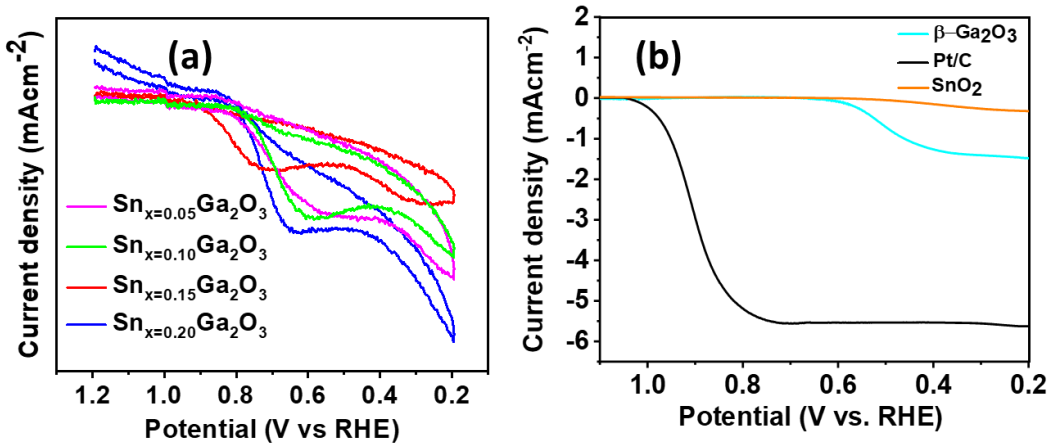

Figure 2.22: (a) cyclic Voltammetry measurements showing the oxygen reduction peak for all Sn doped samples, (b) LSV curves showing ORR activity of pristine β-Ga_2O_3, SnO_2 and Pt/C

separation of secondary phases happened until x≤0.15, even at local nanoscopic levels. It is also evident that the segregation of dopants in the form of tetragonal SnO_2 can be observed only at higher doping concentrations.[204]

Linear sweep voltammetry (LSV) measurements using a rotating disk electrode (RDE) in O_2 saturated 0.1 M KOH solution were performed to investigate the ORR activity of bulk β-Ga_2O_3 and Sn_x-Ga_2O_3 samples. The presence of reduction peak in the ORR region after O_2 saturation and absence of any such peak in N_2 saturated electrolyte indicates the intense ORR activity of the as-synthesized materials (Figure 2.22a). As evident from Figure 6a, the performance improved with increasing the doping ratio up to 15%, beyond which the limiting current decreased. Compared to other dopant ratios, the $Sn_{x=0.15}$-Ga_2O_3 sample displayed an exceptional ORR activity with an onset potential of 0.76 V and half-wave potential ($E_{1/2}$) of 0.7 V, which is one of the best reported for any Ga_2O_3-based materials. Thus, the LSV curves proved that doping of Sn enhances the ORR activity of pristine β-Ga_2O_3 (onset 0.6 V vs. RHE). The ORR activity of pristine SnO_2 revealed a poor activity thereby confirming the importance of doping-based strategy to enhance ORR (Figure

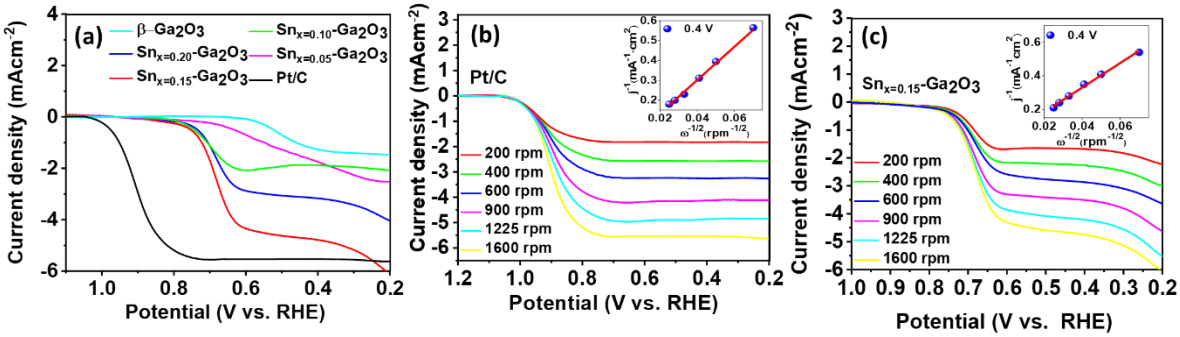

Figure 2.23: a) Linear sweep voltammetry of the Ga_2O_3 and Sn_x-Ga_2O_3 with different ratios (electrode-rotating speed, 1600 rpm. Scan rate: 2 mV s^{-1}) b) The RDE plots of Pt/C in oxygen-saturated 0.1 M KOH at rotation speeds ranging from 200 to 1600 rpm and a scan rate of 10 mV s^{-1} Inset (K-L plots) c) The RDE plots of $Sn_{x=0.15}$-Ga_2O_3 in oxygen-saturated 0.1 M KOH at rotation speeds ranging from 200 to 1600 rpm and a scan rate of 10 mV s^{-1} Inset (K-L plots).

2.22a). The oxygen reduction properties were further analyzed by varying rotation speeds ranging

from 200 to 1600 rpm for Pt/C and $Sn_{x=0.15}$-Ga_2O_3 (Figure 2.23b and 2.23c). From the RDE voltammograms, the limiting current of ORR on $Sn_{x=0.15}$-Ga_2O_3 increased with increasing rotation speed from 200 to 1600 rpm, illustrating first-order reaction kinetics (Figure 2.23c), with a maximum diffusion-limited current density of 4.5 mA/cm^2 at 1600 rpm. The kinetic parameters were estimated by applying the Koutecky−Levich (K−L) equations. The linearity of the K-L plots for Pt/C and $Sn_{x=0.15}$-Ga_2O_3 (insets of Figure 2.23b and Figure 2.23c) also confirms similar first-order reaction kinetics with respect to the dissolved oxygen concentration in the case of both the catalysts. We also investigated the ORR mechanism of ORR to understand whether it proceeds through a four electrons or two electrons pathway.[218, 219] The kinetic parameters obtained from K-L plots demonstrated that Pt/C under dynamic conditions exhibit a 3.8 electrons-based mechanism. The average electron transfer number for $Sn_{x=0.15}$-Ga_2O_3 was calculated to be 3.7 electrons, confirming that the mechanism follows a 4-electron reduction process (Figure 2.23c inset).

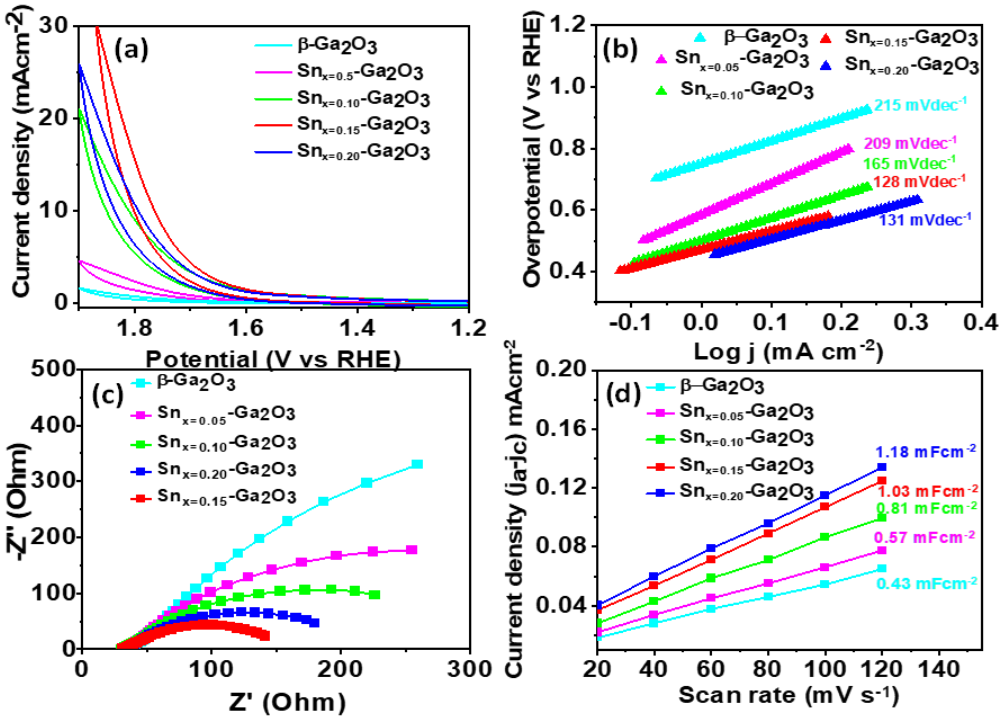

Figure 2.24: (a) iR corrected CV measurements for OER and (b) corresponding Tafel plot (c) Nquist plot and (d) C_{dl} measurements for β-Ga_2O_3 and Sn_x-Ga_2O_3 systems

In addition to ORR, the OER activity of the catalyst is also vital for the cathode material during the charging cycle of the Zn-air battery. Hence to check the bifunctional nature, we investigated the electrocatalytic OER performance for the Sn_x-Ga_2O_3 system in an alkaline electrolyte (0.1 M KOH). Figure 2.24a shows the OER iR corrected CV curves with different Sn loading. Similar to the ORR activity, the polarization curves showed a superior activity for $Sn_{x=0.15}$-Ga_2O_3 compared to other dopant ratios with an onset potential of 1.75 V vs RHE. Additionally, to understand the catalytic mechanism of the electrocatalytic OER process, we evaluated the Tafel slopes (Figure 2.24b). A smaller Tafel slope indicates superior catalytic efficacy and resultant increased OER rate, with decreased overpotentials.[220] A Tafel slope of 128 mV/dec for $Sn_{x=0.15}$-Ga_2O_3 again confirmed the superior OER performance of 15% dopant sample compared to other ratios. It is also evident from the Tafel slope values that the OER mechanism follows a $4e^-$ process for all the samples.

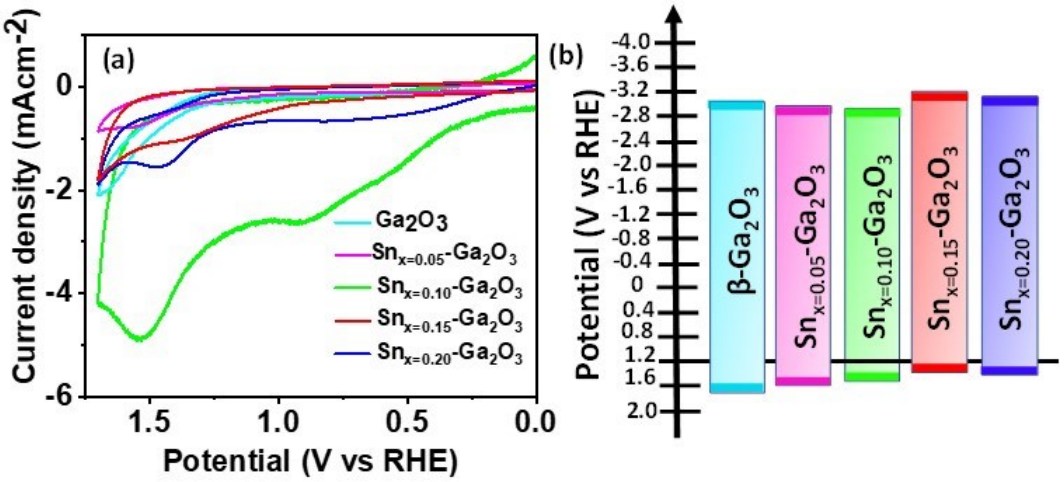

Figure 2.25: (a) Cyclic voltammetry measurements and (b) band structure calculation

To understand the origin of the superior performance of the doped electrocatalysts, we investigated the bandstructure, calculated the double-layer capacitance (C_{dl}), and analyzed the samples using electrochemical impedance spectroscopy (EIS). The band structure of the bulk β-Ga_2O_3 and Sn

doped Ga_2O_3 samples were explored using cyclic voltammetry (CV), and corresponding highest occupied molecular orbital (HOMO) and lowest unoccupied molecular orbital (LUMO) were identified (Figure 2.25). It is evident from the figure that the better proximity of HOMO with the oxygen reduction potential in $Sn_{x=0.15}$-Ga_2O_3 aids in enhanced electron transfer, thereby improving the reaction kinetics. Our EIS analysis demonstrated that $Sn_{x=0.15}$-Ga_2O_3 has the smallest charge transfer resistance amongst all the ratios (Figure 2.24c). Figure 2.24d show the C_{dl} plots, which indicates an increase in the electrochemical surface area with increased doping percentage (x=0.05-0.20). Though a minimal rise in C_{dl} value (1.03 vs. 1.18 $mFcm^{-2}$) is observed between $Sn_{x=0.15}$-Ga_2O_3 and $Sn_{x=0.2}$-Ga_2O_3, as evidenced by the EIS measurements, $Sn_{x=0.15}$-Ga_2O_3 has the lower charge transfer resistance (Figure 2.24d) compared to $Sn_{x=0.2}$-Ga_2O_3, potentially leading to the superior bifunctional activity of $Sn_{x=0.15}$-Ga_2O_3 towards ORR and OER. The turnover frequency (TOF) reveals the intrinsic properties of the catalysts, which is another important parameter for evaluating the performance of the catalysts. The TOF of $Snx_{=0.15}$-Ga_2O_3 was calculated to be 0.88

Table 2.2: ICP-OES measurements of $Sn_{x=0.15}Ga_2O_3$ before and after battery cycling.

Sample	Measurement	Concentration (mg/Kg)	Weight (%)
GaSnO Before	Sn 189.927	3057.738681	0.305774
GaSnO Before	Ga Radial	686611.8525	68.66119
GaSnO After	Sn 189.927	3359.396471	0.33594
GaSnO After	Ga Radial	640005.5064	64.00055

s^{-1} at a current density of 10 $mAcm^{-2}$ (Table 2.2). The amount of generated oxygen for OER was

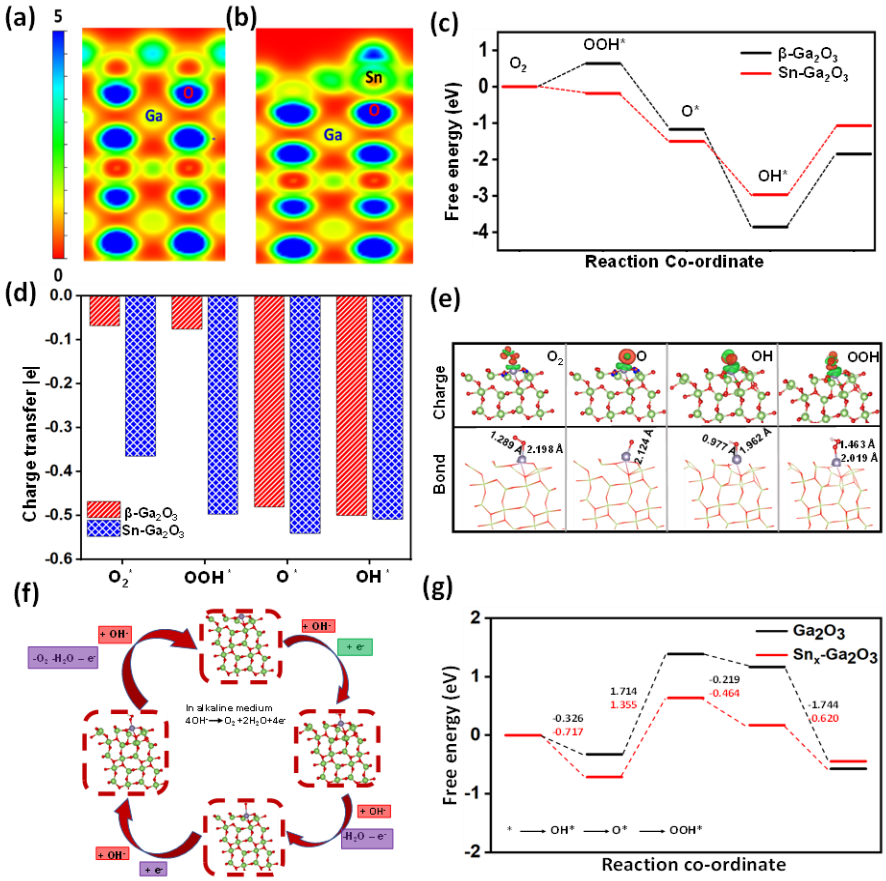

Figure 2.26: Electron localization function plots of (a) β-Ga_2O_3 and (b) Sn_x-Ga_2O_3 (c) Gibbs free energy diagram for ORR (d) Bader charge calculation (e) Charge density difference analysis and Bond length calculation for Sn_x-Ga_2O_3 (f) Mechanism for OER (g) Gibbs free energy diagram for OER.

detected by gas chromatography analysis, and the collected O_2 match well with the theoretical values, indicating the Faradaic efficiency of $Sn_{x=0.15}$-Ga_2O_3 is 98%. Hence, our experimental exploration suggests that in $Sn_{x=0.15}$-Ga_2O_3, the proximity of HOMO to oxygen reduction potential, a lower charge transfer resistance, higher electrochemical surface area, work synergistically to enhance electrocatalytic activity and selectivity compared to the other dopant ratios.

To gather a comprehensive understanding of the ORR and OER mechanism of β-Ga_2O_3 and Sn doped β-Ga_2O_3 samples and identify the active sites on the doped materials, we performed DFT

calculations. Our DFT-based analysis concentrated on the adsorption behavior of reactants (O_2), intermediates (OOH *, O*, and OH*), and products (H_2O) in an alkaline medium. Initially, we employed the electron localization function (ELF) to investigate the electron distribution on the surface of β-Ga_2O_3 and Sn-doped Ga_2O_3. The ELF can be described as a contour plot in real space, as shown in Figures 2.26a and b. The region close to 0 (red) indicates a low electron density area, while a region close to 5 (blue) indicates a highly localized dense electron region coming from the

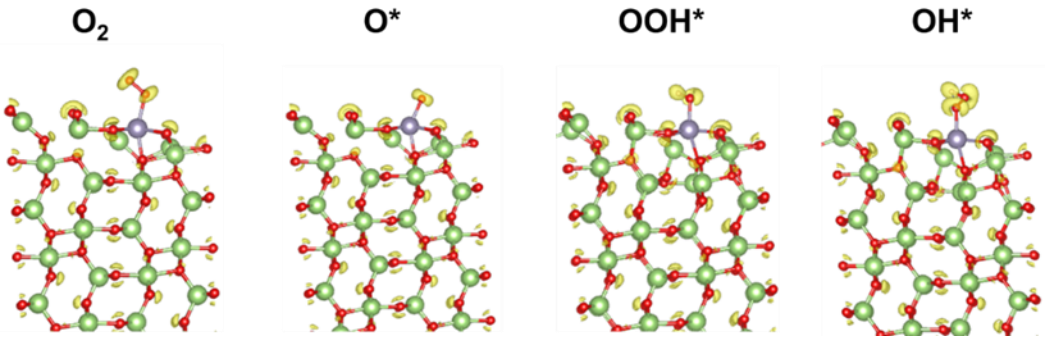

Figure 2.27: The side views of 3D ELF plots of ORR intermediates adsorbed on Sn_x-Ga_2O_3

nucleus or because of the presence of strong covalent electrons or lone-pair electrons. It is plausible that the dense electron accumulation on the Sn atom site arises due to the electron donation from the adjacent Lewis acid sites to the Sn-O bond. This observed electron accumulation on the Sn site is anticipated to exhibit stronger covalent interactions with the ORR and OER intermediates. For ORR and OER, the catalytic activity of the studied substrates in the alkaline medium mainly depends upon the initial adsorption of O_2 followed by the adsorption energies of various reaction intermediates. The Gibbs free energy diagram calculated using the standard $4e^-$ association mechanism is used to study the bifunctional ORR and OER activity on β-Ga_2O_3 and Sn doped Ga_2O_3 substrates. We examined two kinds of adsorption patterns: end on and side on for initial O_2 adsorption and observed that the end-on configuration is more energetically favorable for both β-Ga_2O_3 and Sn doped Ga_2O_3 substrates. To confirm the active sites on the catalyst, we investigated various possible adsorption sites for the reaction intermediates (OOH*, O*, and OH*) on the

substrates. The most stable structural configurations are shown in Figure 2.27, which validates that Sn is the most active site in Sn doped Ga_2O_3, whereas it is Ga site in β-Ga_2O_3. The corresponding reaction free energies for each intermediate step in ORR are shown in Figure 2.26c. From the calculations, we confirmed that the rate-determining step (RDS) is the fourth hydrogenation step ($4OH^-$), with the highest energy barrier[221] corresponding to the stronger or weaker binding energies between the oxygenated species and substrates. For the overall ORR reaction at U = 0 V, the rate-determining step for β-Ga_2O_3 is O* → OH* (2.216 eV), whereas for Sn doped Ga_2O_3, the RDS is OH* → OH^- (1.899 eV). It is worth mentioning that Sn doped Ga_2O_3 requires less energy to make all the reaction intermediate steps to be thermodynamically downhill, revealing its superior ORR activity compared to the parent substrate. Moreover, the initial oxygen adsorption step is thermodynamically uphill for pristine Ga_2O_3. In contrast, Sn doping significantly reduces the energy barrier, making the O_2 adsorption thermodynamically downhill and is well correlated with its stronger adsorption energies and increased charge transfer characteristics. Further, for Sn doped Ga_2O_3, we found electron-dense clouds around incoming O atoms confirming the charge transfer from the metal atoms to incoming O atoms (Figure 2.28).

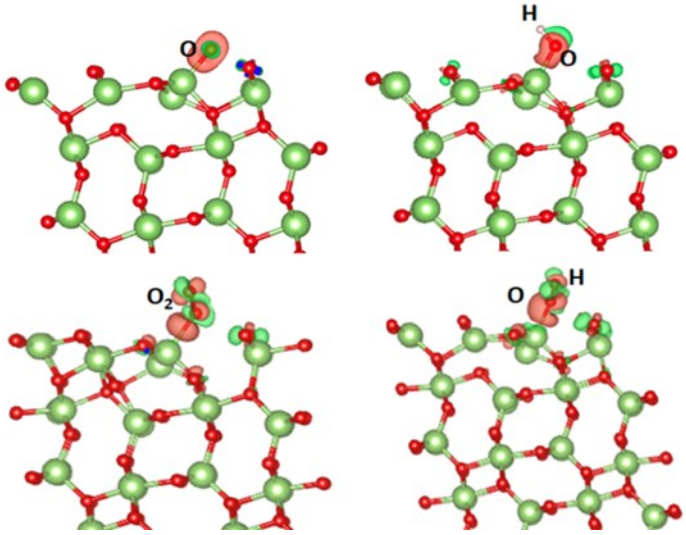

Figure 2.28: Charge density difference of ORR (OER) intermediates adsorbed on pristine β-

We performed Bader charge analysis to establish the increased electron density in Sn doped Ga_2O_3 and electron transfer from Lewis sites (Figure 2.26d). The Lewis acid coordination in Sn doped Ga_2O_3 allows for electron transfer from the Ga^{3+} to the Sn–O bond, facilitating the formation of

intermediates in ORR and OER. The increased electron charge transfer values in the case of Sn doped Ga_2O_3 substrates for all the intermediate steps in ORR and OER also confirmed the charge transfer. Also, as per the Bader charge calculation, the formation of the O* intermediate is enhanced the most due to the strong Lewis acid property of the system. We also observed that while the average charges of Ga and O atoms for the O* intermediate are 1.799 |e| and -0.481|e|, the charges are 2.271 |e| for Sn and -0.541 |e| for O in Sn doped Ga_2O_3, again pointing to the higher charge transfer characteristics of Sn doped substrate. Additionally, a charge density difference analysis was performed to establish the increased chemical interaction between the metal p orbital and л* antibonding orbital of O_2. We found a ~ 2.5% and ~ 7% increase in the O-O bond lengths (Figure 2.26e) for the β-Ga_2O_3 and Sn doped Ga_2O_3 compared to the corresponding gas-phase molecule ($d_{O=O}$ = 1.22 A^o). This is because there is a higher charge transfer of ~ 0.89 |e| from Sn to O_2 in Sn doped Ga_2O_3, compared to ~0.77 |e| from Ga to O_2, corroborating the increased elongation of the O=O bond length (Figure 9e). Charge density difference analysis performed on O_2 adsorbed substrates also reveals a charge accumulation between Sn–O bonds indicating stronger covalent interactions. Hence, experimentally observed superior ORR activity of Sn doped Ga_2O_3 agrees with theoretical DFT calculations. Moreover, the calculated theoretical overpotential of Sn@Ga_2O_3 was lower (0.66 eV) when compared to that of pristine Ga_2O_3 (0.98 eV) illustrating that the Sn doping could improve the ORR catalytic activity than pristine Ga_2O_3. The enhancement in OER activity was also further proved using Gibbs free energy calculations. Figure 2.26f shows the proposed 4e- mechanism for OER on β-Ga_2O_3 and Sn doped Ga_2O_3 substrates. Like ORR, the OER on both β-Ga_2O_3 and Sn doped Ga_2O_3 catalysts also proceeds in four elementary steps with the generation of OH*, O*, and OOH* as the OER intermediates. The computed free energy of each OER intermediate step takes place at corresponding metal sites in β-Ga_2O_3 and Sn doped

Ga_2O_3. From Figure 2.26g, we observed that the intermediate step involving the deprotonation of OH* to O* is the rate-determining step in the overall OER process. The computed difference in Gibbs free energy value of Sn doped Ga_2O_3 (1.355 eV) is much lower than the β-Ga_2O_3 (1.714 eV), indicating that lower overpotential is required for the Sn doped catalyst to drive the water oxidation and thus higher theoretical OER activity.

The superior bifunctional electrocatalytic activity of bulk $Sn_{x=0.15}$-Ga_2O_3 inspired us to construct a rechargeable Zn−air battery using the doped material as the cathode (Figure 2.29a). A solution of 6 M KOH with 0.2 M zinc acetate solution was used as the electrolyte. A charge-discharge cycle

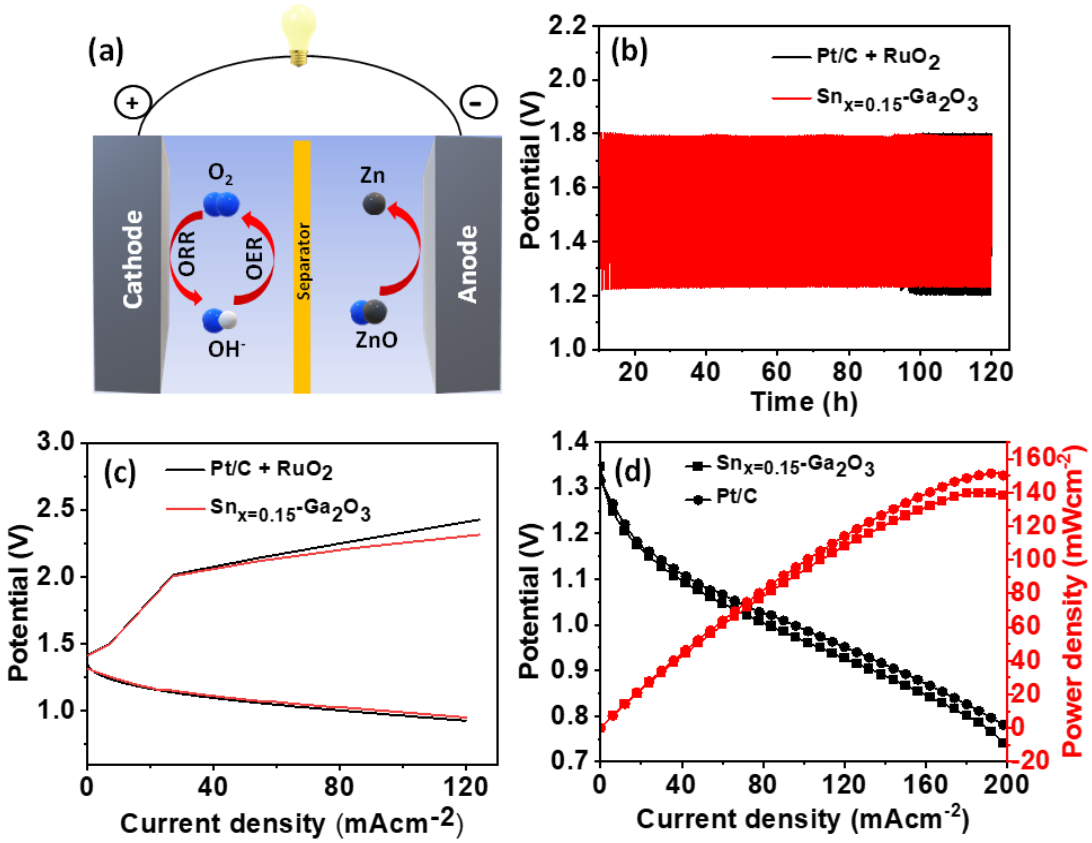

Figure 2.29: (a) Schematic representation of Zn-air battery (b) charge-discharge cycles of $Sn_{x=0.15}$-Ga_2O_3 and Pt/C + RuO_2 mixture (c) charge and discharge cycle showing the polarization in $Sn_{x=0.15}$-Ga_2O_3 and Pt+RuO_2 (d) discharge cycle and power density values at different current densities for $Sn_{x=0.15}$-Ga_2O_3 and Pt/C

test was performed with a current density of 2 mA cm^{-2} on two separate devices using Pt/C + RuO_2 (benchmark) and $Sn_{x=0.15}$-Ga_2O_3 as air cathode (Figure 2.29b, c). As shown in Figure 12b, the initial charge and discharge potentials of $Sn_{x=0.15}$-Ga_2O_3 (red curve) reached 1.80 and 1.22 V, respectively, whereas it was 1.81 and 1.19 V for Pt/C + RuO_2 (black curve) after 120 h. While $Sn_{x=0.15}$-Ga_2O_3 and commercial Pt/C and RuO_2 catalysts exhibited similar charging and discharging potential at low current density (Figure 2.29c), $Sn_{x=0.15}$-Ga_2O_3 has a smaller polarization at high current densities, indicating a better performance at high current densities for the Zn–air battery than the corresponding state-of-the-art battery based on Pt/C + RuO_2 mixture air-cathode. The increased polarization of Pt/C + RuO_2 compared to $Sn_{x=0.15}$-Ga_2O_3 causes a higher reduction in the performance of the battery. Figure 2.29d shows that the maximu m power density of the Zn−air battery using the $Sn_{x=0.15}$-Ga_2O_3 catalyst was determined to be 138 mW cm^{-2}, close to that of benchmark Pt/C + RuO_2 catalyst (150 mW cm^{-2}). Therefore, the Sn doped Ga_2O_3 based Zn−air battery showed comparable power performance and enhanced stability to device with benchmark Pt/C + RuO_2 air-cathode.

2.2.4 Conclusions

In summary, we designed a bulk $Sn_{x=0.15}$-Ga_2O_3 catalyst with superior bifunctional ORR and OER activity and durability in alkaline media. The excellent catalytic activity of Sn doped Ga_2O_3 is attributed to the symbiotic relationship between Ga^{3+} Lewis acid sites and Sn-based active sites with favorable oxygen adsorption characteristics. The symbiotic relationship significantly improved the electronic density distribution around Sn, as confirmed from the electron localization function plots. Further, the Bader charge analysis established that the formation of the intermediates, especially the O*, was significantly improved due to the strong Lewis acid property of Sn doped Ga_2O_3. Finally, $Sn_{x=0.15}$-Ga_2O_3 was successfully employed as cathodes in Zn–air batteries,

displaying the highest power density and excellent charge-discharge stability reported from a bulk system. The rational design of atomically dispersed Lewis acid sites in our study is beneficial for constructing high-performance bifunctional bulk electrocatalysts for electrochemical energy applications.

Chapter 3

Creation of heterostructure and heterojunctions

Heterostructures have become increasingly popular due to their potential for both fundamental research and industrial applications. The unique advantages of heterostructures are not solely due to the combination of materials with different properties, but rather the distinct microstructure of the heterointerfaces. This chapter focuses on the formation of heterostructures and the resultant charge transfer effects in two specific applications: hydrogen evolution and SERS. The first part of the thesis investigates the formation of a heterostructure between graphene nanoribbons (GNRs) and molybdenum disulfide (MoS_2) and the second part of the chapter explores the use of a heterostructure composed of a nickel-silver (Ni-Ag) nanostructure with MXene for SERS detection using Rhodamine 6G dye.

Tailoring the curvature-directed lattice strain in GNRs along with optimal surface anchoring of molybdenum disulfide (MoS_2) quantum dots (QDs) can lead to a unique heterostructure with Pt-like HER activity (onset potential −60 mV). The curvature-induced electronic charge redistribution at the curved region in the graphene nanoribbons allows a facile GNR-MoS_2 interfacial charge transfer in the heterostructure, making the interfacial sulfur (S) more active towards the HER. The DFT calculations confirmed electronically activated interfacial S-based catalytic centers in the curved GNR-based heterostructure leading to Pt-like HER activity.

SERS is a highly sensitive method for detecting various analytes. This technique relies on the use of metallic nanoparticles (NPs) as a substrate for signal amplification, utilizing two mechanisms: Localized Surface Plasmonic Resonance (LSPR) and Short-Range Charge Transfer (CT) between the analyte molecule and the substrate surface. However, the conventional methods based on metallic nanoparticles have limitations in effectively exploiting both mechanisms, as the energy level

of most analytes is not aligned with the Fermi level of the metallic surface. This is mitigated by the rational choice of a 2D material, MXene, which can facilitate the CT effect and Ni-Ag metal nanostructure which can increase SERS signal using surface plasmons. The Ni-Ag/MXene heterostructure displayed lower LOD compared to the individual counterparts.

3.1 Platinum-like HER Onset in GNR/MoS_2 Quantum Dots Heterostructure through Curvature-dependent Electron Density Reconfiguration

3.1.1 Introduction

Low-dimensional carbon materials and their heterostructures are attractive noble-metal-free electrocatalysts, especially for electrocatalytic HER.[222, 223]Formulation of vdW heterostructures with LD materials that can synergistically form a network of heterojunctions in the structure can tailor the interface characteristics and the HER activity. Typically, the enhanced HER activity in vdW heterostructures is known to be due to unique electronic coupling, interfacial electron transfer triggered by distinct work functions, and the creation of new active sites in the heterostructure.[79, 224] Among LDCMs, CNT-based heterostructures are one of the highly explored materials, where CNTs, due to their superior electrical conductivity, are largely used as conductive support for the more active counterparts.[3] Despite significant efforts, the electrocatalytic activity of CNTs and their heterostructures towards HER is still significantly inferior compared to the benchmark Pt catalysts.[4] Compared to CNTs, unzipped CNTs or graphene nanoribbons (GNRs),[5] though relatively less explored, offer additional benefits as HER catalysts, including the presence of new edge sites and higher surface area while retaining the electronic conductivity. One of the most explored pathways to prepare GNRs is the chemical unzipping of MWCNTs.[6] Here, the strength of oxidizing agent will control the kinetics of the unzipping process and create fully or partially unzipped CNTs when strong or weak oxidizing agents are used. Further, it is established that the curvature in graphene matrices can create a local strain, induce rehybridization of π and σ orbitals, and affect the energy dispersions, DOS, and localized electron density distribution.[225, 226] Hence, the surface electron distribution in flat GNR (F-GNRs) from complete unzipping and the curved GNRs (C-GNRs) from partial unzipping of the CNT will be significantly different. However, the influence

of curvature on the local electric fields and charge distributions and engineering it to elicit superior activity are generally not considered in GNRs-based electrocatalysts.

Here, using MoS_2 QDs and GNRs as components, we synthesized a 0D/1D MoS_2/GNR heterostructures and demonstrated for the first time how the local variation in the electron density of GNR can help derive superior catalytic activity from the interfacial Sulfur-based active sites. We chose MoS_2 QDs as the 0D component of the heterostructures because of its reported exceptional HER activity, illustrated by its position close to Pt in the volcano plot.[227] For this, two different GNRs termed C-GNR and F-GNR were synthesized from MWCNTs using a moderate and a strong oxidizing agent under controlled reaction durations. The curvature-induced electronic density redistribution and specific anchoring of MoS_2 QDs on GNRs lead to distinct differences in catalytic behaviors between F-GNR and C-GNRs and their heterostructure catalysts. The changes in electron distribution and observed activities were explored using DFT calculations, which confirm highly active interfacial sites in the vdW heterostructures.

3.1.2 Materials and Methods

3.1.2.1 Oxidative unzipping of multiwalled carbon nanotubes using $KMnO_4$

MWCNTs were used as received from Millipore sigma. For unzipping process initially, the MWCNTs were suspended in concentrated sulfuric acid (H_2SO_4) for a period of 1–12 h and then treated them with 500 wt% potassium permanganate ($KMnO_4$). The reaction mixture was stirred at room temperature for 1 h and then heated to 55–70 ºC for an additional 1 h. The mixture was agitated with a magnetic stirrer until all the $KMnO_4$ was consumed, as noted by the disappearance of the red tint upon diluting a sample of the reaction mixture with water. When all the $KMnO_4$ had been consumed, we quenched the reaction mixture by pouring over ice containing a small amount

of hydrogen peroxide (H_2O_2). The solution was filtered over a polytetrafluoroethylene (PTFE) membrane, and the remaining solid was washed with water followed by ethanol.

3.1.2.2 Oxidative unzipping of multiwalled carbon nanotubes using ammonium persulfate

The MWCNT (200 mg) was added to a 100 mL round-bottom flask containing a mixture of concentrated sulfuric acid (20 mL) and fuming sulfuric acid (20% free SO_3 basis, 20 mL). The suspension was stirred at room temperature for 5 min before adding $(NH_4)_2S_2O_8$ (5.0 g) and the flask was connected to a condenser. The reaction mixture was stirred at 80ºC for 24h and further quenched with ice. The product was then isolated by vacuum filtration, washed with water, ethanol, and acetone.

3.1.2.3 Synthesis of MoS_2 QDs and GNR/MoS_2 heterostructure

A total of 5 mg of ammonium tetra thiomolybdate $(NH_4)_2MoS_4$ was dissolved in 30 mL of H_2O and sonicated up to 1 h. Then, 500 μL of hydrazine hydrate ($N_2H_4 \cdot 4H_2O$) was added and sonicated for another 1 h. The solution was transferred to a 40 mL autoclave and heated at 200 °C for 24 h. The resulting suspensions were centrifuged for 15 min at 10 000 rpm, and the supernatant solution with MoS_2 quantum dots is collected. The supernatant solution was purified by dialysis in water and lyophilized to get solid MoS_2 QDs for analysis. vdW heterostructure of GNRs and MoS_2 QDs (1:10 ratio) were fabricated via ultra-sonication method for 30 mins at room temperature.

3.1.2.4 Characterizations

The morphology of the GNR samples were studied using the S4800 scanning electron microscope. TEM images were obtained with FEI 300/80 Titan TEM and FEI Tecnai G (2) F30 S-Twin 300kV TEM. TEM samples were prepared by drop cast method over C-coated Cu grid. To remove agglomerates, the sample was sonicated to achieve a homogeneous dispersion. XPS measurements were performed using Kratos AXIS ULTRA X-ray Photoelectron Spectrometer.

The Raman spectroscopy was conducted on a NT-MDT Raman spectrophotometer with 532 nm laser illumination. XRD measurements were performed on a p-XRD Empyrean 2 system. KPFM measurements were performed in two-pass amplitude mode (AM) using a Pt-coated conductive Si probe (FMG01/Pt, resonance frequency of 56 kHz).

3.1.2.5 Electrochemical measurements

The electrocatalytic performance was analyzed by cyclic voltammetry (CV), Linear sweep voltammetry (LSV), Electrochemical impedance spectroscopy (EIS) and chronoamperometric test by using an CHI660E CH instrument workstation. All the experiments were performed in a three-electrode configuration using platinum wire as a counter electrode, Ag/AgCl (3 M KCl) as a reference electrode, and a glassy carbon electrode having a 3 mm diameter as a working electrode. The electrolyte used was a 0.5 M aqueous H_2SO_4 solution. The potential against Ag/AgCl was converted into a potential against a reversible hydrogen electrode by using the following equation

$$E\ (RHE) = E\ (Ag/AgCl) + (0.197 + 0.059 * pH) \qquad (1)$$

3.1.2.6 Computational Details

Density Functional theory calculations were carried out using Cambridge sequential total energy package (CASTEP) in Material Studio software.[3] The generalized gradient approximation (GGA) of the Perdew−Burke−Ernzerh (PBE) functional was used to explain the exchange-correlation interactions. The GGA-PBE DFT method was adopted to consider the van der Waals (vdW) heterostructure. For geometric convergence, the thresholds for energy and force were set to 10^{-6} eV/atom and 0.02 eV/Å, respectively. Cutoff energy of 550 eV was selected for a plane wave basis.[4] The Isovalue of the electric field distribution is 0.0028. A 0.82-nm-diameter 2-layer MWCNT (8, 8) is fully and partly unzipped along the longitudinal axis into a flat GNR and partially unzipped curved

GNR, respectively. The MWCNT (8, 8) is radially unzipped into curved and flat GNRs with lengths of 1.5 and 1.8 nm, respectively. Carboxylic acid groups were added to unzipped edges of the CNTs as obtained from the XPS results. MoS_2 Quantum dot structure was designed by creating a 3 × 3 × 1 2H-MoS_2 (002) supercell using crystal build property, from the bulk 2H-MoS_2. For each structure, atomic positions were first relaxed to reach their equilibrium. The structural geometry optimization convergence thresholds for energy changes and displacement were set to be 1×10^{-6} Ha, 0.002 Å, and 2×10^{-4} Ha/Å. The SCF tolerance was set to 1.0×10^{-5} eV/atom and the wiping for the orbital occupancy was set to 0.05 Ha. For each elementary step in the HER, the Gibbs free energy was calculated using $\Delta G = \Delta E_{ad-H} + \Delta E_{ZPE} - T\Delta S_H$, where E_{ad-H} refers to the adsorption energy of H* (* denotes the uncertain ion state) on the catalytic site. ΔE_{ZPE} refers to the variance of zero-point energy, which can be found from vibration frequency calculations. T is temperature and ΔS_H is the half of S_H, which is a known thermodynamic feature for each adsorbate.

3.1.3 Results and Discussion

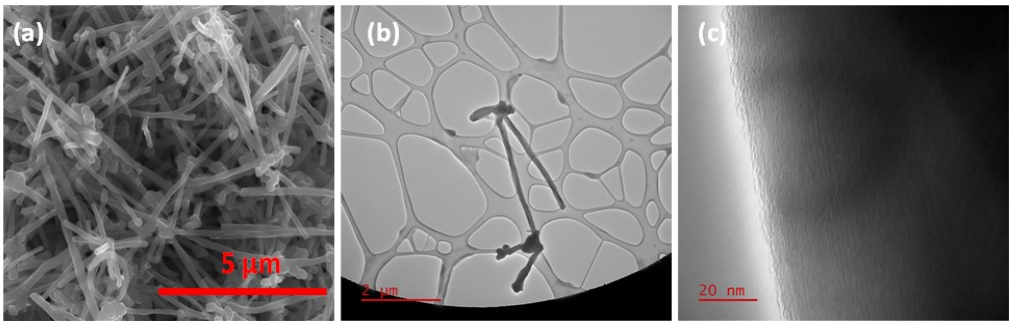

Figure 3.1: (a) SEM image of pristine MWCNTS (b) Low resolution and (c) high resolution TEM images of MWCNT

Unzipping of MWCNTs with a strong oxidizing agent like potassium permanganate ($KMnO_4$) produced F-GNRs, whereas unzipping using milder ammonium persulfate ($(NH_4)_2S_2O_8$) resulted in C-GNRs.[228, 229] The amount of functional groups introduced while unzipping the CNTs is proportional to the strength of the employed oxidizing agent.[229] Hence, we expect more functional groups in samples unzipped using $KMnO_4$. Figure **3.**1 shows the scanning electron microscopy (SEM) and high-resolution transmission electron microscopy (HRTEM) images of pristine MWCNTs with perfect cylindrical morphology. Figure. **3.**2 shows the representative AFM topography and height profiles for MWCNT, F-GNR and C-GNR, respectively. The AFM topography and the height profile (~135 nm) confirmed the partial unzipping and curved nature of C-GNR. Figure. **3.**3 shows the Raman spectra of pristine MWCNTs and the GNRs with three

Table 3.1: I_D/I_G ratio from Raman spectrum for MWCNT, F-GNR and C-GNR

Sample	I_D/I_G
MWCNT	0.14
F-GNR	1.03
C-GNR	0.98

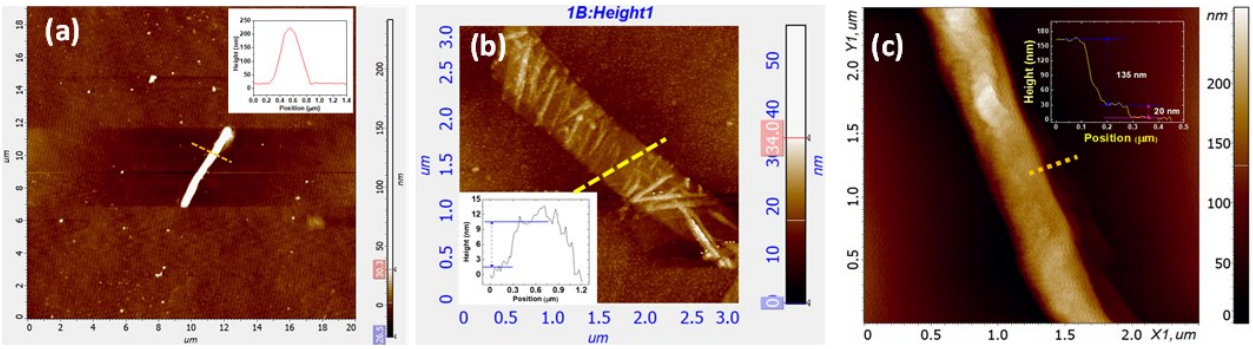

Figure 3.2: AFM topography of (a) MWCNT, (b, c) of F-GNR and C-GNR, respectively. Insets are the height profiles corresponding to the lines marked in the topography images.

characteristic Raman bands around 1350 cm^{-1} (D band), 1580 cm^{-1} (G band), and 2700 cm^{-1} (2D band). The higher I_D/I_G ratio for F-GNR indicates higher defects/degree of edge functionalization (more unzipping) in the F-GNRs (Table S1).[229] The presence of oxygen functionalities on GNR edges leads to increased lattice spacing, as shown in the X-ray diffraction (XRD) spectra (Figure.

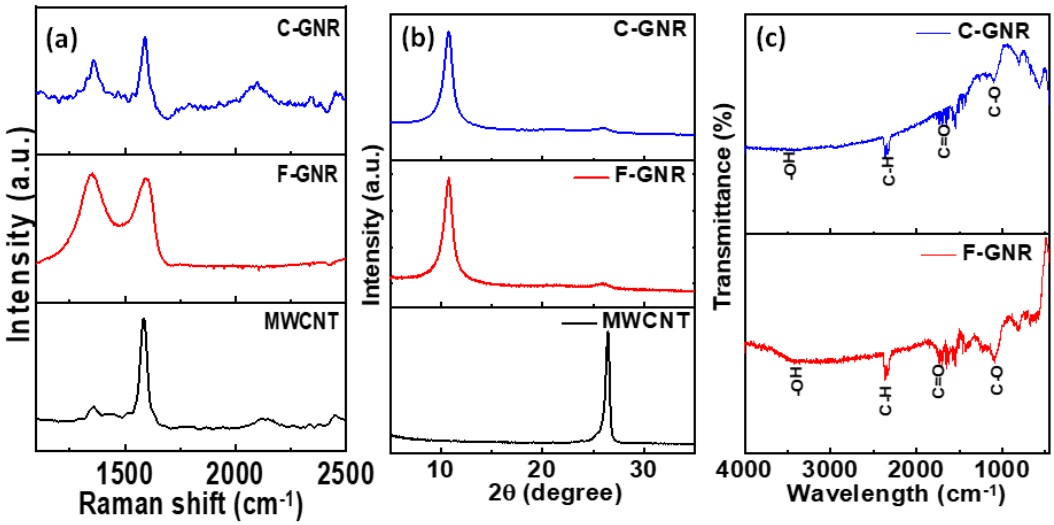

Figure 3.3: Raman spectrum of MWCNT, F-GNR and C-GNR (b) XRD spectrum of MWCNT, F-GNR and C-GNR and (c) FTIR of F-GNR and C-GNR

3.3).[230] Fourier Transform Infra-red (FTIR) analysis and X-ray photoelectron spectroscopy (XPS) indicated that GNRs mainly have carboxyl groups (-COOH) presumably at the edges after unzipping (Figure. 3).[6] The SEM image of F-GNRs (Figure. **3.**4a, b) affirms that $KMnO_4$ completely unzips the MWCNTs leading to F-GNRs. Corresponding HRTEM images (Figure. **3.**4 c, d) also corroborate the sheet-like morphology of F-GNRs with a slightly increased interlayer distance, supporting the XRD results. Unzipping MWCNTs using $(NH_4)_2S_2O_8$ resulted in longitudinal cuts while partially preserving the curved morphology (Figure. **3.**5 a-c). Similarly, the characterization of MoS_2 QDs using Raman

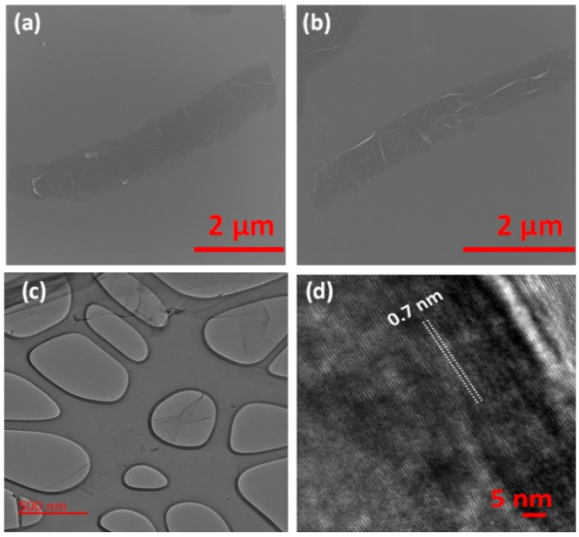

Figure 3.4: (a, b) SEM images of F-GNRs (c) Low resolution TEM and (d) HRTEM images of F-GNR

(Figure. **3.**6a), UV-Vis (Figure. **3.**6b), XPS (Figure. **3.**6 c, d), and XRD (Figure. **3.**6e) confirmed

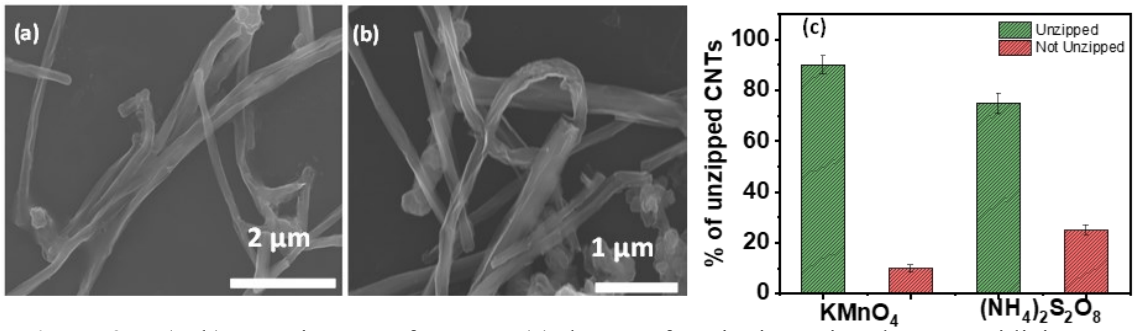

Figure 3.5: (a, b) SEM images of C-GNR (c) degree of unzipping using the two oxidizing agents

that the MoS_2 QDs formed are 2H phase.[11] Different microscopic and spectroscopic investigations were conducted on GNR/MoS_2 vdW heterostructures to ensure their formation, chemical identity of the components, and delineate the interfacial charge transfer through heterojunctions. Figure. **3.**7a and Figure. **3.**7d show the schematic of F-GNR/MoS_2 and C-GNR/MoS_2 heterostructure,

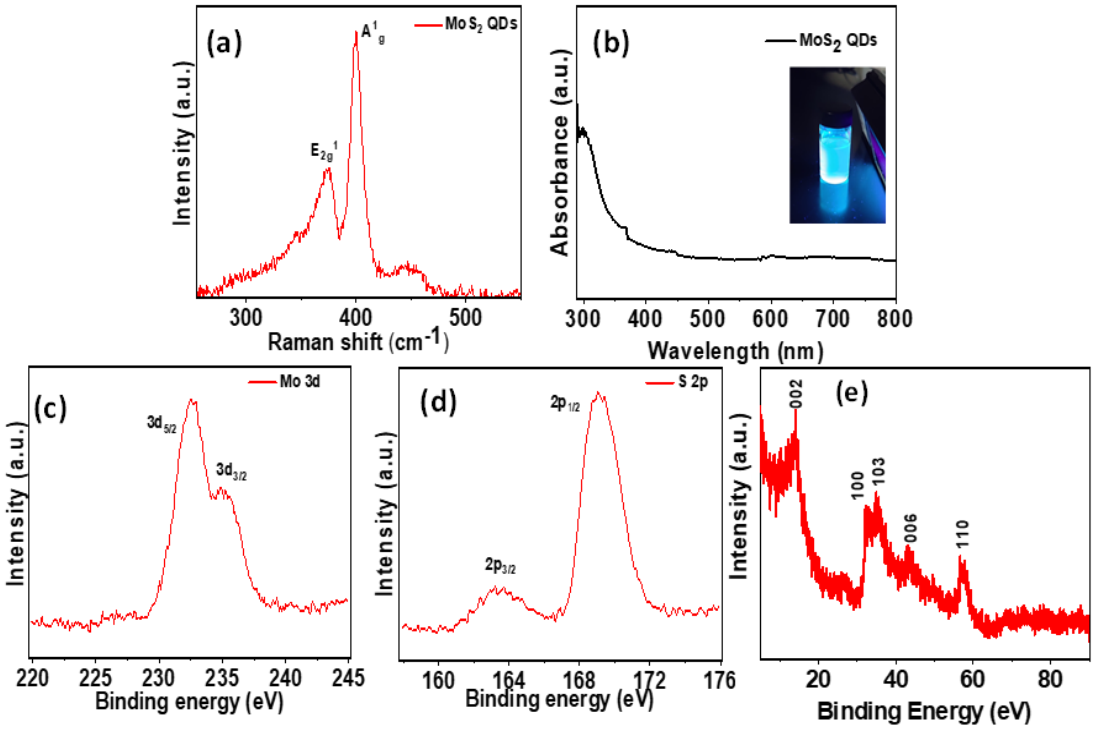

Figure 3.6: (a) Raman spectrum of MoS_2 QDs (b) UV-Vis measurement (c, d) XPS high resolution spectrum of MoS_2 QDs (e) XRD of drop casted MoS_2 QDs solution on a glass slide

respectively. As shown in the schematic, we expect the MoS_2 QDs to be present on the edges in F-GNR while at the edge and the curved center in C-GNRs. Our microscopic and spectroscopic investigations and theoretical energy-based stability calculations confirmed the proposed architecture of the heterostructure. While the MoS_2 QDs were not evident in the SEM images (Figure. 7b and 7e), the HRTEM image in Figure. **3.**7c and **3.**7f proved the formation of the heterostructures. The HRTEM image of F-GNR/MoS_2 (Figure. **3.**7c) revealed that the MoS_2 QDs are primarily attached along the edges of F-GNR. On the other hand, the HRTEM of the C-GNR/MoS_2 heterostructure revealed that MoS_2 QDs are anchored both at the edges and center of the curved basal planes (Figure. **3.**7f). The XPS analysis also validated the presence of GNR and MoS_2 QDs in the heterostructures (Figure. **3.**7 g-j, Figure. **3.**8 a-g) and a potential charge transfer between the components. The comparison of high-resolution XPS scans of the S 2p region in pristine MoS_2, F-GNR/MoS_2, and C-GNR/MoS_2 vdW heterostructures revealed a shift towards lower binding energy for the S 2p peak in the heterostructure compared to pristine MoS_2 QDs, implying the potential transfer of electrons from GNRs to MoS_2 QDs (Figure. **3.**7 h, j).[231] Such charge transfer from GNR to MoS_2 QDs in the vdW heterostructure can enhance their HER activity (as seen in the next section). The Raman spectra of vdW heterostructures (Figure. **3.**7k) show E^1_{2g} and A_{1g} of MoS_2 QDs and the D and G bands of the GNRs, again pointing to the successful formation of GNR/MoS_2 vdW heterostructure. The corresponding blue shift of G band in the heterostructure compared to pristine GNRs also confirms the charge transfer from GNRs to MoS_2 QDs.[232]

After characterizing the GNR/MoS_2 vdW heterostructures, we studied their electrocatalytic HER performance. First, the HER activities of pristine GNRs (i.e., F-GNRs and C-GNRs) and MoS_2 QDs were explored (Figure. **3.**9). The C-GNR exhibited an onset potential of -0.510 V vs. RHE and an overpotential of -0.585 V vs. RHE (at j = 20 mA/cm^2), whereas F-GNR displayed a higher

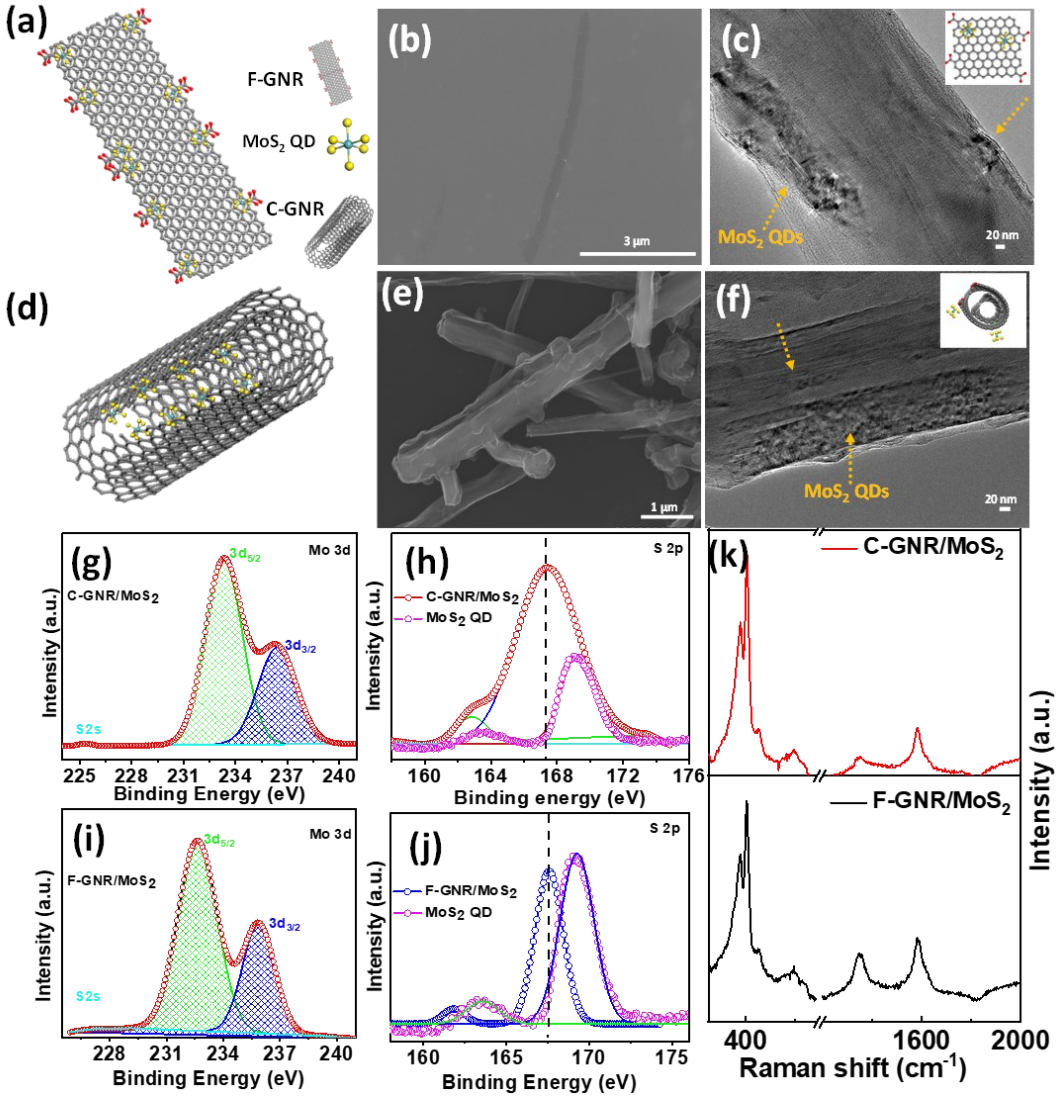

Figure 3.7: (a) Schematic of F-GNR/MoS_2 heterostructure (b) SEM and (c) TEM image of F-GNR/MoS_2. Inset shows the HRTEM image (d) Schematic of C-GNR/MoS_2 heterostructure (e) SEM and (f) TEM image of C-GNR/MoS_2. Inset shows the HRTEM image (g) XPS high resolution spectrum of Mo 3d region in C-GNR/MoS_2 and (h) XPS high resolution spectrum of C-GNR/MoS_2 and pristine MoS_2 QD for S 2p region (i) XPS high resolution spectrum of Mo 3d region in F-GNR/MoS_2 and (h) XPS high resolution spectrum of F-GNR/MoS_2 and pristine MoS_2 QD for S 2p region (k) Raman spectrum of the heterostructures.

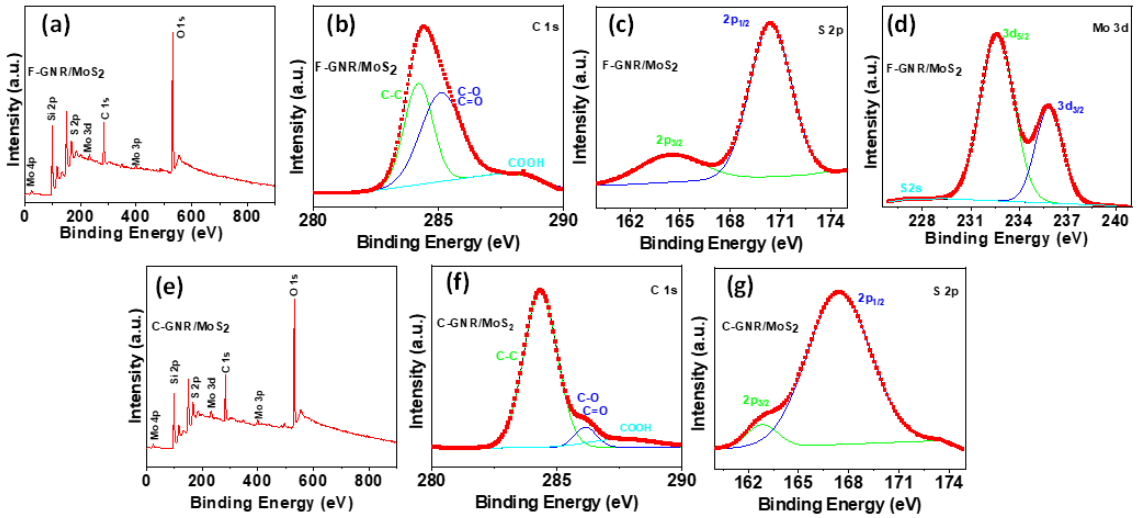

Figure 3.8: (a) XPS survey spectrum of (a) F-GNR/MoS_2, High resolution XPS spectra of F-GNR/MoS_2 (b) C 1s (c) S 2p (d) Mo 3d. XPS survey spectrum of (e) C-GNR/MoS_2 and High resolution XPS spectra of C-GNR/MoS_2 (f) C 1s (g) S 2p

onset potential of -0.534 V vs. RHE and an overpotential of -0.660 V vs. RHE (at j = 20 mA/cm^2). The pristine MoS_2 QDs displayed HER onset potential of -0.350 V vs. RHE and an overpotential of -0.455 V vs. RHE (at j = 20 mA/cm^2). The higher HER activity of MoS_2 QDs compared to GNRs is consistent with previous literature.[233] Interestingly, the polarization curves of the C-GNR/MoS_2 heterostructure displayed a well-defined catalytic wave with two closely placed onsets (Figure. **3.**10a). The initial electrocata-

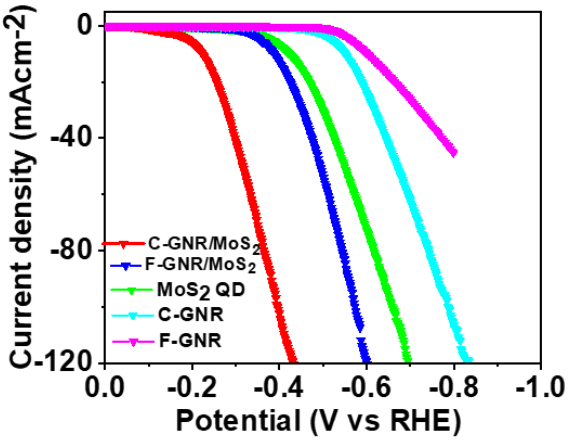

Figure 3.9: Polarization curves for HER

lytic onset potential of -0.06 V vs. RHE demonstrated by C-GNR/MoS_2 is one of the best reported from a carbon-based system (very close to Pt onset potential of -0.03 mV vs. RHE) and superior to many metal-based HER catalysts. The second onset in the catalytic wave was observed at -0.145 V vs. RHE. To the best of our knowledge, this is the first study to report an observation of a catalytic wave with dual onsets in GNR/MoS_2 systems, indicating the presence of multiple catalytically

active centers. The C-GNR/MoS_2 heterostructure also displayed two Tafel slopes, 68.3 mV/dec and 72.9 mV/dec, corresponding to the first and second onset potentials, respectively (Figure. **3.**10b). From Tafel slope analysis, GNRs and MoS_2 have the Volmer step as the rate-determining step (RDS) whereas, in the vdW heterostructures, a combination of Volmer and Heyrovsky steps govern the process.[234] The lower onset potential and Tafel slope, together with a higher current density, signify the superiority of C-GNR/MoS_2 towards HER. Figure. **3.**11 compares onset and overpotential for attaining 20 $mAcm^{-2}$ for all samples. The analysis of the electrochemically active surface area (ECSA) (Figure **3.**10c) implied a higher ESCA for C-GNR/MoS_2 heterostructure (illustrated by the higher C_{dl}) compared to F-GNR/MoS_2. Further, the lower charge transfer resistance

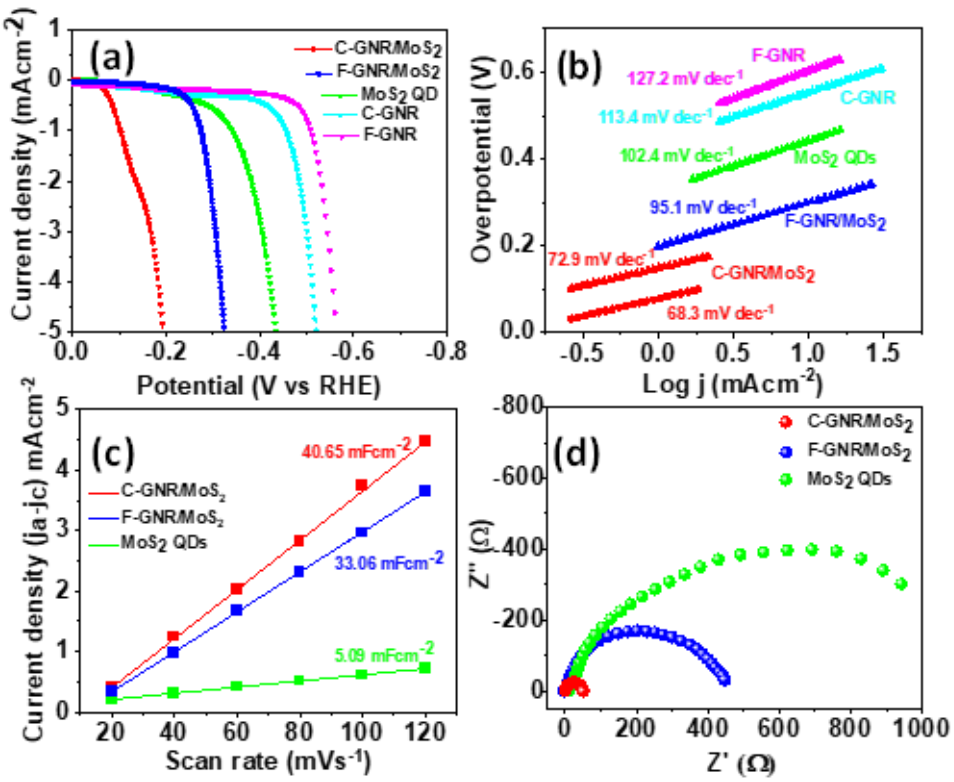

Figure 3.10: (a) LSV polarization measurements (b) Tafel slope (c) ECSA measurements (d) EIS measurements

for the C-GNR/MoS_2 heterostructure, from impedance measurements, suggests faster electron transfer kinetics in the system (Figure. **3.**10d). The C-GNR/ MoS_2 demonstrated excellent stability,

with a stable current density up to 12 h (Figure. S12). No redox process is expected for oxygen functionalities on the GNR edges at the applied potential range as they are reported to be stable in the HER voltage range.[235] Based on our experimental results, we hypothesize that unique strain-dependent electronic charge distribution at the curved basal plane in C-GNRs leads to heterostructure with higher ECSA, dual active sites, and lower charge transfer resistance leading to an excellent HER activity with an ultrasmall onset potential.

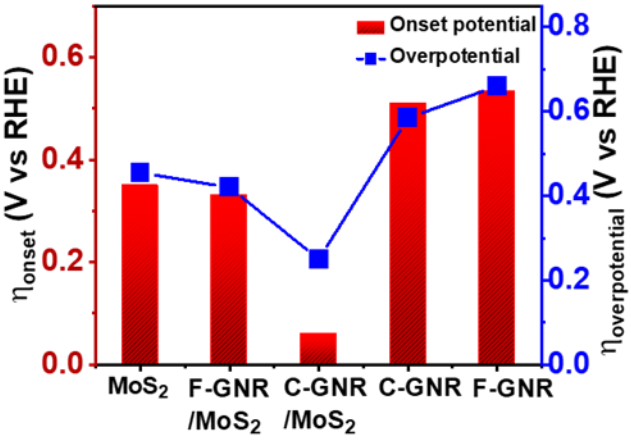

Figure 3.11: (a) LSV polarization measurements (b) Tafel slope (c) ECSA measurements (d) EIS measurements

We performed DFT-based calculations to verify the hypothesis regarding curvature (strain)-dependent charge redistribution and gain insights into the nature of HER active sites. Figure. **3.**13a shows the DFT simulated structures of F-GNR and C-GNR. The electron-withdrawing carboxylic acid groups (produced during the unzipping process) at the edges result in the partial polarization of adjacent C=C. The polarization leads to a slightly higher negative charge on the carbon atom adjacent to the carboxylic acid group, increasing the electronic density on the edges (Figure **3.**13b). However, in C-GNRs, in addition to the edge sites, the rehybridization of π and σ orbitals at the curved region result in high electron density hotspots towards the center of the curved face, opposite to the

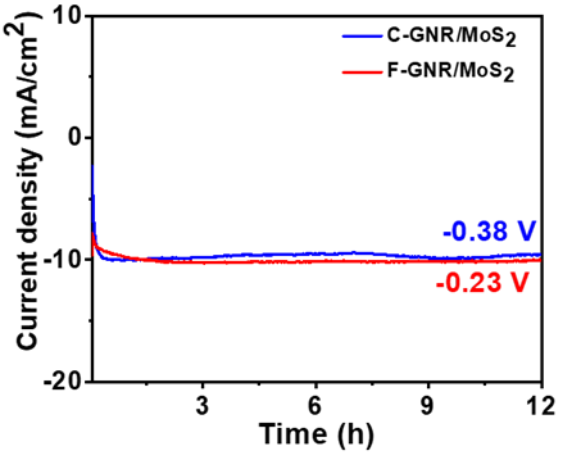

Figure 3.12: Chronoamperometry measurements of C-GNR/MoS_2 and F-GNR/MoS_2

unzipped edges. The enhanced electronic density of edge atoms in F-GNR and atoms around the C-GNR curved face, leads to enhanced dipole-dipole interaction with MoS_2 QDs to form the heterostructure and allows effective charge transfer with adsorbed protons for promoting HER. The lower Gibbs free energy change (ΔG_H) for C-GNRs for the active sites at the center compared to edge sites in C-GNRs and F-GNRs reinforce the experimentally observed higher HER activity (Table 2). Further, the GNR/MoS_2 heterostructures were optimized in various configurations. (Figure. **3.**14, **3.**15). The lowest total energy for the structure confirms the favorable anchoring of QDs near the edges in F-GNR. However, in the case of C-GNR, MoS_2 gets anchored at the edges and towards the curved center (Figure. **3.**16a). Thus, the DFT calculations substantiate the distinctly different distribution of MoS_2 QDs in C-GNR and F-GNR-based heterostructures, as seen in HRTEM images. Moreover, our calculations indicated an increased electron accumulation at the sulfur atom of MoS_2 QDs at the interface in the heterostructure (higher electronic density) (Fig**ure 3.**16b), potentially due to the **t**ransport from GNRs to MoS_2 as seen in the XPS and Raman

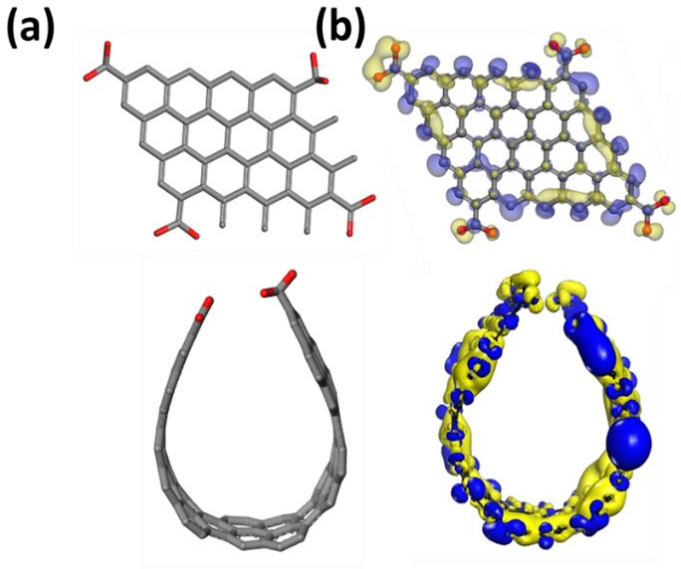

Figure 3.13: DFT simulated structures (a) and electronic charge distribution of F-GNR and C-GNR

Table 3.2: Calculated Gibbs free energy (ΔG_H) for various sites for HER

Adsorption sites	E_{ads} **(eV)**	$\Delta G_{free\ energy}$ **(eV)**
Pristine MoS_2 QD (S-active site)	0.23	0.2
F-GNR (skeletal C adjacent to -COOH group)	-0.152	-0.13
C-GNR (skeletal C near center of curvature)	-0.141	-0.12
F-GNR/MoS_2 (outer S atom)	-0.23	-0.19
F-GNR/MoS_2 (skeletal C adjacent to – COOH group)	-0.133	-0.14
F-GNR/MoS_2 (interfacial S atom)	-0.095	-0.09
C-GNR/MoS_2 (outer S atom)	-0.1265	-0.11
C-GNR.MoS_2 (skeletal C near center of curvature)	-0.150	-0.13
C-GNR/MoS_2 (interfacial S atom at the edge)	-0.1035	-0.08
C-GNR/MoS_2 (interfacial S atom at center of curvature)	-0.0575	-0.05

analysis. The DOS calculations also support the electron transfer, which showed that DOS for MoS_2 in the heterostructure is positioned higher than in pristine MoS_2 QDs (Fig**ure 3.**16c). DFT analysis also suggested that the interfacial sulfur atoms have the lowest ΔG_H among the investi-

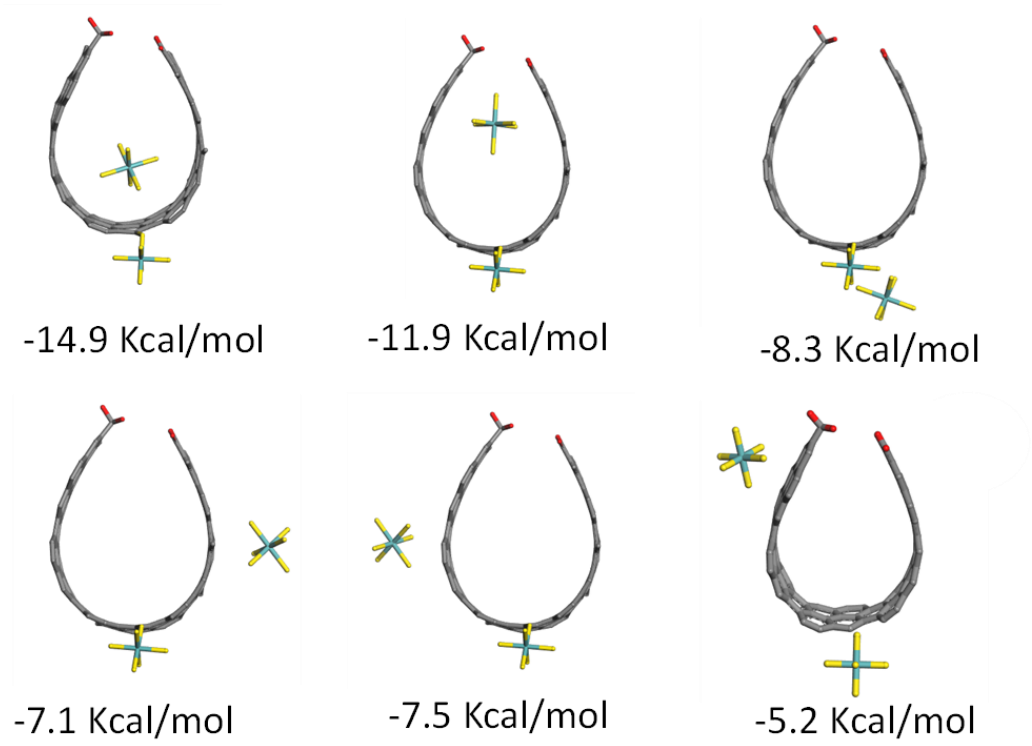

Figure 3.14: Total energy of structures at different sites on C-GNR/ MoS_2.

gated potential active sites (Table **3.**2), confirming the interfacial S as the most efficient active site. The presence of MoS_2 at the edges and center of the curved plane in C-GNRs, could potentially

have different HER activity and is leading to the catalytic wave with dual onsets. The proton adsorption energies for the interfacial S sites at the edge and center in C-GNR/MoS_2 heterostructure were calculated to compare their HER activity. As expected, the DFT analysis showed different proton adsorption energy and ΔG_H for the two interfacial S active sites in C-GNR/MoS_2 heterostructure. The smaller proton adsorption energy (-0.058 eV for center and 0.092 eV for edge) and lower ΔG_H for the interfacial sulfur active sites at the center of the curvature in the C-GNR/MoS_2

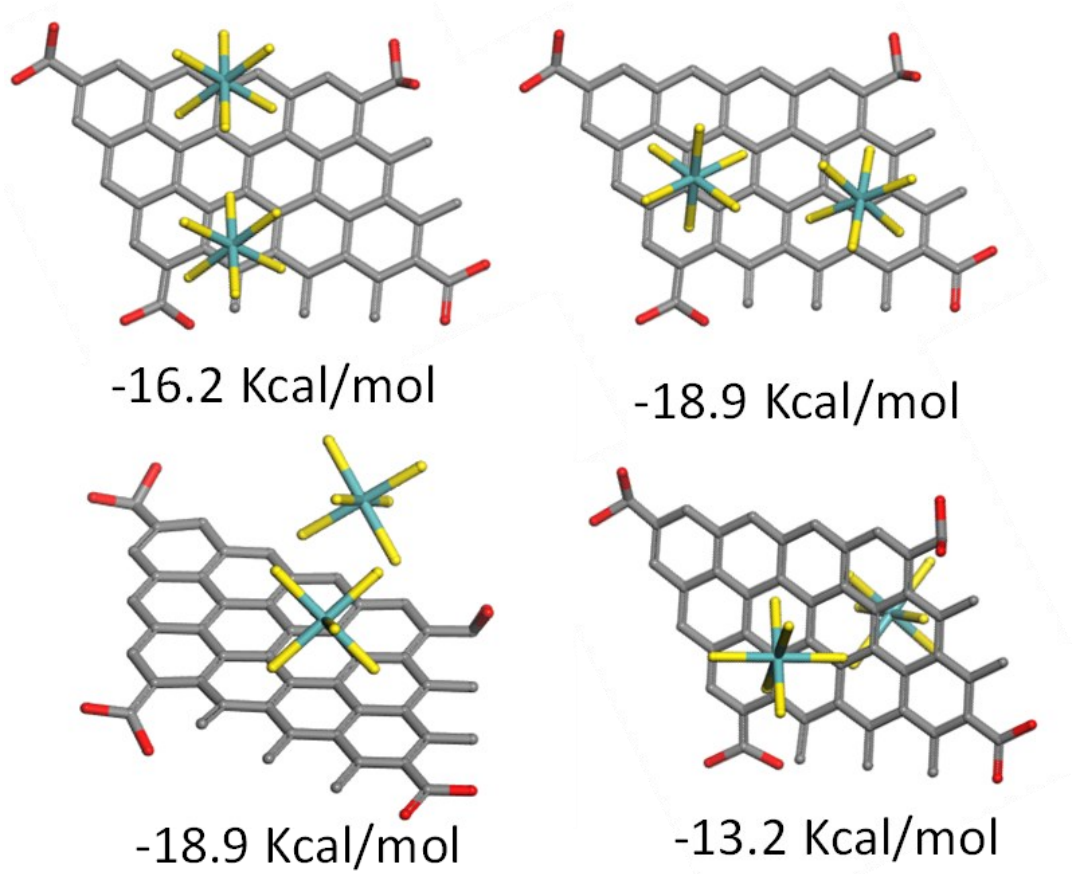

Figure 3.15: Total energy of structures at different sites on F-GNR/ MoS_2. The lowest energy is the most possible and stable structure.

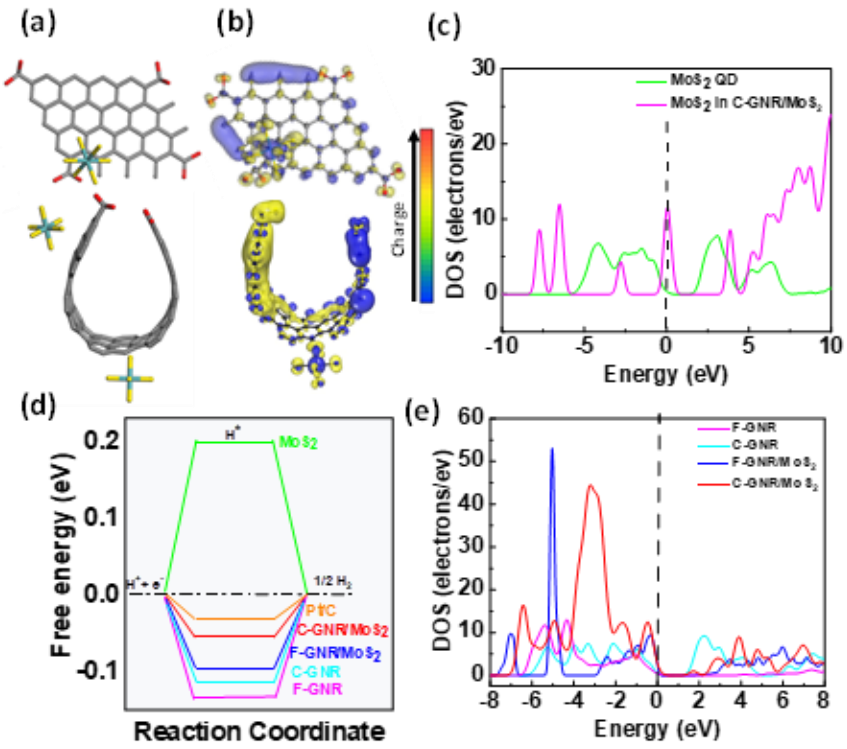

Figure 3.16: (a, b) Stick representation and electric field distribution of idealized F-GNR/MoS_2 (top) and C-GNR/MoS_2 (bottom), respectively (c) DOS plot for MoS_2 alone (d) Gibbs free energy diagram (e) Total density of states representation.

(compared to the one at the edge) leads to optimal binding strengths of H atoms and consequent better onset and HER activity (Fig. **3.**16d). Thus, it can be inferred that the first onset in the catalytic wave in the HER polarization curve of C-GNR/MoS_2 is due to the interfacial S atom near the curved plane in C-GNRs, and the second onset comes from the interfacial S active site at the edges. Moreover, the higher number of electronic states close to the Fermi level in C-GNR/MoS_2 indicates high carrier density and improved charge transfer, which strongly supports the experimental results (Fig. **3.**16e). Hence, our DFT calculations confirm that the variations in local electronic charge distributions play a critical role in determining the activity in GNRs and the interfacial sulfur in MoS_2 are the active sites for C-GNR/MoS_2 heterostructure leading to the catalytic wave.

3.1.4 Conclusions

In summary, the curvature-induced lattice strain and localized electronic density variations, and specific anchoring of MoS_2 QDs in C-GNR lead to significantly different and improved catalytic activity in GNR-based heterostructures. Due to the electron transfer from GNR to the interfacial S in MoS_2 QDs, the interfacial S atom becomes significantly activated towards HER resulting in superior HER activity of the heterostructure. Unlike F-GNR, the curvature-triggered electron re-distribution in C-GNRs led to the anchoring of MoS_2 QDs in C-GNR near the edge and at the center of the curved lattice. The presence of two catalytic sites is demonstrated by a catalytic wave with two closely positioned onsets for HER with the first onset potential as low as -60 mV. Our DFT simulation helped us confirm the identity of the active sites and reinforced the experimental results. The curvature-controlled electron localization in graphenic systems opens avenues to develop novel Pt-group metal-free catalysts with an enhanced and selective catalytic activity that can augment future energy sustainability.

3.2 Surface Enhanced Raman Scattering Sensors Using Ni/Ag/Mxene Substrates

3.2.1 Introduction

SERS is a powerful analytical technique used for the detection of molecules with high sensitivity and specificity.[236, 237] SERS has been widely used for the detection of various molecules, including drugs, pollutants, and biological molecules, and has shown great potential for applications in fields such as medicine, environmental monitoring, and forensic science. The high sensitivity of SERS detection can be attributed to the strong electromagnetic fields generated by the surface plasmon resonance of the metallic nanostructures, which can enhance the Raman signal by several orders of magnitude. Noble metal nanoparticles, nanowires, and other metallic nanostructures are often used in the SERS platform, as they promote collective oscillations of surface plasmon by inducing dipolar interactions around the metallic surface.[238-240] Strong coupling between Raman scattering and LSPR in the 'hotspot' region can greatly enhance the scattering signal by up to the 4th order of the absolute value of the near field. The nanostructured metallic surface can also enhance the Raman scattering signal through CT between the SERS substrate and the target molecule. When the distance between the surface and the analyte molecule is short enough and the energy levels are aligned, intermolecular CT can occur rapidly. However, metallic surfaces typically have zero band gap and energy levels that are not aligned with the target molecule, making effective intermolecular CT rare. As a result, non-aligned energy level-mediated CT is thermodynamically less favorable, limiting CT efficiency.

In comparison to other 2D nanomaterials, MXene nanosheets exhibit high conductivity and abundant surface functional moieties of MXene nanosheets enable their facile modification through

chemical bonding for various sensing applications. MXene is considered a highly promising substrate for precisely tuning the Fermi level of SERS materials. Recently, Yoo et al reported MXene coated with Au nanoparticles for simultaneous enhancement of the electromagnetic and CT mechanisms.[241] MXene nanosheets are better conformally and flexibly placed over the underlying SERS Au substrate due to their low rigidity compared to other 2D nanomaterials. Additionally, MXene layer enables the Fermi level of the substrate to be located between the HOMO and LUMO levels of analytes, thus efficiently facilitating the CT effect. Leveraging this, we intend to investigate the SERS capability of Ni-Ag bimetallic nanostructure on MXene nanosheets. Previous studies have shown that dipolar plasmon excitation is not present in nickel nanoparticles due to the strong extinction coefficient caused by both intraband and interband transitions.[242] However, it is expected that adding silver to nickel would introduce a surface-plasmon resonance due to the contribution of conduction electrons. The performance of the substrate was investigated using Rhodamine 6G (R6G) as the probe molecule.

3.2.2 Materials and Methods

3.2.2.1 Synthesis of Ni and Ag nanoparticles

Synthesis procedure for Ni particles were performed as reported.[243] Nickel (II) chloride hexahydrate ($NiCl_2 \cdot 6H_2O$), sodium hydroxide (NaOH), ethylenediamine (EDA), and hydrazine hydrate ($N_2H_4 \cdot H_2O$) were used as starting materials. In a typical synthesis procedure, 4 g of NaOH (5 mol/L) were dissolved in 20 mL of deionized water. Then, 1 mL of $NiCl_2 \cdot 6H_2O$ (0.5 mol/L) and 0.35 mL of EDA were added to the solution under vigorous stirring for 60 minutes. After that, 0.25 mL of hydrazine hydrate ($N_2H_4 \cdot H_2O$ 30%) were introduced, followed by 30 minutes of continuous stirring. The resulting mixture was then loaded into a Teflon cup, sealed, and maintained at 140°C

for 4 hours, before being cooled down to room temperature. A black product was observed floating on the solution, which was collected using a magnetic bar and then rinsed with distilled water and absolute ethanol several times to remove any impurities. Finally, the product was dried in air at 50°C for 6 hours. Silver nanoparticles were synthesized via chemical reduction method.[244] Silver nitrate ($AgNO_3$) were reacted with ascorbic acid as a reducing agent and citrate as stabilizer in aqueous bath with 30 °C. Further, the metal nanoparticles were mixed in a specific ratio and sonicated for a few hours.

3.2.2.2 Synthesis of Mxene nanosheets and heterostructure

$Ti_3C_2T_x$ MXene was synthesized from MAX phase Ti_3AlC_2 powder using a hydrofluoric acid (HF) (purchased from Acros-Organics) etching process reported previously. Briefly, 0.5 g of Ti_3AlC_2 powder was etched in 10 mL of HF (48%) for 8 h. Following the etching step, the etched solution was washed several times until the pH reached between 6 and 7, vacuum filtered using a 0.5 μm filter paper, and vacuum annealed at 80°C to obtain the $Ti_3C_2T_x$ MXene powder. To further exfoliate and obtain nanosheets of Mxenes, we used dimethyl sulfoxide (DMSO) as the solvent, which intercalates into expanded MXene powder samples. The sonication of DMSO intercalated Mxenes under an Ar atmosphere leads to formation of MXene nanosheets. To fabricate the heterostructure the metal nanoparticles dispersed in D.I water were mixed with MXene nanosheets dissolved in DMSO at an optimal ratio. The resultant solution was sonicated for 2h and the black powder was centrifuged and washed with D.I water and acetone before drying overnight at 30°C.

3.2.2.3 SERS detection

The substrates were prepared by coating the Ni-Ag/MXene heterostructure on a glass slide. SERS experiments were carried out using various concentrations of R6G methanol solutions, dropped

onto the sample substrates as the analyte molecule. The analyte solution was dried in air and measurements were carried out. In all SERS detections, the 532 nm excitation wavelength is adopted, with 60 s acquisition time, and the magnification of the objective is ×100x.

3.2.3 Results and Discussion

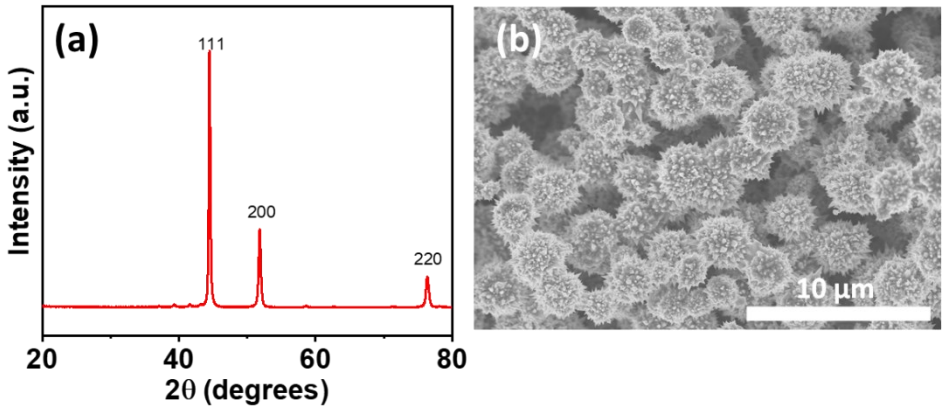

Figure 3.17: (a) XRD and (b) SEM image of Ni

The Ni particles were characterized using XRD and revealed the presence of a metallic Ni phase (Figure 3.17a). The corresponding SEM measurements show that the Ni particles have spikes like features and are 1-2 µm in size (Figure 3.17b). The corresponding XRD, SEM and EDS mapping of Ni-Ag nanostructure is shown in Figure 3.18 a-c. The $Ti_3C_2T_x$ MXene samples synthesized from HF etching of the MAX phase were characterized using different microscopic and spectroscopic techniques. The formation of MXene was confirmed using XRD spectra, as shown in Figure

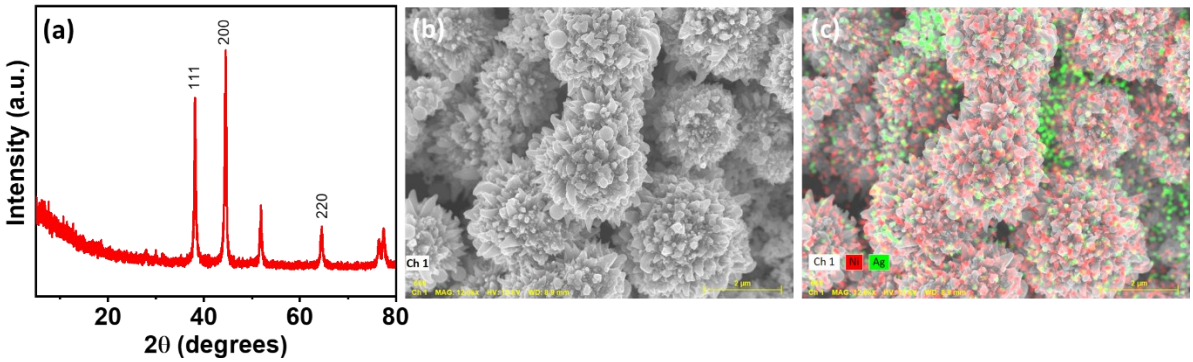

Figure 3.18: (a) XRD and (b) SEM image and (c) EDS mapping of Ni-Ag

3.19a. Figure 3.19b shows an SEM image of the HF-treated MAX-phase powder. Clearly, after the aluminum layer removal from Ti_3AlC_2, an accordion-like layered structure was formed. The EDS measurements revealed presence of Ti, C, O and F in the system (Figure 3.19c). The SEM images of MXene sheets (sizes ranging from 0.2 to 0.5 µm) obtained at the end of the exfoliation and sonication step are shown in Figure 3.20a, b. The SEM image of the corresponding Ni-Ag/MXene heterostructure is shown in Figure 3.20c.

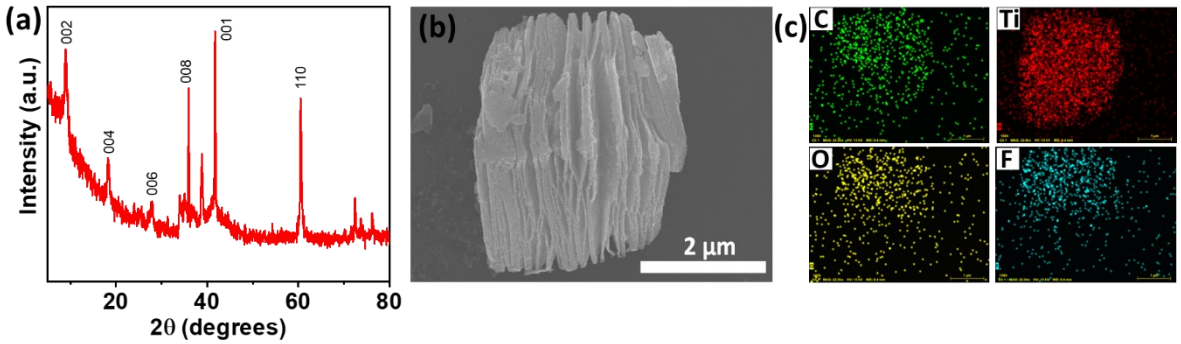

Figure 3.19: (a) XRD and (b) SEM and (c) EDS measurements of $Ti_3C_2T_x$ MXene nano-

After the spectroscopic and microscopic characterization of the Ni-Ag/MXene substrate, we proceeded in to investigating the SERS capability using R6G solution. The R6G aqueous solutions

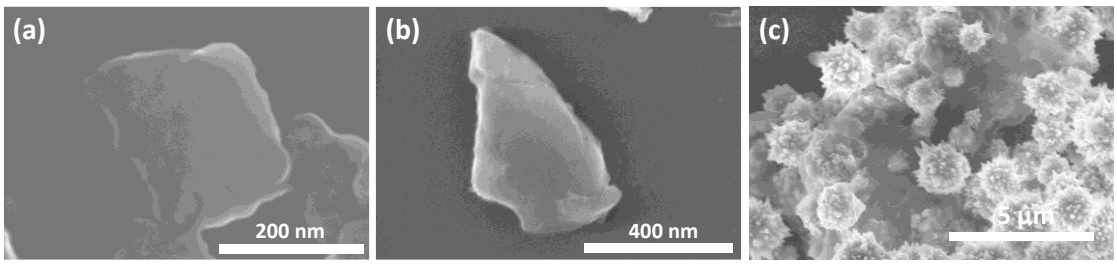

Figure 3.20: (a, b) SEM images of exfoliated MXene sheets

with concentrations ranging from 10^{-6} M up to 10^{-10} M were used as molecular probe to detect the Raman enhancement performance of the Ni-Ag and Ni-Ag/MXene SERS substrates. The characteristic peaks of R6G located at 1190, 1365, 1511, 1576 and 1651 cm^{-1} were observed (Figure 3.21a). The peaks located at 1365 and 1651 cm^{-1} belong to aromatic C−C stretching vibration

modes, which is consistent with literature.[245] As observed, the characteristic peaks of R6G were still conspicuous even at a lower concentration of 10^{-8} M.

It has been reported previously that the Fermi level of the MXene is close to 3.7 eV and is aligned between the HOMO and LUMO levels of analytes (e.g., R6G), thereby enhancing the CT from the underlying SERS substrate to Rh.[246] Accordingly, the Ni-Ag/MXene substrate would show higher SERS signal compared to Ni-Ag alone. Figure 3.21b shows the SERS measurement on Ni-Ag/MXene substrate with R6G concentrations of 10^{-8} M and 10^{-9} M. Both plasmonic and CT effects simultaneously and distinctively enhanced to exceptionally intensify the Raman scattering signal.

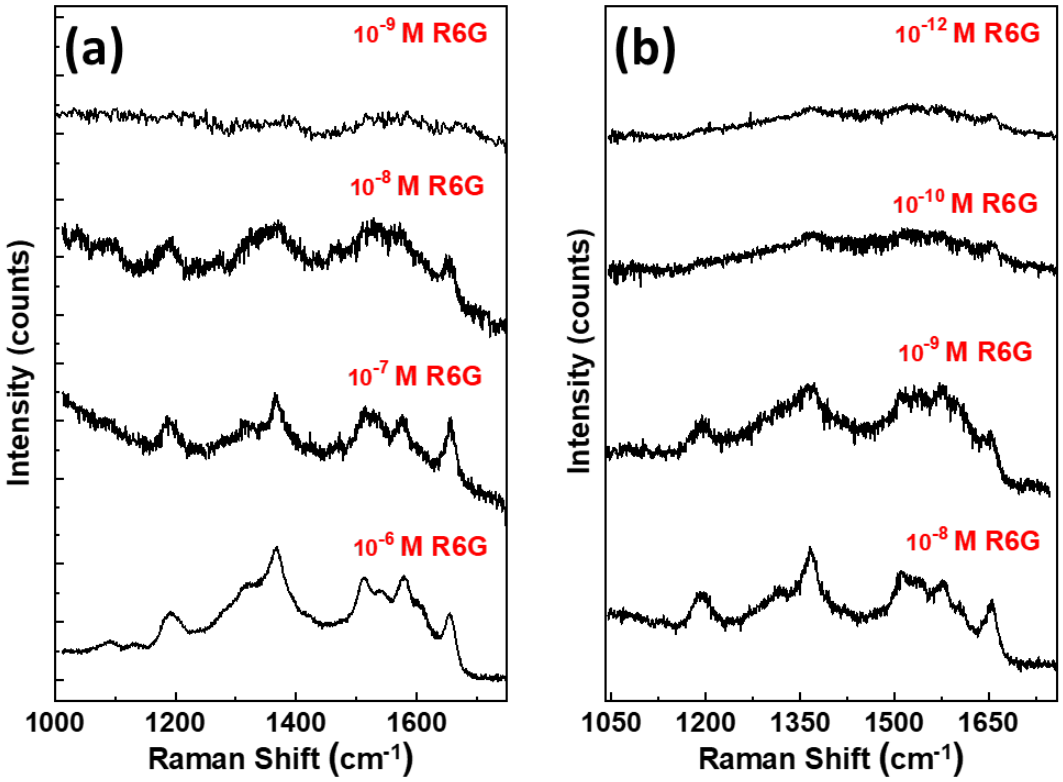

Figure 3.21: SERS detection of R6G on (a) Ni-Ag and (b) Ni-Ag/MXene

3.2.4 Conclusions

SERS has garnered significant attention in the past decade due to its ability to provide information on small numbers of molecules, including single-molecule detection. In this work a novel SERS sensing platform based on a Ni-Ag/MXene heterostructure. By exploiting plasmonic and charge transfer effects in the heterostructure Raman signal from R6G with a low concentration of 10^{-9} M was obtained. The presence of MXene nanosheets in the SERS sensing platform facilitated the CT effect along with the plasmonic enhancement via Ni-Ag particles.

Chapter 4

Spin Modulation in materials

Quantum theory predicts that the rate of chemical reactions will be slow if the spin of the electronic wave function of the products differs from that of the reactants because the Hamiltonian does not contain spin operators. OER is one such reaction where the spin is not conserved as the reactant $^-OH/H_2O$ exists in the singlet ground spin state without any unpaired electrons and the product O_2 is in the spin triplet state with two unpaired electrons. Hence, according to quantum mechanics, OER is forbidden, and an additional energy stimulus is necessary for the reaction to proceed, potentially contributing to the high overpotentials observed.[247, 248] Although the primary goal of an OER electrocatalyst is to minimize the required applied electrical potential for the extraction of at least two electrons with the same spins needed to produce triplet O_2, the significance of the spin attribute of electrons in determining the rate of OER was not well recognized until recently. Despite significant efforts to optimize the chemical and band structure of OER catalysts to improve the adsorbate-catalyst interfacial charge transport, most catalysts still exhibit high OER overpotentials due to the incomplete understanding of the OER mechanism. Hence, to achieve a true breakthrough in reducing the high overpotential of OER, more attention needs to be given to the "spin transition" in addition to "charge transfer". The following chapter explores the influence of an external magnetic field and introduction of chiral molecule for “spin selection” during OER. Specifically, the first part of the chapter investigates the synergistic effect of chirality induced spin selection and magnetic field in superparamagnetic and ferrimagnetic iron oxide catalysts. We also explored the prospect of OER current enhancement with ON-OFF magnetic fields to be utilized for sensing applications. The second part of the chapter focuses on chirality induced spin selection in Ni nanoparticles/MXene heterostructure. The substrate MXene is anchored with chiral

molecules, which enhances the intrinsic activity and triplet oxygen production at the Ni active site. Overall, this work aims to deepen our understanding of the role of spin in OER and explore novel approaches to improving OER catalysts.

4.1 Engineering size-dependent magnetic moment and chirality for enhanced spin-selective oxygen evolution reaction in magnetic catalysts

4.1.1 Introduction

Following the prediction by Garcia et al. various research indicated that spin transitions during OER can be better facilitated by coupling the magnetic field with electrochemistry that can enhance electrochemical reactions, especially OER. When an external magnetic field (H_{ext}) is applied, it induces spin polarization in magnetic catalysts causing spin up and spin down bands to split and the extent of the polarization determines the observed magnetic field enhanced catalysis. Spin polarization can be defined as $P(E_F) = \frac{n(up)-n(down)}{n(up)+n(down)}$, where n(up) and n(down) are densities of state at E_F for majority and minority spins, respectively. The $P(E_F)$ will help in selective screening of specific electron spin via the lower energy electron transfer channel facilitating triplet O_2 production and increasing the OER efficiency. In addition to the above "spin selectivity effect", the use of H_{ext} has been shown to have a positive impact on catalytic activity through various mechanisms such as magnetohydrodynamics (MHD), magnetothermal, Maxwell-stress effect, Kelvin force and magnetoresistance effects. While there have been some initial advances in the field of magnetic field-enhanced electrochemical reactions, the majority of current research has focused on ferromagnetic catalysts, leaving significant gaps in knowledge about the effects of other magnetic catalysts and how they differ in their observed OER enhancements under magnetic fields. Apart from H_{ext}, chiral molecules via CISS effect function as electron spin filters that preferentially transmit electrons into particular spin orientations. According to the CISS effect, charge transport through a chiral system depends on their spin, since the linear momentum of the electron is coupled to its spin, and thus electrons propagating from left to right have opposite spins to those

moving from right to left. Additionally, chiral molecules can maintain the transport of preferred spin over long distances with minimal spin diffusion or loss of spin coherence. Despite the significant influence of the CISS effect on OER, its impact on OER electrocatalytic process has not been thoroughly investigated.

Through quantum exchange interactions, magnetic catalysts can create a spin-selective channel and transfer electrons of the desired spin to the catalyst-adsorbate interface. While it has been reported that an external magnetic field can increase the spin density (manifested by an increase in magnetic moment of the catalytic center) in magnetic catalysts, leading to enhanced improved OER activity, a direct correlation between the magnetic moment and spin polarization (and OER activity) of the magnetic catalytic center is not established. This may be due to the difficulty in creating the same catalytic centers with different magnetic moments in the same material. Magnetite (Fe_3O_4) exhibits interesting catalytic properties and is a half-metallic ferromagnet, demonstrating full spin polarization at the Fermi level. Moreover, Fe_3O_4 is an ideal system to investigate the effect of the magnetic properties of the active center on OER efficiency, as the magnetic properties of the same metal centers can be conveniently modified synthetically. In this study, the correlation between the intrinsic magnetic properties and OER activity of Fe_3O_4 is investigated using ferrimagnetic and superparamagnetic systems (f-Fe_3O_4 and s-Fe_3O_4). The spin selectivity effect under an external magnetic field is examined, and various coexisting effects are decoupled. Additionally, we engineer the total spin polarization externally through the introduction of the Chiral-Induced Spin Selectivity (CISS) phenomenon in the catalyst by anchoring chiral molecules on the surface. Our study reveals that the extent of enhancement (89% improvement in current density at 1.8 V vs RHE and a low onset potential of 270 mV) is intimately dependent on the cumulative spin polarization resulting from the intrinsic nature of exchange interactions and resultant

magnetization in the systems, as well as the CISS-induced spin polarization. Furthermore, in addition to enhancing the OER process, chiral electrodes were able to minimize the formation of hydrogen peroxide (H_2O_2) during the water-splitting process. These findings have significant implications for the identification and selection of magnetic catalysts, as well as the optimization of the water splitting process using the combination of the CISS effect and an external magnetic field.

4.1.2 Materials and Methods

4.1.2.1 Synthesis of Iron Oxide

f-Fe_3O_4 was synthesized using a solvothermal method. $FeCl_3 \cdot 6H_2O$ (2.7 g) was dissolved in 80 mL of ethylene glycol to form a clear yellow solution. After adding sodium acetate (7.2 g) and polyethylene glycol (1.0 g), the mixture was stirred for about 30 min and then transferred to a Teflon-lined stainless-steel autoclave (100 mL capacity). The autoclave was heated at 200 °C for 8 h and then cooled to room temperature. The black iron oxide magnetic f-Fe_3O_4 nanoparticles were washed several times with ethanol and dried at 60 °C for 24 h.

s-Fe_3O_4 nanoparticles were prepared following a reported procedure.[249] In a round bottom flask, 0.68 g of $FeCl_3 \cdot 6H_2O$ (2.5 mmol) were dissolved in 60 mL of ethylene glycol. Then, 3.8 g of ammonium acetate (50 mmol) was added under continuous magnetic stirring until a clear solution was formed. The resulting mixture was transferred to a 100 mL Teflon-lined autoclave vessel and maintained at 200 °C for 12 h after which a black precipitate of Fe_3O_4 was formed. The solid was recovered by magnetic separation, and sequentially washed with DI water followed by ethanol and finally dried under vacuum at 60 °C for 6 h.

4.1.2.2 Characterization

XRD measurements on Fe_3O_4 samples were performed on a p-XRD Empyrean 2 PAN analytical diffractometer with a Cu Kα (λ = 1.5418 Å) radiation source. The morphology of the f- Fe_3O_4 samples were studied using the S4800 scanning electron microscope. TEM images were obtained with FEI 300/80 Titan TEM and FEI Tecnai G (2) F30 S-Twin 300kV. TEM samples were prepared by drop cast method over coated Cu grid. To remove agglomerates, the sample was sonicated to achieve a homogeneous dispersion. CD measurements from 190 to 400 nm were recorded using JASCO spectrophotometer through single accumulation at a data interval of 0.2 nm, bandwidth of 1 nm and single accumulation. VSM measurements were conducted using a Quantum Design Physical Property Measurement System with the AC Measurement System option.

4.1.2.3 Electrochemical analysis

The electrocatalytic performance of all catalysts was analyzed by CV, LSV, and chronoamperometric test by using a CHI6372E CH instrument workstation. The electrochemical workstation is coupled with a rotating disk electrode (Pine Research) system. All the experiments were performed in a three-electrode configuration using platinum wire as a counter electrode, saturated calomel electrode (SCE) as a reference electrode, and a glassy carbon electrode having a 3 mm diameter as a working electrode. The electrolyte used was a 1 M aqueous KOH solution. All potentials reported in this work were calibrated versus the reversible hydrogen electrode (RHE) using the equation.

$$E\ (RHE) = E\ (SCE) + (0.197 + 0.059 * pH) \quad (1)$$

The electrochemical active surface area of the prepared electrocatalysts was assessed from their electrochemical capacitances estimated using CV. The currents were measured in a narrow

potential range, where no faradic processes occurred. The observed currents were predominantly due to the double layer charging, which is anticipated to have a linear correlation with the ECSA. A linear relationship was obtained by plotting the capacitive currents ($\Delta J = J_{anodic} - J_{cathodic}$) vs the scan rate and the double layer capacitance can then be assessed as half of the slope of this linear plot. The ECSA is then calculated using the following equation,

$$ECSA = \frac{C_{dl}}{C_s} \quad (2),$$

where Cs is the specific capacitance.

4.1.2.4 H_2O_2 Detection

Bulk electrolysis measurements in coulometry mode were performed using the Fe_3O_4/achiral and Fe_3O_4/chiral samples in a 0.1 M Na_2SO_4 aqueous solution (pH= 6.56) at 1.4 V. The dissolved H_2O_2 in the Na_2SO_4 electrolyte was detected through colorimetric titration, where o-tolidine was used as a redox indicator. After the reaction in the electrochemical cell, the o-tolidine indicator was added into the electrolyte solution (4 mL). These components were left to react for 60 min. From the UV–vis spectroscopy, the H_2O_2 absorption peak of the solution appeared as a faint yellow color at ~437 nm. Fe_3O_4, Fe_3O_4/chiral and R-DPDC samples were dispersed in methanol at a concentration of 1 mg/ml.

4.1.3 Results and Discussion

X-ray diffraction (XRD) spectra (Figure 4.1a, b) confirmed the inverse cubic spinal crystal struc-

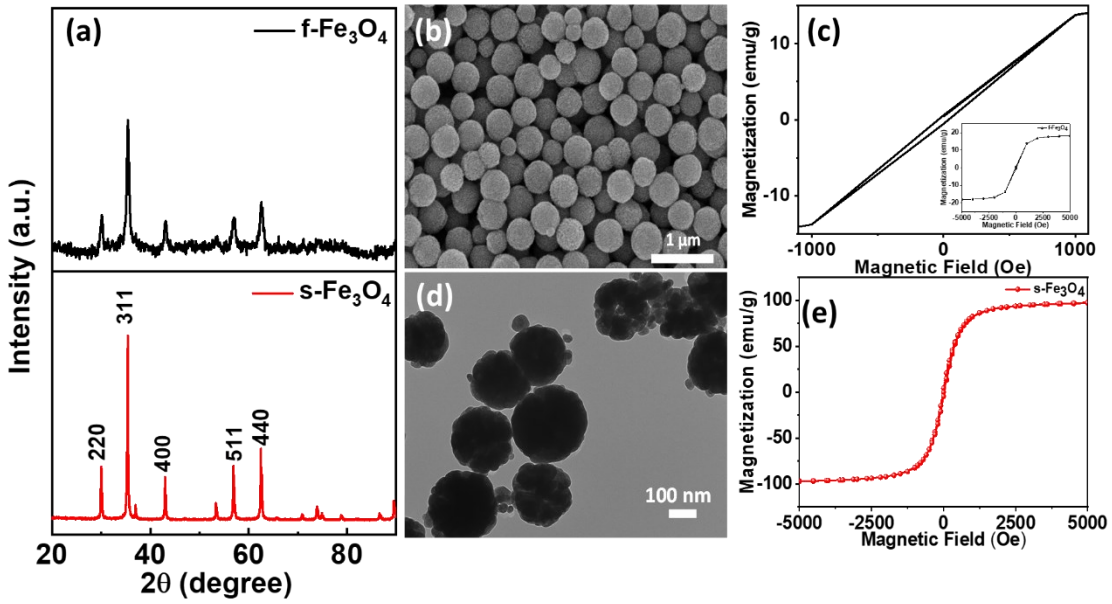

Figure 4.1: (a) XRD of f-Fe_3O_4 (top) and s-Fe_3O_4 (bottom), (b) SEM image of f-Fe_3O_4, (d) TEM image of s-Fe_3O_4, (c) VSM measurements and (d) SQUID measurements of f-Fe_3O_4 and s-Fe_3O_4, respectively.

ture of both types of nanoparticles.[250] The morphologies of the synthesized particles were analyzed

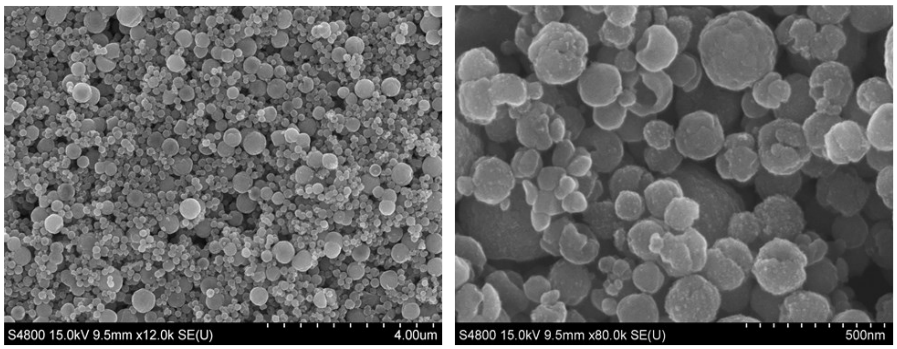

Figure 4.2: SEM images of s-Fe_3O_4 nanoparticles

using scanning electron microscopy (SEM) and transmission electron microscopy (TEM). The f-Fe_3O_4 particles appeared as well-defined spheres of ~200 nm (Figure 4.1c), whereas TEM images showed that s-Fe_3O_4 comprised aggregated smaller nanoparticles with individual sizes of less than 50 nm (corresponding SEM images in Figure 4.2 also confirm the aggregate nature of s- Fe_3O_4).

Magnetic properties were evaluated using vibrating sample magnetometry (VSM) and superconducting quantum interference device (SQUID) measurements, with s-Fe_3O_4 displaying zero rem-

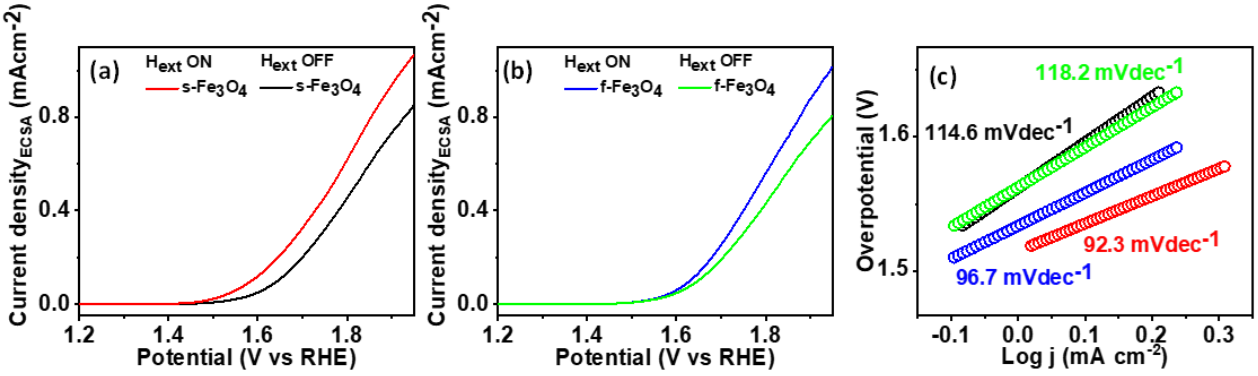

Figure 4.3: (a, b) LSV polarization curve and (c) Tafel slopes for s-Fe_3O_4 and f-Fe_3O_4

nant magnetization at room temperature and a saturation magnetization of 98 emu g^{-1} (Figure 4.1d), which is close to that of bulk magnetite (127 emu g^{-1}). The SQUID measurements along with the size of nanoparticles confirm the superparamagnetic nature. In contrast, f-Fe_3O_4 exhibited

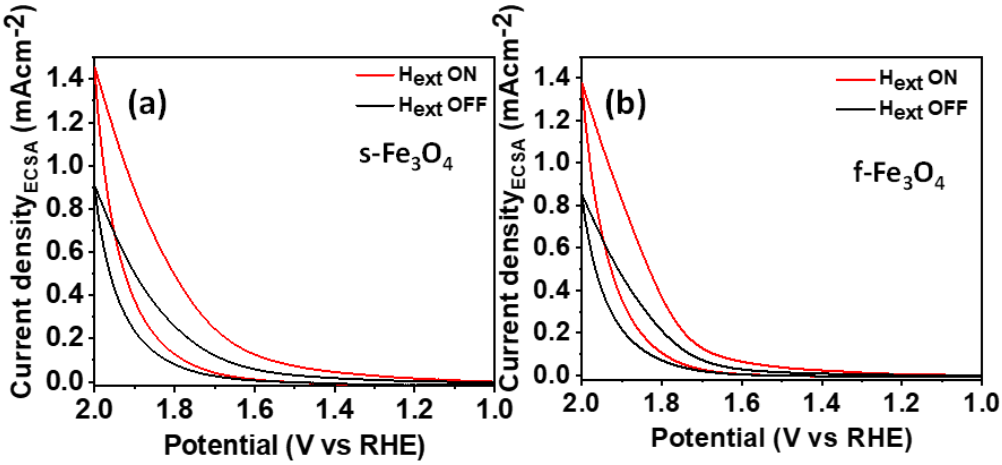

Figure 4.4: CV polarization curve for s-Fe_3O_4 and f-Fe_3O_4

ferrimagnetic behavior with a small remnant magnetization and a mean saturation magnetization of 20 emu g^{-1}.

After confirming the morphology, structure, and magnetic properties of the prepared nanoparticles, we investigated the effect of H_{ext} on their electrocatalytic OER activity using linear sweep voltammetry (LSV) polarization curves as shown in Figure 4.3 a, b. The corresponding changes in tafel slope are shown in Figure 4.3c. To avoid contributions from capacitive background and any

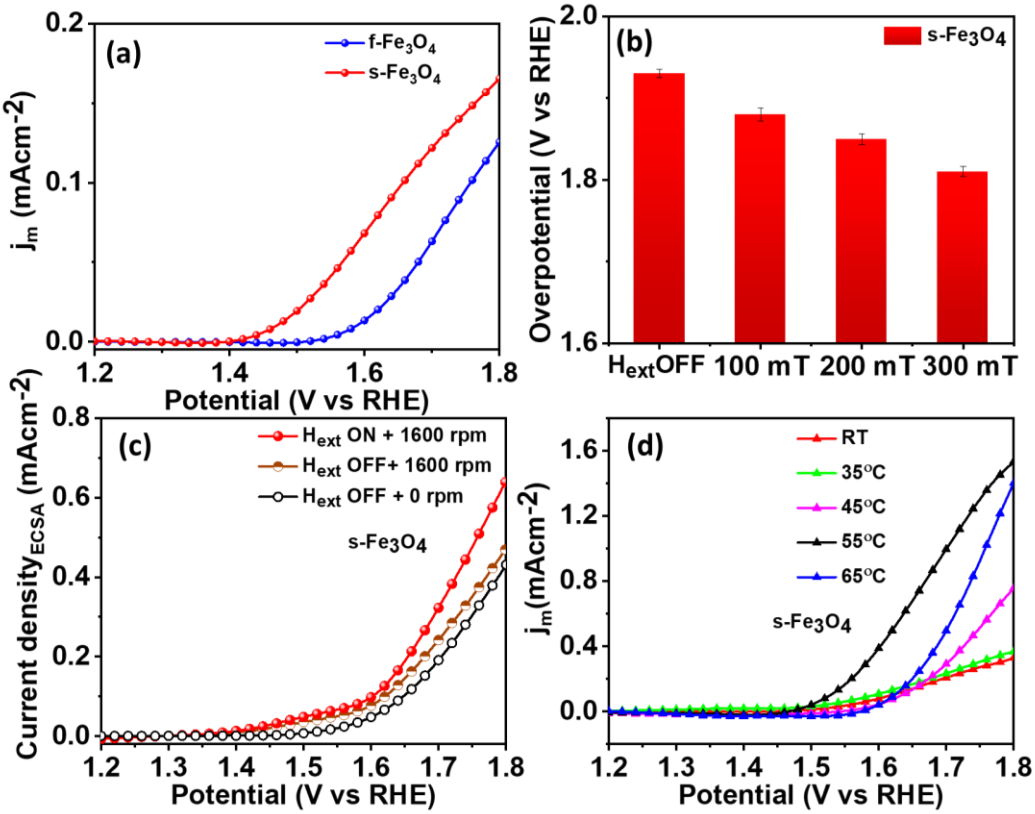

Figure 4.5: (a) Magnetocurrent density curves for OER (b) Comparison of overpotential for 0.8 $mAcm^{-2}$ at various H_{ext} strengths superparamagnetic Fe_3O_4. (c) Temperature dependence of magnetocurrent in s-Fe_3O_4. (d) stirring and H_{ext} effects in s-Fe_3O_4.

anodic oxidation to the OER current, steady-state polarization curves using cyclic voltammetry (CV) were performed (Figure 4.4). The increase in CV current validates the observed enhancement in OER under H_{ext}. To compare the activity enhancement and mitigate the impact of differences in surface area, the current densities for superparamagnetic and ferrimagnetic samples were normalized by their respective electrochemical surface areas (ECSA). Under the absence of H_{ext}, the OER activity of f-Fe_3O_4 and s-Fe_3O_4 was found to be similar, as they possess same active sites. The presence of a static H_{ext} resulted in significantly improved catalytic performance, for f-Fe_3O_4 and s-Fe_3O_4 with the highest enhancement under a magnetic field and the best activity for s-Fe_3O_4 (with the lowest onset potential of 280 mV), as indicated by the magnetocurrent densities (j_m) shown in Figure 4.5a. The Tafel slope for both the samples in the absence of H_{ext} was found to be

closer to 120 mV/decade, suggesting that the first electron transfer step is the rate-determining step (RDS). However, under the influence of a H_{ext}, the slope decreased to ~90 mV/decade for both f-Fe_3O_4 and s-Fe_3O_4, indicating that the RDS now involves a combination of the first and second electron transfer steps (Figure 4.3c). The observed enhancement is plausibly due to a ferromagnetic ordering and subsequent spin selection effect. Figure 4.5b and Figure 4.6 indicate that the overpotential of magnetic Fe_3O_4 samples decrease as the strength of the magnetic field is increased, indicating an acceleration of the OER kinetics. The direct dependence of OER overpotential on magnetic field strength is also an indication of influence of ferromagnetic ordering in OER activity. It is evident that the H_{ext}, accelerates the multi-electron transfer process of the OER on Fe_3O_4 and the effect was larger for superparamagnetic system. The magnetic field induced enhancement was also stable for up to 24h of operation (Figure 4.7).

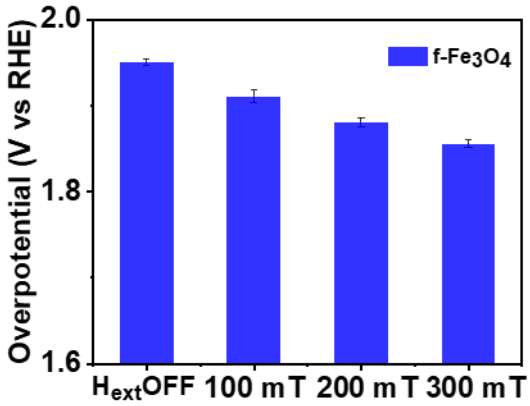

Figure 4.6: Comparison of overpotential for 0.8 $mAcm^{-2}$ at various H_{ext} strengths of f-Fe_3O_4

We conducted various control experiments to elucidate the mechanism underlying the enhanced OER activity induced by H_{ext}, identify the contribution of various indirect effects, and qualitatively measure the spin-selectivity effect. Previous research suggests that the magnetohydrodynamic (MHD) effect, arising from the Lorentz force generated under a magnetic field,

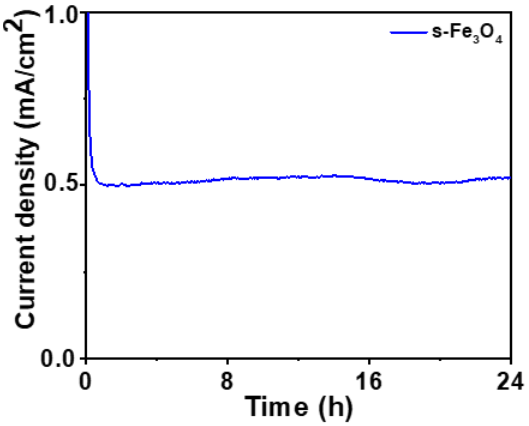

Figure 4.7: Stability of s-Fe_3O_4 at 1.8 V vs RHE under H_{ext}

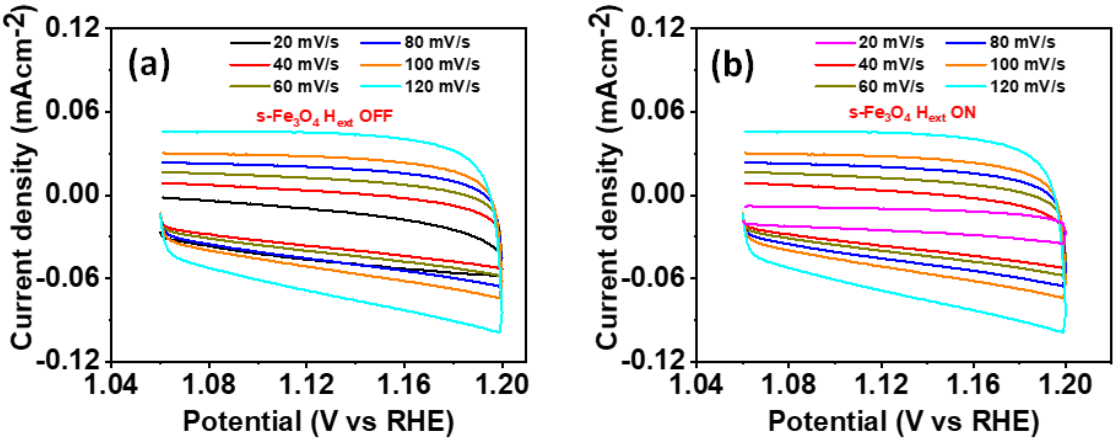

Figure 4.8: CV at various scan rates for s-Fe_3O_4 nanoparticles

creates circular movement of ionic species in the medium and a convective flow near the electrode surface, which can facilitate the faster release of O_2 bubbles, reduce the thickness of the diffusion layer, enhance mass transfer, and reduce ohmic polarization.[251, 252] The difference in the extent of decrease in overpotential observed under H_{ext} for s-Fe_3O_4 and f-Fe_3O_4 indicates that the MHD effect is not the only contributing factor to the enhanced OER performance. Additionally, the OER performance of the both s-Fe_3O_4 and f-Fe_3O_4 is promoted under the H_{ext} at various temperatures. Nonetheless, to verify the contribution of the MHD effect to the observed OER activity of s-Fe_3O_4, we used a rotating disc electrode (RDE) setup, which facilitates bubble removal through electrolyte rotation, and analyzed its OER activity (Figure 4.5c). The improvement in OER activity at 1600 rpm in RDE (without H_{ext}) is ascribed to an enhanced elimination of gas bubbles by agitation, while the subsequent increase under H_{ext} can be attributed to the spin selection effect. Additionally, the ECSA measurements were performed in the presence of H_{ext} and showed no significant changes compared to ESCA without H_{ext}, suggesting that the Maxwell stress effect has minimal contribution to the observed enhanced activity (Figure 4.8). The uniformity of the applied field strength over the entire small area of the glassy carbon electrode rules out any possible influence of the Kelvin force effect on the measurements. It is important to note that any potential impact resulting from magnetic hyperthermia can be dismissed since the localized heating occurs solely

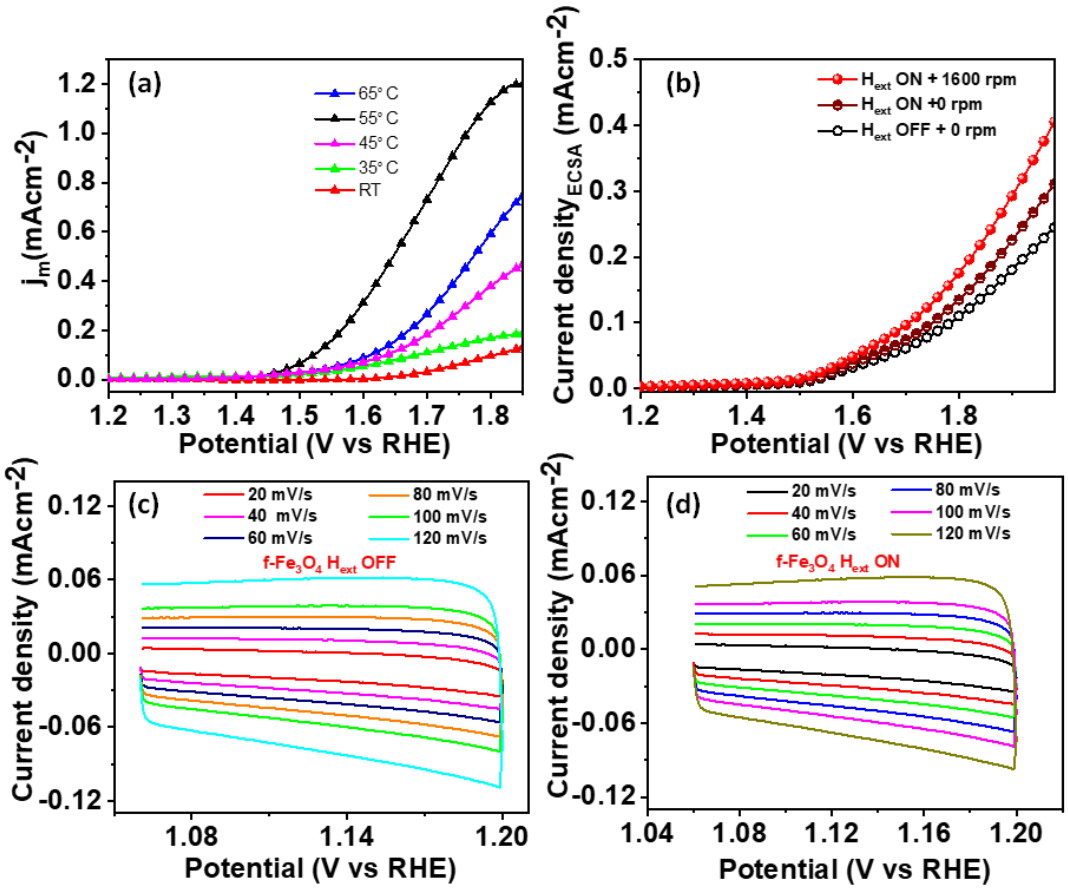

Figure 4.9: Temperature, stirring and ECSA control measurements on f-Fe_3O_4

when an external alternating magnetic field is present. Thus, we concluded that the enhanced OER activity under a magnetic field arises from the spin selectivity effect. To further support the conclusion that the enhanced OER activity under magnetic field arises from the spin selectivity effect, we investigated the magnetocurrent at various temperatures (Figure 4.5d). The results showed that the magnetocurrent decreased beyond a certain temperature, likely due to the disruption in the ferromagnetic ordering of the s-Fe_3O_4 catalysts. This temperature-dependent study reinforced the presence of spin polarization and spin selection in the s-Fe_3O_4, which enhances OER kinetics under magnetic fields. A similar effect of H_{ext} was also observed in temperature, ESCA, and stirring control measurements of f-Fe_3O_4 (Figure 4.9).

The magnetism in Fe_3O_4 arises from the arrangement of Fe cations in the crystal structure through two exchange mechanisms namely anti-ferromagnetic super-exchange interactions and double-exchange interaction (Figure 4.10a).[253, 254] The anti-ferromagnetic super-exchange interaction involves the coupling between octahedral (oct) Fe_{oct}^{3+} and tetrahedral (tet) Fe_{tet}^{3+} cations, where coupling of spin-up 5d electrons in the Fe_{oct}^{3+} with the spin-down electron in the 2p orbital of lattice O^{2-} ions, results in spin-down 5d electrons in the Fe_{tet}^{3+}e cations. Hence, the super-exchange inter-

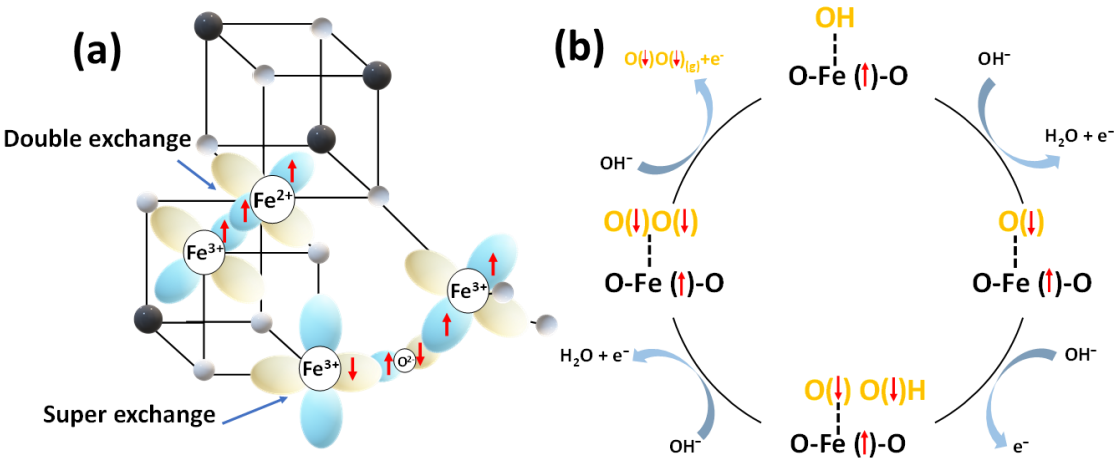

Figure 4.10: Exchange interaction and (b) mechanism of OER on Fe_3O_4

action leads to antiparallel spins between the octahedral and tetrahedral Fe cations and consequent cancellation of their spin magnetic moments. Alternatively, double-exchange interaction, where electrons from the Fe^{2+} ions can hop onto the Fe^{3+} ions, resulting in a transfer of spin angular momentum from the Fe^{2+} to the Fe^{3+} ions, leading to ferromagnetic ordering and generation of the magnetic moment in Fe_3O_4.[255] Thus, the magnetic moment (4μB) of the unit cell comes from Fe^{2+} ions.

Based on the magnetization measurements, it can be inferred that the s-Fe_3O_4 samples, with a higher magnetic moment under H_{ext}, will have a higher degree of spin polarization, which could be the reason behind their superior spin selectivity effect for OER as compared to the f-Fe_3O_4

samples.[256, 257] The superior polarization in s-Fe_3O_4 creates a lower energy spin-selective channel

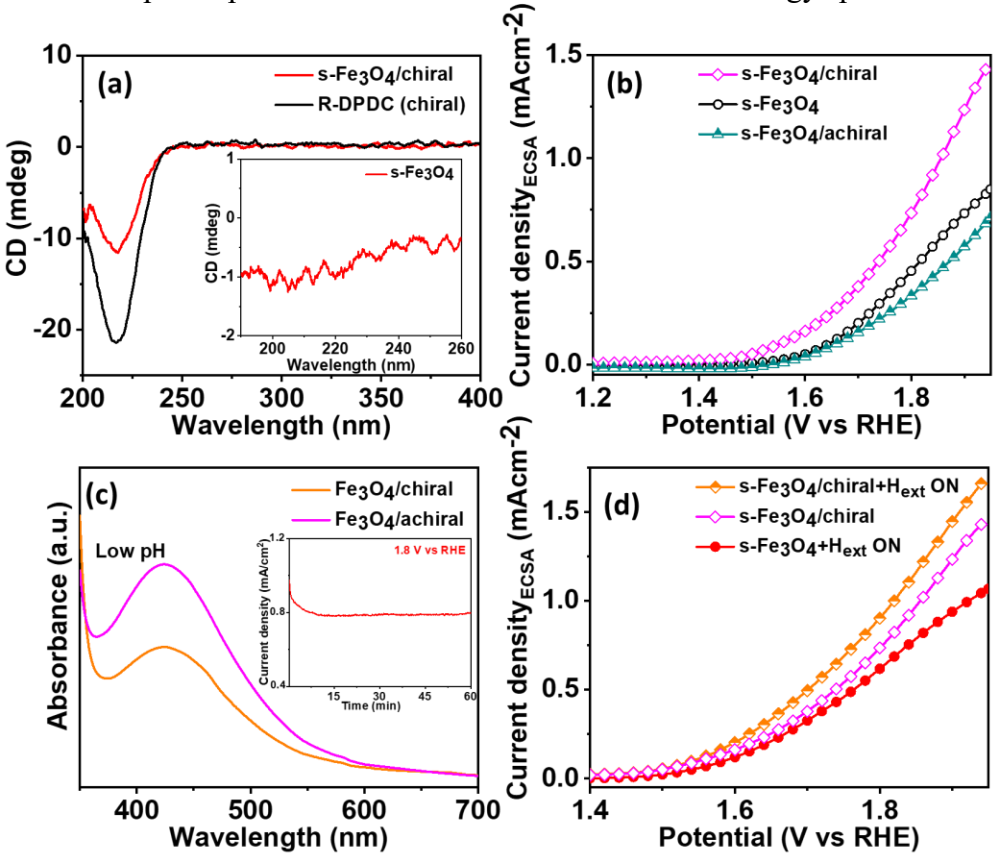

Figure 4.11: (a) CD measurements (b) LSV polarization curves (c) UV-vis absorption curves (d) LSV polarization curves for chiral Fe_3O_4 under H_{ext}

that filters the "correct" electronic spins towards the catalytic interface between the catalyst (e.g., s-Fe_3O_4) and the reaction intermediates. The spin-selective channel helps to screen specific electron spins during the triplet O_2 generation step, as shown in shown in Figure 4.10b. Under H_{ext}, the fixed spin direction at Fe active center leads to the generation of O $(\downarrow)^-$, during the first electron transfer step, due to ferromagnetic exchange between the catalyst and the adsorbed oxygen species under the principle of spin angular momentum conservation. This is followed by subsequent steps with triplet state intermediate O(↓)O(↓)H formation. As a result, the preferential creation of triplet state intermediate O(↓)O(↓)H species will favorably generate the triplet state O_2. Having established the significance of the inherent magnetic moment of s-Fe_3O_4 under H_{ext} for spin-selective OER process, we aimed to further modulate its spin-selectivity through external secondary effects.

Recently, the influence of the CISS effect on the spin of electrons at the catalyst surface and its subsequent impact on OER has been reported. Therefore, we attempted to couple the CISS-induced spin polarization with H_{ext}-induced spin polarization to obtain superior OER activity. To achieve this, s-Fe_3O_4 samples were coated with chiral (R 1, 2 diaminopropane dihydrochloride or R-DPDC) and achiral (ethylene diamine, ED) molecules with similar bonding nature as the chiral system. The chiroptical properties of R-DPDC, R-DPDC functionalized s-Fe_3O_4 (Fe_3O_4/R-DPDC)

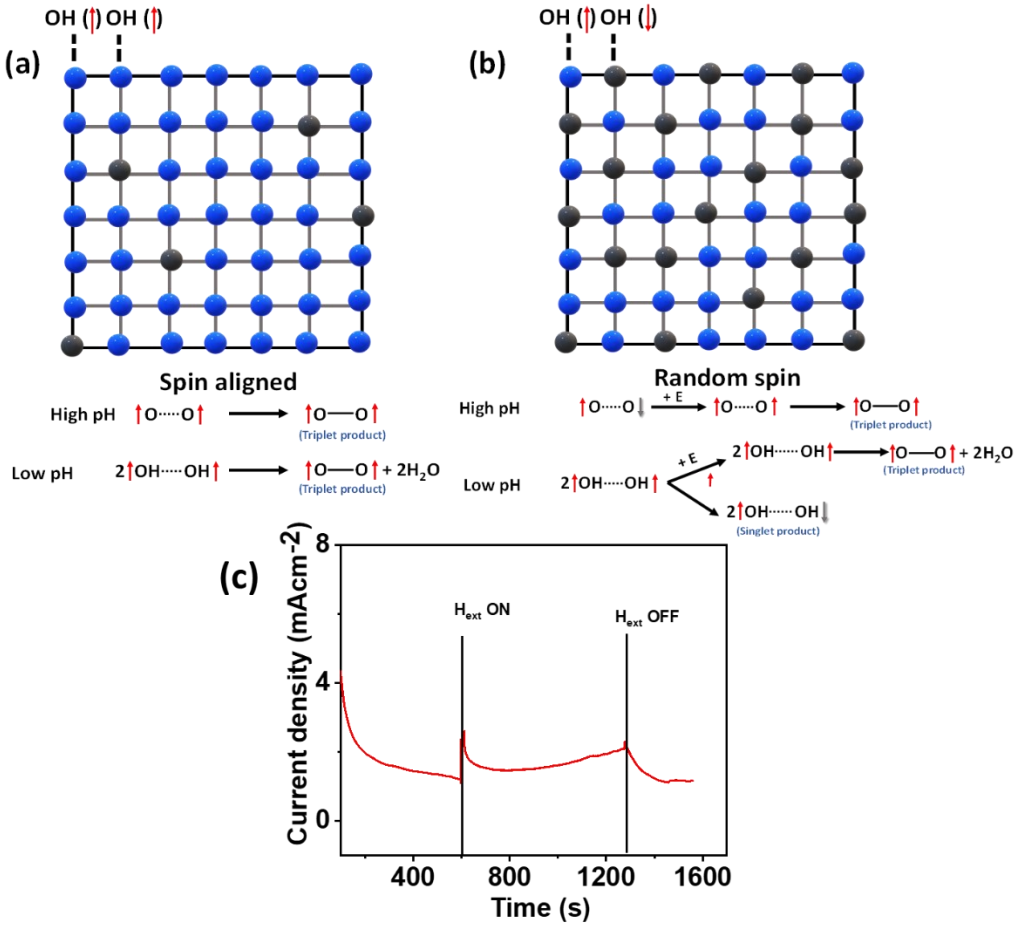

Figure 4.12: (a) schematic of spin alignment and (b) random spin orientation in the lattice (c) Chronoamperometry measurements with and without magnetic field

and ED-functionalized s-Fe_3O_4 (Fe_3O_4/achiral) solutions were studied via circular dichroism (CD) measurements. As seen in Figure 4.11a, similar features were observed for R-DPDC and Fe_3O_4/DPDC samples, but no CD signal was recorded for the spectrum of the s-Fe_3O_4/achiral

solution. Figure 4.11b shows the OER LSV polarization curves (without H_{ext}) and it is evident that the chiral system exhibits substantially higher OER activity compared to the pristine s-Fe_3O_4. Comparison of the effects of the chiral and achiral systems revealed that the enhancement in OER activity is directly related to the chirality of the molecules, rather than the ligand effects introduced by the bonding of the molecules on the catalyst surface. In contrast, a slight decrease in activity was observed in the case of s-Fe_3O_4/achiral compared to pristine s-Fe_3O_4, probably due to blocking of some active sites. Interestingly, the increase in activity for chiral system is 54% (at 1.8 V vs RHE) while it was 43% for spin selection using H_{ext} (300 mT). The results confirms that chiral molecules can play a significant role in enhancing anode currents for water splitting.

To probe the mechanism of the CISS effect, the formation of the H_2O_2 by-product was examined during water-splitting reactions on chiral and achiral s-Fe_3O_4 electrodes at low (pH 6.5) and high (pH 14) pH values (Figure 4.11c). The formation of H_2O_2 was significantly suppressed in the Fe_3O_4/chiral catalyst at low and high pH, while the achiral catalyst showed high H_2O_2 production, particularly at low pH. Based on our experimental results obtained at different pH values, we propose a mechanistic scheme to explain the observed effects. Figure 4.13 shows a model lattice representing the polarization of the electron spin of radical intermediates (with blue indicating down spin and grey indicating up spin) on a chiral (spin aligned) and achiral catalyst (random spin) surface. At high pH (pH 13), electrochemical intermediates are dominated by radical oxygen formation. For chiral catalysts at high pH, the spins at adjacent reaction sites are aligned in a parallel configuration (↑O···O↑), which favors the formation of triplet oxygen (↑O-O↑). In contrast, achiral catalysts at high pH have spins at adjacent sites on the catalyst that are mixed (both parallel (↑O···O↑) and antiparallel (↑O···O↓) configurations). At lower pH levels, both radical oxygen and hydroxyl radicals significantly contribute to the population of intermediates, which causes a shift

in the general mechanistic picture as the H_2O_2 reaction pathway becomes more competitive. For chiral catalysts with hydroxyl intermediates, spin alignment (↑HO···OH↑) favors the formation of triplet oxygen (↑O-O↑). But, for achiral catalysts, the thermodynamically favored pathway for the parallel (↑HO···OH↑) spin alignment is (↑O-O↑) O_2 formation, and for the antiparallel (↑HO···OH↓) alignment, it is H_2O_2 (↑HO-OH↓) formation. Prevailing literature support our proposed mechanism, showing that the reaction leading to molecular intermediates from a separated atom configuration (O···O) at a higher pH is thermodynamically more stable in the case of triplet species compared to singlet species.[112, 258] After understanding the potential of the CISS effect to enhance OER, we investigated the possibility of a cumulative effect by combining the CISS and H_{ext} effects on the chiral s-Fe_3O_4 system (Figure 4.11d). The combination of chirality and magnetic field exhibited a synergistic effect on the OER activity, resulting in a higher enhancement (89% for 1.8 V vs RHE) compared to the individual effects of CISS or H_{ext}. We hypothesize that the chirality and magnetic field contribute two distinct spin-dependent potentials that act in conjunction, increasing both spin polarization and spin selectivity and leading to a significant increase in overall OER activity. Figure 4.12 c shows the chronoamperometry measurements performed using f-Fe_3O_4 with and without magnetic field. The faster response of the OER current to the magnetic field shows the possibility of investigating these systems as sensors.

4.1.4 Conclusions

In summary, the effect of magnetic moment on magnetic field assisted OER activity has been investigated with superparamagnetic and ferrimagnetic Fe_3O_4 catalysts. The increase of spatial spin polarization shows a positive correlation with the magnetic moment and observed enhancement of spin selection during OER. The spin-polarized electron exchange between the ferrimagnetic and superparamagnetic Fe_3O_4 and the adsorbed oxygen species facilitated by quantum

exchange interactions under the principle of spin angular momentum conservation, leads to faster reaction kinetics. This work provides novel perspectives for the design and synthesis of magnetic catalytic materials and opens up new avenues for external magnetic field enhanced electrocatalysis.

4.2 Chiral induced spin selectivity effect in Ni nanoparticles/MXene hetero-structure for superior oxygen evolution reaction

4.2.1 Introduction

Recently, it was reported that electron transport through a chiral molecule induces a spin polarization without external magnetic fields.[259, 260] The chiral organic molecules can act as spin filters that transmit electrons into preferential spin orientations, consequently influencing the reaction pathway and enhancing the reaction kinetics. CISS effect also has the potential to boost electron spin-dependent catalytic reactions beyond the common volcano-plot limits governed by the Sabatier principle.[261] Therefore, it provides a unique opportunity to improve the activity and selectivity of the OER by facilitating triplet oxygen production. Recent scientific literature shows that the CISS effect, which relates to the spin-polarization induced by the chiral molecule, is always observed when the molecule is attached to one or more electrodes that have substantial SOC.[262, 263] In the context of electrocatalysis, directly attaching chiral molecules onto the catalyst can lead to the blocking of active sites to some extent. Additionally, transport experiments have shown that spin polarization can occur over large length scales of up to 100 nanometers to microns.[264] Therefore, it is ideal to use a substrate with high SOC to anchor chiral molecules, which can enhance the activity of the catalyst that is located on top of the substrate.

MXenes are a recently discovered family of 2D transition metal carbonitrides obtained through selective chemical etching of MAX phases, $M_{n+1}AX_n$ (n = 1-3), where M, A, and X are a transition metal, a group 13-14 element, and C or N, respectively. These materials exhibit exceptional mechanical strength, high conductivity, and hydrophilic surfaces containing abundant functional groups that can be modified and processed in solution.[265] In 2011, Gogotsi and his team reported

the first synthesis of $Ti_3C_2T_x$ MXene by etching the MAX phase Ti_3AlC_2 with HF at room temperature, which so far remains the most common synthesis method.[266] MXenes have been proposed as promising candidates for topological insulators due to their large SOC and the presence of a Dirac-like band at the Fermi energy. The excellent properties of MXenes make them a suitable substrate for attaching chiral molecules and observing significant spin polarization effects. In this study, $Ti_3C_2T_x$ with excellent conductivity and high spin orbit coupling was investigated as a substrate to anchor chiral molecules. The electron transfer from Ni/MXene@chiral heterostructure electrodes to OER intermediates is enhanced over that from achiral electrodes. The effect results from the spin selectivity conferred on the electron current by the chiral induced spin selectivity effect.

4.2.2 Materials and Methods

4.2.2.1 Synthesis of MXene and MXene/Ni nps heterostructure

$Ti_3C_2T_x$ MXene was synthesized from MAX phase Ti_3AlC_2 powder using a hydrofluoric acid (HF) (purchased from Acros-Organics) etching process reported previously.[267] Briefly, 0.5 g of Ti_3AlC_2 powder was etched in 10 mL of HF (48%) for 8 h. Following the etching step, the etched solution was washed several times until the pH of the solution reached between 6 and 7, vacuum filtered using a 0.5 μm filter paper, and vacuum annealed at 80 °C to obtain the $Ti_3C_2T_x$ MXene powder. Nanosheets of MXenes were obtained by DMSO intercalation into MXene powder samples followed by sonication in an Ar atmosphere.

In order to anchor chiral molecules to MXene surface, the hydroxyl groups were replaced with carboxylic acid groups using a reported procedure.[268] The COOH–$Ti_3C_2T_x$ was prepared by the addition of 1.7 g chloroacetic acid to a 1 mg/mL delaminated $Ti_3C_2T_x$ solution at 0 °C and stirred

for 2 h to convert OH groups on the surface into carboxyl groups. The mixture was then neutralized with an abundant amount of distilled water to obtain a pH value of ~5.5 for the supernatant. Further, covalent coupling reaction of 1-ethyl-3-(3-dimethylaminopropyl) carbodiimide hydrochloride (EDC) and N-hydroxy succinimide (NHS) with amine functional groups was utilized to anchor chiral (R-diaminopropane dihydrochloride) and achiral (ethylene diamine) on to the MXene substrate.

To fabricate the heterostructure, nanosheets of MXene anchored with chiral molecules in DMSO were mixed with Nickel nanoparticles (purchased from sigma aldrich) in a specific ratio and were sonicated for 20 minutes to form vdW heterostructures. The resultant solution was centrifuged to remove unanchored chiral particles and the powder was dried over night at 50 °C for further use.

4.2.2.2 Electrochemical characterization

Refer to section 4.1.2.3

4.2.2.3 H_2O_2 Detection

Bulk electrolysis measurements in coulometry mode were performed using the Ni/MXene@achiral and the Ni/MXene@chiral samples in a 0.1 M Na_2SO_4 aqueous solution (pH= 6.56) at 1.4 V. The dissolved H_2O_2 in the electrolyte was detected through colorimetric titration, where o-tolidine was used as a redox indicator. After the reaction in the electrochemical cell, the o-tolidine indicator was added into the electrolyte solution. From the UV–vis spectroscopy, the H_2O_2 absorption peak of the solution appeared as a faint yellow color at ~437 nm.

4.2.3 Results and Discussion

The Nickel nanoparticles were characterized using XRD and revealed the presence of metallic Nickel phase (Figure 4.13a). The corresponding SEM measurements shows the nanoparticles are less than 100 nm in size (Figure 4.13b). The synthesis and characterization of MXene from MAX phase is discussed in Chapter 3 section 3.2. The SEM images of the resulting Ni nanoparticles decorated MXene sheets (Ni/MXene) structure are displayed in Figure 4.14a and b. The corresponding EDS spectra and elemental mapping confirmed the presence of Ni, Ti, C and O atoms in the structure (Figure 4.14c). The sample was also characterized using XRD which revealed the peaks of metallic Ni and MXene (Figure 4.14d).

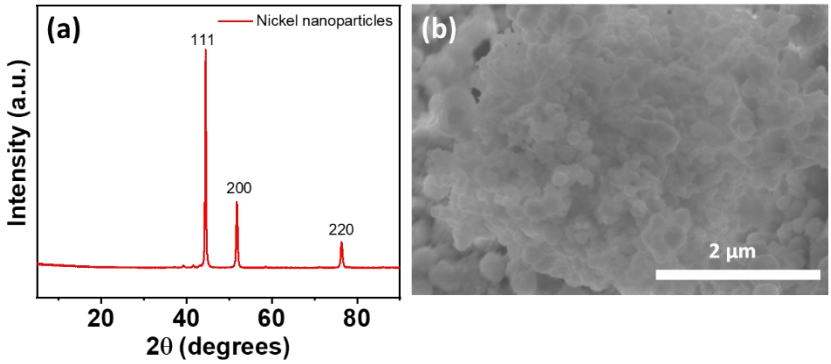

Figure 4.13: (a) XRD and (b) SEM of Ni nanoparticles

The electrocatalytic OER activity of Ni/MXene heterostructure was initially investigated using LSV polarization curves, as depicted in Figure 4.15a. The heterostructure exhibited an improved current density of 20 $mAcm^{-2}$ at a potential of 520 mV, with an onset potential of 320 mV. Tafel slopes were calculated and found to be 96 $mVdec^{-1}$, and 113 $mVdec^{-1}$ for Ni/MXene heterostructure and Ni nanoparticles, respectively. The smaller Tafel slope, coupled with the higher current density, confirmed the superiority of the heterostructure over the individual counterparts for OER. To elucidate the reason behind the observed improved activity, we conducted electrochemical

impedance measurements, as illustrated in Figure 4.15b, c. Our results clearly indicate that the Ni/MXene heterostructure displays a lower charge transfer resistance when compared to Ni nano-particles alone suggesting an increase in conductivity due to the incorporation of MXene, thereby contributing to the enhanced OER activity observed in the heterostructure.

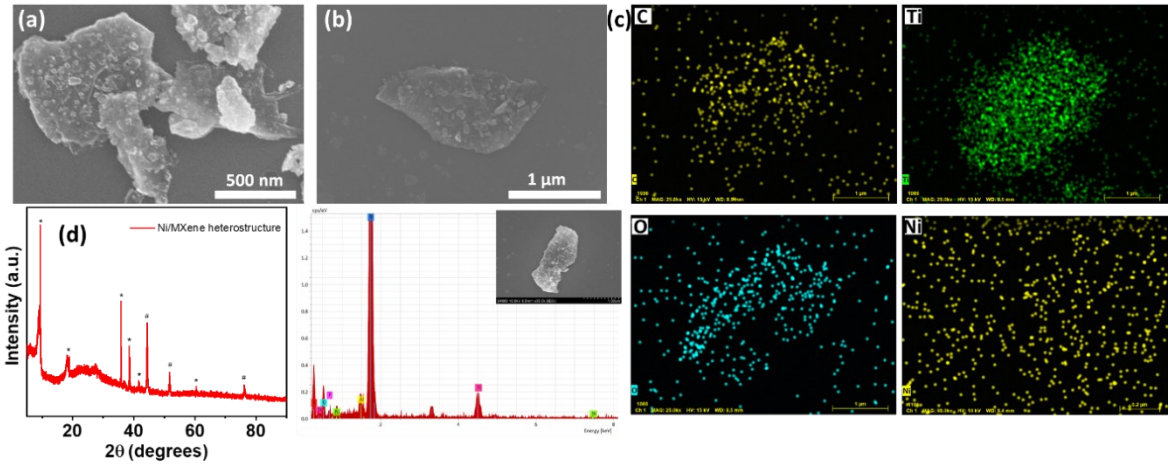

Figure 4.14: (a, b) SEM images of Ni nanoparticles decorated MXene sheets (c) EDS elemental mapping (d) XRD spectra of Ni/MXene

In order to investigate the influence of CISS effect and improve the activity of Ni/MXene, chiral molecule (R-diaminopropane dihydrochloride) was anchored using EDC-NHS coupling on -COOH functionalized MXene sheets. The anchoring of chiral molecule was confirmed using the FT-IR measurements as shown in Figure 4.16a. Further, the chiral molecule anchored Ni/MXene heterostructure (Ni/MXene@chiral) was investigated for its activity towards OER catalysis.

Figure 4.17a shows the LSV curves and it is evident that the Ni/MXene@chiral has substantially higher OER activity compared to the Ni/MXene heterostructure. In order to confirm the enhancement is not due to any local chemical environment changes, we anchored an achiral molecule (ethylene diamine) with similar bonding nature as chiral molecule on MXene. By comparing the

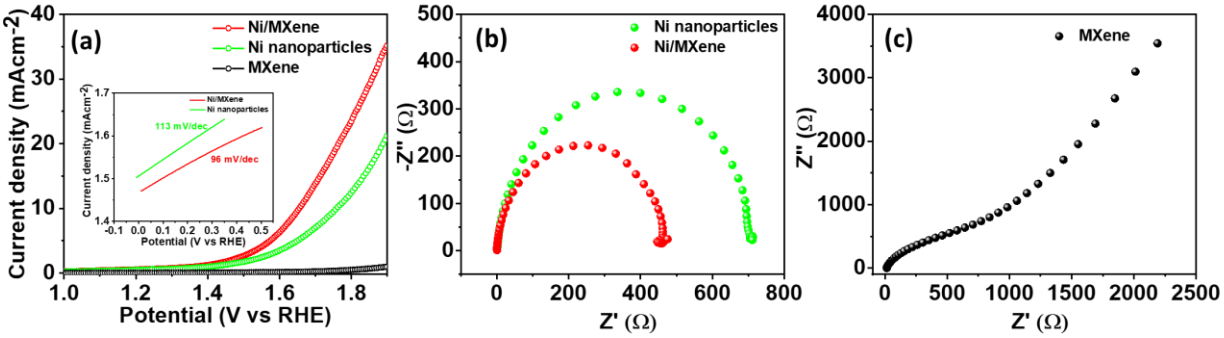

Figure 4.15: (a) LSV polarization curve, inset showing the tafel plots (b, c) Impedance measurements.

effect of chiral and the achiral systems, it is evident that OER activity enhancement is directly related to the chirality of the molecules, rather than ligand effects introduced by the bonding of the molecules on the catalyst surface. The Ni/MXene@chiral showed an onset potential of 300 mV and overpotential of 430 mV for getting 20 $mAcm^{-2}$. In fact, the increase in activity for chiral system is 61% (at 1.8 V vs RHE) compared to pristine heterostructure. These results provide strong

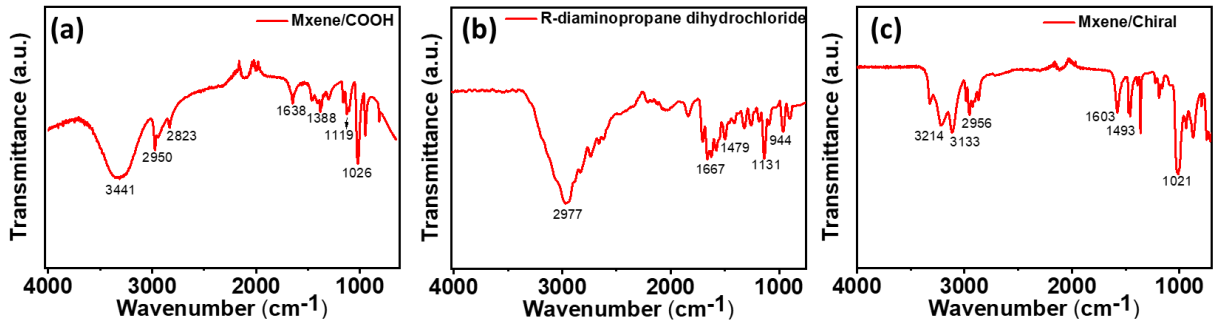

Figure 4.16: (a-c) FT-IR measurements

evidence that chiral molecules play a significant role in enhancing anode currents for water splitting. Based on the spin-selective nature of electrons, it is expected that there would be no

discernible difference in the CISS effect of R or S enantiomers. This is attributed to the fact that, in both scenarios, electron transfer is subject to spin-selectivity, with the principal limitation being the correlation of spin alignment between the electrons, rather than the specific direction of the

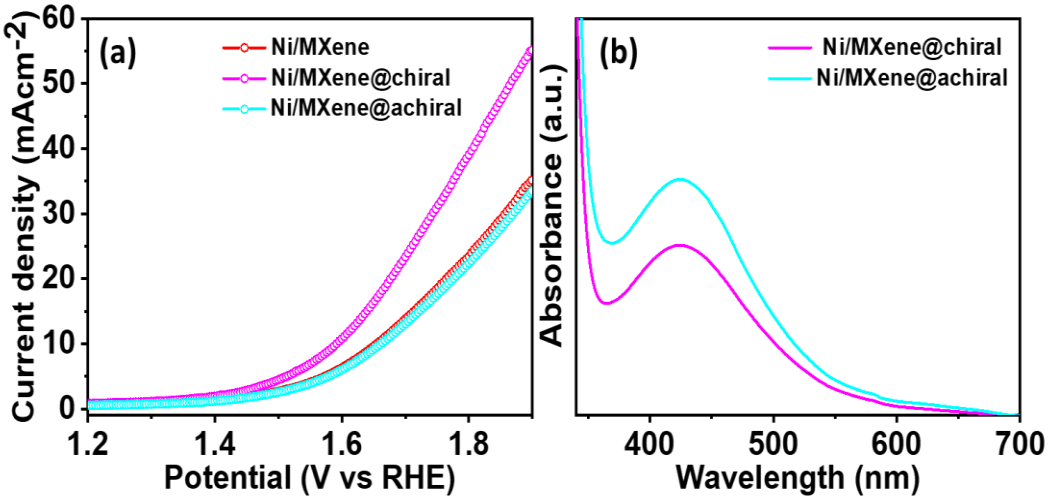

Figure 4.17: (a) LSV polarization curve (b) UV-Vis measurements

spins. To study the role of chirality, more specifically the chirality-induced spin alignment of radical intermediates for inhibiting hydrogen peroxide formation, electrochemical experiments were performed in which 1.5 V vs RHE was applied to Ni/MXene@chiral for 1h in a 0.1 M Na_2SO_4 solution at pH = 6.5. Following the reaction, a spectrophotometric redox indicator, o-tolidine, was added to the solution and the absorbance was measured. Figure 4.17b shows the change in the absorption of o-tolidine and hence the amount of hydrogen peroxide production when the water splitting reaction is performed using Ni/MXene@chiral and Ni/MXene@achiral electrocatalysts. Integrating the absorbance peaks of these data indicates that the Ni/MXene@achiral produces a higher amount of hydrogen peroxide compared to Ni/MXene@chiral.

4.2.4 Conclusions

In this study, we have examined the impact of chiral molecular functionalization on the OER at Ni/MXene chiral electrodes. Our findings demonstrate that the chirality of the electrode plays a

significant role in enhancing the activity of OER catalysts, which are currently considered state-of-the-art. This enhancement is attributed to the electron spin polarization at the interface of the chiral molecule and MXene substrate. The strong SOC of the system results in a large and extensive spin polarization even at Nickel active sites, which is responsible for the observed improvement in catalytic activity.

Chapter 5

Conclusions

The thesis presented a comprehensive investigation into the impact of tailoring charge and spin in materials for electrocatalysis and sensing applications. The primary objective of the research was to devise innovative strategies for enhancing the electronic, physical, and chemical properties of materials through the manipulation of their charge and spin states. Through this research, we demonstrated the effectiveness of several approaches for modulating the electronic charge distribution in materials, such as doping, heterostructure formation, and lattice strain.

In Chapter 2, investigated the effectiveness of heteroatom doping in materials to tune charge distribution and hence the resultant impact on sensing and electrocatalytic properties. Doping was conducted on a nanomaterial (GQD) and bulk material system (Ga_2O_3). Our research proved that external doping by heteroatoms in GQDs can effectively modify the band structure, resulting in tunable quantum efficiency and superior limit of detection for Hg^{2+} ions. Moreover, we employed a doping strategy using Sn atoms to enhance the bifunctional OER and ORR activity of gallium oxide electrocatalysts, leading to improved performance in Zn-air battery applications. These findings underscore the effectiveness of doping as a strategy to tailor the charge properties of nanostructured materials, including low-dimensional materials.

In Chapter 3, we focused on the formation of heterostructures between various dimensional nanomaterials to improve their properties at the interface and exploit them for applications such as renewable H_2 production though HER and pollutant detection through SERS. Notably, the heterostructure approach significantly enhanced the HER activity in GNR/MoS_2 based LDMs compared to the enhancement in Ga_2O_3, emphasizing the profound impact of such strategies in modulating

the electronic properties of LDMs. The research also illustrated the superiority of graphene and MXene-based LDMs for catalysis and sensing applications.

Chapter 4 delves into the importance of spin modulation in materials, specifically for spin dependent OER. Magnetic interactions and spin-orbit coupling play a pivotal role in reaction mechanisms by altering spin multiplicity and enabling transitions between forbidden and spin-allowed reaction pathways. These effects form the theoretical underpinnings behind the methodologies of the CISS effect and external magnetic field application. In this chapter, we investigated the impact of an external magnetic field on enhancing OER activity in superparamagnetic and ferrimagnetic systems. This exploration led to a deeper understanding of the significance of exchange interactions and dipole moment in magnetic materials. Building on this knowledge, we extended the concept of external magnetic field induced OER activity to highly intrinsically active Ni nanoparticle/MXene heterostructure systems. Furthermore, we augmented the CISS effect in these systems by employing high spin-orbit coupling (SOC) materials such as MXene. The synergistic effect of LDM-based catalysts, high SOC substrates, and ferromagnetic Ni nanoparticles led to exceptional activity and enhancement in OER performance. By examining the role of spin modulation and its influence on OER activity, Chapter 4 contributes to the development of advanced materials and a deeper understanding of spin-dependent effects in catalytic systems. This knowledge is vital for designing next-generation catalysts with improved performance, ultimately driving advancements in renewable energy production and sustainable technologies.

In summary, the present thesis has made substantial contributions to the fields of electrocatalysis and sensing by providing an in-depth understanding of the impact of charge and spin manipulation in materials for these applications. The research offers valuable insights and promotes the development of advanced materials for a diverse range of applications. The strategies and findings

presented herein hold the potential to significantly impact the fields of electrocatalysis and sensing, ultimately fostering a more sustainable and technologically advanced future. In particular, the insights gleaned from this research will prove invaluable in developing novel materials and strategies for enhancing the performance of electrocatalysts across various applications, including energy-relevant reactions such as HER, OER, and ORR, as well as advanced sensing strategies based on PL and SERS for detecting environmental pollutants. It is our hope that this work will inspire further research in this area and contribute to a sustainable future powered by renewable energy technologies and bolstered by the enhanced security provided by ultrasensitive sensors.

References

1. Neto, A. C.; Guinea, F.; Peres, N. M.; Novoselov, K. S.; Geim, A. K., The electronic properties of graphene. *Reviews of modern physics* **2009,** *81* (1), 109.
2. Zhan, B.; Li, C.; Yang, J.; Jenkins, G.; Huang, W.; Dong, X., Graphene field-effect transistor and its application for electronic sensing. *Small* **2014,** *10* (20), 4042-4065.
3. Yin, Z.; Zhu, J.; He, Q.; Cao, X.; Tan, C.; Chen, H.; Yan, Q.; Zhang, H., Graphene-based materials for solar cell applications. *Advanced energy materials* **2014,** *4* (1), 1300574.
4. Pumera, M., Graphene in biosensing. *Materials today* **2011,** *14* (7-8), 308-315.
5. Yang, Z.; Zhang, J.; Kintner-Meyer, M. C.; Lu, X.; Choi, D.; Lemmon, J. P.; Liu, J., Electrochemical energy storage for green grid. *Chemical reviews* **2011,** *111* (5), 3577-3613.
6. Greeley, J.; Markovic, N. M., The road from animal electricity to green energy: combining experiment and theory in electrocatalysis. *Energy & Environmental Science* **2012,** *5* (11), 9246-9256.
7. Zeradjanin, A. R.; Grote, J. P.; Polymeros, G.; Mayrhofer, K. J., A critical review on hydrogen evolution electrocatalysis: Re-exploring the volcano-relationship. *Electroanalysis* **2016,** *28* (10), 2256-2269.
8. Sharma, V.; Tiwari, P.; Mobin, S. M., Sustainable carbon-dots: recent advances in green carbon dots for sensing and bioimaging. *Journal of Materials Chemistry B* **2017,** *5* (45), 8904-8924.
9. Li, M.; Chen, T.; Gooding, J. J.; Liu, J., Review of carbon and graphene quantum dots for sensing. *ACS sensors* **2019,** *4* (7), 1732-1748.
10. Perumal, J.; Wang, Y.; Attia, A. B. E.; Dinish, U.; Olivo, M., Towards a point-of-care SERS sensor for biomedical and agri-food analysis applications: A review of recent advancements. *Nanoscale* **2021,** *13* (2), 553-580.
11. Schuler, B.; Lee, J.-H.; Kastl, C.; Cochrane, K. A.; Chen, C. T.; Refaely-Abramson, S.; Yuan, S.; van Veen, E.; Roldán, R.; Borys, N. J., How substitutional point defects in two-dimensional WS2 induce charge localization, spin–orbit splitting, and strain. *ACS nano* **2019,** *13* (9), 10520-10534.
12. Chen, A.; Su, Q.; Han, H.; Enriquez, E.; Jia, Q., Metal oxide nanocomposites: a perspective from strain, defect, and interface. *Advanced Materials* **2019,** *31* (4), 1803241.
13. Beyerlein, K. R.; Snyder, R. L.; Li, M.; Scardi, P., Simulation and modeling of nanoparticle surface strain. *Journal of Nanoscience and Nanotechnology* **2012,** *12* (11), 8554-8560.
14. Alinezhad, A.; Gloag, L.; Benedetti, T. M.; Cheong, S.; Webster, R. F.; Roelsgaard, M.; Iversen, B. B.; Schuhmann, W.; Gooding, J. J.; Tilley, R. D., Direct growth of highly strained Pt islands on branched Ni nanoparticles for improved hydrogen evolution reaction activity. *Journal of the American Chemical Society* **2019,** *141* (41), 16202-16207.
15. Wang, H.; Xu, S.; Tsai, C.; Li, Y.; Liu, C.; Zhao, J.; Liu, Y.; Yuan, H.; Abild-Pedersen, F.; Prinz, F. B., Direct and continuous strain control of catalysts with tunable battery electrode materials. *Science* **2016,** *354* (6315), 1031-1036.
16. Williams, B. P.; Young, A. P.; Andoni, I.; Han, Y.; Lo, W. S.; Golden, M.; Yang, J.; Lyu, L. M.; Kuo, C. H.; Evans, J. W., Strain-Enhanced Metallic Intermixing in Shape-Controlled Multilayered Core–Shell Nanostructures: Toward Shaped Intermetallics. *Angewandte Chemie International Edition* **2020,** *59* (26), 10574-10580.

17. Wang, Y.; Li, X.; Zhang, M.; Zhou, Y.; Rao, D.; Zhong, C.; Zhang, J.; Han, X.; Hu, W.; Zhang, Y., Lattice-Strain Engineering of Homogeneous NiS0. 5Se0. 5 Core–Shell Nanostructure as a Highly Efficient and Robust Electrocatalyst for Overall Water Splitting. *Advanced Materials* **2020,** *32* (40), 2000231.
18. Li, Z.; Lv, Y.; Ren, L.; Li, J.; Kong, L.; Zeng, Y.; Tao, Q.; Wu, R.; Ma, H.; Zhao, B., Efficient strain modulation of 2D materials via polymer encapsulation. *Nature communications* **2020,** *11* (1), 1-8.
19. Aslan, B.; Datye, I. M.; Mleczko, M. J.; Sze Cheung, K.; Krylyuk, S.; Bruma, A.; Kalish, I.; Davydov, A. V.; Pop, E.; Heinz, T. F., Probing the optical properties and strain-tuning of ultrathin Mo1–x W x Te2. *Nano letters* **2018,** *18* (4), 2485-2491.
20. Wu, Y.; Nan, P.; Chen, Z.; Zeng, Z.; Liu, R.; Dong, H.; Xie, L.; Xiao, Y.; Chen, Z.; Gu, H., Thermoelectric enhancements in PbTe alloys due to dislocation-induced strains and converged bands. *Advanced Science* **2020,** *7* (12), 1902628.
21. Chen, S.; Oh, H. S.; Gludovatz, B.; Kim, S. J.; Park, E. S.; Zhang, Z.; Ritchie, R. O.; Yu, Q., Real-time observations of TRIP-induced ultrahigh strain hardening in a dual-phase CrMnFeCoNi high-entropy alloy. *Nature communications* **2020,** *11* (1), 1-8.
22. Tan, Y.; Liu, P.; Chen, L.; Cong, W.; Ito, Y.; Han, J.; Guo, X.; Tang, Z.; Fujita, T.; Hirata, A., Monolayer MoS2 films supported by 3D nanoporous metals for high-efficiency electrocatalytic hydrogen production. *Advanced Materials* **2014,** *26* (47), 8023-8028.
23. Xia, Z.; Guo, S., Strain engineering of metal-based nanomaterials for energy electrocatalysis. *Chemical Society Reviews* **2019,** *48* (12), 3265-3278.
24. Mavrikakis, M.; Hammer, B.; Nørskov, J. K., Effect of strain on the reactivity of metal surfaces. *Physical Review Letters* **1998,** *81* (13), 2819.
25. Shao, Q.; Wang, P.; Zhu, T.; Huang, X., Low dimensional platinum-based bimetallic nanostructures for advanced catalysis. *Accounts of Chemical Research* **2019,** *52* (12), 3384-3396.
26. Zhang, J.; Yin, S.; Yin, H.-M., Strain engineering to enhance the oxidation reduction reaction performance of atomic-layer pt on nanoporous gold. *ACS Applied Energy Materials* **2020,** *3* (12), 11956-11963.
27. Schnur, S.; Groß, A., Strain and coordination effects in the adsorption properties of early transition metals: A density-functional theory study. *Physical Review B* **2010,** *81* (3), 033402.
28. Luo, M.; Guo, S., Strain-controlled electrocatalysis on multimetallic nanomaterials. *Nature Reviews Materials* **2017,** *2* (11), 1-13.
29. Liu, F.; Shi, C.; Guo, X.; He, Z.; Pan, L.; Huang, Z. F.; Zhang, X.; Zou, J. J., Rational Design of Better Hydrogen Evolution Electrocatalysts for Water Splitting: A Review. *Advanced Science* **2022**, 2200307.
30. You, B.; Tang, M. T.; Tsai, C.; Abild-Pedersen, F.; Zheng, X.; Li, H., Enhancing electrocatalytic water splitting by strain engineering. *Advanced Materials* **2019,** *31* (17), 1807001.
31. Chang, C.-H.; Fan, X.; Lin, S.-H.; Kuo, J.-L., Orbital analysis of electronic structure and phonon dispersion in MoS 2, MoSe 2, WS 2, and WSe 2 monolayers under strain. *Physical Review B* **2013,** *88* (19), 195420.
32. Johari, P.; Shenoy, V. B., Tuning the electronic properties of semiconducting transition metal dichalcogenides by applying mechanical strains. *ACS nano* **2012,** *6* (6), 5449-5456.
33. He, K.; Poole, C.; Mak, K. F.; Shan, J., Experimental demonstration of continuous electronic structure tuning via strain in atomically thin MoS2. *Nano letters* **2013,** *13* (6), 2931-2936.

34. Wang, Y.; Cong, C.; Yang, W.; Shang, J.; Peimyoo, N.; Chen, Y.; Kang, J.; Wang, J.; Huang, W.; Yu, T., Strain-induced direct–indirect bandgap transition and phonon modulation in monolayer WS2. *Nano Research* **2015,** *8* (8), 2562-2572.
35. Niu, T.; Meng, Q.; Zhou, D.; Si, N.; Zhai, S.; Hao, X.; Zhou, M.; Fuchs, H., Large-scale synthesis of strain-tunable semiconducting antimonene on copper oxide. *Advanced Materials* **2020,** *32* (4), 1906873.
36. Li, Y.; Yang, S.; Li, J., Modulation of the electronic properties of ultrathin black phosphorus by strain and electrical field. *The Journal of Physical Chemistry C* **2014,** *118* (41), 23970-23976.
37. Pető, J.; Dobrik, G.; Kukucska, G.; Vancsó, P.; Koós, A. A.; Koltai, J.; Nemes-Incze, P.; Hwang, C.; Tapasztó, L., Moderate strain induced indirect bandgap and conduction electrons in MoS2 single layers. *npj 2D Materials and Applications* **2019,** *3* (1), 1-6.
38. Shi, J.; Huan, Y.; Xiao, M.; Hong, M.; Zhao, X.; Gao, Y.; Cui, F.; Yang, P.; Pennycook, S. J.; Zhao, J., Two-dimensional metallic NiTe2 with ultrahigh environmental stability, conductivity, and electrocatalytic activity. *ACS nano* **2020,** *14* (7), 9011-9020.
39. Ma, N.; Li, N.; Wang, T.; Ma, X.; Fan, J., Strain engineering in the oxygen reduction reaction and oxygen evolution reaction catalyzed by Pt-doped Ti 2 CF 2. *Journal of Materials Chemistry A* **2022,** *10* (3), 1390-1401.
40. Chen, X.; Wang, G., Tuning the hydrogen evolution activity of MS 2 (M= Mo or Nb) monolayers by strain engineering. *Physical Chemistry Chemical Physics* **2016,** *18* (14), 9388-9395.
41. Wang, X.; Wu, H.; Xi, S.; Lee, W.; Zhang, J.; Wu, Z.; Wang, J.; Hu, T.; Liu, L.; Han, Y., Strain stabilized nickel hydroxide nanoribbons for efficient water splitting. *Energy & Environmental Science* **2020,** *13* (1), 229-237.
42. Nair, A. N.; Sanad, M. F.; Chava, V. S.; Sreenivasan, S. T., Platinum-like HER onset in a GNR/MoS 2 quantum dot heterostructure through curvature-dependent electron density reconfiguration. *Chemical Communications* **2022,** *58* (74), 10368-10371.
43. Ling, T.; Yan, D.-Y.; Wang, H.; Jiao, Y.; Hu, Z.; Zheng, Y.; Zheng, L.; Mao, J.; Liu, H.; Du, X.-W., Activating cobalt (II) oxide nanorods for efficient electrocatalysis by strain engineering. *Nature communications* **2017,** *8* (1), 1-7.
44. Chang, F.; Bai, Z.; Li, M.; Ren, M.; Liu, T.; Yang, L.; Zhong, C.-J.; Lu, J., Strain-modulated platinum–palladium nanowires for oxygen reduction reaction. *Nano Letters* **2020,** *20* (4), 2416-2422.
45. Jin, H.; Liu, X.; Chen, S.; Vasileff, A.; Li, L.; Jiao, Y.; Song, L.; Zheng, Y.; Qiao, S.-Z., Heteroatom-doped transition metal electrocatalysts for hydrogen evolution reaction. *ACS Energy Letters* **2019,** *4* (4), 805-810.
46. Xiao, Z.; Xie, C.; Wang, Y.; Chen, R.; Wang, S., Recent advances in defect electrocatalysts: Preparation and characterization. *Journal of Energy Chemistry* **2021,** *53*, 208-225.
47. Ma, Y.; Leng, D.; Zhang, X.; Fu, J.; Pi, C.; Zheng, Y.; Gao, B.; Li, X.; Li, N.; Chu, P. K., Enhanced Activities in Alkaline Hydrogen and Oxygen Evolution Reactions on MoS2 Electrocatalysts by In-Plane Sulfur Defects Coupled with Transition Metal Doping. *Small* **2022,** *18* (39), 2203173.
48. Anand, R.; Nissimagoudar, A. S.; Umer, M.; Ha, M.; Zafari, M.; Umer, S.; Lee, G.; Kim, K. S., Late transition metal doped MXenes showing superb bifunctional electrocatalytic

activities for water splitting via distinctive mechanistic pathways. *Advanced Energy Materials* **2021,** *11* (48), 2102388.
49. Fu, C.; Luo, L.; Yang, L.; Shen, S.; Yan, X.; Yin, J.; Wei, G.; Zhang, J., An In-Depth Theoretical Exploration of Influences of Non-Metal-Elements Doping on the ORR Performance of Co− gN4. *ChemCatChem* **2021,** *13* (9), 2303-2310.
50. Yang, C.; Tao, S.; Huang, N.; Zhang, X.; Duan, J.; Makiura, R.; Maenosono, S., Heteroatom-doped carbon electrocatalysts derived from nanoporous two-dimensional covalent organic frameworks for oxygen reduction and hydrogen evolution. *ACS Applied Nano Materials* **2020,** *3* (6), 5481-5488.
51. Pan, C.; Liu, Z.; Huang, M., 2D iron-doped nickel MOF nanosheets grown on nickel foam for highly efficient oxygen evolution reaction. *Applied Surface Science* **2020,** *529*, 147201.
52. Nair, A. N.; Chava, V. S.; Bose, S.; Zheng, T.; Pilla, S.; Sreenivasan, S. T., In situ doping-enabled metal and nonmetal codoping in graphene quantum dots: synthesis and application for contaminant sensing. *ACS Sustainable Chemistry & Engineering* **2020,** *8* (44), 16565-16576.
53. Du, Z.; Shen, S.-l.; Tang, Z.-h.; Yang, J.-h., Graphene quantum dots-based heterogeneous catalysts. *New Carbon Materials* **2021,** *36* (3), 449-467.
54. Cui, P., Effect of boron and nitrogen doping on carrier relaxation dynamics of graphene quantum dots. *Materials Research Express* **2018,** *5* (6), 065034.
55. Guo, X.; Zhu, Y.; Han, W.; Fan, X.; Li, Y.; Zhang, F.; Zhang, G.; Peng, W.; Wang, S., Nitrogen-doped graphene quantum dots decorated graphite foam as ultra-high active free-standing electrode for electrochemical hydrogen evolution and phenol degradation. *Chemical Engineering Science* **2019,** *194*, 54-57.
56. Tong, X.; Zhao, Y.; Zhuo, Z.; Yang, Z.; Wang, S.; Liu, Y.; Lu, N.; Li, H.; Zhai, T., Dual-Regulation of Defect Sites and Vertical Conduction by Spiral Domain for Electrocatalytic Hydrogen Evolution. *Angewandte Chemie International Edition* **2022,** *61* (7), e202112953.
57. Li, X.; Su, X.; Pei, Y.; Liu, J.; Zheng, X.; Tang, K.; Guan, G.; Hao, X., Generation of edge dislocation defects in Co 3 O 4 catalysts: an efficient tactic to improve catalytic activity for oxygen evolution. *Journal of Materials Chemistry A* **2019,** *7* (17), 10745-10750.
58. Qin, M.; Li, S.; Zhao, Y.; Lao, C. Y.; Zhang, Z.; Liu, L.; Fang, F.; Wu, H.; Jia, B.; Liu, Z., Unprecedented synthesis of holey 2D layered double hydroxide nanomesh for enhanced oxygen evolution. *Advanced Energy Materials* **2019,** *9* (1), 1803060.
59. Zhao, G.; Rui, K.; Dou, S. X.; Sun, W., Boosting electrochemical water oxidation: the merits of heterostructured electrocatalysts. *Journal of materials chemistry A* **2020,** *8* (14), 6393-6405.
60. Deng, D.; Novoselov, K.; Fu, Q.; Zheng, N.; Tian, Z.; Bao, X., Catalysis with two-dimensional materials and their heterostructures. *Nature nanotechnology* **2016,** *11* (3), 218-230.
61. Du, X.; Huang, J.; Zhang, J.; Yan, Y.; Wu, C.; Hu, Y.; Yan, C.; Lei, T.; Chen, W.; Fan, C., Modulating electronic structures of inorganic nanomaterials for efficient electrocatalytic water splitting. *Angewandte Chemie International Edition* **2019,** *58* (14), 4484-4502.
62. Wang, H.; Zhang, L.; Chen, Z.; Hu, J.; Li, S.; Wang, Z.; Liu, J.; Wang, X., Semiconductor heterojunction photocatalysts: design, construction, and photocatalytic performances. *Chemical Society Reviews* **2014,** *43* (15), 5234-5244.
63. Su, J.; Li, G. D.; Li, X. H.; Chen, J. S., 2D/2D heterojunctions for catalysis. *Advanced Science* **2019,** *6* (7), 1801702.

64. Liu, Y.; Guo, J.; Zhu, E.; Liao, L.; Lee, S.-J.; Ding, M.; Shakir, I.; Gambin, V.; Huang, Y.; Duan, X., Approaching the Schottky–Mott limit in van der Waals metal–semiconductor junctions. *Nature* **2018,** *557* (7707), 696-700.
65. Liu, Y.; Weiss, N. O.; Duan, X.; Cheng, H.-C.; Huang, Y.; Duan, X., Van der Waals heterostructures and devices. *Nature Reviews Materials* **2016,** *1* (9), 1-17.
66. Yan, Y.; Zeng, Z.; Huang, M.; Chen, P., Van der waals heterojunctions for catalysis. *Materials Today Advances* **2020,** *6*, 100059.
67. Aras, M.; Kılıç, C. e.; Ciraci, S., Lateral and vertical heterostructures of transition metal dichalcogenides. *The Journal of Physical Chemistry C* **2018,** *122* (3), 1547-1555.
68. Zhang, K. X.; Su, H.; Wang, H. H.; Zhang, J. J.; Zhao, S. Y.; Lei, W.; Wei, X.; Li, X. H.; Chen, J. S., Atomic-Scale Mott–Schottky Heterojunctions of Boron Nitride Monolayer and Graphene as Metal-Free Photocatalysts for Artificial Photosynthesis. *Advanced Science* **2018,** *5* (7), 1800062.
69. Laleyan, D. A.; Zhao, S.; Woo, S. Y.; Tran, H. N.; Le, H. B.; Szkopek, T.; Guo, H.; Botton, G. A.; Mi, Z., AlN/h-BN heterostructures for Mg dopant-free deep ultraviolet photonics. *Nano letters* **2017,** *17* (6), 3738-3743.
70. Liu, Y.; Yudhistira, I.; Yang, M.; Laksono, E.; Luo, Y. Z.; Chen, J.; Lu, J.; Feng, Y. P.; Adam, S.; Loh, K. P., Phonon-mediated colossal magnetoresistance in graphene/black phosphorus heterostructures. *Nano Letters* **2018,** *18* (6), 3377-3383.
71. Huber, M. A.; Mooshammer, F.; Plankl, M.; Viti, L.; Sandner, F.; Kastner, L. Z.; Frank, T.; Fabian, J.; Vitiello, M. S.; Cocker, T. L., Femtosecond photo-switching of interface polaritons in black phosphorus heterostructures. *Nature Nanotechnology* **2017,** *12* (3), 207-211.
72. Rodenas, T.; Luz, I.; Prieto, G.; Seoane, B.; Miro, H.; Corma, A.; Kapteijn, F.; Llabrés i Xamena, F. X.; Gascon, J., Metal–organic framework nanosheets in polymer composite materials for gas separation. *Nature materials* **2015,** *14* (1), 48-55.
73. Tao, Y.; Ji, W.; Ding, X.; Han, B.-H., Exfoliated covalent organic framework nanosheets. *Journal of Materials Chemistry A* **2021,** *9* (12), 7336-7365.
74. Rodríguez-San-Miguel, D.; Montoro, C.; Zamora, F., Covalent organic framework nanosheets: preparation, properties and applications. *Chemical Society Reviews* **2020,** *49* (8), 2291-2302.
75. Yuan, Z.; Li, J.; Yang, M.; Fang, Z.; Jian, J.; Yu, D.; Chen, X.; Dai, L., Ultrathin black phosphorus-on-nitrogen doped graphene for efficient overall water splitting: dual modulation roles of directional interfacial charge transfer. *Journal of the American Chemical Society* **2019,** *141* (12), 4972-4979.
76. Ge, K.; Zhang, Y.; Zhao, Y.; Zhang, Z.; Wang, S.; Cao, J.; Yang, Y.; Sun, S.; Pan, M.; Zhu, L., Room Temperature Preparation of Two-Dimensional Black Phosphorus@ Metal Organic Framework Heterojunctions and Their Efficient Overall Water-Splitting Electrocatalytic Reactions. *ACS Applied Materials & Interfaces* **2022,** *14* (27), 31502-31509.
77. Jiang, L.; Duan, J.; Zhu, J.; Chen, S.; Antonietti, M., Iron-cluster-directed synthesis of 2D/2D Fe–N–C/MXene superlattice-like heterostructure with enhanced oxygen reduction electrocatalysis. *ACS nano* **2020,** *14* (2), 2436-2444.
78. Prasannachandran, R.; Vineesh, T.; Lithin, M.; Nandakishore, R.; Shaijumon, M., Phosphorene-quantum-dot-interspersed few-layered MoS 2 hybrids as efficient bifunctional electrocatalysts for hydrogen and oxygen evolution. *Chemical Communications* **2020,** *56* (61), 8623-8626.

79. Puente Santiago, A. R.; He, T.; Eraso, O.; Ahsan, M. A.; Nair, A. N.; Chava, V. S.; Zheng, T.; Pilla, S.; Fernandez-Delgado, O.; Du, A., Tailoring the interfacial interactions of van der Waals 1T-MoS2/C60 heterostructures for high-performance hydrogen evolution reaction electrocatalysis. *Journal of the American Chemical Society* **2020,** *142* (42), 17923-17927.
80. Wang, S.; Zhao, R.; Zheng, T.; Lu, Z.; Fang, Y.; Xie, H.; Wang, W.; Xue, W., Rational Design of a Low-Dimensional and Metal-free Heterostructure for Efficient Water Oxidation: DFT and Experimental Studies. *Langmuir* **2022,** *38* (41), 12562-12569.
81. Lu, Z.; Dai, W.; Lin, X.; Liu, B.; Zhang, J.; Ye, J.; Ye, J., Facile one-step fabrication of a novel 3D honeycomb-like bismuth nanoparticles decorated N-doped carbon nanosheet frameworks: Ultrasensitive electrochemical sensing of heavy metal ions. *Electrochimica Acta* **2018,** *266*, 94-102.
82. Pang, J.; Fu, H.; Kong, W.; Jiang, R.; Ye, J.; Zhao, Z.; Hou, J.; Sun, K.; Zheng, Y.; Chen, L., Design of NiCo2O4 nanoparticles decorated N, S co-doped reduced graphene oxide composites for electrochemical simultaneous detection of trace multiple heavy metal ions and hydrogen evolution reaction. *Chemical Engineering Journal* **2022,** *433*, 133854.
83. Kwon, B.; Bae, H.; Lee, H.; Kim, S.; Hwang, J.; Lim, H.; Lee, J. H.; Cho, K.; Ye, J.; Lee, S., Ultrasensitive N-channel graphene gas sensors by nondestructive molecular doping. *ACS nano* **2022,** *16* (2), 2176-2187.
84. Urbanos, F. J.; Gullace, S.; Samorì, P., MoS2 Defect Healing for High-Performance Chemical Sensing of Polycyclic Aromatic Hydrocarbons. *ACS nano* **2022,** *16* (7), 11234-11243.
85. Gu, S.; Hsieh, C.-T.; Tsai, Y.-Y.; Ashraf Gandomi, Y.; Yeom, S.; Kihm, K. D.; Fu, C.-C.; Juang, R.-S., Sulfur and nitrogen co-doped graphene quantum dots as a fluorescent quenching probe for highly sensitive detection toward mercury ions. *ACS Applied Nano Materials* **2019,** *2* (2), 790-798.
86. Kaur, M.; Mehta, S. K.; Kansal, S. K., A fluorescent probe based on nitrogen doped graphene quantum dots for turn off sensing of explosive and detrimental water pollutant, TNP in aqueous medium. *Spectrochimica Acta Part A: Molecular and Biomolecular Spectroscopy* **2017,** *180*, 37-43.
87. Guselnikova, O.; Lim, H.; Kim, H. J.; Kim, S. H.; Gorbunova, A.; Eguchi, M.; Postnikov, P.; Nakanishi, T.; Asahi, T.; Na, J., New trends in nanoarchitectured SERS substrates: nanospaces, 2D materials, and organic heterostructures. *Small* **2022,** *18* (25), 2107182.
88. Song, C.; Abell, J. L.; He, Y.; Murph, S. H.; Cui, Y.; Zhao, Y., Gold-modified silver nanorod arrays: growth dynamics and improved SERS properties. *Journal of materials chemistry* **2012,** *22* (3), 1150-1159.
89. Gutés, A.; Maboudian, R.; Carraro, C., Gold-coated silver dendrites as SERS substrates with an improved lifetime. *Langmuir* **2012,** *28* (51), 17846-17850.
90. Yu, X.; Cai, H.; Zhang, W.; Li, X.; Pan, N.; Luo, Y.; Wang, X.; Hou, J., Tuning chemical enhancement of SERS by controlling the chemical reduction of graphene oxide nanosheets. *ACS nano* **2011,** *5* (2), 952-958.
91. Sarycheva, A.; Makaryan, T.; Maleski, K.; Satheeshkumar, E.; Melikyan, A.; Minassian, H.; Yoshimura, M.; Gogotsi, Y., Two-dimensional titanium carbide (MXene) as surface-enhanced Raman scattering substrate. *The Journal of Physical Chemistry C* **2017,** *121* (36), 19983-19988.
92. Duan, H.; Wang, C.; Li, G.; Tan, H.; Hu, W.; Cai, L.; Liu, W.; Li, N.; Ji, Q.; Wang, Y., Single-Atom-Layer Catalysis in a MoS2 Monolayer Activated by Long-Range Ferromagnetism for the Hydrogen Evolution Reaction: Beyond Single-Atom Catalysis. *Angewandte Chemie* **2021,** *133* (13), 7327-7334.

93. Zhang, Y.; Liang, C.; Wu, J.; Liu, H.; Zhang, B.; Jiang, Z.; Li, S.; Xu, P., Recent advances in magnetic field-enhanced electrocatalysis. *ACS Applied Energy Materials* **2020,** *3* (11), 10303-10316.
94. Qin, X.; Teng, J.; Guo, W.; Wang, L.; Xiao, S.; Xu, Q.; Min, Y.; Fan, J., Magnetic Field Enhancing OER Electrocatalysis of NiFe Layered Double Hydroxide. *Catalysis Letters* **2022**, 1-9.
95. Zhang, Y.; Guo, P.; Li, S.; Sun, J.; Wang, W.; Song, B.; Yang, X.; Wang, X.; Jiang, Z.; Wu, G., Magnetic field assisted electrocatalytic oxygen evolution reaction of nickel-based materials. *Journal of Materials Chemistry A* **2022,** *10* (4), 1760-1767.
96. Ren, X.; Wu, T.; Sun, Y.; Li, Y.; Xian, G.; Liu, X.; Shen, C.; Gracia, J.; Gao, H.-J.; Yang, H., Spin-polarized oxygen evolution reaction under magnetic field. *Nature communications* **2021,** *12* (1), 1-12.
97. Garcés-Pineda, F. A.; Blasco-Ahicart, M.; Nieto-Castro, D.; López, N.; Galán-Mascarós, J. R., Direct magnetic enhancement of electrocatalytic water oxidation in alkaline media. *Nature Energy* **2019,** *4* (6), 519-525.
98. Niether, C.; Faure, S.; Bordet, A.; Deseure, J.; Chatenet, M.; Carrey, J.; Chaudret, B.; Rouet, A., Improved water electrolysis using magnetic heating of FeC–Ni core–shell nanoparticles. *Nature Energy* **2018,** *3* (6), 476-483.
99. Zhou, G.; Wang, P.; Li, H.; Hu, B.; Sun, Y.; Huang, R.; Liu, L., Spin-state reconfiguration induced by alternating magnetic field for efficient oxygen evolution reaction. *Nature Communications* **2021,** *12* (1), 4827.
100. Gong, X.; Jiang, Z.; Zeng, W.; Hu, C.; Luo, X.; Lei, W.; Yuan, C., Alternating Magnetic Field Induced Magnetic Heating in Ferromagnetic Cobalt Single-Atom Catalysts for Efficient Oxygen Evolution Reaction. *Nano Letters* **2022,** *22* (23), 9411-9417.
101. Ray, K.; Ananthavel, S.; Waldeck, D.; Naaman, R., Asymmetric scattering of polarized electrons by organized organic films of chiral molecules. *Science* **1999,** *283* (5403), 814-816.
102. Lu, H.; Wang, J.; Xiao, C.; Pan, X.; Chen, X.; Brunecky, R.; Berry, J. J.; Zhu, K.; Beard, M. C.; Vardeny, Z. V., Spin-dependent charge transport through 2D chiral hybrid lead-iodide perovskites. *Science advances* **2019,** *5* (12), eaay0571.
103. Gersten, J.; Kaasbjerg, K.; Nitzan, A., Induced spin filtering in electron transmission through chiral molecular layers adsorbed on metals with strong spin-orbit coupling. *The Journal of Chemical Physics* **2013,** *139* (11), 114111.
104. Dalum, S.; Hedegård, P., Theory of chiral induced spin selectivity. *Nano letters* **2019,** *19* (8), 5253-5259.
105. Naaman, R.; Paltiel, Y.; Waldeck, D. H., Chiral molecules and the spin selectivity effect. *The Journal of Physical Chemistry Letters* **2020,** *11* (9), 3660-3666.
106. Bloom, B.; Lu, Y.; Metzger, T.; Yochelis, S.; Paltiel, Y.; Fontanesi, C.; Mishra, S.; Tassinari, F.; Naaman, R.; Waldeck, D., Asymmetric reactions induced by electron spin polarization. *Physical Chemistry Chemical Physics* **2020,** *22* (38), 21570-21582.
107. Kuzmin, S.; Duley, W., Properties of specific electron helical states leads to spin filtering effect in dsDNA molecules. *Physics Letters A* **2014,** *378* (22-23), 1647-1650.
108. Aragonès, A. C.; Medina, E.; Ferrer-Huerta, M.; Gimeno, N.; Teixidó, M.; Palma, J. L.; Tao, N.; Ugalde, J. M.; Giralt, E.; Díez-Pérez, I., Measuring the spin-polarization power of a single chiral molecule. *small* **2017,** *13* (2), 1602519.
109. Mtangi, W.; Kiran, V.; Fontanesi, C.; Naaman, R., Role of the electron spin polarization in water splitting. *The journal of physical chemistry letters* **2015,** *6* (24), 4916-4922.

110. Mtangi, W.; Tassinari, F.; Vankayala, K.; Vargas Jentzsch, A.; Adelizzi, B.; Palmans, A. R.; Fontanesi, C.; Meijer, E.; Naaman, R., Control of electrons' spin eliminates hydrogen peroxide formation during water splitting. *Journal of the American Chemical Society* **2017,** *139* (7), 2794-2798.
111. Tassinari, F.; Banerjee-Ghosh, K.; Parenti, F.; Kiran, V.; Mucci, A.; Naaman, R., Enhanced hydrogen production with chiral conductive polymer-based electrodes. *The Journal of Physical Chemistry C* **2017,** *121* (29), 15777-15783.
112. Ghosh, K.; Zhang, W.; Tassinari, F.; Mastai, Y.; Lidor-Shalev, O.; Naaman, R.; Möllers, P.; Nürenberg, D.; Zacharias, H.; Wei, J., Controlling chemical selectivity in electrocatalysis with chiral CuO-coated electrodes. *The Journal of Physical Chemistry C* **2019,** *123* (5), 3024-3031.
113. Bian, Z.; Kato, K.; Ogoshi, T.; Cui, Z.; Sa, B.; Tsutsui, Y.; Seki, S.; Suda, M., Hybrid Chiral MoS2 Layers for Spin-Polarized Charge Transport and Spin-Dependent Electrocatalytic Applications. *Advanced Science* **2022**, 2201063.
114. Liang, Y.; Banjac, K.; Martin, K.; Zigon, N.; Lee, S.; Vanthuyne, N.; Garcés-Pineda, F. A.; Galan-Mascaros, J. R.; Hu, X.; Avarvari, N., Enhancement of electrocatalytic oxygen evolution by chiral molecular functionalization of hybrid 2D electrodes. *Nature Communications* **2022,** *13* (1), 1-9.
115. Fan, L.; Zhu, M.; Lee, X.; Zhang, R.; Wang, K.; Wei, J.; Zhong, M.; Wu, D.; Zhu, H., Direct synthesis of graphene quantum dots by chemical vapor deposition. *Particle & Particle Systems Characterization* **2013,** *30* (9), 764-769.
116. Liu, R.; Wu, D.; Feng, X.; Müllen, K., Bottom-up fabrication of photoluminescent graphene quantum dots with uniform morphology. *Journal of the American Chemical Society* **2011,** *133* (39), 15221-15223.
117. Tang, L.; Ji, R.; Cao, X.; Lin, J.; Jiang, H.; Li, X.; Teng, K. S.; Luk, C. M.; Zeng, S.; Hao, J., Deep ultraviolet photoluminescence of water-soluble self-passivated graphene quantum dots. *ACS nano* **2012,** *6* (6), 5102-5110.
118. Atienzar, P.; Primo, A.; Lavorato, C.; Molinari, R.; García, H., Preparation of graphene quantum dots from pyrolyzed alginate. *Langmuir* **2013,** *29* (20), 6141-6146.
119. Prasannan, A.; Imae, T., One-pot synthesis of fluorescent carbon dots from orange waste peels. *Industrial & Engineering Chemistry Research* **2013,** *52* (44), 15673-15678.
120. Tan, X. W.; Romainor, A. N. B.; Chin, S. F.; Ng, S. M., Carbon dots production via pyrolysis of sago waste as potential probe for metal ions sensing. *Journal of analytical and applied pyrolysis* **2014,** *105*, 157-165.
121. Chen, W.; Li, D.; Tian, L.; Xiang, W.; Wang, T.; Hu, W.; Hu, Y.; Chen, S.; Chen, J.; Dai, Z., Synthesis of graphene quantum dots from natural polymer starch for cell imaging. *Green chemistry* **2018,** *20* (19), 4438-4442.
122. Wang, Z.; Yu, J.; Zhang, X.; Li, N.; Liu, B.; Li, Y.; Wang, Y.; Wang, W.; Li, Y.; Zhang, L., Large-scale and controllable synthesis of graphene quantum dots from rice husk biomass: a comprehensive utilization strategy. *ACS applied materials & interfaces* **2016,** *8* (2), 1434-1439.
123. Ding, Z.; Li, F.; Wen, J.; Wang, X.; Sun, R., Gram-scale synthesis of single-crystalline graphene quantum dots derived from lignin biomass. *Green chemistry* **2018,** *20* (6), 1383-1390.
124. Park, S. Y.; Lee, H. U.; Park, E. S.; Lee, S. C.; Lee, J.-W.; Jeong, S. W.; Kim, C. H.; Lee, Y.-C.; Huh, Y. S.; Lee, J., Photoluminescent green carbon nanodots from food-waste-derived sources: large-scale synthesis, properties, and biomedical applications. *ACS applied materials & interfaces* **2014,** *6* (5), 3365-3370.

125. Suryawanshi, A.; Biswal, M.; Mhamane, D.; Gokhale, R.; Patil, S.; Guin, D.; Ogale, S., Large scale synthesis of graphene quantum dots (GQDs) from waste biomass and their use as an efficient and selective photoluminescence on–off–on probe for Ag+ ions. *Nanoscale* **2014,** *6* (20), 11664-11670.
126. Yang, L.; Qin, A.; Chen, S.; Liao, L.; Qin, J.; Zhang, K., Manganese (ii) enhanced fluorescent nitrogen-doped graphene quantum dots: a facile and efficient synthesis and their applications for bioimaging and detection of Hg 2+ ions. *RSC advances* **2018,** *8* (11), 5902-5911.
127. Hao, Y.-N.; Guo, H.-L.; Tian, L.; Kang, X., Enhanced photoluminescence of pyrrolic-nitrogen enriched graphene quantum dots. *RSC advances* **2015,** *5* (54), 43750-43755.
128. Gu, J.; Zhang, X.; Pang, A.; Yang, J., Facile synthesis and photoluminescence characteristics of blue-emitting nitrogen-doped graphene quantum dots. *Nanotechnology* **2016,** *27* (16), 165704.
129. Yang, G.; Wu, C.; Luo, X.; Liu, X.; Gao, Y.; Wu, P.; Cai, C.; Saavedra, S. S., Exploring the emissive states of heteroatom-doped graphene quantum dots. *The Journal of Physical Chemistry C* **2018,** *122* (11), 6483-6492.
130. Wang, R.; Xia, G.; Zhong, W.; Chen, L.; Chen, L.; Wang, Y.; Min, Y.; Li, K., Direct transformation of lignin into fluorescence-switchable graphene quantum dots and their application in ultrasensitive profiling of a physiological oxidant. *Green Chemistry* **2019**.
131. Li, X.; Lau, S. P.; Tang, L.; Ji, R.; Yang, P., Sulphur doping: a facile approach to tune the electronic structure and optical properties of graphene quantum dots. *Nanoscale* **2014,** *6* (10), 5323-5328.
132. Kharangarh, P. R.; Gupta, V.; Singh, A.; Bhardwaj, P.; Grace, A. N., An efficient pseudocapacitor electrode material with co-doping of iron (II) and sulfur in luminescent graphene quantum dots. *Diamond and Related Materials* **2020**, 107913.
133. Lin, L.; Song, X.; Chen, Y.; Rong, M.; Wang, Y.; Zhao, L.; Zhao, T.; Chen, X., Europium-decorated graphene quantum dots as a fluorescent probe for label-free, rapid and sensitive detection of Cu2+ and L-cysteine. *Analytica Chimica Acta* **2015,** *891*, 261-268.
134. Lin, L.; Luo, Y.; Tsai, P.; Wang, J.; Chen, X., Metal ions doped carbon quantum dots: Synthesis, physicochemical properties, and their applications. *TrAC Trends in Analytical Chemistry* **2018,** *103*, 87-101.
135. Pang, J.; Zhang, W.; Zhang, H.; Zhang, J.; Zhang, H.; Cao, G.; Han, M.; Yang, Y., Sustainable nitrogen-containing hierarchical porous carbon spheres derived from sodium lignosulfonate for high-performance supercapacitors. *Carbon* **2018,** *132*, 280-293.
136. Ye, B.-J.; Kim, B.-G.; Jeon, M.-J.; Kim, S.-Y.; Kim, H.-C.; Jang, T.-W.; Chae, H.-J.; Choi, W.-J.; Ha, M.-N.; Hong, Y.-S., Evaluation of mercury exposure level, clinical diagnosis and treatment for mercury intoxication. *Annals of Occupational and Environmental Medicine* **2016,** *28* (1).
137. Wang, L.; Wang, Y.; Xu, T.; Liao, H.; Yao, C.; Liu, Y.; Li, Z.; Chen, Z.; Pan, D.; Sun, L., Gram-scale synthesis of single-crystalline graphene quantum dots with superior optical properties. *Nature communications* **2014,** *5*, 5357.
138. Xu, Q.; Liu, Y.; Su, R.; Cai, L.; Li, B.; Zhang, Y.; Zhang, L.; Wang, Y.; Wang, Y.; Li, N., Highly fluorescent Zn-doped carbon dots as Fenton reaction-based bio-sensors: an integrative experimental–theoretical consideration. *Nanoscale* **2016,** *8* (41), 17919-17927.
139. Kadian, S.; Manik, G.; Kalkal, A.; Singh, M.; Chauhan, R. P., Effect of sulfur doping on fluorescence and quantum yield of graphene quantum dots: an experimental and theoretical investigation. *Nanotechnology* **2019,** *30* (43), 435704.

140. Lingam, K.; Podila, R.; Qian, H.; Serkiz, S.; Rao, A. M., Evidence for Edge-State Photoluminescence in Graphene Quantum Dots. *Advanced Functional Materials* **2013,** *23* (40), 5062-5065.
141. Li, L.; Dong, T., Photoluminescence tuning in carbon dots: Surface passivation or/and functionalization, heteroatom doping. *Journal of Materials Chemistry C* **2018,** *6* (30), 7944-7970.
142. Shen, J.; Zhu, Y.; Yang, X.; Zong, J.; Zhang, J.; Li, C., One-pot hydrothermal synthesis of graphene quantum dots surface-passivated by polyethylene glycol and their photoelectric conversion under near-infrared light. *New Journal of Chemistry* **2012,** *36* (1), 97-101.
143. Li, X.; Zhang, S.; Kulinich, S. A.; Liu, Y.; Zeng, H., Engineering surface states of carbon dots to achieve controllable luminescence for solid-luminescent composites and sensitive Be 2+ detection. *Scientific reports* **2014,** *4*, 4976.
144. Zhu, S.; Song, Y.; Zhao, X.; Shao, J.; Zhang, J.; Yang, B., The photoluminescence mechanism in carbon dots (graphene quantum dots, carbon nanodots, and polymer dots): current state and future perspective. *Nano research* **2015,** *8* (2), 355-381.
145. Xu, Q.; Pu, P.; Zhao, J.; Dong, C.; Gao, C.; Chen, Y.; Chen, J.; Liu, Y.; Zhou, H., Preparation of highly photoluminescent sulfur-doped carbon dots for Fe (III) detection. *Journal of Materials Chemistry A* **2015,** *3* (2), 542-546.
146. Ferrari, A. C.; Meyer, J.; Scardaci, V.; Casiraghi, C.; Lazzeri, M.; Mauri, F.; Piscanec, S.; Jiang, D.; Novoselov, K.; Roth, S., Raman spectrum of graphene and graphene layers. *Physical review letters* **2006,** *97* (18), 187401.
147. Zheng, X. T.; Than, A.; Ananthanaraya, A.; Kim, D.-H.; Chen, P., Graphene quantum dots as universal fluorophores and their use in revealing regulated trafficking of insulin receptors in adipocytes. *ACS nano* **2013,** *7* (7), 6278-6286.
148. Gliniak, J.; Lin, J. H.; Chen, Y. T.; Li, C. R.; Jokar, E.; Chang, C. H.; Peng, C. S.; Lin, J. N.; Lien, W. H.; Tsai, H. M., Sulfur-doped graphene oxide quantum dots as photocatalysts for hydrogen generation in the aqueous phase. *ChemSusChem* **2017,** *10* (16), 3260-3267.
149. Xu, Y.; Li, D.; Liu, M.; Niu, F.; Liu, J.; Wang, E., Enhanced-quantum yield sulfur/nitrogen co-doped fluorescent carbon nanodots produced from biomass Enteromorpha prolifera: synthesis, posttreatment, applications and mechanism study. *Scientific reports* **2017,** *7* (1), 1-12.
150. Wu, M.; Cao, C.; Jiang, J., Electronic structure of substitutionally Mn-doped graphene. *New Journal of Physics* **2010,** *12* (6), 063020.
151. Wang, R.; Xie, T.; Sun, Z.; Pu, T.; Li, W.; Ao, J.-P., Graphene quantum dot modified gC 3 N 4 for enhanced photocatalytic oxidation of ammonia performance. *RSC advances* **2017,** *7* (81), 51687-51694.
152. Permatasari, F. A.; Aimon, A. H.; Iskandar, F.; Ogi, T.; Okuyama, K., Role of C–N configurations in the photoluminescence of graphene quantum dots synthesized by a hydrothermal route. *Scientific reports* **2016,** *6*, 21042.
153. Jin, S. H.; Kim, D. H.; Jun, G. H.; Hong, S. H.; Jeon, S., Tuning the photoluminescence of graphene quantum dots through the charge transfer effect of functional groups. *ACS nano* **2013,** *7* (2), 1239-1245.
154. Sudolska, M.; Dubecky, M.; Sarkar, S.; Reckmeier, C. J.; Zboril, R.; Rogach, A. L.; Otyepka, M., Nature of absorption bands in oxygen-functionalized graphitic carbon dots. *The Journal of Physical Chemistry C* **2015,** *119* (23), 13369-13373.

155. Yeh, T. F.; Teng, C. Y.; Chen, S. J.; Teng, H., Nitrogen-doped graphene oxide quantum dots as photocatalysts for overall water-splitting under visible light Illumination. *Advanced materials* **2014,** *26* (20), 3297-3303.
156. Wang, X.; Sun, G.; Routh, P.; Kim, D.-H.; Huang, W.; Chen, P., Heteroatom-doped graphene materials: syntheses, properties and applications. *Chemical Society Reviews* **2014,** *43* (20), 7067-7098.
157. Qian, F.; Li, X.; Tang, L.; Lai, S. K.; Lu, C.; Lau, S. P., Potassium doping: tuning the optical properties of graphene quantum dots. *AIP advances* **2016,** *6* (7), 075116.
158. Xu, Q.; Su, R.; Chen, Y.; Theruvakkattil Sreenivasan, S.; Li, N.; Zheng, X.; Zhu, J.; Pan, H.; Li, W.; Xu, C., Metal Charge Transfer Doped Carbon Dots with Reversibly Switchable, Ultra-High Quantum Yield Photoluminescence. *ACS Applied Nano Materials* **2018,** *1* (4), 1886-1893.
159. Hui, W.; Yang, Y.; Xu, Q.; Gu, H.; Feng, S.; Su, Z.; Zhang, M.; Wang, J.; Li, X.; Fang, J., Red-Carbon-Quantum-Dot-Doped SnO2 Composite with Enhanced Electron Mobility for Efficient and Stable Perovskite Solar Cells. *Advanced Materials* **2020,** *32* (4), 1906374.
160. Zhang, B.; Liu, Y.; Ren, M.; Li, W.; Zhang, X.; Vajtai, R.; Ajayan, P. M.; Tour, J. M.; Wang, L., Sustainable Synthesis of Bright Green Fluorescent Nitrogen-Doped Carbon Quantum Dots from Alkali Lignin. *ChemSusChem* **2019,** *12* (18), 4202-4210.
161. Liu, G.; Li, S.; Cheng, M.; Zhao, L.; Zhang, B.; Gao, Y.; Xu, Y.; Liu, F.; Lu, G., Facile synthesis of nitrogen and sulfur co-doped carbon dots for multiple sensing capacities: alkaline fluorescence enhancement effect, temperature sensing, and selective detection of Fe 3+ ions. *New Journal of Chemistry* **2018,** *42* (15), 13147-13156.
162. Park, C. H.; Yang, H.; Lee, J.; Cho, H.-H.; Kim, D.; Lee, D. C.; Kim, B. J., Multicolor emitting block copolymer-integrated graphene quantum dots for colorimetric, simultaneous sensing of temperature, pH, and metal ions. *Chemistry of Materials* **2015,** *27* (15), 5288-5294.
163. Wang, L.; Li, W.; Li, M.; Su, Q.; Li, Z.; Pan, D.; Wu, M., Ultrastable amine, sulfo cofunctionalized graphene quantum dots with high two-photon fluorescence for cellular imaging. *ACS Sustainable Chemistry & Engineering* **2018,** *6* (4), 4711-4716.
164. Ma, M.; Hu, X.; Zhang, C.; Deng, C.; Wang, X., The optimum parameters to synthesize bright and stable graphene quantum dots by hydrothermal method. *Journal of Materials Science: Materials in Electronics* **2017,** *28* (9), 6493-6497.
165. Ma, Y.; Chen, A.; Xie, X.; Wang, X.; Wang, D.; Wang, P.; Li, H.; Yang, J.; Li, Y., Doping effect and fluorescence quenching mechanism of N-doped graphene quantum dots in the detection of dopamine. *Talanta* **2019,** *196*, 563-571.
166. Liu, Y.; Tang, X.; Deng, M.; Cao, Y.; Li, Y.; Zheng, H.; Li, F.; Yan, F.; Lan, T.; Shi, L., Nitrogen doped graphene quantum dots as a fluorescent probe for mercury (II) ions. *Microchimica Acta* **2019,** *186* (3), 1-8.
167. Cotruvo, J. A., 2017 WHO guidelines for drinking water quality: first addendum to the fourth edition. *Journal-American Water Works Association* **2017,** *109* (7), 44-51.
168. Wu, Z.; Feng, M.; Chen, X.; Tang, X., N-dots as a photoluminescent probe for the rapid and selective detection of Hg 2+ and Ag+ in aqueous solution. *Journal of Materials Chemistry B* **2016,** *4* (12), 2086-2089.
169. Chakraborti, H.; Sinha, S.; Ghosh, S.; Pal, S. K., Interfacing water soluble nanomaterials with fluorescence chemosensing: Graphene quantum dot to detect Hg2+ in 100% aqueous solution. *Materials letters* **2013,** *97*, 78-80.

170. Kappen, J.; Ponkarpagam, S.; John, S. A., Study on the interactions between graphene quantum dots and Hg (II): Unraveling the origin of photoluminescence quenching of graphene quantum dots by Hg (II). *Colloids and Surfaces A: Physicochemical and Engineering Aspects* **2020,** *591*, 124551.
171. Mukherjee, S.; Kumar, A. A.; Sudhakar, C.; Kumar, R.; Ahuja, T.; Mondal, B.; Srikrishnarka, P.; Philip, L.; Pradeep, T., Sustainable and affordable composites built using microstructures performing better than nanostructures for arsenic removal. *ACS Sustainable Chemistry & Engineering* **2018,** *7* (3), 3222-3233.
172. Sheldon, R. A., Metrics of green chemistry and sustainability: past, present, and future. *ACS Sustainable Chemistry & Engineering* **2018,** *6* (1), 32-48.
173. Zhang, L.; Yang, X.; Cai, R.; Chen, C.; Xia, Y.; Zhang, H.; Yang, D.; Yao, X., Air cathode of zinc–air batteries: a highly efficient and durable aerogel catalyst for oxygen reduction. *Nanoscale* **2019,** *11* (3), 826-832.
174. Li, Y.; Dai, H., Recent advances in zinc–air batteries. *Chemical Society Reviews* **2014,** *43* (15), 5257-5275.
175. Cai, X.; Lai, L.; Lin, J.; Shen, Z., Recent advances in air electrodes for Zn–air batteries: electrocatalysis and structural design. *Materials Horizons* **2017,** *4* (6), 945-976.
176. Goswami, C.; Hazarika, K. K.; Bharali, P., Transition metal oxide nanocatalysts for oxygen reduction reaction. *Materials Science for Energy Technologies* **2018,** *1* (2), 117-128.
177. Wei, L.; Ang, E. H.; Yang, Y.; Qin, Y.; Zhang, Y.; Ye, M.; Liu, Q.; Li, C. C., Recent advances of transition metal based bifunctional electrocatalysts for rechargeable zinc-air batteries. *Journal of Power Sources* **2020,** *477*, 228696.
178. Ibrahim, K. B.; Tsai, M. C.; Chala, S. A.; Berihun, M. K.; Kahsay, A. W.; Berhe, T. A.; Su, W. N.; Hwang, B. J., A review of transition metal-based bifunctional oxygen electrocatalysts. *Journal of the Chinese Chemical Society* **2019,** *66* (8), 829-865.
179. Zhang, X.; Dong, C.-L.; Diao, Z.; Lu, Y.-R.; Shen, S., Identifying the crystal and electronic structure evolution in tri-component transition metal oxide nanosheets for efficient electrocatalytic oxygen evolution. *EcoMat* **2019,** *1* (1), e12005.
180. Wang, H.-Y.; Hsu, Y.-Y.; Chen, R.; Chan, T.-S.; Chen, H. M.; Liu, B., Ni3+-Induced Formation of Active NiOOH on the Spinel Ni–Co Oxide Surface for Efficient Oxygen Evolution Reaction. *Advanced Energy Materials* **2015,** *5* (10), 1500091.
181. Louie, M. W.; Bell, A. T., An Investigation of Thin-Film Ni–Fe Oxide Catalysts for the Electrochemical Evolution of Oxygen. *Journal of the American Chemical Society* **2013,** *135* (33), 12329-12337.
182. Shahid, M. M.; Rameshkumar, P.; Basirun, W. J.; Juan, J. C.; Huang, N. M., Cobalt oxide nanocubes interleaved reduced graphene oxide as an efficient electrocatalyst for oxygen reduction reaction in alkaline medium. *Electrochimica Acta* **2017,** *237*, 61-68.
183. Liang, Y.; Li, Y.; Wang, H.; Zhou, J.; Wang, J.; Regier, T.; Dai, H., Co 3 O 4 nanocrystals on graphene as a synergistic catalyst for oxygen reduction reaction. *Nature materials* **2011,** *10* (10), 780-786.
184. Hong, Q.; Lu, H.; Wang, J., CuO Nanoplatelets with Highly Dispersed Ce-Doping Derived from Intercalated Layered Double Hydroxides for Synergistically Enhanced Oxygen Reduction Reaction in Al–Air Batteries. *ACS Sustainable Chemistry & Engineering* **2017,** *5* (10), 9169-9175.
185. Zhao, A.; Masa, J.; Xia, W.; Maljusch, A.; Willinger, M.-G.; Clavel, G.; Xie, K.; Schlögl, R.; Schuhmann, W.; Muhler, M., Spinel Mn–Co oxide in N-doped carbon nanotubes as

a bifunctional electrocatalyst synthesized by oxidative cutting. *Journal of the American chemical society* **2014,** *136* (21), 7551-7554.
186. Bhandary, N.; Ingole, P. P.; Basu, S., Electrosynthesis of Mn-Fe oxide nanopetals on carbon paper as bi-functional electrocatalyst for oxygen reduction and oxygen evolution reaction. *International Journal of Hydrogen Energy* **2018,** *43* (6), 3165-3171.
187. Yang, Q.; Xu, W.; Gong, S.; Zheng, G.; Tian, Z.; Wen, Y.; Peng, L.; Zhang, L.; Lu, Z.; Chen, L., Atomically dispersed Lewis acid sites boost 2-electron oxygen reduction activity of carbon-based catalysts. *Nature communications* **2020,** *11* (1), 1-10.
188. Carey, F. A.; Sundberg, R. J., *Advanced organic chemistry: part A: structure and mechanisms*. Springer Science & Business Media: 2007.
189. Delgado, M. R.; Areán, C. O., Surface chemistry and pore structure of β-Ga2O3. *Materials Letters* **2003,** *57* (15), 2292-2297.
190. Shao, C.-T.; Lang, W.-Z.; Yan, X.; Guo, Y.-J., Catalytic performance of gallium oxide based-catalysts for the propane dehydrogenation reaction: effects of support and loading amount. *RSC Advances* **2017,** *7* (8), 4710-4723.
191. Nakagawa, K.; Okamura, M.; Ikenaga, N.; Suzuki, T.; Nakagawa, K.; Okamura, M.; Suzuki, T.; Kobayashi, T.; Kobayashi, T., Dehydrogenation of ethane over gallium oxide in the presence of carbon dioxide. *Chemical Communications* **1998,** (9), 1025-1026.
192. Sun, Y.; Li, X.; Zhang, T.; Xu, K.; Yang, Y.; Chen, G.; Li, C.; Xie, Y., Nitrogen-Doped Cobalt Diselenide with Cubic Phase Maintained for Enhanced Alkaline Hydrogen Evolution. *Angewandte Chemie* **2021,** *133* (39), 21745-21752.
193. Swaminathan, J.; Puthirath, A. B.; Sahoo, M. R.; Nayak, S. K.; Costin, G.; Vajtai, R.; Sharifi, T.; Ajayan, P. M., Tuning the Electrocatalytic Activity of Co3O4 through Discrete Elemental Doping. *ACS applied materials & interfaces* **2019,** *11* (43), 39706-39714.
194. Feng, H.; Tang, L.; Zeng, G.; Yu, J.; Deng, Y.; Zhou, Y.; Wang, J.; Feng, C.; Luo, T.; Shao, B., Electron density modulation of Fe1-xCoxP nanosheet arrays by iron incorporation for highly efficient water splitting. *Nano Energy* **2020,** *67*, 104174.
195. Wang, J.; Liao, T.; Wei, Z.; Sun, J.; Guo, J.; Sun, Z., Heteroatom-Doping of Non-Noble Metal-Based Catalysts for Electrocatalytic Hydrogen Evolution: An Electronic Structure Tuning Strategy. *Small Methods* **2021,** *5* (4), 2000988.
196. Bandi, M.; Zade, V.; Roy, S.; Nair, A. N.; Seacat, S.; Sreenivasan, S.; Shutthanandan, V.; Van de Walle, C. G.; Peelaers, H.; Ramana, C. V., Effect of Titanium Induced Chemical Inhomogeneity on Crystal Structure, Electronic Structure, and Optical Properties of Wide Band Gap Ga2O3. *Crystal Growth & Design* **2020,** *20* (3), 1422-1433.
197. Mallesham, B.; Roy, S.; Bose, S.; Nair, A. N.; Sreenivasan, S.; Shutthanandan, V.; Ramana, C. V., Crystal Chemistry, Band-Gap Red Shift, and Electrocatalytic Activity of Iron-Doped Gallium Oxide Ceramics. *ACS Omega* **2020,** *5* (1), 104-112.
198. Gutierrez, G.; Sundin, E. M.; Nalam, P. G.; Zade, V.; Romero, R.; Nair, A. N.; Sreenivasan, S.; Das, D.; Li, C.; Ramana, C. V., Interfacial Phase Modulation-Induced Structural Distortion, Band Gap Reduction, and Nonlinear Optical Activity in Tin-Incorporated Ga2O3. *The Journal of Physical Chemistry C* **2021,** *125* (37), 20468-20481.
199. Feaster, J. T.; Shi, C.; Cave, E. R.; Hatsukade, T.; Abram, D. N.; Kuhl, K. P.; Hahn, C.; Nørskov, J. K.; Jaramillo, T. F., Understanding selectivity for the electrochemical reduction of carbon dioxide to formic acid and carbon monoxide on metal electrodes. *Acs Catalysis* **2017,** *7* (7), 4822-4827.

200. Dutta, A.; Rahaman, M.; Luedi, N. C.; Mohos, M.; Broekmann, P., Morphology matters: tuning the product distribution of CO2 electroreduction on oxide-derived Cu foam catalysts. *ACS Catalysis* **2016,** *6* (6), 3804-3814.
201. Ling, Y.; Wang, G.; Wheeler, D. A.; Zhang, J. Z.; Li, Y., Sn-doped hematite nanostructures for photoelectrochemical water splitting. *Nano letters* **2011,** *11* (5), 2119-2125.
202. Sun, L.; Han, C.; Zhang, T.; Zhu, H.; Xia, X.; Li, L., CoOx (OH) 2 (1-x) doped with Sn urchin-like spheres for enhanced oxygen evolution reaction. *Materials Science in Semiconductor Processing* **2020,** *110*, 104935.
203. Kim, N.-I.; Sa, Y. J.; Cho, S.-H.; So, I.; Kwon, K.; Joo, S. H.; Park, J.-Y., Enhancing activity and stability of cobalt oxide electrocatalysts for the oxygen evolution reaction via transition metal doping. *Journal of The Electrochemical Society* **2016,** *163* (11), F3020.
204. Gutierrez, G.; Sundin, E. M.; Nalam, P. G.; Zade, V.; Romero, R.; Nair, A. N.; Sreenivasan, S.; Das, D.; Li, C.; Ramana, C., Interfacial Phase Modulation-Induced Structural Distortion, Band Gap Reduction, and Nonlinear Optical Activity in Tin-Incorporated Ga2O3. *The Journal of Physical Chemistry C* **2021**.
205. Kresse, G.; Furthmüller, J., Efficient iterative schemes for ab initio total-energy calculations using a plane-wave basis set. *Physical Review B* **1996,** *54* (16), 11169-11186.
206. Momma, K.; Izumi, F., VESTA 3 for three-dimensional visualization of crystal, volumetric and morphology data. *Journal of applied crystallography* **2011,** *44* (6), 1272-1276.
207. Mallesham, B.; Roy, S.; Bose, S.; Nair, A. N.; Sreenivasan, S.; Shutthanandan, V.; Ramana, C. V., Crystal chemistry, band-gap red shift, and electrocatalytic activity of iron-doped gallium oxide ceramics. *ACS omega* **2019,** *5* (1), 104-112.
208. Ramana, C.; Roy, S.; Zade, V.; Battu, A. K.; Makeswaran, N.; Shutthanandan, V., Electronic Structure and Chemical Bonding in Transition-Metal-Mixed Gallium Oxide (Ga2O3) Compounds. *Journal of Physics and Chemistry of Solids* **2021**, 110174.
209. Yao, Y.; Ishikawa, Y.; Sugawara, Y., X-ray diffraction and Raman characterization of β-Ga2O3 single crystal grown by edge-defined film-fed growth method. *Journal of Applied Physics* **2019,** *126* (20), 205106.
210. Kranert, C.; Sturm, C.; Schmidt-Grund, R.; Grundmann, M., Raman tensor elements of β-Ga 2 O 3. *Scientific reports* **2016,** *6* (1), 1-9.
211. Khan, A.; Khan, S. N.; Jadwisienczak, W.; Kordesch, M. E., Raman Spectroscopic Studies of Monoclinic Gallium Oxide (□-Ga2O3) Nanostructures: A Comparison Between Nanowires and Nanobelts. *Science of Advanced Materials* **2009,** *1* (3), 236-240.
212. Wang, Y.; Li, N.; Duan, P.; Sun, X.; Chu, B.; He, Q., Properties and Photocatalytic Activity of β-Ga₂O₃ Nanorods under Simulated Solar Irradiation. *Journal of Nanomaterials* **2015,** *2015*, 191793.
213. Kumar, S.; Singh, R., Nanofunctional gallium oxide (Ga2O3) nanowires/nanostructures and their applications in nanodevices. *physica status solidi (RRL) – Rapid Research Letters* **2013,** *7* (10), 781-792.
214. Åhman, J.; Svensson, G.; Albertsson, J., A Reinvestigation of β-Gallium Oxide. *Acta Crystallographica Section C* **1996,** *52* (6), 1336-1338.
215. Janowitz, C.; Scherer, V.; Mohamed, M.; Krapf, A.; Dwelk, H.; Manzke, R.; Galazka, Z.; Uecker, R.; Irmscher, K.; Fornari, R.; Michling, M.; Schmeißer, D.; Weber, J. R.; Varley, J. B.; Walle, C. G. V. d., Experimental electronic structure of In2O3and Ga2O3. *New Journal of Physics* **2011,** *13* (8), 085014.

216. Zhang, Y.; Yan, J.; Zhao, G.; Xie, W., First-principles study on electronic structure and optical properties of Sn-doped β-Ga2O3. *Physica B: Condensed Matter* **2010,** *405* (18), 3899-3903.
217. Ryou, H.; Yoo, T. H.; Yoon, Y.; Lee, I. G.; Shin, M.; Cho, J.; Cho, B. J.; Hwang, W. S., Hydrothermal Synthesis and Photocatalytic Property of Sn-doped β-Ga2O3 Nanostructure. *ECS Journal of Solid State Science and Technology* **2020,** *9* (4), 045009.
218. Xu, S.; Kim, Y.; Higgins, D.; Yusuf, M.; Jaramillo, T. F.; Prinz, F. B., Building upon the Koutecky-Levich equation for evaluation of next-generation oxygen reduction reaction catalysts. *Electrochimica Acta* **2017,** *255*, 99-108.
219. Kulkarni, A.; Siahrostami, S.; Patel, A.; Nørskov, J. K., Understanding catalytic activity trends in the oxygen reduction reaction. *Chemical reviews* **2018,** *118* (5), 2302-2312.
220. Holewinski, A.; Linic, S., Elementary mechanisms in electrocatalysis: revisiting the ORR Tafel slope. *Journal of The Electrochemical Society* **2012,** *159* (11), H864.
221. Duan, Z.; Henkelman, G., Theoretical Resolution of the Exceptional Oxygen Reduction Activity of Au(100) in Alkaline Media. *ACS Catalysis* **2019,** *9* (6), 5567-5573.
222. Zhao, Y.; Nakamura, R.; Kamiya, K.; Nakanishi, S.; Hashimoto, K., Nitrogen-doped carbon nanomaterials as non-metal electrocatalysts for water oxidation. *Nature communications* **2013,** *4* (1), 1-7.
223. Zheng, Y.; Jiao, Y.; Zhu, Y.; Li, L. H.; Han, Y.; Chen, Y.; Du, A.; Jaroniec, M.; Qiao, S. Z., Hydrogen evolution by a metal-free electrocatalyst. *Nature communications* **2014,** *5* (1), 1-8.
224. Chang, K.; Chen, W., In situ synthesis of MoS 2/graphene nanosheet composites with extraordinarily high electrochemical performance for lithium ion batteries. *Chemical Communications* **2011,** *47* (14), 4252-4254.
225. López-Sancho, M.; Munoz, M., Intrinsic spin-orbit interactions in flat and curved graphene nanoribbons. *Physical Review B* **2011,** *83* (7), 075406.
226. Kleiner, A.; Eggert, S., Curvature, hybridization, and STM images of carbon nanotubes. *Physical Review B* **2001,** *64* (11), 113402.
227. Deng, J.; Li, H.; Xiao, J.; Tu, Y.; Deng, D.; Yang, H.; Tian, H.; Li, J.; Ren, P.; Bao, X., Triggering the electrocatalytic hydrogen evolution activity of the inert two-dimensional MoS 2 surface via single-atom metal doping. *Energy & Environmental Science* **2015,** *8* (5), 1594-1601.
228. Kosynkin, D. V.; Higginbotham, A. L.; Sinitskii, A.; Lomeda, J. R.; Dimiev, A.; Price, B. K.; Tour, J. M., Longitudinal unzipping of carbon nanotubes to form graphene nanoribbons. *Nature* **2009,** *458* (7240), 872-876.
229. Wang, T.; Wang, Z.; Salvatierra, R. V.; McHugh, E.; Tour, J. M., Top-down synthesis of graphene nanoribbons using different sources of carbon nanotubes. *Carbon* **2020,** *158*, 615-623.
230. Shang, S.; Gan, L.; Yuen, C. W. M.; Jiang, S.-x.; Luo, N. M., The synthesis of graphene nanoribbon and its reinforcing effect on poly (vinyl alcohol). *Composites Part A: Applied Science and Manufacturing* **2015,** *68*, 149-154.
231. Joucken, F.; Tison, Y.; Le Fèvre, P.; Tejeda, A.; Taleb-Ibrahimi, A.; Conrad, E.; Repain, V.; Chacon, C.; Bellec, A.; Girard, Y., Charge transfer and electronic doping in nitrogen-doped graphene. *Scientific reports* **2015,** *5* (1), 1-10.
232. Pandey, T.; Nayak, A. P.; Liu, J.; Moran, S. T.; Kim, J. S.; Li, L. J.; Lin, J. F.; Akinwande, D.; Singh, A. K., Pressure-induced charge transfer doping of monolayer graphene/MoS2 heterostructure. *Small* **2016,** *12* (30), 4063-4069.

233. Najafi, L.; Bellani, S.; Martin-Garcia, B.; Oropesa-Nunez, R.; Del Rio Castillo, A. E.; Prato, M.; Moreels, I.; Bonaccorso, F., Solution-processed hybrid graphene flake/2H-MoS2 quantum dot heterostructures for efficient electrochemical hydrogen evolution. *Chemistry of Materials* **2017,** *29* (14), 5782-5786.
234. Murthy, A. P.; Theerthagiri, J.; Madhavan, J., Insights on Tafel constant in the analysis of hydrogen evolution reaction. *The Journal of Physical Chemistry C* **2018,** *122* (42), 23943-23949.
235. Kobets, A. A.; Iurchenkova, A. A.; Asanov, I. P.; Okotrub, A. V.; Fedorovskaya, E. O., Redox processes in reduced graphite oxide decorated by carboxyl functional groups. *physica status solidi (b)* **2019,** *256* (9), 1800700.
236. Campion, A.; Kambhampati, P., Surface-enhanced Raman scattering. *Chemical society reviews* **1998,** *27* (4), 241-250.
237. Langer, J.; Jimenez de Aberasturi, D.; Aizpurua, J.; Alvarez-Puebla, R. A.; Auguié, B.; Baumberg, J. J.; Bazan, G. C.; Bell, S. E.; Boisen, A.; Brolo, A. G., Present and future of surface-enhanced Raman scattering. *ACS nano* **2019,** *14* (1), 28-117.
238. De Albuquerque, C. D. L.; Hokanson, K. M.; Thorud, S. R.; Sobral-Filho, R. G.; Lindquist, N. C.; Brolo, A. G., Dynamic imaging of multiple SERS hotspots on single nanoparticles. *ACS Photonics* **2020,** *7* (2), 434-443.
239. Lee, K. L.; Hung, C. Y.; Pan, M. Y.; Wu, T. Y.; Yang, S. Y.; Wei, P. K., Dual Sensing Arrays for Surface Plasmon Resonance (SPR) and Surface-Enhanced Raman Scattering (SERS) Based on Nanowire/Nanorod Hybrid Nanostructures. *Advanced Materials Interfaces* **2018,** *5* (21), 1801064.
240. Pande, S.; Ghosh, S. K.; Praharaj, S.; Panigrahi, S.; Basu, S.; Jana, S.; Pal, A.; Tsukuda, T.; Pal, T., Synthesis of normal and inverted gold− silver core− shell architectures in β-cyclodextrin and their applications in SERS. *The Journal of Physical Chemistry C* **2007,** *111* (29), 10806-10813.
241. Yoo, S. S.; Ho, J.-W.; Shin, D.-I.; Kim, M.; Hong, S.; Lee, J. H.; Jeong, H. J.; Jeong, M. S.; Yi, G.-R.; Kwon, S. J., Simultaneously intensified plasmonic and charge transfer effects in surface enhanced Raman scattering sensors using an MXene-blanketed Au nanoparticle assembly. *Journal of Materials Chemistry A* **2022,** *10* (6), 2945-2956.
242. Portales, H.; Saviot, L.; Duval, E.; Gaudry, M.; Cottancin, E.; Pellarin, M.; Lermé, J.; Broyer, M., Resonant Raman scattering by quadrupolar vibrations of Ni-Ag core-shell nanoparticles. *Physical Review B* **2002,** *65* (16), 165422.
243. Bouremana, A.; Guittoum, A.; Hemmous, M.; Martínez-Blanco, D.; Gorria, P.; Blanco, J.; Benrekaa, N., Microstructure, morphology and magnetic properties of Ni nanoparticles synthesized by hydrothermal method. *Materials Chemistry and Physics* **2015,** *160*, 435-439.
244. Khodashenas, B.; Ghorbani, H. R., Synthesis of silver nanoparticles with different shapes. *Arabian Journal of Chemistry* **2019,** *12* (8), 1823-1838.
245. Cao, Y.; Liang, P.; Dong, Q.; Wang, D.; Zhang, D.; Tang, L.; Wang, L.; Jin, S.; Ni, D.; Yu, Z., Facile reduction method synthesis of defective MoO2–x nanospheres used for SERS detection with high chemical enhancement. *Analytical chemistry* **2019,** *91* (13), 8683-8690.
246. Chava, V. S.; Chandrasekhar, P.; Gomez, A.; Echegoyen, L.; Sreenivasan, S. T., MXene-based tailoring of carrier dynamics, defect passivation, and interfacial band alignment for efficient planar p–i–n perovskite solar cells. *ACS Applied Energy Materials* **2021,** *4* (11), 12137-12148.
247. Biz, C.; Fianchini, M.; Gracia, J., Strongly correlated electrons in catalysis: focus on quantum exchange. *ACS Catalysis* **2021,** *11* (22), 14249-14261.

248. Li, J.; Ma, J.; Ma, Z.; Zhao, E.; Du, K.; Guo, J.; Ling, T., Spin effect on oxygen electrocatalysis. *Advanced Energy and Sustainability Research* **2021,** *2* (8), 2100034.
249. Marcos-Hernández, M.; Cerrón-Calle, G. A.; Ge, Y.; Garcia-Segura, S.; Sánchez-Sánchez, C. M.; Fajardo, A. S.; Villagrán, D., Effect of surface functionalization of Fe3O4 nano-enabled electrodes on the electrochemical reduction of nitrate. *Separation and Purification Technology* **2022,** *282*, 119771.
250. Testa-Anta, M.; Ramos-Docampo, M. A.; Comesaña-Hermo, M.; Rivas-Murias, B.; Salgueiriño, V., Raman spectroscopy to unravel the magnetic properties of iron oxide nanocrystals for bio-related applications. *Nanoscale Advances* **2019,** *1* (6), 2086-2103.
251. Gatard, V.; Deseure, J.; Chatenet, M., Use of magnetic fields in electrochemistry: a selected review. *Current Opinion in Electrochemistry* **2020,** *23*, 96-105.
252. Lin, M.-Y.; Hourng, L.-W.; Wu, C.-H., The effectiveness of a magnetic field in increasing hydrogen production by water electrolysis. *Energy Sources, Part A: Recovery, Utilization, and Environmental Effects* **2017,** *39* (2), 140-147.
253. Gilleo, M., Superexchange interaction energy for Fe 3+-O 2−-Fe 3+ linkages. *Physical Review* **1958,** *109* (3), 777.
254. Cuenca, J. A.; Bugler, K.; Taylor, S.; Morgan, D.; Williams, P.; Bauer, J.; Porch, A., Study of the magnetite to maghemite transition using microwave permittivity and permeability measurements. *Journal of Physics: Condensed Matter* **2016,** *28* (10), 106002.
255. Rosencwaig, A., Double exchange and electron hopping in magnetite. *Canadian Journal of Physics* **1969,** *47* (21), 2309-2317.
256. Ren, X.; Wu, T.; Sun, Y.; Li, Y.; Xian, G.; Liu, X.; Shen, C.; Gracia, J.; Gao, H.-J.; Yang, H., Spin-polarized oxygen evolution reaction under magnetic field. *Nature Communications* **2021,** *12* (1), 2608.
257. Choy, T.-S.; Chen, J.; Hershfield, S., Correlation between spin polarization and magnetic moment in ferromagnetic alloys. *Journal of applied physics* **1999,** *86* (1), 562-564.
258. Chrétien, S.; Metiu, H., O 2 evolution on a clean partially reduced rutile TiO 2 (110) surface and on the same surface precovered with Au 1 and Au 2: The importance of spin conservation. *The Journal of chemical physics* **2008,** *129* (7), 074705.
259. Im, H.; Ma, S.; Lee, H.; Park, J.; Park, Y. S.; Yun, J.; Lee, J.; Moon, S.; Moon, J., Elucidating the chirality transfer mechanisms during enantioselective synthesis for the spin-controlled oxygen evolution reaction. *Energy & Environmental Science* **2023**.
260. Bian, Z.; Kato, K.; Ogoshi, T.; Cui, Z.; Sa, B.; Tsutsui, Y.; Seki, S.; Suda, M., Hybrid Chiral MoS2 Layers for Spin-Polarized Charge Transport and Spin-Dependent Electrocatalytic Applications. *Advanced Science* **2022,** *9* (17), 2201063.
261. Liang, Y.; Banjac, K.; Martin, K.; Zigon, N.; Lee, S.; Vanthuyne, N.; Garcés-Pineda, F. A.; Galán-Mascarós, J. R.; Hu, X.; Avarvari, N., Enhancement of electrocatalytic oxygen evolution by chiral molecular functionalization of hybrid 2D electrodes. *Nature Communications* **2022,** *13* (1), 3356.
262. Fransson, J., Chirality-induced spin selectivity: The role of electron correlations. *The journal of physical chemistry letters* **2019,** *10* (22), 7126-7132.
263. Naaman, R.; Waldeck, D. H., Chiral-induced spin selectivity effect. *The journal of physical chemistry letters* **2012,** *3* (16), 2178-2187.
264. Shiota, K.; Inui, A.; Hosaka, Y.; Amano, R.; Ōnuki, Y.; Hedo, M.; Nakama, T.; Hirobe, D.; Ohe, J.-i.; Kishine, J.-i., Chirality-induced spin polarization over macroscopic distances in chiral disilicide crystals. *Physical Review Letters* **2021,** *127* (12), 126602.

265. Lei, J.-C.; Zhang, X.; Zhou, Z., Recent advances in MXene: Preparation, properties, and applications. *Frontiers of Physics* **2015,** *10*, 276-286.
266. Gogotsi, Y.; Anasori, B., The rise of MXenes. ACS Publications: 2019; Vol. 13, pp 8491-8494.
267. Alhabeb, M.; Maleski, K.; Anasori, B.; Lelyukh, P.; Clark, L.; Sin, S.; Gogotsi, Y., Guidelines for synthesis and processing of two-dimensional titanium carbide (Ti3C2T x MXene). *Chemistry of Materials* **2017,** *29* (18), 7633-7644.
268. Isfahani, A. P.; Shamsabadi, A. A.; Alimohammadi, F.; Soroush, M., Efficient mercury removal from aqueous solutions using carboxylated Ti3C2Tx MXene. *Journal of Hazardous Materials* **2022,** *434*, 128780.

Appendix

CCC | RightsLink

Home | Help | Live Chat | Sign in | Create Account

ACS Publications
Most Trusted. Most Cited. Most Read.

In Situ Doping-Enabled Metal and Nonmetal Codoping in Graphene Quantum Dots: Synthesis and Application for Contaminant Sensing

Author: Aruna N. Nair, Venkata S.N. Chava, Saptasree Bose, et al
Publication: ACS Sustainable Chemistry & Engineering
Publisher: American Chemical Society
Date: Nov 1, 2020

Copyright © 2020, American Chemical Society

PERMISSION/LICENSE IS GRANTED FOR YOUR ORDER AT NO CHARGE

This type of permission/license, instead of the standard Terms and Conditions, is sent to you because no fee is being charged for your order. Please note the following:

- Permission is granted for your request in both print and electronic formats, and translations.
- If figures and/or tables were requested, they may be adapted or used in part.
- Please print this page for your records and send a copy of it to your publisher/graduate school.
- Appropriate credit for the requested material should be given as follows: "Reprinted (adapted) with permission from {COMPLETE REFERENCE CITATION}. Copyright {YEAR} American Chemical Society." Insert appropriate information in place of the capitalized words.
- One-time permission is granted only for the use specified in your RightsLink request. No additional uses are granted (such as derivative works or other editions). For any uses, please submit a new request.

If credit is given to another source for the material you requested from RightsLink, permission must be obtained from that source.

BACK | CLOSE WINDOW

CCC Marketplace

CCC | RightsLink

Home | Help | Live Chat | Aruna Nair

Lewis Acid Site Assisted Bifunctional Activity of Tin Doped Gallium Oxide and Its Application in Rechargeable Zn-Air Batteries

Author: Aruna Narayanan Nair, Mohamed F. Sanad, Rahul Jayan, et al
Publication: Small
Publisher: John Wiley and Sons
Date: Jul 28, 2022

© 2022 Wiley-VCH GmbH

Order Completed

Thank you for your order.

This Agreement between Aruna Nair ("You") and John Wiley and Sons ("John Wiley and Sons") consists of your license details and the terms and conditions provided by John Wiley and Sons and Copyright Clearance Center.

Your confirmation email will contain your order number for future reference.

License Number	5503360693999	Printable Details
License date	Mar 06, 2023	

CCC RightsLink

Home | Help | Live Chat | Aruna Nair

ACS Publications
Most Trusted. Most Cited. Most Read.

Heteroatom-Doped Transition Metal Electrocatalysts for Hydrogen Evolution Reaction

Author: Huanyu Jin, Xin Liu, Shuangming Chen, et al
Publication: ACS Energy Letters
Publisher: American Chemical Society
Date: Apr 1, 2019

Copyright © 2019, American Chemical Society

PERMISSION/LICENSE IS GRANTED FOR YOUR ORDER AT NO CHARGE

This type of permission/license, instead of the standard Terms and Conditions, is sent to you because no fee is being charged for your order. Please note the following:

- Permission is granted for your request in both print and electronic formats, and translations.
- If figures and/or tables were requested, they may be adapted or used in part.
- Please print this page for your records and send a copy of it to your publisher/graduate school.
- Appropriate credit for the requested material should be given as follows: "Reprinted (adapted) with permission from {COMPLETE REFERENCE CITATION}. Copyright {YEAR} American Chemical Society." Insert appropriate information in place of the capitalized words.
- One-time permission is granted only for the use specified in your RightsLink request. No additional uses are granted (such as derivative works or other editions). For any uses, please submit a new request.

CCC RightsLink

Home | Help | Live Chat | Aruna Nair

SPRINGER NATURE

Improved water electrolysis using magnetic heating of FeC–Ni core–shell nanoparticles

Author: Christiane Niether et al
Publication: Nature Energy
Publisher: Springer Nature
Date: May 14, 2018

Copyright © 2018, The Author(s)

Order Completed

Thank you for your order.

This Agreement between Aruna Nair ("You") and Springer Nature ("Springer Nature") consists of your license details and the terms and conditions provided by Springer Nature and Copyright Clearance Center.

Your confirmation email will contain your order number for future reference.

License Number	5507370791859
License date	Mar 13, 2023

Printable Details

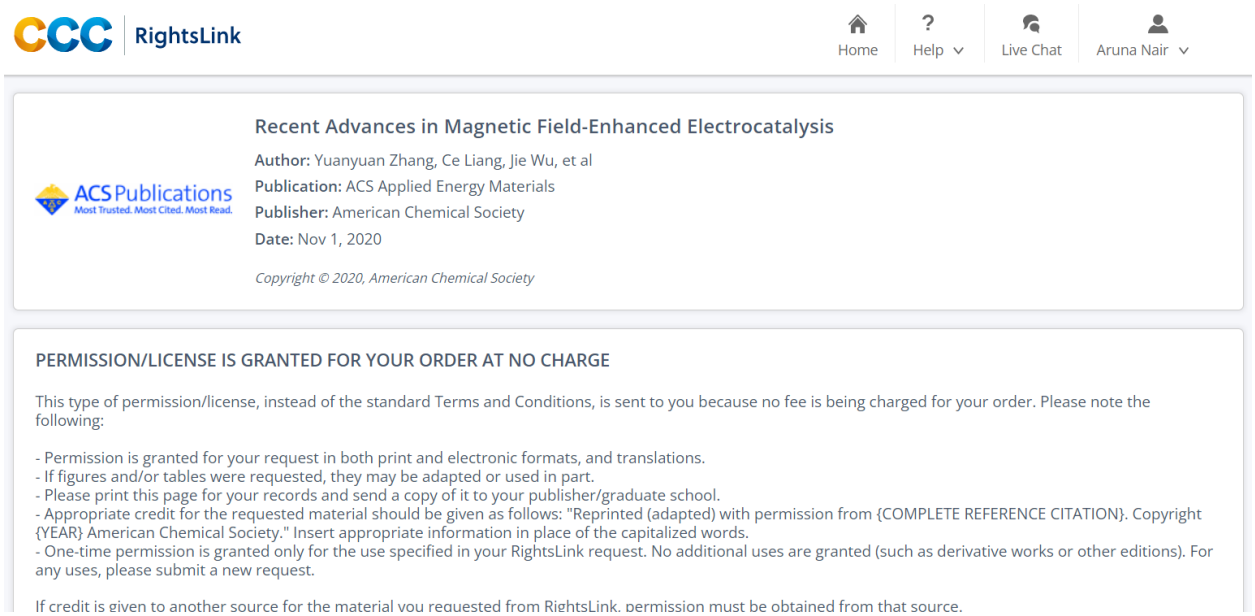
RightsLink
Home
Help
Live Chat
Aruna Nair
Recent Advances in Magnetic Field-Enhanced Electrocatalysis
Author: Yuanyuan Zhang, Ce Liang, Jie Wu, et al
Publication: ACS Applied Energy Materials
Publisher: American Chemical Society
Date: Nov 1, 2020
Copyright © 2020, American Chemical Society
PERMISSION/LICENSE IS GRANTED FOR YOUR ORDER AT NO CHARGE
This type of permission/license, instead of the standard Terms and Conditions, is sent to you because no fee is being charged for your order. Please note the following:
- Permission is granted for your request in both print and electronic formats, and translations.
- If figures and/or tables were requested, they may be adapted or used in part.
- Please print this page for your records and send a copy of it to your publisher/graduate school.
- Appropriate credit for the requested material should be given as follows: "Reprinted (adapted) with permission from {COMPLETE REFERENCE CITATION}. Copyright {YEAR} American Chemical Society." Insert appropriate information in place of the capitalized words.
- One-time permission is granted only for the use specified in your RightsLink request. No additional uses are granted (such as derivative works or other editions). For any uses, please submit a new request.
If credit is given to another source for the material you requested from RightsLink, permission must be obtained from that source.

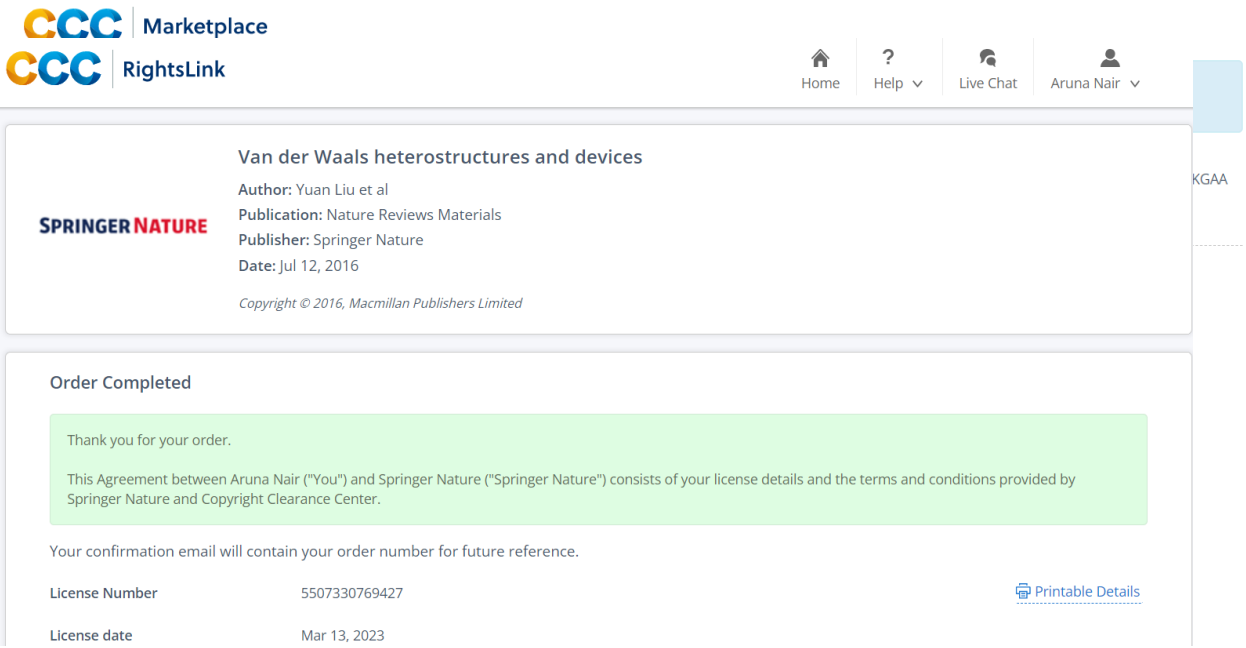
Marketplace
RightsLink
Home
Help
Live Chat
Aruna Nair
Van der Waals heterostructures and devices
Author: Yuan Liu et al
Publication: Nature Reviews Materials
Publisher: Springer Nature
Date: Jul 12, 2016
Copyright © 2016, Macmillan Publishers Limited
Order Completed
Thank you for your order.
This Agreement between Aruna Nair ("You") and Springer Nature ("Springer Nature") consists of your license details and the terms and conditions provided by Springer Nature and Copyright Clearance Center.
Your confirmation email will contain your order number for future reference.
License Number 5507330769427
Printable Details
License date Mar 13, 2023

CCC RightsLink

Home | Help | Live Chat | Aruna Nair

Superparamagnetic nanoadsorbents for the removal of trace As(III) in drinking water

Author:
Mariana Marcos-Hernández,Roy A. Arrieta,Karen Ventura,José Hernández,Camilah D. Powell,Ariel J. Atkinson,Jasmina S. Markovski,Jorge Gardea-Torresdey,Kiril D. Hristovski,Paul Westerhoff,Michael S. Wong,Dino Villagrán

Publication: Environmental Advances

Publisher: Elsevier

Date: July 2021

© 2021 The Authors. Published by Elsevier Ltd.

Creative Commons Attribution-NonCommercial-No Derivatives License (CC BY NC ND)

This article is published under the terms of the Creative Commons Attribution-NonCommercial-No Derivatives License (CC BY NC ND).
For non-commercial purposes you may copy and distribute the article, use portions or extracts from the article in other works, and text or data mine the article, provided you do not alter or modify the article without permission from Elsevier. You may also create adaptations of the article for your own personal use only, but not distribute these to others. You must give appropriate credit to the original work, together with a link to the formal publication through the relevant DOI, and a link to the Creative Commons user license above. If changes are permitted, you must indicate if any changes are made but not in any way that suggests the licensor endorses you or your use of the work.

Permission is not required for this non-commercial use. For commercial use please continue to request permission via RightsLink.

CCC Marketplace

This is a License Agreement between ARUNA ("User") and Copyright Clearance Center, Inc. ("CCC") on behalf of the Rightsholder identified in the order details below. The license consists of the order details, the Marketplace Permissions General Terms and Conditions below, and any Rightsholder Terms and Conditions which are included below.

All payments must be made in full to CCC in accordance with the Marketplace Permissions General Terms and Conditions below.

Order Date	13-Mar-2023	Type of Use	Republish in a thesis/dissertation
Order License ID	1333353-1	Publisher	ROYAL SOCIETY OF CHEMISTRY
ISSN	1463-9084	Portion	Image/photo/illustration

LICENSED CONTENT

Publication Title	Physical chemistry chemical physics	Publication Type	e-Journal
Article Title	Asymmetric reactions induced by electron spin polarization.	Start Page	21570
		End Page	21582
Author/Editor	Royal Society of Chemistry (Great Britain)	Issue	38
Date	01/01/1999	Volume	22
Language	English	URL	http://firstsearch.oclc.org/journal=1463-9...
Country	United Kingdom of Great Britain and Northern Ireland		
Rightsholder	Royal Society of Chemistry		

Curriculum Vita

Aruna Narayanan Nair graduated with BS-MS in Physics from Indian Institute of Science Education and Research, Thiruvananthapuram. She is currently enrolled in the Ph.D. program with Dr Sreeprasad Sreenivasan at the Department of Chemistry and Biochemistry at The University of Texas at El paso. During her Ph.D., she worked on synthesis of several functional materials including low dimensional materials for electrochemical energy and sensing applications. She has published 12 articles to her credit, including several works in collaboration. She is a recipient of the prestigious Les and Harriet Dodson Endowment Research Grant, Graduate School Research Grant, and recipient of Three Minute Thesis and People's Choice award at The University of Texas at El Paso. She has mentored several undergraduate chemistry students in developing and directing quantum material synthesis research projects, as well as providing first-hand training for characterization and application. She is also proud to have been highlighted as an excellent researcher in the HBCU-OMI Program, sponsored by the US Department of Energy Office of Fossil Energy and Carbon Management.